INVESTIGATION OF NiO REDUCTION DYNAMICS AND PROPERTIES OF NiO-(Al/Ti/Mg) BASED NANOCOMPOSITES

A thesis submitted

by

Aneeta Manjari Padhan

to

Indian Institute of Technology Guwahati

in

Partial fulfillment of the requirement for the award of the degree of
Doctor of Philosophy in Physics

Department of Physics
Indian Institute of Technology Guwahati
Guwahati 781 039, Assam, India
March 2020

INVESTIGATION OF NiO REDUCTION DYNAMICS AND PROPERTIES OF NiO-(Al/Ti/Mg) BASED NANOCOMPOSITES

A thesis submitted

by

Aneeta Manjari Padhan

to

Indian Institute of Technology Guwahati

in

Partial fulfillment of the requirement for the award of the degree of
Doctor of Philosophy in Physics

Department of Physics
Indian Institute of Technology Guwahati
Guwahati 781 039, Assam, India
March 2020

Statement

The work contained in the thesis entitled "***Investigation of NiO reduction dynamics and properties of NiO-(Al/Ti/Mg) based nanocomposites***" has been carried out by me under the supervision of Prof. Perumal Alagarsamy at the Department of Physics, Indian Institute of Technology Guwahati. This work has not been submitted elsewhere for the award of any degree.

March 2020

(Aneeta Manjari Padhan)
Roll No: 146121018
Department of Physics
Indian Institute of Technology Guwahati
Guwahati – 781039
India.

Certificate

It is certified that the work contained in the thesis, entitled "***Investigation of NiO reduction dynamics and properties of NiO-(Al/Ti/Mg) based nanocomposites***", submitted by Aneeta Manjari Padhan, a Ph.D. student of the Department of Physics, Indian Institute of Technology Guwahati for the award of the degree of Doctor of Philosophy, has been carried out under the supervision of Prof. Perumal Alagarsamy. This work has not been submitted elsewhere for the award of any degree.

March 2020

(Prof. Perumal Alagarsamy)
Professor
Department of Physics
Indian Institute of Technology Guwahati
Guwahati – 781039
India.

Dedicated to

my beloved parents…

Acknowledgments

First, I would like to express my utmost gratitude to my thesis supervisor, Prof. Perumal Alagarsamy, for allowing me to work with him. During my doctoral research, I have not only learned Physics in a better way but also got to know from him what an energetic spirit truly means for. I must acknowledge him for his patience, motivation, immense support, and guidance towards my research work and providing me unconditional freedom to work, think and express my thoughts from the very first day of joining in the lab. This thesis work would not have come to its conclusion without his timely guidance and excellent mentorship.

I am grateful to the Doctoral committee members (Prof. S. Ravi, Dr. D. Pamu, and Prof. M. Qureshi) for their meaningful insights, constructive criticism, and valuable feedback for the improvement of my research work. My earnest thanks to the current Head of the Department, Prof. S. Ghosh, and the former department Heads, Prof. P. Poulose, and Prof. S. Basu for their extensive administrative cooperation. I extend my sincere appreciation to all the faculty members of the Department of Physics during my research life in IIT Guwahati.

My sincere thanks also go to Dr. P. Saravanan, DMRL Hyderabad, for helping with the DSC measurements for thermal studies, and Dr. M. Sathish, CECRI Karaikudi, India, for supporting with the TEM measurements for microstructural studies.

I sincerely thank the Department of Physics, Indian Institute of Technology, Guwahati, and the Ministry of Human Resource Development, Government of India, for providing the opportunity and facilities to pursue my Ph.D. study.

I convey my gratitude to Dr. Sidananda Sarma, scientific officer in the Department of Physics, for providing me the opportunity to handle requisite experimental set-ups in the department. Also, I thank Mr. Chandan Borgohain, Dr. Kula Kamal Senapati, Mr. Madhurjya Borah, and Mr. Kesho Singh, scientific officers of CIF, IIT Guwahati for extending their expertise in handling various instruments, which I have used for my research work. I am forever grateful to the non-teaching staff of the Physics department for their continuous help and kind support whenever necessary.

I much appreciate and acknowledge my seniors Dr. Bhagaban Kisan, Dr. Anabil Gayen, Dr. Patta Ravikumar, Dr. Camelia Das, and Dr. Koushik Saikia, who helped me in various ways throughout my research work. Special thanks to my lab-mates Dolly, Subrata, Manisha, Pushpesh, Nitu, Alok, Madhav, Dev, and Didwamsha for sharing a beautiful and supportive working environment in the lab and for all the wonderful times we spent together.

Special thanks to my dearest friend, Dr. Rajkumar Modak, for always standing by my side and guiding me in every possible way. Indeed, without you, I couldn't have come this far to finish this job. Bikrant and Manas, these two deserve a special mention for all their moral support and love. I really adore you both and our friendship a lot.

Finally, my deep and sincere gratitude to my family for encouraging me in all of my pursuits and inspiring me to follow my dreams. I sincerely thank both of my sisters for being there as my friends, mentors, and my happiness sources. I am forever indebted to my parents, who helped me a lot to pursue my Ph.D. career. Thank you, papa and maa, for always walking through each and every step I took since I know of and the ones I don't even remember. You will forever remain my biggest motivation to achieve anything I wish for. My nephew Anwesh also deserves a special mention for playing the funniest and cutest part of my Ph.D. journey, who perhaps wanted the most to help me in my research at just the age of eight. Also, sincere thanks to every person who helped me directly or indirectly during the completion of my study, some of whom I may have inadvertently missed mentioning in this acknowledgment.

Aneeta Manjari Padhan

PREFACE

Nanoscale transition metal-metal oxide matrix composites are significant materials for a wide range of potential technological applications due to their tunable physical properties. These nanocomposites are produced by the addition of reinforcement particles to the metal oxide matrix. Based on the processability, transition metal nanoparticles embedded in a transition metal oxide matrix have been extensively implemented in various areas of research, such as catalysis, gas sensors, Li-storage anodes, supercapacitors, spintronic devices, and hard magnetic materials. For ferromagnetic transition metals, the changes in the magnetic properties reflect the progression of *in-situ* or *ex-situ* reduction in transition metal-oxides. This forms an exciting part of the research for the creation of ferromagnetic nanoparticles embedded in the antiferromagnetic oxide matrix.

Among them, NiO-based nanocomposite obtained through the *in-situ* reduction process is a significant area for industrial applications. Most of the NiO reductions reported in the literature are the high temperature based displacement reactions. Thus, a preferable solid-solid or solid-liquid mechanochemical reduction by reactive milling process can lead to the fabrication of NiO-based nanocomposites with tunable structural and magnetic properties. Reactive milling or the mechanochemical synthesis by using a high-energy ball milling route is a cost-effective and industrially viable process for the fabrication of materials in fine powder form with the requisite shape and dimension. However, most of the reported NiO reduction works are limited either to the evaluation of the structure of nanocomposites or to their magnetic behavior. Although the microstructure and magnetic properties of a system at the nanoscale are closely connected, detailed studies involving both the features are rare in the literature.

Therefore, in this thesis, we present a detailed investigation of NiO reduction dynamics and the properties of the resulting NiO-(Al/Ti/Mg) based nanocomposites prepared by using the high-energy planetary ball milling technique under dry milling conditions. This study includes (i) the effect of the substitutional elements on the nature and types of NiO reduction dynamics; (ii) the impact of reduction process on the structural, vibrational, and magnetic properties of NiO-(Al/Ti/Mg) nanocomposites as a function of specified compositions and milling periods; (iii) understanding of the temperature and field-dependent magnetic properties of the as-milled powders; and (iv) obtaining correlations between the structural,

microstructural, vibrational and magnetic properties of the nanocomposites with the mechanochemical reduction dynamics and composition-dependent behaviors.

The present thesis is organized as follows: **Chapter 1** presents a brief introduction to the content of the thesis, along with the relevant literature review in detail. **Chapter 2** summarizes the fundamental aspects, including the brief overview of the structure of NiO, defects, mechanochemical reduction process, the basics of magnetism, intrinsic properties of magnetic materials, types of anisotropies and magnetic interactions, *etc*. **Chapter 3** discusses the experimental techniques, including the sample preparation methodologies used in the present studies. The basic principle and theory behind the experiments, the experimental set-up, and the measurements/methodologies leading to the determination of the physical properties are also discussed. The results and discussions of NiO-(Al/Ti/Mg) based nanocomposite powders, obtained by using high-energy ball milling technique, are presented in Chapters 04 to 06.

Chapter 4 discusses the effects of Al (x at.%) content and milling time (t_m) on the structural and magnetic properties of NiO-Al based nanocomposites. *In-situ* NiO-Ni-Al_2O_3 nanocomposites are prepared by varying (i) the compositions of the initial powders as NiO-Al (x at.%) with x = 0 - 40 for a constant milling time (t_m) of 30 hrs and (ii) t_m from 0 to 30 hrs and by fixing the compositions as NiO-Al (x at.%) with x = 0, 20, 40. The dynamics of mechanically activated aluminothermic reduction of NiO involving two different types of reaction kinetics, and the resulting structural and magnetic properties are reported in detail. **Chapter 5** is meant for the detailed study of the structural, vibrational, and magnetic properties of NiO-Ti based nanocomposites prepared (i) by varying the compositions of the initial powders as NiO-Ti (x at.%) with x = 0 - 35 for a constant t_m of 30 hrs and (ii) by varying t_m from 0 to 30 hrs and by fixing the compositions as NiO-Ti (x at.%) with x = 20, 35. The correlation between structural, vibrational, and magnetic properties of the milled powders concerning the reduction dynamics is presented elaborately. **Chapter 6** is focused on the systematic investigations on the structural, vibrational, and magnetic properties of NiO-Mg based nanocomposites prepared by varying the composition of the powders as NiO-Mg (x at.%) with x = 0 – 50.

The above systematic investigations have several interesting outcomes, which contribute to the understanding of (i) the reduction dynamics and the resulting physical properties of NiO-(Al/Ti/Mg) powders under different compositions and milling periods, (ii) the magnetic phase transitions, temperature-induced structural phase transformation and the associated magnetic behaviors, and (iii) the exchange bias effect and its magnitude depending

on the relative fractions of NiO and Ni phases. Furthermore, the present studies have also revealed the strong correlation between structure, vibrational, and magnetic properties of NiO-(Al/Ti/Mg) based nanocomposites prepared under optimum milling conditions. To the best of our knowledge, this is the first time we are reporting the mechanochemical reduction dynamics and the correlative magnetic behavior over a wide range of compositions. The controlled reduction of NiO by Al/Mg/Ti into the *in-situ* nanocomposites may find possible applications in the fields of metallurgy, ore reduction, and catalysis.

Chapter 7 provides a summary of the results obtained in the thesis and briefly points out the scope for further work on these topics. References and lists of publications arising out of the present investigations are listed at the end of the thesis.

CONTENTS

Chapter 1

Prologue

1.1. Introduction:

'There's Plenty of Room at the Bottom', the technological vision of extreme miniaturization, envisioned and presented by the esteemed Nobel Laureate Richard P. Feynman [FEYN1960] at the California Institute of Technology has now become a classic in the 20th-century science. This embodied the next scientific and industrial revolution through the introduction of the newer and exciting world of 'NANOSCIENCE' [FEYN1960, DAVI1999, DUPA2007, SCHO2018]. Often regarded as 'the science of extremely tiny', nanoscience in a broader sense envisions a technology using the ultimate toolbox of nature, through the atomic built-up of materials with smallest functional organizations lying within the dimension of nanometer-scale or one billionth of a meter scale [BHUS2007]. Coined in the year 1974 by Norio Taniguchi to describe extra-high precision and ultra-fine dimensions, nanotechnology is the controlled manipulation of individual constituent molecules and interacting groups of molecules to produce nanostructured materials and submicron objects, which can have practical applications in the real world. The nanomaterial synthesis is divided broadly into two categories (Top-to-bottom and bottom-to-top approaches) and find the most profound impact on the 21st century economic and social stature. Scientific research in nanoscale science and technology promises breakthroughs in the diverse areas of materials and manufacturing, electronics, biotechnology, healthcare, energy, environment, and the field of information technology [CHON2004, KELS2005, SING2011, WOLF2012, PATR2018, STEF2018].

In this context, due to the rapid progress in the fabrication and processing of nanostructures, the nanomaterials are classified depending upon their size, geometries, crystalline textures, chemistries, and physical properties, which are known as nanoparticles, nanowires, nanoribbons, nanofibers, nanocomposites, nanofoams, nanopores, nanocrystals, *etc.* [RAOC2004]. Among them, nanocomposites are the example of a real and rapidly growing application through the still futuristic image of the nanotechnological world [BHUS2007, PAUL2008, CAMA2009, CHOI2019]. In general, composite is an assemblage of two or more phases of chemical constituents or structures of different natures. It usually consists of a matrix and a reinforcement (either in metal, ceramic, or polymer phase) and completes a better performance material than their individual counterparts [CHAW2012, HUN2012]. Especially, nanocomposites are the unique architectured composite/hetero-structures with multiple phase domains (as shown in Figure 1.01), and at least one of the domains has a nanometric dimension. It is also possible that all the phases

can have nanometer dimensions. Nanocomposites have emerged as suitable alternatives to outdo the limitations of Monolithics and micro composites by the incorporation of nanosized particles into the matrix of a standard material.

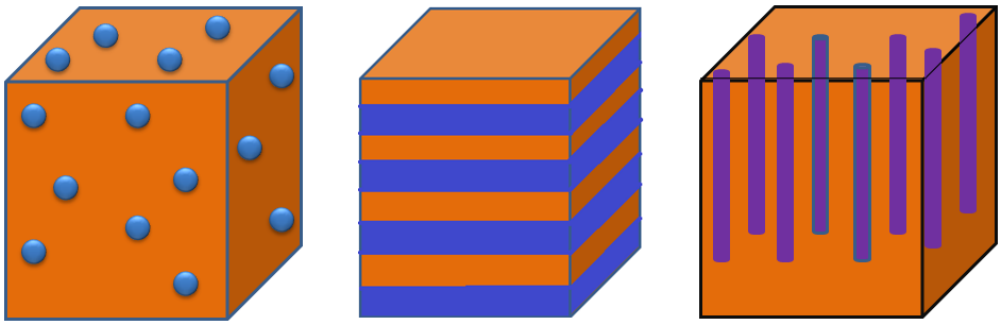

Figure 1.01: Schematic representation of types of nanocomposites.

Recently, they also attracted much attention owing to the synergistic properties induced by the interactions between different nanometer-scale objects. Nanocomposites show fascinating magnetic, magneto-optical, and semiconducting properties, which can easily be modulated by the interfacial interactions between the different nano-components. This opens up novel opportunities to develop advanced multifunctional nanomaterials for device concepts and applications [KREM2012]. Among the different nanocomposite systems, metal-oxide based nanocomposites with tailored properties find potential applications in the fields of photocatalytic [LINI2011, PRAJ2019], photovoltaic [CLAV2014], electronic [COST2009], and magnetic properties [YIJB2005, FIGU2008]. Also, the metallic nanoparticles coupled/dispersed finely with metal oxides are of promising applications in catalysis, plasmonics, sensors, nanomagnetism, ore-reduction, metallurgy processes [PATE2019], *etc*.

1.2. Motivation behind the work:

With the recent advances in the processability and applications of metal-metal oxide nanocomposite systems, there has been a considerable search for new metal oxides, which can be directed towards controlled compositions and structures. Nevertheless, to reach a suitable transition metal oxide (TMO), care has to be taken on the choice of the materials. Among all the TMOs, Nickel Oxide (NiO) is one of the most promising materials owing to its excellent characteristics such as high chemical and thermal stabilities with environmental

benignity, low cost, and enhanced physical and chemical properties from the reduction of bulk to nanostructure [KATE2018]. Being a transition metal monoxide with a simple face-centered-cubic (*fcc*) structure (Space group $Fm\bar{3}m$ and number 225), it possesses a strongly correlated electron system. NiO is the known antiferromagnetic oxide that presents the highest Néel temperature ($T_N \sim 525$ K) [RINA2014] and hence, plays a crucial role in addressing the challenge of storage density increase in magnetic recording media [DETO2015]. In the last decade, nanoscale NiO has generated renewed interest owing to its properties such as high surface-area-to-volume-ratio, presence of defects like Ni and O vacancies, tunable magnetic and electric properties, *etc*. and find applications in catalysis [XIAO2011], biosensors [TYAG2013], electrochromics [RUNN2014], anodic capacitors [PILB2015], fuel and solar cells [GIBS2013], smart windows [PATI2013] and spintronic devices [VARD2015]. Besides, NiO shows effective particle size-dependent magnetic properties with competitive finite-size versus surface effects where the AFM behavior of NiO is mostly tuned at nanolevel [RICH1956, KODA19971, TIWA2005, MAND2011, KISA2014, GAND20171]. With the strong interplay between finite-size effects, defects and oxygen vacancies, NiO nanoparticles exhibit significant moments, high coercivity, loop shifts, and size-dependent Curie temperature (T_C) [MAKH1997, KODA19971, TIWA2005, YIJB2007].

Besides, with the recent amalgamations of metal-metal oxide nanocomposites having one and/or more magnetic constituents, there has been considerable research attention towards the 'Magnetic Nanocomposites' systems, which possess unique and novel properties induced by magnetic interactions between their constituents [BEHR2011, GOVA2014, HAUS2015, TIET2015, ZHAN2017, SWIA2018]. Hence, metal-oxide based magnetic nanocomposites containing AFM ordered NiO and/or FM Ni are extensively studied to tune the overall structural and magnetic behavior of the nanocomposite systems. As the properties of the multi-component particles depend not only on their size and structure but also by their composition, these NiO/Ni-based nanocomposites are of extensive applications than the single component particles. Hence, these composites have received increased attention not only for their interesting chemical characteristics, such as applications in bioseparation [LEEI2006], Li-storage [CHEN2018], catalysts [SONG2017], fuel cell electrodes [MURA1996], gas sensors [FASA2013], or supercapacitors/battery hybrids [LUQ2011] but also for their magnetic properties [SORT1999, SALG2008, JOHL2014, YAOX2014]. In particular, the NiO/Ni nanocomposites having FM Ni

nanoparticles embedded in the AFM NiO matrix show interesting magnetic phenomena, like the exchange bias effect, tunable blocking temperature, and T_C [SETO2005, NOGU2008. DELB2011, DUAN2012, KREM2012, KISA2014, GOKU2015, BHAN2019].

However, to tailor the properties of these nanocomposites, a relevant synthesis route is necessitated to control the chemical composition, crystal structure, morphology, and mutual interaction between metallic and oxide phases. Depending upon the synthesis routes, these nanocomposites can be classified into two groups: *ex-situ* and *in-situ*. The *ex-situ* processes consist of the addition of reinforcements prior to the synthesis [XIAK2010, CASA20141]. In contrast, the *in-situ* composites have reinforcement phases formed through the chemical reactions between different components in the system during the processing itself [CASA20142]. There are several techniques implied for the synthesis of metal-metal oxide nanocomposites, like hydrothermal [TUW2015], sputtering [YIJB2005, ABIY2007], pulsed electro-deposition [LIAN2015], physical vapor depositions [HONC2010], sol-gel [KWIA2000, ENNA2004], solution combustion [PRAB2015], eruption combustion [WENW2011], ball-milling [TAKA1993], *etc*. Amongst all these techniques, the *in-situ* mechanochemical approaches coupling both the mechanical and physical phenomena using the high-energy ball milling technique have gained unprecedented attention for the synthesis of nanocomposites with tunable properties [DOPP2004, NOGU2008, KAUP2011].

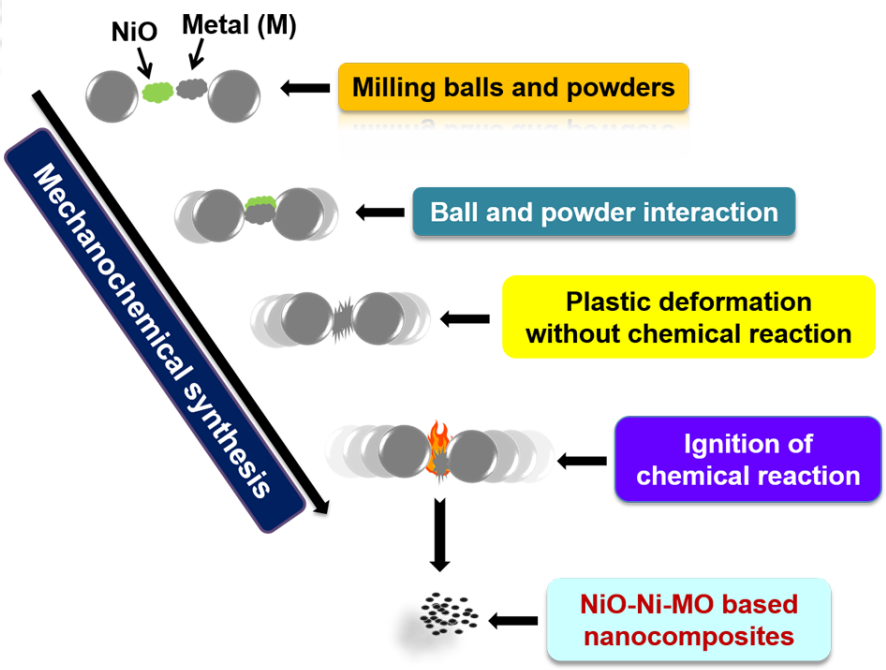

Figure 1.02: Schematic diagram of a mechanochemical reaction process in NiO.

Ball milling/mechanical alloying (MA), in general, represents a solid-state powder processing technique that involves repetitive welding, fracturing, and rewelding of the powder particles in a high-energy ball mill [SURY2001]. This preparation route is not only used to synthesize nanocrystalline materials, amorphous alloys, solid-solutions, and intermetallic phases but also activates the solid-solid and even solid-liquid chemical reactions during the milling process effectively [SURY2001, SURY2004]. If the initial powder mixtures are chemically reactive by nature, the milling is not only associated with the size refinement but also accompanied by the chemical reactions [KOCH1991]. As the mechanical energy supplied during the milling process is utilized for processing the *in-situ* chemical reactions, it has been termed as the mechanochemical synthesis/reactive milling. In reactive milling, the intensive mechanical treatment of crystalline solids occurs through the repetitive welding and fracturing of powders as schematically presented in Figure 1.02. This leads to the increasing area of contact between the reactant powder particles due to significant plastic deformation and the size refinement. This allows the fresh surfaces to come into contact repeatedly with the simultaneous accumulation of structural defects, and the reaction proceeds without any diffusion process through the product phases. As a consequence, it induces chemical reactions with a kinetic and thermodynamic behavior much different from the thermochemical reactions [TSUZ2004]. This method is one of the most inexpensive techniques for studying the metal-oxide based reduction processes on the different reaction kinetics, which is predominantly suitable for the synthesis of advanced materials, composites, nanoparticles, and nanostructured materials at moderately low temperatures in a ball mill without any need for external heating.

The mechanochemical reduction processes in different oxide systems have been reported: (1) Schaffer *et al*. [SCHA1989] reported reaction between Ca and CuO to produce metallic Cu; (2) Takacs [TAKA1992] illustrated the reduction of Fe_3O_4 by Al; (3) Lu *et al.* [LUY1993] also showed the reduction of Fe_3O_4 by Al for the formation of both ferromagnetic and superparamagnetic Fe particle; (4) Mulas *et al.* [MULA2001] demonstrated for Cu_2O and CuO by reacting with Ti and Zr; (5) Botta *et al.* [BOTT2003] revealed the formation of Fe-$FeAl_2O_4$-Al_2O_3 metal ceramics complex by the mechanochemical activation of the Al and Fe_3O_4 powder mixtures; (6) Venugopal *et al.* [VENU2005] showed the reduction of CuO and Cu_2O by Al to develop Cu and Al_2O_3 nanoparticles; (7) Heidarpour *et al.* [HEID2009] illustrated the formation of Al_2O_3/Mo nanocomposite by reacting Al with MoO_3; (8) Hosseini *et al.* [HOSS2012] studied the

synthesis of Co and Al_2O_3 from Co_3O_4/Al powder mixture, *etc*. In addition, the careful review of the literature suggests that most of these reduction reactions are conducted by Al.

In the case of NiO, the solid-state reaction of NiO and a solid-metallic reducing agent has been reported earlier. Matteazzi *et al.* [MATT1992] initially investigated the solid-state reaction of NiO-Al using the planetary ball mill to produce the Ni/Al_2O_3 nanocomposite. Li *et al.* [LIJ2004] studied the preparation of Ni/Al_2O_3 nanocomposite powders by using the high-energy ball milling and observed the non-occurrence of self-propagation reactions due to the presence of dilute alumina in the raw powder mixture. Anvari *et al.* [ANVA2009] and Oleszak [OLES2004] have shown the formation of α-Al_2O_3 during dry milling of NiO-Al. Similarly, the effect of mechanical activation on the NiO-Al reaction process was reported by Udhayabanu *et al.* [UDHA2010] using toluene as a process controlling agent. The reduction reaction was observed to progress gradually during milling. But, after heating at 1000 °C, the amorphous alumina formed during the milling transformed into a stable α-Al_2O_3. Reactive ball milling of NiO by H_2 was reported by Doppiu *et al.* [DOPP2004]. Similarly, Jagtap *et al.* [JAGT1992] and Yang *et al.* [YANG1998] demonstrated the carbothermal reduction of NiO. The $Ni_{0.6}Zn_{0.4}O$ composites have been prepared in NiO-Zn mixture at lower temperatures using the high-energy ball milling procedure, and the reduction reaction was observed to progress gradually during the milling [SETO2015]. Setoudeh *et al.* [SETO2017] studied the reduction reaction between NiO and Mg and observed the complete magnesiothermic reduction of NiO within 15 minutes of milling for the stoichiometric composition of Mg and NiO.

These literature reviews summarize that the process of reduction in NiO and, in particular, studied via the mechanochemical reduction processes has been carried out randomly for the limited compositions without any systematic investigations. Furthermore, the detailed analyses of the resulting magnetic properties of the *in-situ* nanocomposites, formed due to different types of reduction, are still missing. It may be noted that the study of NiO reduction and the control of properties of subsequent Ni are of practical importance in the fields of ore reduction [HIDA2009], catalysis [LESC2004] and solid-oxide fuel cells [SING2003, GUOL2014], and resistive random access memory [BRUC2003]. However, most of the reported literature is based on the change in the structural properties of the composite systems, and no systematic work has been carried out to study the magnetic properties of the resultant nanocomposites products.

This motivated us to plan the current thesis work with the following objectives as given below:

1.3. Objectives of the thesis work:

- To prepare the NiO-(Al, Ti, Mg) based nanocomposites by the reactive milling process in a high-energy ball mill under dry milling conditions and argon gas environment.
- To study the effect of (i) the substitutional elements for a particular milling period, and (ii) the milling periods for the selected composition on the nature and types of NiO reduction dynamics.
- To investigate the effect of the reduction process on the structural, vibrational, and magnetic properties of NiO-(Al/Ti/Mg) nanocomposites as a function of compositions and milling periods.
- To understand temperature and field-dependent magnetic properties of the as-milled powders.
- To study the effect of temperature-induced structural phase changes in the milled NiO-(Al, Ti, Mg) powders.
- To analyze the correlation between the structural, microstructural, vibrational, and magnetic properties of the nanocomposites with the mechanochemical reduction dynamics and composition-dependent behaviors.

Chapter 2

Fundamental aspects and theoretical Models

2.1. Introduction:

Magnetism is a class of physical phenomena by which materials affirm an attractive or repulsive force. Dated back to almost a thousand years, the history of magnetism is coeval with the history of science. However, to date, the underlying principles and mechanisms, which elucidate the magnetic properties of the materials are quite complex and mysterious. It is well-known that most of the modern technological devices such as sensors, electric motors, hard disk drives, *etc.* rely on magnetism and magnetic materials. This triggered extensive studies of various types of magnetic materials from both fundamental and application points of view over the last few decades. Throughout the years, magnetic materials have evolved from bulk form to the nanostructures to cater to newer demands via novel technologies. In particular, the recent endeavors on the development of magnetic properties in new types of magnetic materials in the abundant oxide forms and the broad latitude of tunability of the magnetic properties in the nanoscale region has received widespread recognition in the field of artificial engineering. This chapter provides an insight into the structural properties, crystal structure, magnetic structures, defects, reduction reactions of metal-oxide materials, and the origin of magnetism in solids, the phenomena of different types of magnetism, and anisotropy.

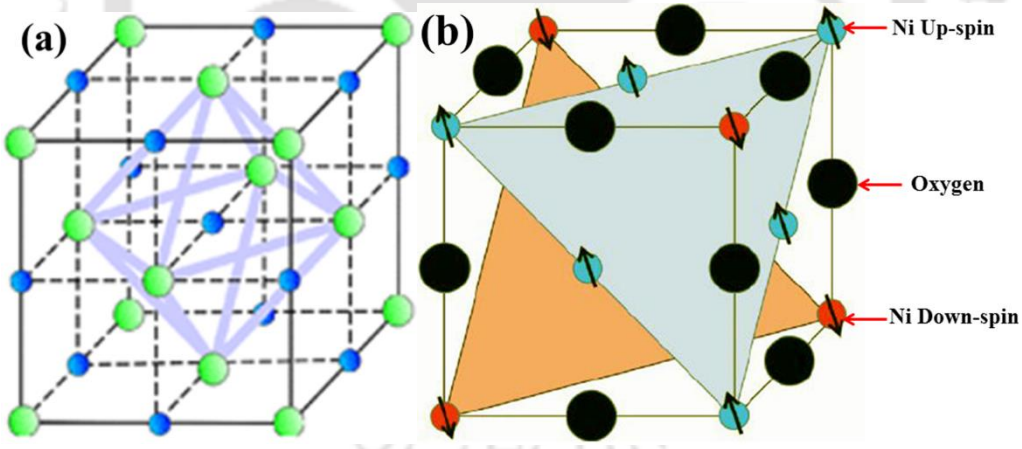

Figure 2.01: Schematic representation of the collinear arrangement of (a) crystal structure, and (b) magnetic structure.

2.2. Structural properties:

The high degree of correlation between the structural, morphological, chemical, and magnetic properties of Transition-metal oxides (TMOs) makes way to the myriad of fundamental science and research activities [DUOL2010]. Among all these TMOs, Nickel oxide (NiO) is one of the most extensively studied low dimensional oxide system owing to

its potential applicability in the fields of catalysis [CHAI2017, KUCH2017, SONG2017], batteries [NIS2013, XUD2017], gas sensors [MILL1997], electrochromic films [FARI1998, HUAN2011, MOUL2014, BROW2016], and magnetic materials [MAKH1997, ICHI2003, MORI2018, MORI2019]. Due to its simple crystallographic and well-known magnetic structure with an ordering temperature far above the room temperature, it is easy to grow single crystals as well as the thin films due to its high chemical and mechanical stability. The crystal structure and magnetic structure of NiO under the present investigations are discussed briefly in the following section.

2.2.1. Crystal structure:

NiO belongs to the group of binary 3*d* transition metal monoxides, RO (R = Mn, Fe, Co, Ni, Cu) having strongly correlated electron system of space group $Fm\bar{3}m$ [group number: 225]. It adopts the classic NaCl structure as shown in Figure 2.01(a) with octahedral Ni(II) and O^{2-} sites with the bulk lattice constant of (a_{NiO} =) 4.1705 Å at 0 K [BERT1971]. In general, NiO is cubic rock-salt structured and exhibits pale green color when Ni and O are in a 1:1 stoichiometric ratio.

2.2.2. Magnetic structure:

The bulk NiO, due to its electronic structure and chemical bonding, is a prototypic collinear antiferromagnet having an easy-plane type-II antiferromagnetic (AFM) ordering with the standard Néel temperature (T_N) of 523 K. Among all the TM monoxides, NiO possesses highest magnetic ordering temperature and consequently plays a crucial role for addressing the challenges in magnetic recording applications by allowing magnetic stability at low volumes well above the room-temperature range. The prototype magnetic unit cell of NiO is close to cubic, but with a doubled lattice parameter in order to accommodate the AFM spin arrangement, as shown in Figure 2.01(b). For $T < T_N$, in the AFM form, amongst the twelve nearest neighbors surrounding any Ni ion, six are oriented parallel to the central ion, and six are arranged in an antiparallel manner [SHUL1951]. However, the number of next-nearest neighbors for an infinite crystal of NiO is six, all coupled antiparallel to the central ion. The AFM order of NiO can be treated via two ferromagnetic (FM) spin lattices, which consists of the FM alignment of the magnetic moments of the Ni^{2+} ions order ferromagnetically in the (111) planes with adjacent (111) planes aligned antiparallel. Hence, the overall crystal shows a typical AFM ordering [SHUL1951, ROTH19581, ROTH1960,

HUTC1972, HILL2001]. In the paramagnetic state (above T_N), the symmetry follows a typical face-centered cubic (*fcc*) structure [RICH1956]. However, passing from the paramagnetic state to the antiferromagnetic state, *fcc* structured NiO is accompanied by spontaneous strain and slightly departs from the cubic symmetry. This influences a weak cubic-to-rhombohedral distortion ($R\bar{3}m$) due to magnetostriction [RICH1956, ROTH19582, MASS1991]. The relative orientation of the spins concerning each other is determined by the exchange interactions.

In NiO, two components of spin configurations exist due to the non-local exchange interactions: (i) Direct exchange interaction between the nearest neighbors Ni ions, which favors the paring of spins to lower energy; and (ii) Super-exchange interaction, a very strong and dominant interaction, which originates from the next-nearest neighbor Ni ions. In line with this, the dominant coupling through the 180° super-exchange interaction is strengthened by the rhombohedral distortion, which enables the next nearest neighbor Ni ions to get closer together [SHUL1951, LOUD2012]. According to the concepts of Anderson [ANDE1950], the dominant exchange forces are produced by the phenomenon of super-exchange interaction where the electronic wave functions of the magnetic Ni ions overlap with the intermediate oxygen ions; thus the next-nearest neighbors are especially significant in controlling the alignment of the magnetic moments, thereby determining the type of magnetic lattice [ROTH1960]. Experimental measurements of the magnetic moments give values between 1.77 and 2.2 ± 0.2μ_B per Ni ion, and usually, each Ni 2p ion has its spin-only magnetic moment of 2μ_B [KWON2000].

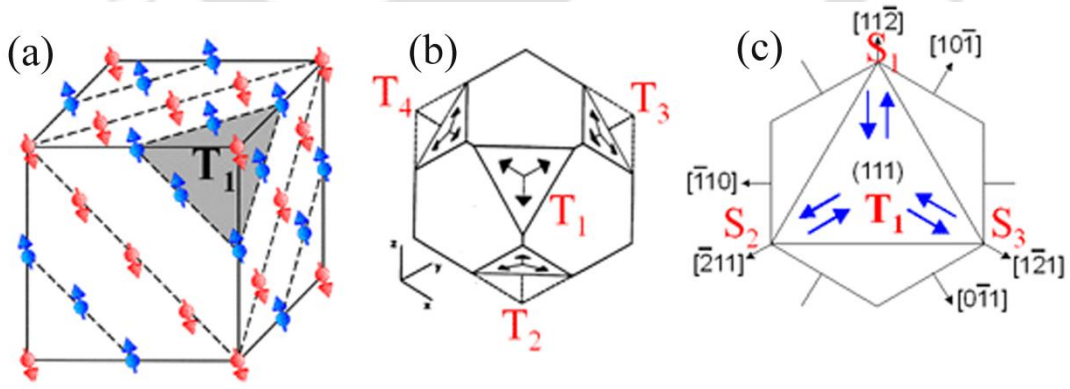

Figure 2.02: Schematic representation of the collinear arrangement of (a) magnetic structure, (b) T-domain, and (c) S-domain of bulk NiO [HTTP0001].

NiO was the first material where the antiferromagnetic domain structure was directly observed. This was supposedly due to its ordering at room temperature and thereby proved

the Néel's hypothesis proposed in 1954 [TANN1979]. As said before, due to the exchange striction of NiO below T_N, the cubic symmetry at the antiferromagnetic state is lowered to the trigonal symmetry and becomes normal to the ferromagnetic (111) plane. Therefore, each of the magnetic domains in NiO possesses its unique trigonal axis. As the ferromagnetic ordering is observed in alternate (111) planes and there are possible four equivalent (111) planes where ordering can occur; four types of possible domains called as 'T domains' are observed [ROTH1960, SLAC1960, HUTC1972, MARM1979, MADE1984, SANG2006]. The T domains are, in fact, quite equivalent to the crystallographic twins and hence called as the T (or twin) domains. Moreover, within each T domain, the alignment of spins happens in three equivalent (112) directions due to magnetostriction [as shown in Figure 2.02(a, b, c)] and hence a further subset of three domains is observed known as the 'S domains'. Table 2.01 summarizes the crystallographic directions of the T and S domains of NiO. The top row presents the stacking directions of ferromagnetic Ni^{2+} planes in the four T domains, whereas the other rows show spin directions in all the 12 orientational domains.

Table 2.01: Crystallographic directions of the T and S domains of bulk NiO.

S	**T**			
	$T_1[1,1,1]$	$T_2[1,1,\bar{1}]$	$T_3[1,\bar{1},1]$	$T_4[\bar{1},1,1]$
S_1	$[1,1,\bar{2}]$	[1,1,2]	[1,2,1]	[2,1,1]
S_2	$[\bar{2},1,1]$	$[1,\bar{2},\bar{1}]$	$[\bar{2},\bar{1},1]$	$[\bar{1},1,\bar{2}]$
S_3	$[1,\bar{2},1]$	$[\bar{2},1,\bar{1}]$	$[1,\bar{1},\bar{2}]$	$[\bar{1},\bar{2},1]$

2.3. Crystallographic defects:

Defect engineered NiO nanostructures/composites have received unprecedented attention due to the presence of various extended as well as point defects. Defects are the wanted or un-wanted disruptions to an otherwise perfect arrangement of atoms in a crystal lattice and in any way affect the overall behavior of the system [MOUR2012]. The defects in any crystal structure are classified broadly into two types, *i.e.*, extended defects and point defects. The extended defects are mainly the dislocations, where an extra line of atoms has been inserted or removed in/from the crystal, which does not extend throughout the crystal and significantly alter the electrical, mechanical, and magnetic properties of the material [SUGI2013]. On the other hand, the point defects are the zero-dimensional defects and

basically the localized disruptions involving a single atom or pair of atoms, but often extend to larger distances in the lattice structure. However, the major defects governing the NiO nanoparticles fabricated via the top-to-bottom approach are the point defects such as misplaced lattice atoms/ions, vacancies, foreign atoms/ions as schematically shown in Figure 2.03. These point defects are classified further into intrinsic/native defects and extrinsic or external impurity defects (dopants), which are found either on the lattice (substitutional site) or at the interstitial positions [SPAI2014]. These all-inclusive dominant point defects permit the possibility of tailoring the material properties into requisite diverse combinations, which play a crucial and fundamental role in enhancing the materials/device performance.

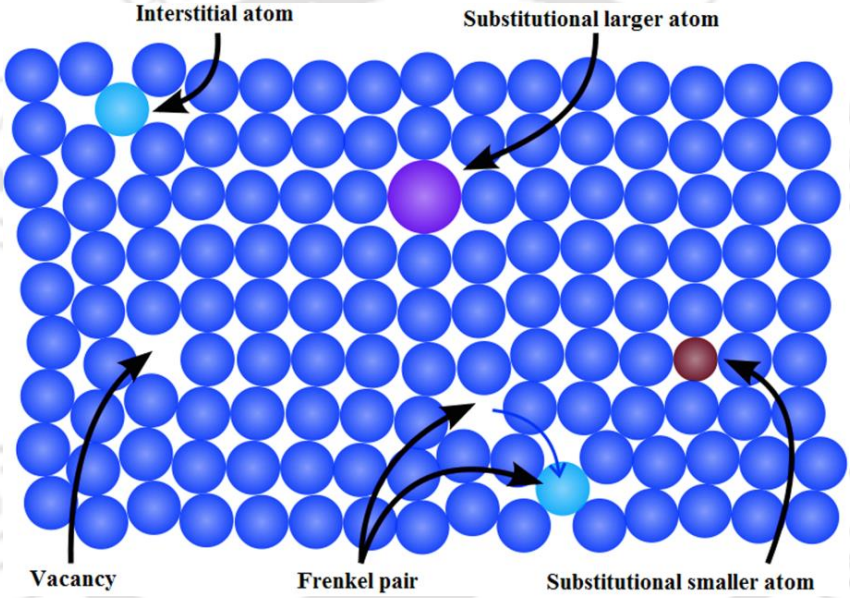

Figure 2.03: Schematic illustration of some simple point defect types in a solid [HTTP0002].

2.3.1. Intrinsic defects:

An intrinsic defect is formed when an atom is missing from a crystal position by creating a vacancy or occupies an interstitial position where no atom would usually appear, creating an interstitialcy. As interstitial sites in most crystals are small or have an unfavorable bonding configuration, interstitialcy is comparatively uncommon and a type of high-energy defect. In contrast, vacancies are abundant in all crystalline solids, and their most manifested effect is to govern the migration of atoms in a crystal lattice through the solid-state diffusion process. In ordered compounds, the well-known point defects are the Schottky and Frenkel defects. The Schottky defect involves paired vacancies on the cation and anion sublattices, whereas a Frenkel defect is created between a paired vacancy and an interstitial [TILL2010].

The understanding of these defect mechanisms is quite essential in metal-oxide systems to improve the device performances [DAWS2015, FLYN2016, ZHUY2019] and to understand the underlying unique properties in different nanostructures, which, due to the defect engineering, show markedly distinct behavior as compared to their bulk counterpart [ZHUY2019]. In specific, for the NiO system, the point defects like oxygen vacancies play a significant role in altering the electronic and magnetic properties [PARK2008, GAND20172, ARCI2018, ZHAN2018]. As reported earlier by Roberts *et al.* [ROBE1984] through the XPS spectral analysis, high binding energy components of O 1s spectra at 531.4 eV and Ni $2p_{3/2}$ spectra at 856.1 eV are correlated with the oxide defect structure of NiO. Nickel vacancy in NiO has been reported as the dominant point defect in the NiO systems [PARK2008], which results in the electrical conductivity of NiO thin-film structures [JANG2009]. Hong Bi *et al.* reported the weak ferromagnetic behavior in NiO nanocrystallites attributing to the reduced coordination and broken bonds combined with the lattice distortion [BIH2004].

Ni vacancy in dislocation cores was attributed as the prime source of ferromagnetic behavior in antiferromagnetically ordered NiO [SUGI2013]. Similarly, Nickel vacancies as the dominant defect type that determine the electrical properties of NiO were reported by Zhang *et al.* [ZHAN2016]. Thus, intrinsic defects can significantly alter the lattice parameters in NiO [EKUM2011]. Likewise, the chemical and electronic property of NiO nanorod structure was successfully optimized through O-vacancy engineering by Zhang *et al.* [ZHAN2018] and observed that the O-vacancies on the surface of NiO nanorods could remarkably enhance their electronic conduction and promote the hydrogen evolution reaction kinetics simultaneously. The intrinsic p-type conductivity in single-domain NiO nanoparticles was attributed to hole states induced by Ni vacancies by Gandhi *et al.* [GAND20171]. Peck *et al.* [PECK2012] reported that the prolonged exposure of bulk NiO to the ambient environment leads to hydroxylation of NiO, which changes the chemical environment and hence the importance of sample condition.

Moreover, when NiO is heat-treated in an O-rich environment, the oxygen interstitial O_i becomes as the O-excess defect and is observed as a type of surface defect. Vacancies and interstitial atoms are responsible for the occurrence of nonstoichiometric compounds, and NiO is an appropriate candidate with somewhat variable stoichiometry. When NiO is prepared at relatively low temperature, *i.e.*, 1100 K, by the partial oxidation of excess nickel, its composition becomes $Ni_{1.0}O_{1.0}$ that exhibits pale green color and has insulating behavior.

If the same material is treated with excess oxygen at 1500 K, the cation vacancies occur, leading to a composition of $Ni_{1.0-\delta}O_{1.0}$. This nonstoichiometry changes the color of the powder into black, which posses semiconducting properties. The deficiency of the positive charge that would otherwise accompany cation vacancies is compensated by the presence of an appropriate amount of Ni^{3+}, which accounts for the electrical conductivity in non-stoichiometric NiO. If a Ni^{3+} ion exists at some point, an electron from elsewhere in the lattice may jump to it, converting it to Ni^{2+} and simultaneously creating a Ni^{3+} ion at a new lattice point. By a series of such electron jumps, the charge can migrate through the crystal and show strikingly different behavior than the stoichiometric NiO.

2.3.2 Extrinsic defects:

The extrinsic point defects are termed as solutes if they are added intentionally to the material and are called impurity if they are formed unintentionally. The foreign atoms occupying a lattice site is known as a substitutional solute, and that occupying an interstitial site is called as interstitial solute. As the interstitial sites are relatively small in a crystal structure, smaller atoms often fill the interstitial sites (example: carbon, hydrogen, and nitrogen). Meanwhile, the larger atoms are often found in the substitutional sites (example: Aluminium, Silicon). More complex extrinsic defects appear in compounds. Another form of extrinsic defects added in a material is the process of doping. Doping/substitution in this context is a process of adding a small amount of foreign atoms/ions into the host matrix without forming any secondary phases within the solubility limit. When a foreign atom is added beyond the solubility limit, there is a formation of either different oxides or a secondary phase depending upon the mutual solubility limit of the two components. The distribution of the dopant in the crystals/grains of the matrix material may be homogeneous or heterogeneous. Doping/substitution in NiO is performed with the aim of enhancing the properties of parent NiO for potential technological applications. These extrinsic point defects affect most of the properties in defect engineering but are of utmost importance in controlling the electrical properties in semiconducting crystals. Similarly, in the case of nanostructures, physical and electrical properties are controlled by the structure and concentration of the defects.

Moreover, the defects are often accountable for mass transport, which reins the properties of materials for advanced functionalities like oxygen ion conductors and diffusion barriers. For oxidation/reduction of the metals, these defects accelerate the reaction by

tuning a pathway for the fast oxygen diffusion or having a favorable place for the reaction to occur. For instance, in Ni(110), substantial changes in both the atomistic structure and morphology were observed when immersed in water and Pb-contained solution. This provided a simple and direct experimental evidence of the role of the defects in the chemical reaction of oxide surfaces with both water and Pb-contained solution where the introduction of defects could accelerate the reaction process in NiO. Doping in NiO is performed to enhance the properties of the parent NiO for potential applications. For instance, Mg doping in NiO enhances the bandgap of NiO significantly [BENA2014], Li doping in NiO thin films enhances the p-type conductivity owing to the occupancy of substitutional sites in the films by Li ions [DUTT2010], Zn doping in NiO, *i.e.*, $Ni_{0.98}Zn_{0.02}O$ induces ferromagnetism at about 70 K [MAST2014], and Fe doping in NiO enhances the oxygen evolution reaction kinetics, and the Fe incorporation leads to an increase in the catalytic activity of the NiO surface [PEBL2017].

2.4. Reduction reactions:

Reduction, in terms of oxygen transfer, is a process where an atom within a molecular entity loses oxygen atom from a molecule. Reduction processes are the half of a full chemical reaction where if one molecule is reduced, the other half gets oxidized, and the full reaction is termed as the Redox reaction. The term reduction comes from the Latin stem, which means ‘to lead back’ and defines anything that leads back to the metallic form of the corresponding metal oxide. The type of redox reaction where an element replaces or displaces from a compound is called the displacement reactions. Depending upon the stimuli used for performing the reaction, these reactions can be categorized majorly as the thermochemical, electrochemical, and mechanochemical types. For our current investigations, we have taken into account the comparison between the thermochemical and mechanochemical processes, as described below.

2.4.1. Thermochemical reduction:

The type of chemical reaction, which takes place by the evolution/absorption of heat, is known as the Thermochemical reactions. The type of thermochemical reaction, which occurs with the evolution of heat, is called ‘exothermic’ reaction, whereas, that occurs by the absorption of heat, is termed as the ‘endothermic’ reaction. Among these, a prominent thermochemical redox reaction is the metal-oxide based ‘thermite’ reaction. This was first

coined by Goldschmidt in 1908. 'Thermit' describes the exothermic metal oxide reduction reactions with Al to form metals/alloys and Al_2O_3. Being highly exothermic by nature, the reactions involve a large heat release as sufficient to heat the product phases above their individual melting points [WANG1993]. For instance, the thermite reaction

$$2Al + Fe_2O_3 = 2Fe + Al_2O_3 + \Delta H;\ \Delta H > 3000\ ℃ \qquad (2.01)$$

The reaction temperature of >3000°C is higher than the individual melting points of Fe and Al_2O_3 and leads to the synthesis of stable product phases.

Though initially meant for the Al-based reduction processes, the term 'thermite reaction' in the current industrial and research scenarios, describes to a much broader class of reactions and is redefined as the exothermic redox reaction, which comprises a metal reacting with a metallic/non-metallic oxide to form the corresponding metal/nonmetal of the reactant oxide and a stable oxide of the reactive metallic agent. This oxidation-reduction reaction takes the form as,

$$AO + M = A + MO + \Delta H \qquad (2.02)$$

Where M is a reactive metal, A is a metal/non-metal with MO and AO being their corresponding oxide forms, and ΔH is the total heat generated during the reaction. Being exothermic, the value of ΔH is largely negative. In most of the cases due to high exothermic heat, the reaction proceeds locally at the initial stage of the reaction, which is followed by a self-sustaining process, a striking feature of the reaction to be used as a highly energy-efficient route for a wide range of metallurgical applications [GOLD1898, GOLD1908, GOLD1909, PERF1967, BALA1971, BELI1972, CARL1973, MEHR1973, TARL1974, ASTO1977, KEYA1985, STOI1985, JHAB1989].

Despite all the well-versed studies on the thermochemical reactions and having a myriad of applicability, the inherent limitation of these reactions is that the product phases remain spatially separated. As the solid-state reactions involve the formation of product phases at the reactants' interfaces and the growth of the product phases involve diffusion of atoms of the reactant phases through the product phase, a barrier layer is formed, which prevents further diffusion. Hence, these reactions are carried out at elevated temperatures for the conventional thermochemical processes. The reactivity of solids is, therefore, dependent on initial contact areas and hence particle size, on factors that influence diffusion rates, such as defect densities, and local temperatures, and on product morphology [CART1961, RAPP1973, GOME1976]. In conventional thermochemical systems, the reactants remain mostly unperturbed and hence, are spatially separated during the reaction.

Besides, high-temperature processes invariably lead to the formation of coarse-grained products due to the occurrence of grain growth. These types of coarse-grained materials are usually undesirable for the manufacturing of advanced engineering components due to their poor mechanical properties, poor sinterability, *etc*. As a consequence, there is considerable interest in finding alternative synthesis procedures that either reduce the requisite processing temperature or eliminate the need for applied heating altogether [MCCO1995, MCCO1998]. Hence, to increase the reaction rate and to have the desired product at moderate temperatures, a different fabrication approach is necessitated, which can easily bring unreacted materials to frequent contact with each other. This noble thought gave rise to the widely recognized area of mechanochemical reduction processes.

2.4.2. Mechanochemical reduction:

Mechanochemical processes are the chemical transformations induced/ initiated/ accelerated by mechanical means such as frictions, compression, and shear stress [TAKA2013]. Therefore, it is a complementary process to the conventional methods of activation like heat, irradiation, and electrochemistry [BALA2008]. It is a well-recognized technique that forms an important category for the synthesis of composites, nanomaterials, ceramic metal-matrix composites, *etc.* and requires an ample amount of energy for the activation of chemical reactions via mechanical treatment in the form of heat energy [WUH2012, SAHA2014, XUC2015, LUM2017, HOWA2018]. Known for promoting solid-solid and solid-liquid reduction reactions rapidly and quantitatively, mechanochemical processes possess a strong persevere in having high importance in the material synthesis [SURY2001]. The mechanochemical reactions comprise exchange reactions, oxidation/reduction reactions, phase transformations, and decomposition in both inorganic and organic compounds, among which the present thesis work will mostly involve the solid-solid mechanochemical reduction processes.

The notable feature of these mechanical-assisted processes is the attainment of chemical changes by the mechanical action of grinding/milling. Grinding, in a broader sense, describes the effect of mechanical forces on a material that allows a solid to break into small parts. Through the process, an excess of potential energy through shear/friction contributions introduce shape and surface defects in the mixture of reactants without using any solvent. These defects/changes can significantly improve/modify the chemical reactivity to give the final product of the materials [KUBI2008, RALP2013, XUC2015].

Boldyrev in 1986 [BOLD1986] described the mechanical activation being responsible for the change in the solid-state reactivity owing to the induced defects, which play a crucial role in the chemical reactions. For instance, dislocations generally improve the solid solubility limits, whereas point defects or free radicals find crucial importance in the decomposition reactions. The exchange reactions involving the mechanochemical reductions take the form as follows [IVAN2000]:

$$MO + R = M + RO + \Delta H \qquad (2.03)$$

Where a metal oxide (MO) is reduced by a more reactive metal (also termed as reductant (R)) to form the pure metal M of the corresponding oxide. The mechanochemical reduction reactions are characterized through a large negative free-energy change and hence, are thermodynamically achievable at room temperature [SURY2001, SURY2004].

Though no detailed historical demonstrations is available to the most basic question of 'why and when' the first mechanochemical process was commenced, a reference of cinnabar reduction to mercury at around 350 BC was reported on a booklet entitled 'On stones' by Theophrastus, a student of Aristotle, by using a copper mortar and pestle (followed reaction as $HgS + Cu \rightarrow Hg + CuS$) and is perhaps the earliest surviving document of mechanochemical reaction process [TAKA2000, XUC2015]. However, the preliminary mechano-chemically self-sustained reaction (MSR) was put forward by Faraday in 1820 on the decomposition of silver chloride. He described the silver chloride reduction process by grinding with Zn, Cu and Fe in a mortar and the reactions were observed to be exothermic (For instance, $2AgCl + Zn \rightarrow 2Ag + ZnCl_2$) [FARA1820, TAKA2007]. Though the process was described as the 'dry way' of inducing reduction, this gave a possibility to the conventional MSR type reaction.

Nonetheless, the first mechanochemical reaction was reported by Matthew Carey Lea in 1866 [LEAM1866, LEAM1893] by taking into consideration of a broad range of compounds and establishing the theory of mechanical grinding. This method is much different in prospect to the conventional thermochemical reactions [TAKA2007]. Hence, the process of mechanochemical reactions has emerged as a growing research field in the scientific and industrial arena having the prime attributes of mechanical-assisted processes to the fields of mineral and waste processing, metals refining, ultrafine powder production, combustion reactions, extension of solubility limits, production of a fine dispersion of second-phase particles, synthesis of novel crystalline phases and the possibility of alloying difficult-to alloy elements, *etc*. [SUND1987, FROE1990, WARD1994, FROE1995,

POLK1995]. Some of the metal oxide systems processed through the mechanochemical reductions are summarized in Table 2.02. Since the earliest manual mechanochemical synthesis (by mortar and pastel) could not provide a proper control of the synthesis parameters (such as frequency or grinding force), the more advanced non-manual electronic instrumentations like mixer and planetary mills are currently used to achieve high reproducibility of the mechanochemical synthesis as well as to accomplish solvent-free processes through well-defined reaction parameters like milling/grinding speed and milling force. The main mechanical energy applied to the reactants in mixer mills is the compact force, whereas the planetary ball mills use shear force to provide the mechanical energy required for the chemical reactions [HOWA2018].

Table 2.02: Some of the mechanochemical reactions in oxide compounds are stated below.

Reaction	**ΔH^0 kJ/mol**	**ΔG^0 kJ/mol**	**References**
$3SiO_2 + 4Al \rightarrow 3Si + 2Al_2O_3$			[MATT1992]
$WO_3 + 2Al \rightarrow W + Al_2O_3$			[MATT1992]
$2WO_3 + 3Ti \rightarrow 2W + 3TiO_2$			[MATT1992]
$3SnO_2 + 2W \rightarrow 3Sn + 2WO_3$		+25	[VARN1974]
$SnO_2 + Si \rightarrow Sn + SiO_2$		-276	[BOLD1971]
$3SnO_2 + 4Al \rightarrow 3Sn + 2Al_2O_3$		-535	[BOLD1971]
$2Sb_2O_3 + 3Si \rightarrow 4Sb + 3SiO_2$		-2823	[PATE2004]
$4CdO + 4S + 3Fe \rightarrow Fe_3O_4 + 4CdS$		-673	[SAIT2004]
$2CuO + Ti \rightarrow 2Cu + TiO_2$	−620		[MULA2001]
$2CuO + Zr \rightarrow 2Cu + ZrO_2$	−777		[MULA2001]
$2CuO + Hf \rightarrow 2Cu + HfO_2$	−796		[MULA2001]
$3CuO + 2Al \rightarrow 3Cu + Al_2O_3$	−273		[SCHA1990, MATT1992]
$CuO + Ca \rightarrow Cu + CaO$	−475		[SCHA1989, MCCO1995]
$2CuO + C \rightarrow 2Cu + CO_2$	−138		[TSCH1982]
$4CuO + 3Fe \rightarrow 4Cu + Fe_3O_4$	−488		[SCHA1990, MCCO1995]
$CuO + Mg \rightarrow Cu + MgO$	−445		[SCHA1990, MCCO1995]
$CuO + Mn \rightarrow Cu + MnO$	−231		[SCHA1990, MCCO1995]

$CuO + Ni \rightarrow Cu + NiO$	−382		[SCHA1990]
$2Cu_2O + Ti \rightarrow 4Cu + TiO_2$	−598		[MULA2001]
$2Cu_2O + Zr \rightarrow 4Cu + ZrO_2$	−754		[MULA2001]
$Cu_2O + Mg \rightarrow 2Cu + MgO$	−430		[PAVL2018]
$CdO + Ca \rightarrow Cd + CaO$	−377		[MCCO1995]
$Cr_2O_3 + 2Al \rightarrow 2Cr + Al_2O_3$	−273		[MATT1992, TAKA1993]
$Cr_2O_3 + 3Zn \rightarrow 2Cr + 3ZnO$	+49		[TAKA1993]
$V_2O_5 + 5Mg \rightarrow 2V + 5MgO$	−1457		[MATT1992, YANG1994]
$2V_2O_5 + 5Ti \rightarrow 4V + 5TiO_2$	−1623		[YANG1994]
$3V_2O_5 + 10Al \rightarrow 6V + 5Al_2O_3$	−3727		[YANG1994]
$3MnO_2 + 2Al \rightarrow 3Mn + Al_2O_3$			[MATT1992]
$Fe_2O_3 + 2Al \rightarrow 2Fe + Al_2O_3$			[NASU1999]
$Fe_2O_3 + 2B \rightarrow 2Fe + B_2O_3$			[MATT1992]
$Fe_2O_3 + 2Cr \rightarrow 2Fe + Cr_2O_3$			[MATT1992]
$3ZnO + 2Al \rightarrow 3Zn + Al_2O_3$			[MATT1992]
$3CoO + 2Al \rightarrow 3Co + Al_2O_3$			[MATT1992]
$MoO_3 + 2Al \rightarrow Mo + Al_2O_3$			[MATT1992]
$6Nb_2O_5 + 10Al \rightarrow 12Nb + 5Al_2O_3$			[MATT1992]
$3NiO + 2Al \rightarrow 3Ni + Al_2O_3$	-968		[MATT1992, UDHA2010]
$NiO + C \rightarrow Ni + CO$			[YANG1998]
$NiO + H_2 \rightarrow Ni + H_2O$			[DOPP2004]
$NiO + Mg \rightarrow Ni + MgO$	-361		[SETO2017]

Mechanochemical processes by using the ball milling technique or the reactive milling process involve the typical alloying of materials with an advantage of chemical and physicochemical transformations in amalgamation with the effective mechanical energy generated during the milling process. Milling of powders in the presence of reactive solids/liquids/gases is now regularly employed to synthesize various composites, alloys, intermetallics, *etc.* by enabling a displacement reaction *via in-situ* or *ex-situ* approaches. These displacement reactions are characterized by a large negative free energy change and thereby attainable thermodynamically at room temperature but are mostly limited by kinetic

considerations. As the initial powder mixtures are chemically reactive by nature, the milling is not only associated with the size refinement but also is accompanied by the chemical reactions occurring at the interfaces of the nanometric grains, re-generated incessantly during the milling process [KOCH1991]. The mechanochemical synthesis substantially enhances the kinetics of the reduction reactions through the repetitive welding and fracturing of powders. This leads to the increasing area of contact between the reactant powder particles due to the size refinement. This allows the fresh surfaces to come into contact repeatedly with the simultaneous increase in defect densities, and the reaction proceeds without any diffusion process through the product phases. As a consequence, chemical reactions, that, due to the separation of the reacting phases by the product phases necessitate high-temperature synthesis techniques (or thermochemical processes), are attained at a somewhat lower temperature in a ball mill without the obligatory external heat supply and create an intimate mixture of reactants at atomic level [TSUZ2004].

The mechanochemical processes proceed through the consumptions of educts and the formation of products as per the physicochemical laws and are characterized by using the fundamental Gibbs-Helmholtz thermodynamical equation as

$$\Delta G = \Delta H - T\Delta S \tag{2.04}$$

Where ΔH is the reaction enthalpy, ΔS is the entropy, and ΔG is Gibb's free energy at a specified reaction temperature (T). If the value of ΔS is small, *i.e.*, the crystal structure is almost preserved and less disordered, then ΔG is determined predominantly by the change of enthalpy ΔH. However, for highly disordered crystals, ΔS becomes the most crucial term in the thermodynamic relation. As the chemical reactions are more or less dependent on the crystal defects, the major possibility for the favorability of the chemical reaction depends upon the sign of ΔG. Based on the laws of thermodynamics, the chemical reaction can thermodynamically be favorable and can proceed spontaneously when the value of ΔG stands negative. Hence, Gibb's free energy of the reaction (ΔG_{reac}) is given as,

$$\Delta G_{reac} = \sum \Delta G_{product} - \sum \Delta G_{reactant} \ , \Delta G < 0 \tag{2.05}$$

If a chemical reaction is accompanied by the formation of gas or fluid phases (melts, solutions), solid-solutions, or by the generation of defects, then, for a more strict thermodynamic forecast, it is necessary to take into account the changes of entropy and specific heat capacity during phase transitions of the components (melting, vaporization, dissolution), changes of volume and other parameters.

The prime features of these mechanochemical processing/reactive milling carry the applications of this technique for the manufacturing of advanced materials and provide an ample opportunity to make products with unique characteristics and have some of the following benefits:

1. The resultant powders show not only a substantial size reduction but also an exceptionally high reactivity due to the higher free energy being accumulated in the defective crystal lattice and an increased grain boundary volume.
2. A significant decrease in crystallite size at the nanometric level or the transformation to an amorphous structure owing to growing crystal cell disordering with prolonged mechanochemical treatment is observed.
3. Extension of solid-solubility limit is obtained due to the formation of metastable equilibrium between the terminal solid solution and an amorphous phase.
4. Nucleation of various complex oxides and composites at ambient temperature by the formation of hetero-bridging bonds, owing to intimate mixing under the controlled shear stress conditions in dry solid process and short-range atomic transfer across the boundaries of solids, can be achieved. This is otherwise not possible to synthesize by conventional chemical processes.
5. Fabrication of a variety of equilibrium solid compounds is possible.

The mechanochemical reductions in solids can occur in two broad types as follows:

2.4.2.1. Solid-Solid reduction:

The solid-solid mechanochemical reductions involve all the initial reactants in the solid-state form without the aid of any liquids or gases. The solid-solid mechanochemical reductions were established by Tamman and Hedvall [TAMM1932, HEDV1938] in the 1930s and were accepted by the end of the 1960s that the solid-solid reaction between solids could become significant if individual compounds are mixed intimately and heated. As the lattice vibrations with increasing amplitudes result in the frequent exchange of atomic positions in a crystal lattice and, in turn, bring about a faster microscopic diffusion, the mechanochemical reduction process is favorably initiated. This exchange of atomic positions in a crystal is especially effective in disordered structures [HABA1969]. In fact, when there is an intimate mixing of the initial solid reactants occurs during milling, the commencement of the mechanochemical reduction process is observed.

The characteristic feature of the conventional solid-solid reactions involves the formation of product phases at the reactant interfaces. Moreover, the reaction rates are strictly limited by the diffusion of atoms of the reactant phases through the freshly formed surface layer of product phases, and this, in turn, constitutes a barrier layer that prevents further reaction processes. Meanwhile, reactive milling substantially provides means to enhance the reaction kinetics of the reduction processes significantly and is attributed to the particle size reduction owing to the repeated deformation, fragmentation, mixing, and cold-welding of powder particles during milling. The reduction of particle size of the reactants leads to the fresh surfaces to come into contact repeatedly via increased specific surface area of solids, and the reaction can proceed without diffusion through the product layer. Consequently, reactions requiring high-temperature processes can occur at moderate temperatures without any external heat supply. Besides, mechanical alloying induces high structural disorders, which contribute significantly to the acceleration of diffusion processes. In contrast, the particle size refinement and subsequent reduction in diffusion distances due to the microstructural refinement result in decreased reaction temperatures of mechanochemical processes [SURY2001]. Depending upon the mechanical synthesis kinetics and milling criteria, the displacement reactions between a metal oxide and a more reactive metal induced by the ball milling process is categorized into two types; (i) Gradual reduction and, (ii) Self-propagation reduction [SCHA1990, TAKA1992, TAKA1993, SEIF2016].

2.4.2.1.1. Gradual reduction:

If the reaction proceeds through a very small volume during each collision, the reaction is known as the gradual transformation process. The heat generated during the gradual processes is inadequate enough for the reaction to occur instantaneously, and hence the reaction progresses slowly over time. As oxides and metals are usually immiscible, gradual transformations lead to the formation of nanocomposite structures with the maximum components of initial powder combinations.

2.4.2.1.2. Self-propagation reduction:

If sufficiently exothermic reactants are processed in a high-energy ball mill, a self-sustaining reaction can be mechanically induced after an activation time (processing time ranging from a few minutes to several hours), known as the mechanically induced self-sustaining reaction

(MSR) process [TAKA2014, EBRA2015]. The MSR process, akin to any other mechanical alloying processes, is characterized by the activation period, during which size refinement, intimate mixing of reactants, and the formation of crystalline defects occur [EBRA2016]. Most of the MSR type reactions occur at some critical time moment, known as 'ignition time' where the rate of the reaction starts to increase, and the released reaction heat of the exothermic process causes a sudden increase of the mill temperature and rate of the reaction. The requisite ignition time relies not only on the processing parameters but also depends upon the thermodynamic and kinetic properties of systems under concern [GOTO2013]. A self-sustaining reaction requires sufficient self-heating to propagate the reaction, where the measure of self-heating is determined to form the adiabatic temperature and is obtained to be at least 1800 K [TAKA2002, TAKA2014]. Hence, the occurrence of MSR mainly depends on the ratio of reaction enthalpy to the heat capacity of the products at room temperature, $(-\Delta H^0_{298K})/(\sum C_{P_{298K}})$, as the known substitute for the adiabatic temperature at the beginning of the reaction.

For a standard MSR, the value of $(-\Delta H^0_{298K})/(\sum C_{P_{298K}})$ is found to be >2000 K. However, the occurrence of MSR depends largely upon several factors such as processing parameters during high-energy ball milling (for instance, the ignition time is inversely proportional to the ball-to-powder weight ratio), mechanical behavior of the powders, activation energy, and heat conductivity, *etc*. [TAKA2014]. The critical milling time where ignition of the self-propagating reaction takes place is determined from the sudden temperature increase in the milling [ATZM1990] or from the jump in pressure [JALA2013] caused by the rapid exothermic reactions. Hence, the ignition time serves as the reference point in a self-sustaining process, because its variation with milling conditions reflects the changes in the milling rate of the mechanochemical reactions [EBRA2015]. Thus by measuring the temperature and pressure profiles of the vial during the mechanochemical reductions, the synthesis time of a chemical reaction can be obtained.

The first milling based study on the thermite-type self-propagating reductions was reported by Schaffer and McCormick in 1989 [SCHA1989] by using Ca reactant to reduce CuO, ZnO, and CuO-ZnO oxide mixtures. They also gave a further investigation of the metal-metal oxide displacement reactions for the CuO reduction process with Ca, Mg, Al, Ti, Mn, and Fe [SCHA1990]. Similar types of work were reported by McCormick for a large number of oxide-metal and chloride-metal reactions [MCCO1995] followed by the other displacement reactions being studied such as CuO-Fe [SHEN1991], Fe_3O_4-Al

[TAKA1992], $Cu_2O/MoO_3/FeO/WO_3/VO/TiO/B_2O_3$-Mg and Cu_2O/FeO-Al [POPO1993], PbO-Si [FANG1996] and CuO-Me (Me = Al, Cr, Mg, Ti, Si, Fe) [EBRA2015] systems by using the self-propagating approach.

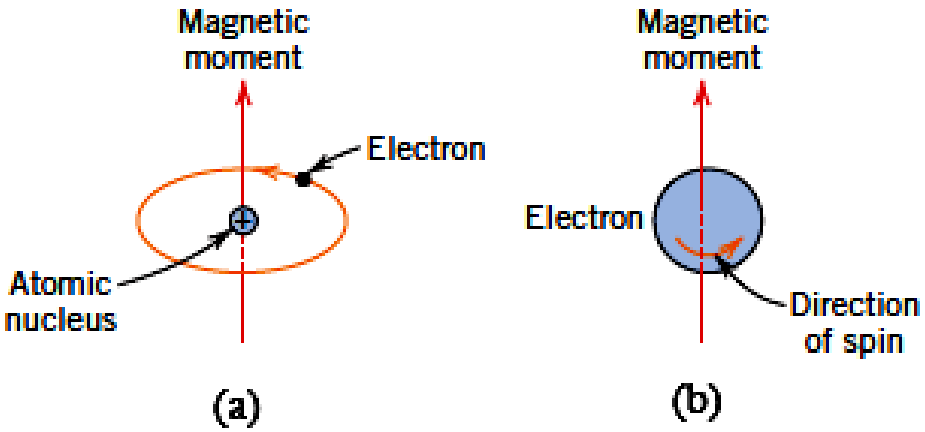

Figure 2.04: Schematic representation of the magnetic moment associated with (a) an orbiting electron, and (b) a spinning electron [HTTP0003].

2.5. Magnetic ordering:

2.5.1. Origin of magnetism:

The macroscopic magnetic properties of the materials are the consequence of magnetic moments associated with individual electrons in an atom [OHAN2000, KITT2004]. Each electron has magnetic moment originated from two different sources: (a) Orbital motion of electron around the nucleus, which generates a small magnetic field having magnetic moment along the axis of rotation (see Figure 2.04a) and (b) Magnetic moment originating from the electron spin directed along the spin axis either up or down depending on the mode of rotation (see Figure 2.04b). This reveals that in an atom, each electron may be considered as a small magnet having permanent orbital and spin magnetic moments. Moreover, the electrons in an atom are occupied according to Pauli's Exclusion Principle and Hund's rule. Therefore, the net magnetic moment of an atom is the sum of the individual magnetic moments of each constituting electrons, including both orbital and spin contributions and accounting moment cancellation. For an atom having completely filled electron shells or subshells, when all electrons are taken into account, there is a total cancellation of both the moments. Hence, materials composed of atoms having completely filled electron shells are not able to be permanently magnetized. Based on the number of unpaired electrons in an atom, their orientation in the orbitals and the spin-orbit interaction between the electron

orbital angular momentum and spin angular momentum, and their response in the applied magnetic field, materials are broadly categorized into diamagnetic, paramagnetic, ferromagnetic, antiferromagnetic and ferrimagnetic types [KRON2003].

2.5.2. Diamagnetism:

Diamagnetism is one of the fundamental properties of the materials and is the manifestation of Lenz's law, *i.e.*, if one applies a field to a system of moving charges, then their motions change in such a way that they create a magnetization, which opposes the original applied magnetic field [OHAN2000]. Such effect is existent in all materials, but is often suppressed by other types of magnetism and hence is taken into account in only those materials, which possess completely filled electronic configuration. The atoms and molecules of diamagnetic substances do not possess any net magnetic moment (*i.e.*, all the orbital shells are filled, and there is no unpaired electron). However, when exposed to a magnetic field, the electrons orient themselves in such a direction to oppose the applied magnetic field and thereby register negative magnetization and negative susceptibility. Most of the semiconducting materials like ZnO and SnO_2 are diamagnetic by nature.

2.5.3. Paramagnetism:

In some solids, each atom possesses a permanent dipole moment owing to incomplete cancellation of electron spin and/or orbital magnetic moments. The orientations of these atomic magnetic moments are random in the absence of an external magnetic field, resulting in no net macroscopic magnetization. However, these atomic dipoles are free to rotate, and paramagnetism occurs when they preferentially align by rotation with an external magnetic field [KITT2004]. Some of the atoms or ions in this class of materials have a net magnetic moment due to unpaired electrons in the partially filled orbital. However, the individual magnetic moments are magnetically non-interactive ones. In the presence of an applied magnetic field, there is a partial alignment of atomic magnetic moments in the applied field direction, resulting in a net positive magnetization and positive susceptibility. Both diamagnetic and paramagnetic materials are, in general, considered to be non-magnetic as they exhibit magnetization only in the presence of an external field. The tendency of alignment of magnetic moments along the field direction is opposed by the thermal energy, which tries to randomize the spin orientation. Hence they exhibit a small and temperature (T) dependent paramagnetic susceptibility, χ_{para}, known as the Curie Law,

$$\chi_{para} = \frac{C}{T} \tag{2.06}$$

with a Curie constant '*C'* [BLUN2003]. In classical theory, each atomic moment is considered as magnetic dipole alignment in a particular direction with an angle θ with respect to the applied magnetic field and average magnetic moment along the field direction, *z* is illustrated as

$$< \mu^z > = \mu L(y) \tag{2.07}$$

Here, μ is the magnetic moment of each dipole, and $L(y)$ is the Langevin function, $L(y) = Coth(y) - 1/y$, where $L(y) = \mu B/(k_B T)$. This Langevin function elucidates the magnetization of small particles made up of atomic clusters. In case of low applied field or at high temperature, such that *y* is small, $L(y)$ tends to $y/3$. So,

$$< \mu^z > = \frac{\mu y}{3} = \frac{\mu^2 B}{3k_B T} \tag{2.08}$$

Or, the magnetization

$$M = N < \mu^z > = \frac{N\mu^2 B}{3k_B T} \tag{2.09}$$

So, the susceptibility

$$\chi_{para} = \frac{M}{H} = \frac{\mu^2 N \mu_0}{3k_B T} = \frac{C}{T} \tag{2.10}$$

The above expression is the Curie law, as obtained by the classical theory. Based on the quantum mechanical treatment and taking into account the quantization of total angular momentum of each atom, the average magnetic moment per atom aligned along the direction of the applied magnetic field (*i.e.*, '*z'* direction) of any paramagnetic sample can be stated as [JILE1997, GUIM1998, BLUN2003].

$$< \mu_J{}^z > = g\mu_B J B_J(x) \tag{2.11}$$

Here *g* is the Landé *g*-factor, which depends on the spin-orbit coupling of electrons in each atom, *J* is the total angular momentum quantum number, μ_B is the Bohr magneton with a value of 9.27×10^{-24} J/T, and $B_J(x)$ is the Brillouin function. The Brillouin function is defined as,

$$B_J(x) = \frac{1}{J}\left[\left(J + \frac{1}{2}\right) Coth\left(J + \frac{1}{2}\right)x - \frac{1}{2} Coth\frac{x}{2}\right] \tag{2.12}$$

Here, the variable $x = g\mu_B B/(k_B T)$, where k_B is the Boltzmann constant, and T is the temperature. If N is the number of atoms per unit volume, the volume magnetization M can be written as,

$$M = N < \mu_J{}^z > = Ng\mu_B J B_J(x) \tag{2.13}$$

For the selection of magnetic field B and temperature T such that x is small, $B_J(x) = [J(J+1)/3]x$. This assumption holds true for paramagnetic samples over a wide temperature range and low applied field. Therefore,

$$< \mu^z > = Ng\mu_B J \frac{(J+1)}{3} x = \frac{Ng^2\mu_B^2 B}{3k_B T} J(J+1) \tag{2.14}$$

Or the susceptibility,

$$\chi_{para} = \frac{\mu_0 N g^2 \mu_B^2}{3k_B T} J(J+1) \tag{2.15}$$

It is in the form of Curie law, C/T. Thus, the magnetic susceptibility based on Brillouin function expression reduces to Curie-law. Some examples of paramagnetic materials are W, Ce, Al, Li, Mg, *etc.* with typical χ_{para} values of 6.8×10^{-5}, 5.1×10^{-5}, 2.2×10^{-5}, 1.4×10^{-5} and 1.2×10^{-5}, respectively in SI units [BLUN2003].

2.5.4. Ferromagnetism:

Certain materials exhibit a permanent magnetic moment resulting from the strong interaction between the magnetic moments of atoms, even in the absence of an external magnetic field. This dominates over the thermal energy and reveals an alignment of magnetic moments in a particular direction. Such behavior is exhibited by some of the transition metals like Fe, Co, Ni, and some rare earth metals. Ferromagnetic materials show two distinct characteristics: (1) spontaneous magnetization and (2) existence of magnetic ordering temperature. Spontaneous magnetization is the net magnetization, which exists inside a uniformly magnetized microscopic volume, even in the absence of an external magnetic field. The magnitude of this magnetization at absolute temperature depends on the spin magnetic moments of electrons. The atomic moments in ferromagnetic materials align either in a parallel or an antiparallel arrangement exhibiting very strong interactions, which are produced by the electronic exchange forces. Therefore, a large net magnetization exists in ferromagnetic materials even after the removal of the external applied magnetic field.

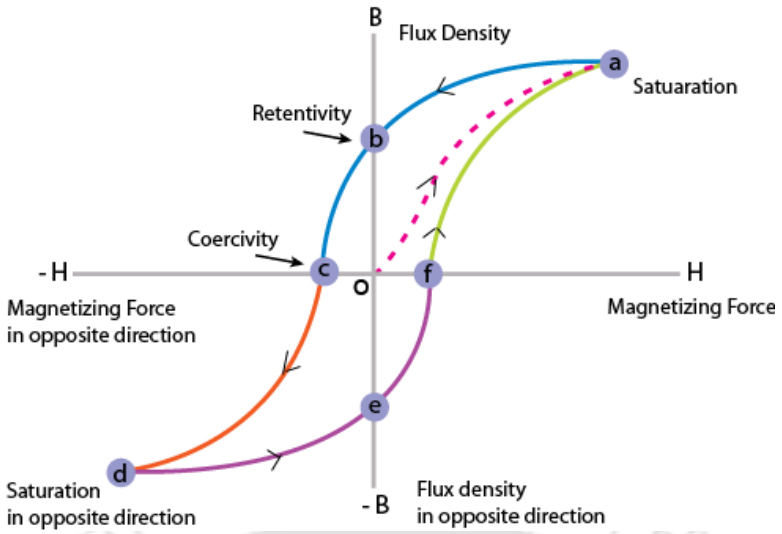

Figure 2.05: Magnetic hysteresis loop of a ferromagnetic material.

All ferromagnetic materials exhibit a magnetic hysteresis loop (*M-H* loop) under the application of an external magnetic field, as displayed in Figure 2.05. By studying the *M-H* loop, we can have detailed information about the magnetic properties of the corresponding ferromagnetic material. The loop is generated by measuring the magnetic flux of a ferromagnetic material while the magnetizing field is changed continuously. In the virgin state, the ferromagnetic materials follow the dashed line starting from the origin ‘o’. As the applied field is increased, it reaches the point 'a' where almost all of the magnetic domains are aligned to field direction, and a further increase in the magnetizing field produces a very little or no increase in magnetic flux. The magnetization obtained at this point is known as the saturation magnetization (M_S). When the applied field is reduced to zero, the curve goes from point ‘a’ to ‘b’ and not to ‘o’. Therefore, some magnetic flux remains in the material even at zero magnetic fields. This is called as retentivity and indicates the remanence or level of residual magnetism in the ferromagnetic material. As the magnetic field is reversed, the curve moves to point ‘c’, where the magnetization truly reaches zero. This point is termed as the coercivity (H_C) or coercive force. With further increasing the applied field in a negative direction, materials again become magnetically saturated, but the moments align exactly in the opposite direction (point ‘d’). Further reducing the field to zero brings the curve to point ‘e’. At this point, the level of residual magnetism is almost equal to that achieved in the other direction (point ‘b’). Increasing the field back in the positive direction returns the magnetization to zero. Successively, the magnetization curve takes a different path from point 'f' back to the saturation point (point ‘a’), where it completes the loop. From

the *M-H* loop, the following magnetic parameters can be obtained: (i) Retentivity: the material's ability to retain a certain amount of magnetization when the magnetizing field is removed after attaining saturation, (ii) Coercivity: the magnitude of the reverse magnetic field necessitated to make the magnetization to zero; (iii) Permeability: property of the material that describes the ease with which a magnetic flux is established in the component. These hysteresis or magnetic parameters are not only intrinsic properties but are also dependent on various parameters such as grain size, domain state, internal stresses, and temperature. As the magnetic parameters depend on the grain size, they are useful for the magnetic grain sizing of natural samples. The elements Fe, Ni, and Co and their alloys are typical examples of ferromagnetic materials. Ferromagnetic materials are categorized broadly into two types: (a) hard ferromagnetic materials exhibiting a very high H_C (> 1000 Oe) and are used mostly as permanent magnets and media for data storage and (b) soft ferromagnetic materials with low H_C (< 100 Oe), which are used for transformer core, read head and magnetic sensor applications. With increasing temperature, ferromagnetic materials exhibit a transition from a ferromagnetic state to the paramagnetic state at a temperature termed as the Curie temperature (T_C) when the thermal energy eventually overcomes the exchange energy and produces a randomizing effect leading to paramagnetism.

The phenomenon of ferromagnetism can often be described by the Mean-field or Molecular field model. The molecular field model merely assumes that all the interactions from the neighboring magnetic species can be explained in terms of an effective internal or molecular field B_m, which is proportional to the magnetization, *i.e.*, $B_m = \lambda M$, where λ is the Weiss molecular field constant. So the total magnetic field experienced by each dipole is the sum of applied magnetic field B and the molecular field B_m. Then, the expression for magnetization, as stated in eqn. (2.13) can be modified as

$$M = \frac{Ng^2\mu_B^2 J(J+1)}{3k_B T}(B_a + \lambda M) \qquad (2.16)$$

2.5.5. Antiferromagnetism:

In certain materials, the spins of electrons have a tendency to align in a regular pattern with neighboring spins pointing in opposite directions, below a specific temperature, known as the Néel temperature (T_N). Hence, within T_N, the overall magnetization gets canceled out and gives to an almost zero magnetic moment. Pointed out by Néel in 1936, these materials are

called as the antiferromagnetic materials. Above T_N, the material is typically paramagnetic due to the randomization of magnetic moments. The magnetic susceptibility of antiferromagnetic materials appears to go through a maximum as the temperature is lowered. The antiferromagnetic ordering in a material is possible based on different types of magnetic unit cell structure, as shown in Figure 2.06 except for the *B* type, which is a ferromagnetically ordered.

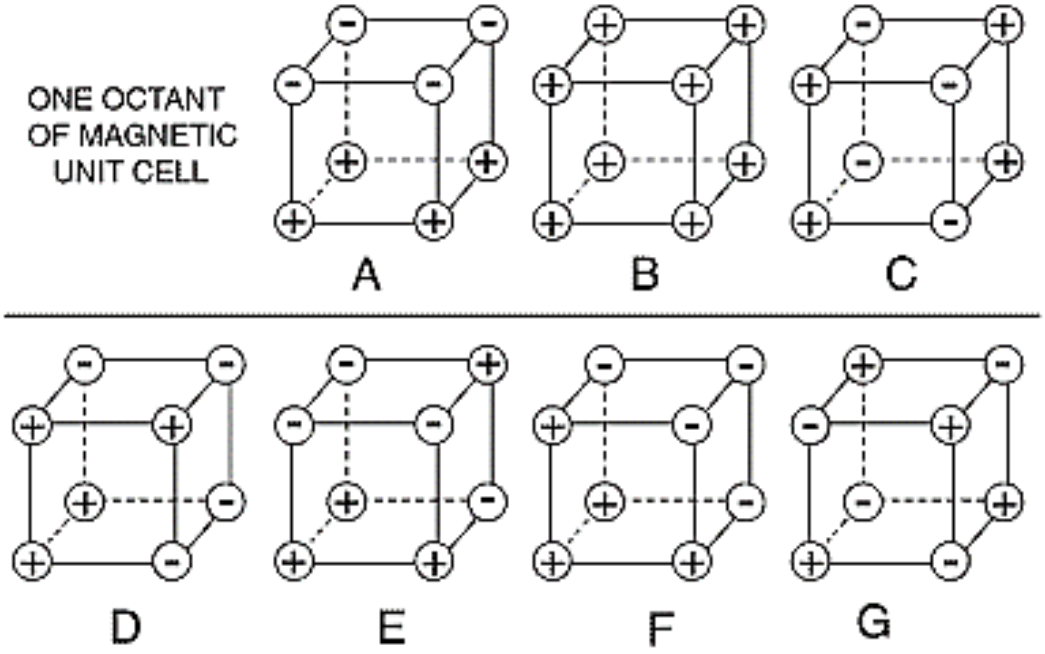

Figure 2.06: Different types of antiferromagnetic arrangement in a unit cell [HTTP0004].

In *A*-type structure, the magnetic ions are coupled ferromagnetically in each (001) plane but with alternate planes aligned in an opposite spin orientation such that a net antiferromagnetic interaction is exhibited. The *B*-type structure is a ferromagnetic one with all the six nearest neighbor magnetic ions coupled ferromagnetically. In *C*-type structure, the atoms in (101) and (110) planes are ferromagnetically aligned where each atom has two ferromagnetic and four antiferromagnetic nearest neighbors to form a net antiferromagnetic unit cell. In *G*-type structure, each ion is coupled antiferromagnetically to all of its six nearest neighbors. Some materials follow a structure, which is a result of the coupling of two types of magnetic structures. One such example is the *CE*-type, where there is coherent stacking of octants of *C* and *E*-type structures. The examples of antiferromagnetic materials are MnF_2, MnO, CoO, FeO, Cr_2O_3, NiO, α-Fe_2O_3 with T_N of 67 K, 116 K, 292 K, 116 K, 307 K, 525 K, and 950 K, respectively [BLUN2003].

2.6. Intrinsic properties of magnetic materials:

2.6.1. Exchange interaction:

Weiss (1907) reported that in addition to any externally applied field *H*, there is an internal molecular field or exchange field in a ferromagnetic material proportional to its magnetization.

$$\overrightarrow{B_E} = \lambda \vec{M} \tag{2.17}$$

Where λ is a constant and independent of temperature. According to eqn. (2.17), each spin sees the average magnetization of all the other spins. This molecular field is not truly a magnetic field, and so does not enter into the Maxwell equations. For instance, there is no current density $\vec{j}$ related to $\overrightarrow{B_E}$ by $\vec{\nabla} \times \vec{H} = 4\pi\vec{j}/c$. The magnitude of the molecular field may be as high as 10^3 Tesla. Now the major question which arises is, what is the origin of such a huge internal molecular field? For example, the magnetic field at distance *r* due to a magnetic dipole of dipole moment *m* is [KITT2004],

$$\overrightarrow{B_{dip}} = \left(\frac{\mu_0 M}{4\pi r^3}\right)[2cos\theta\overrightarrow{e_r} + sin\theta\overrightarrow{e_\theta}] \tag{2.18}$$

The order of magnitude of, $B_{dip}(= \mu_0 H_{dip})$ is, $\mu_0 M/4\pi r^3$. Taking m = 1 μ_B and r = 0.1 nm, it provides, $B_{dip} \approx$ 1 Tesla or 10 kG only. This reveals that the huge molecular field is not due to the magnetic dipole interaction. This mystery was a lingering topic until 1928 after the concept of exchange interaction was put forward by Heisenberg [HEIS1928]. The origin of the Heisenberg exchange interaction is electrostatic but involves quantum mechanical explanations. The charge distribution of a system of two spins depends on whether the spins are parallel or antiparallel. Pauli's exclusion principle dismisses the possibility of two identical electrons occupying the same quantum state simultaneously. However, it does not exclude the same criterion for two electrons of opposite spin. Hence, the electrostatic energy of a system depends on the relative orientation of the spins: the difference in energy defines the exchange energy. The energy of interaction between the atoms *i* and *j* bearing electron spins S_i and S_j is defined from the Heisenberg model as [OHAN2000],

$$E_{exch} = -2\sum_{i<j} J_{ij} S_i . S_j \tag{2.19}$$

Where J_{ij} is the exchange integral and is correlated to the overlap of the charge distribution of the atoms *i* and *j*. Supposing that the exchange interaction is the same for each nearest-neighbor pair, eqn. (2.19) turns as

$$E_{exch} = -2J \sum_{i<j}^{nn} S_i . S_j \tag{2.20}$$

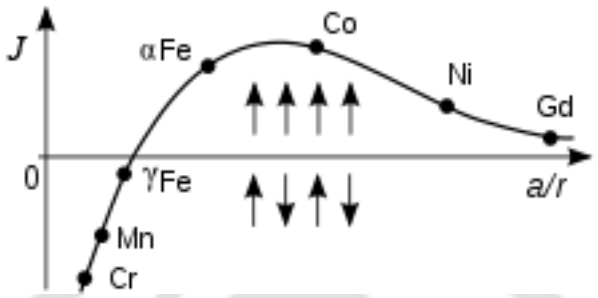

Figure 2.07: Bethe-slater curve: Elements above (below) the horizontal axis are ferromagnetic (antiferromagnetic) [HTTP0005].

For the parallel orientation of the magnetization (ferromagnet), *J* should be positive, and for the antiparallel alignment of spins, *J* should be negative. The variation of *J* with respect to inter-atomic distance is known as the 'Bethe-Slater curve' and is displayed in Figure 2.07. It is clear from Figure 2.07 that the value of *J* and hence the short-range exchange interaction depends strongly on the inter-atomic distance. Eqn. (2.20) can further be simplified by taking into account the energy of a particular atom *i* interacting with its *j* nearest neighbor:

$$E_{exch}^{i} = -2JS_i \sum_{j} S_j \tag{2.21}$$

While for the entire material,

$$E_{exch} = -\frac{1}{2} \sum_{j} E_{exch}^{i} \tag{2.22}$$

Thus, the discrete, pairwise interaction can be replaced by assuming that the magnetic moment $\mu_m^i = g\mu_B S_i$ at the site, *i* interact with a molecular field. H_{eff} given by the net effect of the *z* nearest-neighbor spins:

$$E_{exch}^{i} = -\mu_0 \mu_m^i H_{eff} = -g\mu_0 \mu_B S_i H_{eff} \tag{2.23}$$

Where g is the Landé *g*-factor, μ_B is the Bohr magneton, and μ_0 is the permeability of the free space (= $4\pi \times 10^{-7}$ H/m or 1.256×10^{-6} H/m). Comparing eqn. (2.23) with eqn. (2.21), the effective field can be written as,

$$H_{eff} = \frac{2J}{g\mu_0\mu_B}\sum_j S_j \cong \frac{2zJ}{g\mu_0\mu_B}\langle S_j\rangle \tag{2.24}$$

Here, the sum over *z* neighboring spins has been replaced by *z* times the average spin value $\langle S_j\rangle$. Using $M = N_v g\mu_B\langle S_j\rangle$, eqn. (2.24) gives,

$$H_{eff} \cong \frac{2zJ}{N_v g^2 {\mu_B}^2 \mu_0} M \tag{2.25}$$

From eqn. (2.25), it can be seen that H_{eff} is the Weiss molecular field defined as, $H_{mol} = \lambda M$ provided

$$\lambda = \frac{2zJ}{N_v g^2 {\mu_B}^2 \mu_0} \tag{2.26}$$

Using the value of the molecular field coefficient λ as 10^3, *J* is calculated to be 2×10^{-21} J or 0.01 eV/atom. Exchange interactions are weaker than the Coulomb interactions that distinguish levels of different principal and orbital quantum numbers, but stronger than spin-orbit interaction. Following the treatment of Weiss molecular field that $T_C = \lambda C$ with $C = N_v {\mu_m}^2 \mu_0/3k_B$, the expression for T_C can be obtained from eqn. (2.26) as

$$T_C = \frac{2zJ{\mu_m}^2}{g^2{\mu_B}^2 3k_B} = \frac{2zJs(s+1)}{3k_B} \tag{2.27}$$

where, $\mu_m = \sqrt{g\mu_B s(s+1)}$. Another vital relation between exchange energy and the magnetization is defined as,

$$\frac{E_{exch}^{ij}}{V} = \frac{s^2a^2JN_v'}{2}\left(\frac{\nabla M}{M}\right)^2 = A\left(\frac{\nabla M}{M}\right)^2 \tag{2.28}$$

Where *a* is the distance between the spins, *A* is the exchange stiffness constant having a value of 5×10^{-12} J/m to 30×10^{-12} J/m for most ferromagnets, and N_v' is the number of nearest-neighbor atoms per unit volume. Thus, it is clear from the above equations that the exchange energy or the Heisenberg exchange interaction strongly depends on temperature due to the dependence of interatomic distance with temperature. In particular, the disordered ferromagnetic system is the subject of low T_C value due to the low value of *J*.

2.7. Anisotropy:

In a material, when a physical property relies on the direction, that property is said to exhibit anisotropy. In magnetism, the preference of magnetization to lie in a particular direction of the material is called magnetic anisotropy. As anisotropy contributes prominently in tuning

the nature of the *M-H* loop, it is crucial to understand the various possible sources of its origin and influence on controlling the magnetic properties. The anisotropy of a material can be intrinsic as a result of its crystal chemistry or shape or induced by a suitable processing technique. Figure 2.08 displays a typical situation where for zero applied field, the magnetization would point along the easy axis shown (α = 0). When a field is applied, the magnetization is pulled towards the field direction and approaches closer to the field direction with increasing applied field. For any intermediate values of α, the magnetization gets attracted in opposite directions, *i.e.*, up by the field and down by the anisotropy.

Let us assume that all the magnetization in a magnetic material is pointing in the same direction, and the material exhibits an easy axis of magnetization. In such a scenario, the energy per unit volume of the magnetization is described as,

$$E = K\,sin^2\alpha \tag{2.29}$$

Where *K* is the anisotropy constant with a unit of energy per unit volume (J/m^3 or erg/cc). Hence, the energy term, *E*, is also energy per unit volume. Generally, the magnitude of uniaxial anisotropy is described in terms of the anisotropy field, which is defined as the field required to saturate the magnetization of a uniaxial crystal in the hard axis direction, as stated in eqn. (2.30) as,

$$H_k = \frac{2K}{\mu_0 M} \tag{2.30}$$

In general, the energy of the magnetization is,

$$E = K\,sin^2\alpha - \mu_0 MH\,cos(\beta - \alpha) \tag{2.31}$$

Where the first term is the anisotropy energy whereas the second term is due to the magnetic field, and the difference in the angle (β - α) is the angle between *H* and *M*. In order to have equilibrium, the first derivative is required to be zero. Therefore, the derivative of eqn. (2.31) with respect to the angle α provides,

$$\frac{dE}{d\alpha} = 2K \sin\alpha \cos\alpha - \mu_0 MH\,sin(\beta - \alpha) = 0 \tag{2.32}$$

Taking the value of β as 90° for the equilibrium angle for magnetization relative to the easy axis and considering the eqn. (2.30), we have

$$\sin\alpha = \frac{H}{H_k} \tag{2.33}$$

The above equation implies that when H = 0, the magnetization points along the easy axis, and when $H = H_K$, the magnetization points along the direction of the field. For any

intermediate values of the field, the magnetization points at a value of angle as given by eqn. (2.33) rotating smoothly between the easy axis and the applied field.

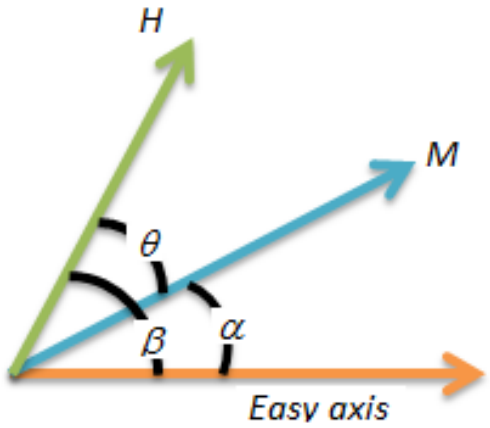

Figure 2.08: Schematic diagram of magnetization, applied field, and easy axis for a given material.

2.7.1. Magnetocrystalline anisotropy:

The tendency of the magnetization to align itself along a preferred crystallographic direction is termed as the magnetocrystalline anisotropy and is an intrinsic property of the magnetic material. The preferred crystallographic direction is called the 'easy' axis since it is easiest to magnetize a demagnetized sample to saturation if the applied field is along the preferred direction, meanwhile, the direction where a much larger field is required to reach saturation is known as the 'hard' axis. Hence, the crystal is higher in energy when the magnetization points along the hard direction as compared to the easy axis, and the energy difference per unit volume between the samples magnetized along the easy and hard axis is called the magnetocrystalline anisotropy energy and is measured through the area between the hard and easy magnetization curves. The isothermal initial magnetization (*IM*) curves of single crystals of different 3*d* ferromagnetic elements are shown in Figure 2.09 for explaining the same. It can be observed that the magnetization approaches saturation in different ways when magnetized in different directions. For instance, body-centered cubic iron displays [100] as easy axis and [111] as hard direction, while nickel with face-centered cubic crystal structure has [111] as easy axis and [100] as hard directions. This behavior can well be understood by analyzing the development of anisotropy energy in different symmetries as stated below,

For hexagonal:

$$E_a = K_1 \sin^2\theta + K_2 \sin^4\theta + K_3 \sin^6\theta + K_3' \sin^6\theta \sin 6\phi \quad (2.34)$$

For tetragonal:

$$E_a = K_1 \sin^2\theta + K_2 \sin^4\theta + K_2' \sin^4\theta \cos 4\phi + K_3 \sin^6\theta + K_3' \sin^6\theta \sin 6\phi \quad (2.35)$$

For cubic:

$$E_a = K_{1c}(\alpha_1^2\alpha_2^2 + \alpha_2^2\alpha_3^2 + \alpha_3^2\alpha_1^2) + K_{2c}(\alpha_1^2\alpha_2^2\alpha_3^2) \quad (2.36)$$

Where α_i are the direction cosines of the magnetization. K_{1c} term is equivalent to $K_{1c}(\sin^2\theta\, cos^2\phi \sin^2\phi + \cos^2\theta \sin^2\theta)$. When, θ = 0, ϕ = 0, this term reduces to eqn. (2.29) [COEY2010].

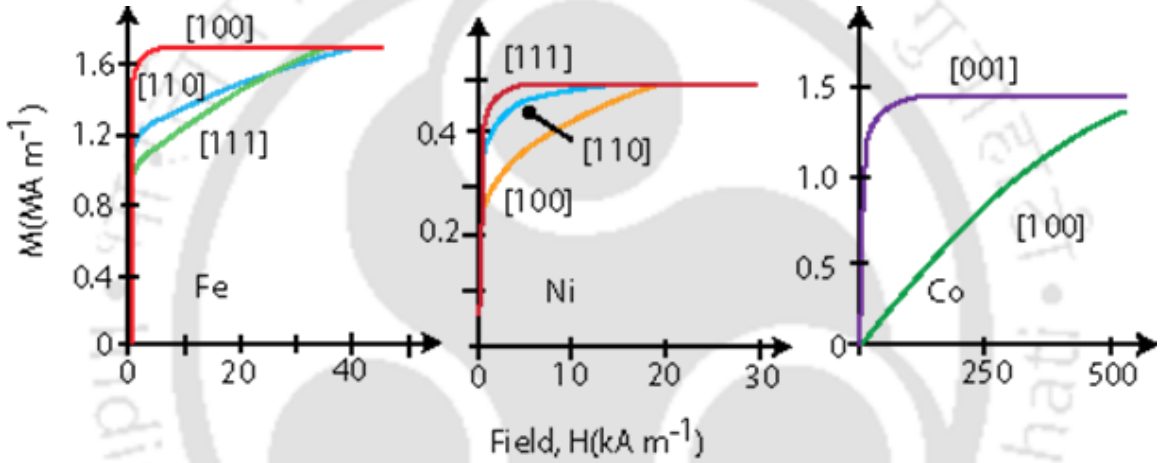

Figure 2.09: Magnetization of single crystals of Iron, Nickel, and Cobalt [COEY2010].

Figure 2.10: Schematic drawing of broadside and head-to-tail configurations for a pair of ferromagnetically coupled magnetic moments.

Origin of magnetocrystalline anisotropy: There are two distinct sources of magnetocrystalline anisotropy: (i) single-ion contributions and (ii) two-ion contributions. The single-ion contribution is due to the electrostatic interaction of the orbitals containing the magnetic electrons with the potential created at the atomic site by the rest of the crystal. This crystal field interaction stabilizes a particular orbital, and then by the spin-orbit interaction, the magnetic moment is aligned in a specific crystallographic direction. For instance, a uniaxial crystal having 2×10^{28} ions/m^3 described by a spin Hamiltonian DS^2 with

D/k_B = 1 K and S = 2 will have the anisotropy constant as, $K_1 = nDS^2 = 1.1\times10^6$ J/m^3. This single ion contribution is a major anisotropic component in hard magnetic materials where the tendency for the magnetization to align along a particular crystallographic direction turns the susceptibility to a tensor rather than a scalar quantity. On the contrary, the two-ion contribution replicates the anisotropy of the dipole-dipole interaction. Taking into consideration the broadside and head-to-tail configurations of two dipoles, each having moment m, as shown in Figure 2.10, the energy of the head-to-tail configuration is lower by $3\mu_0 m^2/(4\pi r^3)$, and hence the magnets tend to align head-to-tail. In non-cubic lattices, the dipole interaction is a prime source of ferromagnetic anisotropy.

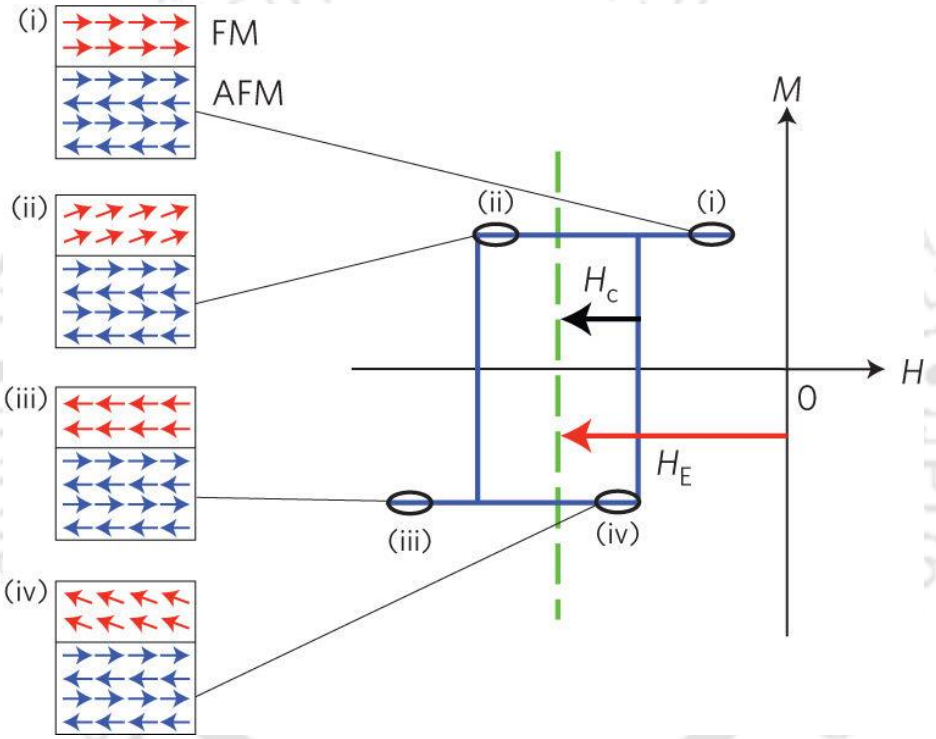

Figure 2.11: Schematic of relative orientations of the atomic moments in the antiferromagnetic and ferromagnetic materials, illustrating the lateral offset in the magnetization curve. The magnitude of the exchange bias field H_E and coercive field H_C are defined [FANY2013].

2.7.2. Exchange anisotropy (bulk):

Exchange anisotropy refers to the magnetic manifestations of an exchange coupling at the interface between two varyingly ordered magnetic systems. First proposed by Meiklejohn and Bean [MEIK1956] for Co particles embedded in antiferromagnetic CoO, the surface exchange anisotropy generally arises due to the exchange coupling between the antiferromagnetic regions with the ferrimagnetic or ferromagnetic regions. The

antiferromagnetic regions of the material are deemed as the regions of stronger magnetocrystalline anisotropy, and therefore, the preferential direction of magnetization gets transmitted to the adjacent ferromagnetic region by exchange coupling across the interface. Exchange bias is usually defined by an asymmetric *M-H* loop and is characterized by an exchange bias field H_E. For the Co (T_C = 1390 K)/CoO (T_N = 291 K) system reported by Meiklejohn and Bean, shifted *M-H* loops of partially oxidized Co particles is observed at 77 K in a field of 1 Tesla [MEIK1956] due to the resulting interaction between the antiferromagnetic CoO and ferromagnetic Co particles. In the case of thin films with proper layer structures of antiferromagnetic/ferromagnetic material [FANY2013], the nature of the *M-H* loop and shift in the loop can be controlled, as shown in the Figure 2.11.

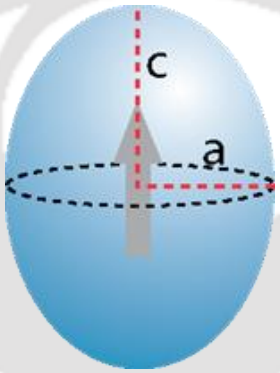

Figure 2.12: Magnetization of a prolate ellipsoid of revolution with $c > a$ and no magnetocrystalline anisotropy. *c*-axis is the easy direction of magnetization.

2.7.3. Shape anisotropy:

Though most of the magnetic samples show some magnetocrystalline anisotropy, a polycrystalline sample with no preferential orientation of its grains cannot possess an overall crystalline anisotropy. However, only if the sample is exactly spherical, then the same field is required to magnetize the sample to the same extent in every direction, and if non-spherical, then it is easier to magnetize it along a long axis. This phenomenon arising in the materials due to the asymmetric shapes is called shape anisotropy [SPAL2010]. This is, in particular, important for thin films where one dimension is very short as compared to other dimensions. The demagnetization field inside the material or the stray field outside the magnetic material depends on the magnetization and shape of the material [JILE1997, OHAN2000, BLUN2003]. The magnetostatic energy of a ferromagnetic ellipsoid (Figure 2.12) with magnetization M_S is given as

$$E_m = \frac{1}{2}\mu_0 VNM_S^2 \tag{2.37}$$

The anisotropy energy is related to the difference in energy ΔE when the ellipsoid is magnetized along its hard and easy directions. N is the demagnetization factor tensor for the easy direction. $N' = (1/2)\,(1 - N)$ is the demagnetization factor tensor for the hard directions. Hence,

$$\Delta E_m = \frac{1}{2}\mu_0 VM_S^2\left[\frac{1}{2}(1-N) - N\right]$$

$$\Delta E_m = \frac{1}{4}\mu_0 VM_S^2[1-3N]$$

$$K_{sh} = \frac{1}{4}\mu_0 M_S^2[1-3N] \tag{2.38}$$

Also, the demagnetization factor tensor, which relates the demagnetization field with a specimen magnetization as a function of the position is given by [NEAL1994],

$$N(r) = -\frac{1}{4\pi}\iiint d^3r'\nabla'\left(\nabla'\left(\frac{1}{r-r'}\right)\right) \tag{2.39}$$

Table 2.03: Demagnetization factors (in Gaussian units) of selected shapes.

Shape	N_1	N_2	N_3
Sphere	4π/3	4π/3	4π/3
Long Cylinder along the z-axis	2π	2π	0
Infinite plate normal to the *z*-axis	0	0	4π
Strip film normal to the *z*-axis (with *t* – thickness, *W* – Width, *L* – Length; $t \le W \le L$)	0	8*t*/*W*	4π

This tensor is given by the integral over the object volume and can be evaluated either inside or exterior to the body. The value of tensor N depends mostly on the specimen shape, which is difficult to obtain in closed-form and can only be calculated for an ellipsoidal shape precisely. In many symmetrical materials such as any ellipsoids of revolution, the demagnetization factor tensor has only three principal components, *i.e.*,

$$\begin{pmatrix} H_1 \\ H_2 \\ H_3 \end{pmatrix} = -\begin{pmatrix} N_1 & 0 & 0 \\ 0 & N_2 & 0 \\ 0 & 0 & N_3 \end{pmatrix}\begin{pmatrix} M_1 \\ M_2 \\ M_3 \end{pmatrix} \tag{2.40}$$

where, $N_1 + N_2 + N_3 = 1$ (in SI) and $N_1 + N_2 + N_3 = 4\pi$ (Gaussian). The demagnetization factors for the selected shapes are summarized in Table 2.03. A meticulous calculation of the demagnetization factor for various objects can be found in [NEAL1994]. As $N = 1/3$ for a sphere, it does not have any shape anisotropy. This anisotropy is fully effective in samples that are so small that they do not break up into any further domains [COEY2010].

2.7.4. Surface anisotropy:

The magnetic anisotropy originated due to the reduced magnetic coordination of the surface spins as compared to the bulk surface spin is called the surface anisotropy. This anisotropy arises due to the missing neighbors for the surface spins and the breaking of their crystal field symmetry. Surface anisotropy contributes to a significant anisotropic component in magnetic nanoparticles where a significant fraction of atoms reside on the surface, and their magnetic properties such as exchange and anisotropy are starkly modified as compared to their massive counterpart. Proposed by Néel [NEEL1953] and microscopically modeled by Victora and MacLaren [MACL1994], this anisotropy is much stronger than a typical crystallographic anisotropy experienced by the particle's core. The general form of the Néel's approach to the surface anisotropy is, $E_{SA}^{N\acute{e}el} = -K_s \sum_i \sum_{j \neq i} (S_i . e_{ij})^2$, where, S_i defines to the unit vector spin on-site, i of the nanoparticle, e_{ij} is the unit vector connecting site i to its nearest neighbors, the second summation is over the nearest neighbors j of site i, and K_S is the surface anisotropy term. In the case of weak magnetic anisotropies in magnetic nanoparticles, the surface component is generally approximated as a cubic contribution.

2.7.5. Magneto-elastic anisotropy:

When a ferromagnetic material is exposed to an applied magnetic field, and a change in magnetization occurs due to the presence of the mechanical strain of the lattice, it produces a unique easy axis of magnetization and the anisotropy involved in the process is known as the magnetoelastic anisotropy (MEA). The inverse effect, *i.e.*, when a ferromagnetic material is exposed to an external magnetic field, the dimensions of the material change and thereby experience strain. This process is known as magnetostriction. The anisotropy energy associated with the magnetoelastic effect can be expressed as [JOHN1996],

$$E_{mea} = -K_{mea}\ cos^2\phi \qquad (2.41)$$

Where ϕ is the angle between the magnetization and the plane of isotropic anisotropy. The value of K_{mea} can be stated as

$$K_{mea} = \frac{3}{2}\lambda\sigma = \frac{3}{2}\lambda E\varepsilon \qquad (2.42)$$

Where λ is the magnetostriction coefficient, and σ is the stress, which relates to the strain (ε) through the elastic modulus E.

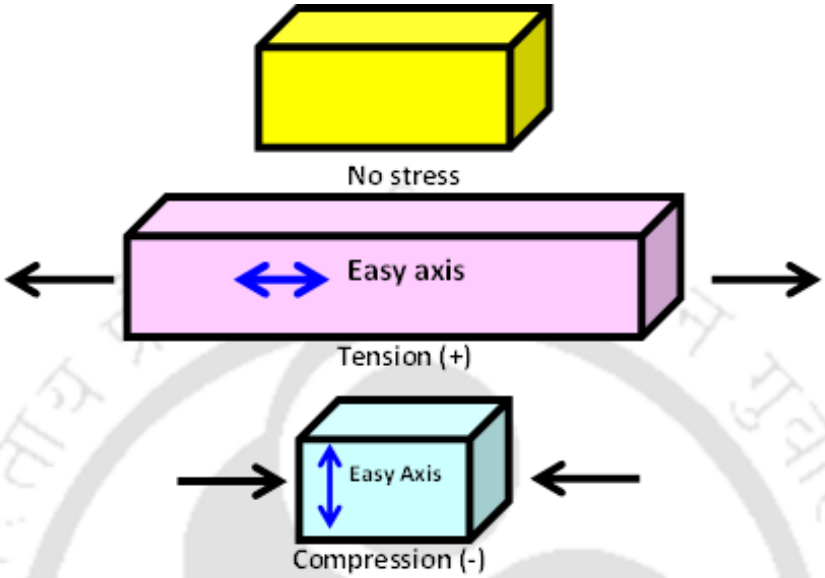

Figure 2.13: Schematic drawing of bars to demonstrate inducing an easy-axis in a material with positive magnetostriction.

The experimental values of λ for Fe, Ni, and Fe_3O_4 are -7×10^{-6}, -33×10^{-6} and -40×10^{-6}, respectively. Figure 2.13 shows the schematic view of bars with varying applied stress conditions. If λ is positive, then the application of tensile stress to the bar creates an easy axis in the direction of the applied stress. If compressive stress is applied, then the direction of the easy axis created remains perpendicular to the stress direction. On the contrary, if the magnetostriction constant of the material is negative, then the above phenomena would be reversed: tensile stress will create an easy axis perpendicular to the stress direction, and compressive stress will create an easy axis in the direction of the applied stress.

2.7.6. Induced anisotropy:

In certain magnetic materials, the magnetic anisotropy can be induced extrinsically in several ways: (i) By fabricating the nanoparticles in the presence of a magnetic field, (ii) heat-treating the materials in the presence of an externally applied field, and (iii) by applying uniaxial stress. For the first two cases after such treatment, the material may exhibit an easy axis of magnetization that points in the direction of the applied magnetic field. This induced

anisotropy is undeniably independent of any crystalline anisotropy or any other form of anisotropy that might be existent.

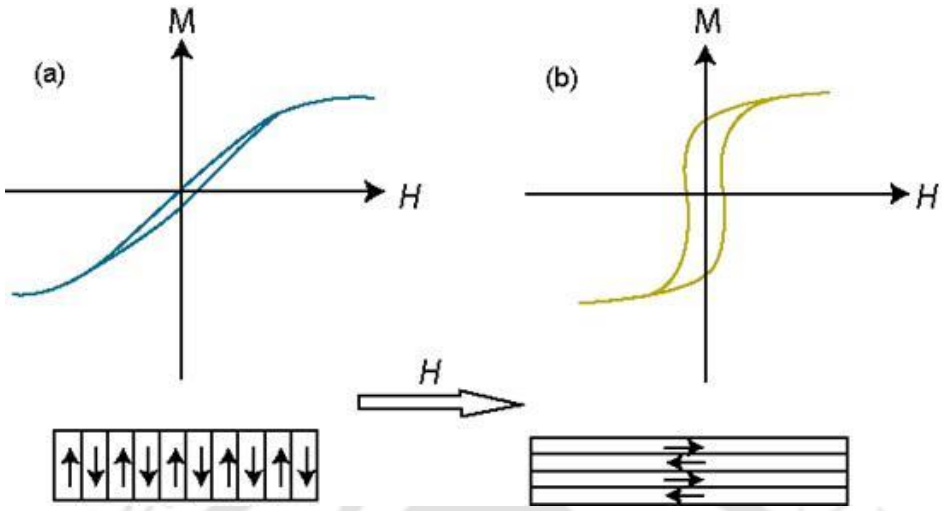

Figure 2.14: Magnetization of a thin film with induced anisotropy created by annealing in a magnetic field. The sheared (a) and open (b) loops are observed when the measuring field *H* is applied perpendicular and parallel to the annealing field direction, respectively.

Figure 2.14 represents a typical example of inducing the anisotropy in ferromagnetic materials by field annealing. In the last case, the uniaxial anisotropy is induced by applying uniaxial stress (σ) in a ferromagnetic solid [KRON2003]. The magnitude of the stress-induced anisotropy is

$$K_{u\sigma} = \frac{3}{2}\sigma\lambda_S \qquad (2.43)$$

Where λ_S is the saturation magnetostriction. The single-ion and two-ion anisotropy contribute to the stress-induced anisotropy. The highest values of uniaxial anisotropy are found in hexagonal and other uniaxial crystals. Smallest values are found in cubic alloys and amorphous ferromagnets.

2.8. Size effects and magnetism:

'God made the solid-state; He left the surface to the devil' stated by Enrico Fermi truly exemplifies the nanostructures through the prominent size/surface effect. Having smaller sizes, the nanostructures have a larger surface-area-to-volume ratio, and for small enough feature sizes, their properties are no longer dominated by the bulk of the material but by the surface atoms [BATL2002, BIEN2009]. A foremost effect of finite size on magnetic nanoparticles is the breaking of a large number of exchange bonds for surface atoms. This

has significant importance on ionic materials, as the exchange interactions observed in them are largely antiferromagnetic super-exchange interactions [ANDE1950] between the 3*d* orbitals of the metal ions and 2*p* orbitals of the oxygen ions. The strength of the super-exchange interaction is directly proportional to the overlap between these orbitals, so it depends on the bond length and bond angle between the metal ions and the intervening oxygen ion. Furthermore, contingent on the coordination, the finite size, and the large surface can have effects not only on the structural order like reduced coordination, lattice disorder, contracted bond lengths, *etc.* but also dominates the magnetic properties of the nanosized particles [TIWA2005, WINK2005, THOT2007, YIJB2007]. In most cases, the size effect is originated owing to the competition between the surface and core magnetic behaviors and is of great technological attention in the fields of magnetic storage media, spin valves, spin transistors, and spin-dependent tunneling devices [KODA19971, KODA19991, RUBI2001]. Theoretically, the magnetic nanoparticles are pictured as a perfectly ordered single spin, which rotates synchronously as a large spin pointing either 'up' or 'down' in a zero field along the easy axis. However, this cannot be said for surface atoms of the nanostructures where the structural defects like vacancies, dangling bonds, reduced atomic coordination, breaking of lattice symmetry result in site-specific surface anisotropy, weakened exchange coupling and misaligned surface spin leading to a net surface magnetization (Ferromagnetism or Antiferromagnetism). This surface magnetization largely depends on the finite size and degree of surface disorder [DOBR2005, HOCH2006, ZYSL2006, KODA19992].

Simultaneously, the large perturbations to the crystal symmetry at surfaces give rise to magnetocrystalline anisotropy of different magnitude and symmetry for surface sites as proposed by Néel in 1954 [NEEL1954]. The combined effect of reduced coordination and surface anisotropy, as reported by Kodama *et al.* [KODA1996, KODA19972, KODA19992], stated that the pairwise exchange interactions had the same magnitude for bulk and surface atoms. However, the total exchange interaction was found to be less (*i.e.*, fewer neighbors) for surface atoms due to reduced coordination, and the surface anisotropy was accounted as the uniaxial anisotropy.

These finite-size and surface effects are particularly significant in antiferromagnetic oxide nanoparticles. When the dimensions of antiferromagnetic oxides are decreased to the nanometric level, they exhibit weak ferromagnetism at the surface, and finite-size effects or a net magnetic moment originated from the uncompensated spins as proposed by Néel in

1961 and was attributed to the spin non-compensation of the two antiferromagnetic sublattices. Besides, due to structural disorder and broken bonds, the surface spin directions show deviation of the magnetic state from the perfect antiferromagnetic alignment resulting in a large magnetic anisotropy and observed finite magnetic moment [MAND2011]. For instance, NiO in bulk form is antiferromagnetic, with a T_N of 524 K [SRIN1984]. Interestingly, the magnetic behavior of NiO at the nanoscale is observed to be strongly dependent on the intercalated finite size effect, surface effect, and interface effect [MENE2010, TADI2010]. This is related to the observation of anomalous magnetic behaviors such as magnetic enhancement, large coercivity, spin-glass freezing, and unusual hysteretic behaviors [GHOS2006, MAND2011]. These anomalous properties of NiO nanoparticles have been explained through various models like the two-sublattice model [TAYL1993], multi-sublattice model [KODA19971], and core/shell model [CARN2010, ARAG2012]. NiO nanoparticle is observed to have a small net magnetic moment owing to an unequal number of spins on the two sublattices as a result of the finite size [RICH1956, SCHU1962]. Similarly, larger magnetic moments have been observed in NiO nanoparticles due to multi-sublattice structures in the nanometric level [JAGO2009]. Kodama *et al.* reported the finite-size effects in antiferromagnetic NiO nanoparticles and stated a huge magnetic moment of 700μ_B and an H_C of 10 kOe [KODA19971]. Vaidya *et al.* reported NiO/SiO_2 core-shell nanostructures with the uncompensated spin magnetism for a NiO particle size of 25-100 nm. [VAID2009]. A high M_S of 65 emu/g and a huge magnetic moment (500μ_B) in 3 nm NiO nanoparticles due to strong surface effect was reported by Winkler *et al.* [WINK2005]. However, the finite size and surface effects on the magnetic properties of NiO reported in the literature have been found to be somewhat inconsistent and dedicated to different factors altogether.

Among the finite-size effects, one of the most obvious and heavily studied one is the superparamagnetism. This is a form of magnetism appearing in small ferromagnetic and ferrimagnetic particles. The basic principle lying within is that the magnetic anisotropy energy, which keeps a particle magnetized in a particular direction is generally proportional to the particle volume as stated by the Stoner-Wohlfarth model [$K = 25K_BT/V$, where K is the anisotropy, V is the volume of the nanoparticle, K_B is the Boltzmann constant, and T is the temperature]. Hence for sufficiently small nanoparticles at a specific critical size, thermal excitations become sufficient to rotate the particle magnetization and thereby demagnetize the whole assembly of such fine particles [MARG2015]. The effect of

superparamagnetism is observed in nanoparticles having a single magnetic domain and a subsequent diameter ranging between 3-50 nm depending upon the material. Hence, the magnetization of the nanoparticle is considered as a single giant magnet, which is the sum of all the individual magnetic moments of the atoms in the nanoparticle. However, in specific nanoparticles, the critical temperature of the superparamagnetic limit can be considerably tuned by the presence of large magnetic anisotropy [SKUM2003]. Mostly, the significant contributions to the magnetic anisotropy in nanoparticles are the magnetocrystalline, shape, and exchange anisotropies. The shape anisotropy becomes prominent for smaller nanoparticles having highly anisotropic shapes [PARK2000, ROCA2006]. Similarly, it has been observed that the exchange anisotropy increases with increasing surface-area-to-volume atomic ratio [ROCA2006]. Hence, the magnetocrystalline anisotropy, shape anisotropy, and exchange anisotropy play the key role in the enhanced total magnetic anisotropy in the nanoparticles and are plausibly induced by the surface, size, and shape effect. The magnetic anisotropy constant decreases with increasing particle size, which further confirms the effect of finite size on the total magnetic behavior of the nanoparticle systems.

2.9. Magnetic interaction:

2.9.1. Direct exchange interaction:

If the two neighboring magnetic moments interact via an exchange interaction, the interaction is known as the direct exchange interaction. As the name suggests, this exchange interaction proceeds directly without the need for any intermediate molecules or ions**.** Though this looks like the most obvious route for an interaction to occur, the physical realm of the situations is scarcely simple. In reality, there is hardly seen any interesting magnetic phenomenon that could be explained based on the direct exchange. As there is insufficient overlapping of the participating magnetic dipoles, the direct exchange is not an important mechanism in controlling the magnetic properties of the materials.

2.9.2. Super-exchange interaction:

The long-ranged indirect exchange interaction between two non-neighboring magnetic ions mediated through a non-magnetic ion situated in between the magnetic ions is known as the super-exchange interaction. It was pointed out by Kramer [KRAM1934], Anderson *et al.* [ANDE1955, ANDE1958], Goodenough [GOOD1995], and Kanamori [KANA1959] that,

ferromagnetic and anti-ferromagnetic exchange interactions are possible via the super-exchange interaction. Mostly valid for the antiferromagnetic materials, the super-exchange interaction arises due to the kinetic energy advantage of the antiferromagnetic state where the magnetic ions are commonly separated by the intermediate non-magnetic oxygen ions and is a typical interaction experienced in many ionic solids, including antiferromagnetic oxides and fluorides.

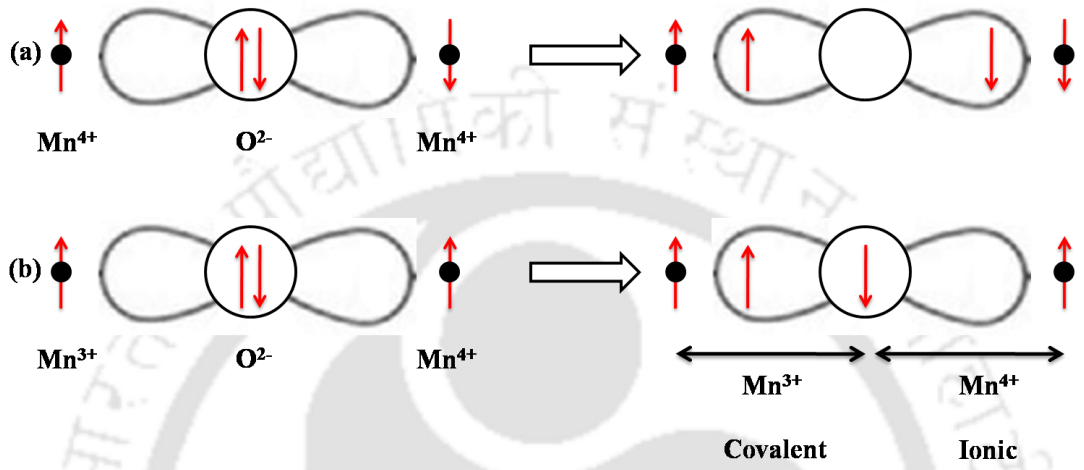

Figure 2.15: Arrangement of spins and orbitals in (a) an antiferromagnetic super-exchange interaction, and (b) a ferromagnetic super-exchange interaction.

A schematic representation of antiferromagnetic and ferromagnetic super-exchange interaction in MnO is shown in Figure 2.15 (a) and (b), respectively. In this case, there is no direct overlap between the Mn^{4+} cations. Figure 2.15 (a) presents the condition where the 3*d* orbitals point towards the O-2*p* orbital. The overlapping between the 3*d* and *p* orbitals enables the concurrent covalent bond formation between the cations (Mn^{4+}) and anions (O^{2-}) on both sides since the electrons of O^{2-} anion is shared with the 3*d* electrons. Here, out of two valence electrons of oxygen, the up spin electron spends some time with the cation in one side having up spin configuration, and the down spin electron spends some time with other cation having down spin configuration to satisfy the Hund's rule. In this process, each cation-anion pair has a ferromagnetic (parallel) alignment of electrons, and the net cation-cation interaction is antiferromagnetic.

According to Goodenough [GOOD1995], the above covalent bonding is not permissible if the core spins of magnetic cations are aligned parallel, as shown in Figure 2.15(b). Within this situation, out of two valence electrons of O^{2-}, the spin-up electron forms covalent bonding with left side cation (Mn^{3+}) having spin up electron, while the spin-down

electron of oxygen forms an ionic bond with right side cation (Mn^{4+}). The direct exchange between oxygen and the right side cation is antiferromagnetic. So, overall ferromagnetic interaction prevails between Mn^{3+} and Mn^{4+} ions.

2.9.3. Magnetic dipole-dipole interaction:

Magnetic dipole-dipole interaction [BLUN2003] or dipolar coupling refers to the direct interaction between two magnetic dipoles. The energy of the interaction is given as

$$H = -\frac{\mu_0}{4\pi r_{ij}^3}[3(\mu_i.\hat{r}_{ij})(\mu_j.\hat{r}_{ij}) - (\mu_i.\mu_j)] \qquad (2.44)$$

where $\hat{r}_{ij}$ is a unit vector parallel to the line joining the centers of the two dipoles, μ_i, μ_j are the moments of two dipoles separated by a distance $|r_{ij}|$. This interaction is important in the properties of those materials, which order at milli-Kelvin temperature. The magnetic dipolar interaction is too weak to account for the ordering of most magnetic materials with high material ordering temperatures. There is a built-in anisotropy to the dipolar interaction, which can orient the spins either parallel (ferromagnetic) or antiparallel (antiferromagnetic) alignment. If the spins are oriented along r_{ij}, they couple ferromagnetically. Otherwise, they couple antiferromagnetically.

2.9.4. Anisotropy interaction:

Dzyaloshinskii [DZYA1958] postulated a contribution to the exchange interaction between two neighboring spins, which was later identified by Moriya [MORI1960] as the spin-orbit coupling between the spins. This is a probable case where spin-orbit interaction plays a vital role as a substitute for the oxygen atom for superexchange interaction. Here, the excited state of one of the participating ions is not connected with oxygen ion but is produced by the spin-orbit coupling in one of the magnetic ions. So there is an exchange interaction that arises between the excited state of one ion with the ground state of the other ion and known as the anisotropic exchange interaction or the Dzyaloshinskii-Moriya interaction.

2.10. Law of approach to magnetic saturation:

The theoretical model based on the micro-magnetism of ferromagnetic materials was developed by Brown to describe the law of approach to saturation magnetization [BROW1940, BROW1941]. A generalized equation [KRON1959] for the high-field magnetization is expressed in the form of a series as,

$$M(H) = M_S\left(1 - \frac{a_1}{\sqrt{H}} - \frac{a_2}{H} - \frac{a_3}{H^{3/2}} - \frac{a_4}{H^2}\ldots\right) + \alpha T\sqrt{H} + \chi_p H \qquad (2.45)$$

Where *M(H)* is the magnetization in an external field *H*, M_S is the saturation magnetic moment, χ_p is the high-field susceptibility terms. The values of constant coefficients a_1, a_2, *etc.* result from the intrinsic properties such as magnetocrystalline anisotropy, spin-waves, and Pauli's paramagnetic susceptibility, as well as from extrinsic properties such as point defects, dislocations, grain boundaries, and non-magnetic precipitations.

(i) Intrinsic contributions:

The intrinsic contributions to the law of approach to magnetic saturation are as follows:

- The$1/H^2$ dependency of the expression is originated due to the magnetocrystalline anisotropy. Local fluctuations of the magnetocrystalline anisotropy as in the amorphous alloys result in the $1/H^{1/2}$ term at low fields region and $1/H^2$ term at higher applied fields.
- The energy gap in the spin-wave spectrum due to the Zeeman energy gives the $\sqrt{H}$ term.
- $\chi_P H$ represents the enhanced Pauli's paramagnetism of the band structure.

(ii) Extrinsic contributions:

Inhomogeneous spin states are produced by the stress sources due to the magneto-elastic interaction. Hence, the corresponding deviations of magnetization from the saturation values [$\Delta M = M_S - M(H)$] depend on the geometry of the defects, spatial variation of the stresses, and the correlation between the defects. The change in the values of ΔM due to the defects is as follows:

- Point defects of radius result in $\Delta M = a_4/H^2$, when $r_0 > L_{ex}$.
- Straight dislocation dipoles of width *D* contribute as $\Delta M = a_2/H$, when $D < L_{ex}$ and $\Delta M = a_4/H^2$, when $D > L_{ex}$.
- Non-magnetic spherical precipitations of radius r_0 contribute as $\Delta M = a_1/H^{1/2}$, when $r_0 < L_{ex}$ and $\Delta M = a_3/H^{3/2}$, when $r_0 > L_{ex}$. Similarly, the effect of intrinsic fluctuations of the materials parameters such as local spin density, local magnetic anisotropy energy, and local magnetic stray fields resulting from the local fluctuations of the spin density also affect M_S. Magnetoelastic coupling due to the stress-induced sources has also effect on M_S of magnetic materials.

भारतीय प्रौद्योगिकी संस्थान गुवाहाटी
Indian Institute of Technology Guwahati

Chapter 3

Experimental Methods

3.1. Introduction:

This chapter majorly provides a brief description of the various experimental techniques employed for the preparation and characterization of the samples together with the relevant theory associated with those techniques. Experimental data and results of the present thesis are based on the experimental techniques outlined in this chapter.

3.2. Techniques used for sample preparation:

Material processing was carried out by using a high-energy planetary ball milling technique. A brief discussion of the said preparation method is stated below.

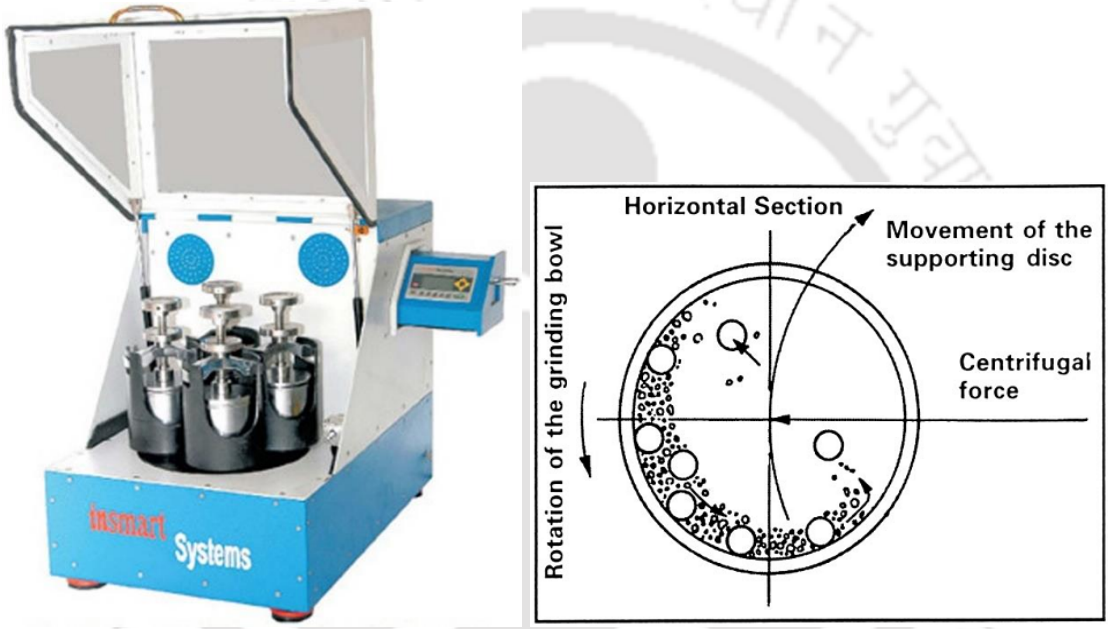

Figure 3.01: (left) Photographic view of the planetary ball mill used, and (right) schematic diagram of the horizontal section of a vial depicting the movement of the balls inside the vial due to its planet-like movement [LUY2015].

3.2.1. Ball milling technique:

3.2.1.1. Mechanical milling:

High-energy ball milling of the initial raw mixtures (powders) was carried out in a planetary ball mill (Insmart, India) under dry milling conditions in controlled argon (Ar) gas environment. The photographic view of the planetary ball mill comprising of a horizontal rotating support disc on which the vials are mounted and the schematic depiction of the ball motion inside the vial is shown in Figure 3.01. The vials mounted on the horizontal disc are equipped with a special drive mechanism that causes them to rotate along their own axes and in a direction opposite to that of the disc and thereby simulates a planet-like movement,

hence been named as the planetary ball mill. This leads to a large centrifugal force on the balls kept within the vial and allows for the highly impacted ball-powder-ball and ball-powder-wall collisions within the vials.

When the powders are placed inside the vial together with the grinding balls, the centrifugal forces acting interchangeably in like and opposite directions cause first the grinding balls to run down inside the wall of the vial by the friction effect. It is followed by the powders being ground and the milling balls lifting off and traveling through the inner chamber of the vial freely and colliding against the opposing wall by the impact effect. Hence, the powders are subjected to repeated cold welding and fracture at the surfaces of the balls and the vial, leading to the disintegration of the powders. In fact, welding and fracture are the two basic events that produce the permanent exchange of matter between the particles and ensure intimate mixing of individual elements of the raw powder mixture. This first results in a size refinement process to produce nanocrystalline alloys along with a large number of defects and ultimately attains an amorphous state at sufficiently high milling periods [SONI2001, SURY2001, KOCH2002, SURY2004]. Hence, size refinement is a natural consequence of the ball milling process. The size refinement and alloying processes are determined by the careful optimization of milling parameters such as ball-to-powder weight ratio, ball size, rotation speed, milling time, *etc*. The nature of the milling vial and types of balls' materials also play an important role in the process, along with the milling media.

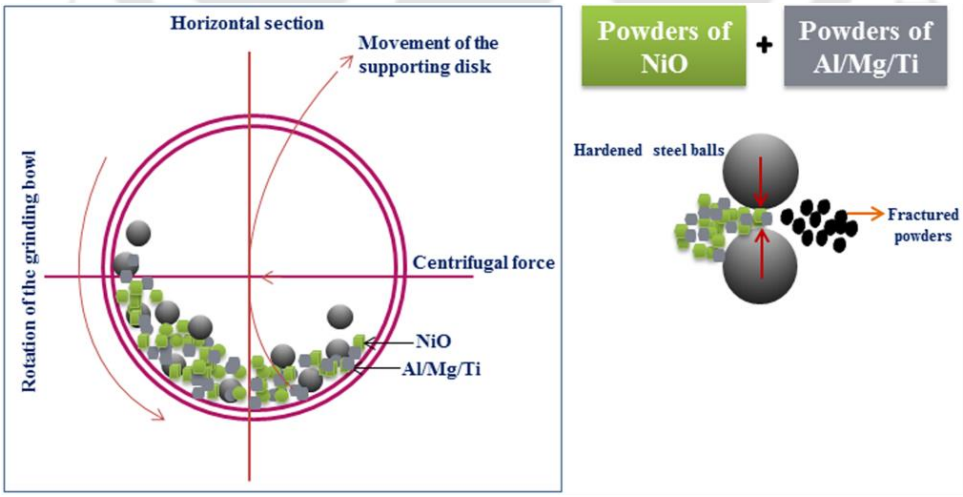

Figure 3.02: (left) Schematic view of the planetary ball mill under reactive milling process, and (right) the ball-powder-ball collision, leading to the structural and chemical transformation of the raw powder mixture.

3.2.1.2. Reaction milling:

Reaction milling of the initial raw powder mixtures (reactants) was carried out in the high-energy planetary ball mill. Reaction milling is basically a ball milling mechanosynthesis process characterized by the repeated welding, deformation, and fracture of the mixture of reactants. As the initial powder mixtures are chemically reactive and the displacement reactions occurring at the interfaces of the nanometric grains are mostly exothermic by nature, the milling associates both the natural size refinement/structural transformations along with the chemical transformations at ambient temperature [KOCH1991, TSUZ2004]. Hence, the type of reaction eventuated, and the controlled reaction rates are determined by the appropriate selection of processing parameters such as stoichiometry/relative proportion of the starting materials, chemical reaction paths, ball size, milling speed, milling time, *etc*. As the reactions in most of the scenarios are highly exothermic ones, milling media and the controlled gas atmosphere plays a crucial role in the reaction milling processes. The schematic view of the ball motion inside the vial along with the ball-powder-ball collision of the mixture of reactants used in the present thesis work is shown in Figure 3.02.

In the present work, reaction milling of high purity powders has been carried out under dry milling conditions and a controlled high purity Ar gas atmosphere. Hardened steel vial and hardened steel balls (8 mm in diameter) were used for milling of all the powders. After a careful and systematic investigation, the rotating speed and ball-to-powder weight ratio were kept constant at 500 rotations per minute and 10:1, respectively. Prolonged dry milling results in a temperature rise inside the vial, which usually deteriorates the final product and sometimes even the constitution of the powders. So, the milling was programmed to pause for 15 minutes after every minute 15 minutes of continuous milling to elude the excessive heating. Furthermore, the time of milling throughout the thesis work was optimized depending upon the requisite reaction conditions.

3.3. Structural characterization:

3.3.1. X-ray diffraction:

Put forwarded by W.H. Bragg and W.L. Bragg in 1912, X-ray powder diffraction (XRPD) is a rapid analytical technique predominantly used for the identification of various phases, degree of crystalline order and the quantification of secondary phases present in a crystalline material. High-power X-ray diffractometer (Rigaku TTRAX III 18KW) was used in the present work with a Cu-K_α source having a wavelength of 1.54056 Å. Figure 3.03 shows

the typical photographic view of the Rigaku TTRAX III X-ray diffractometer and the conventional symmetrical Bragg-Brentano geometry of powder X-ray diffractometer. The theta-theta (θ–θ) goniometer was used in the reflection (Bragg-Brentano) geometry [CULL2001].

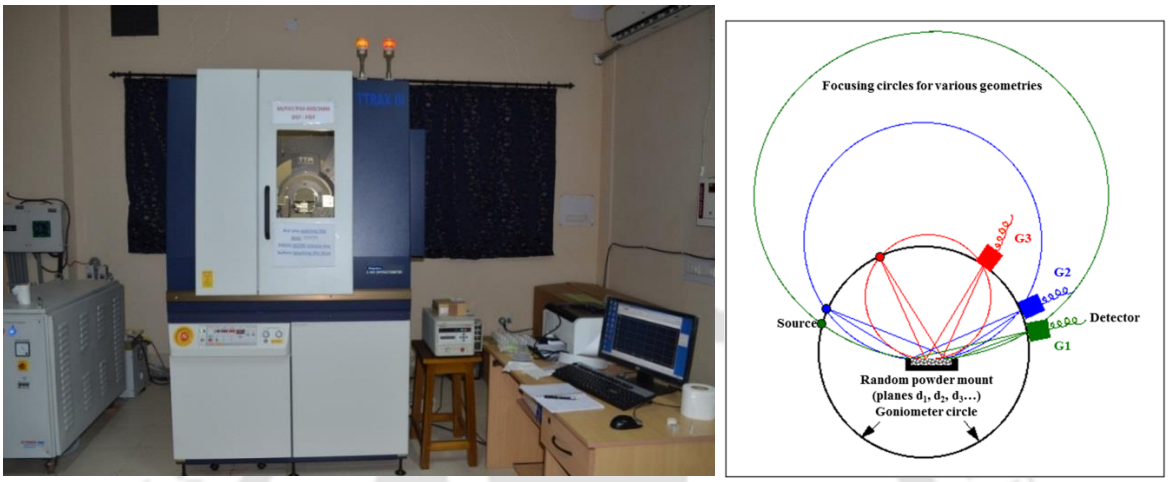

Figure 3.03: (left) Photographic view of Rigaku TTRAX III 18 kW X-ray diffractometer and (right) Bragg-Brentano diffraction geometry of a powder X-ray diffractometer [HTTP0006].

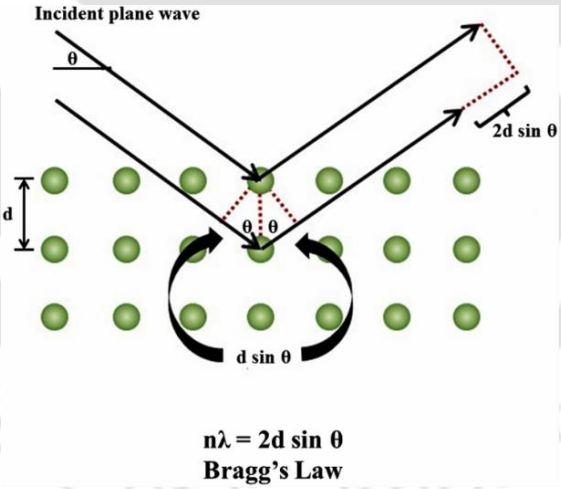

Figure 3.04: Schematic ray diagram of diffraction of X-rays by a crystal.

XRPD technique allows the identification of various crystalline phases existent in the material and renders other structural information such as the size of the crystallites, lattice strain, the lattice constant, *etc*. It is well-known that an ideal crystal has a periodic planar arrangement of atoms with an inter-planar spacing of the order of a few angstroms, as shown in Figure 3.04. Diffraction of X-ray occurs through constructive interference of X-ray scattered from atoms of a set of parallel atomic planes in a crystal lattice at a particular

angular position of the incident wave known as Bragg angles [CULL2001]. So, the condition for obtaining the constructive interference is known as the Bragg's law given by the relation [CULL2001],

$$2d_{hkl}sin\theta = n\lambda \quad (3.01)$$

where d_{hkl} is the inter-planer spacing, θ is the angle of incidence of the X-ray beam with the atomic plane, λ is the wavelength of X-ray (Cu-K_α = 1.54056 Å) and n is the order of diffraction (we consider only the first-order diffraction, n =1, as the second-order peaks are mostly difficult to detect experimentally). A sequence of these angles is used to determine the Miller indices (*hkl*), and the crystal structure can be identified from the systematic behavior of these indices. Figure 3.04 clearly shows the diffraction of X-ray from crystal lattice planes illustrating Bragg's law. The different structural parameters such as the average crystallite size, *d*-spacing, the lattice constant and strain present inside the crystallites, *etc*. can be determined by a careful analysis of the XRPD patterns using various models [CULL2001].

All the XRPD measurements in the present thesis have been carried out by employing a high-power X-ray diffractometer (Rigaku TTRAX III 18 kW) with Cu-K_α radiation (λ=1.5406 Å). The diffractometer was equipped with a pyrolytic graphite monochromator and a silicon scintillation counter. The generator power was set at 50 kV/180 mA condition. Divergence and receiving slits were kept at 2/3° and 0.3 mm, respectively. XRPD patterns were collected at a slow scan rate of 0.005°/s with 100 steps per degree. To subtract the instrumental broadening, the diffraction pattern of the standard silicon reference sample was recorded under similar diffraction conditions. The instrumental broadening corrected line profile full width at half maximum $\delta(2\theta)$, in radians, of each X-ray reflection was calculated from the parabolic approximation correction [SHAA2014] defined as, $\delta(2\theta) = \sqrt{F^2(1 - f^2/F^2)}$. The terms *F* and *f* are the widths (in radians) of the Bragg peaks from the XRPD patterns of the milled powders and standard silicon reference sample, respectively. Both *F* and *f* were estimated by a non-linear curve fitting routine using Microcal Origin software. In addition, the exact peak position, full-width-half-maxima (FWHM), and integrated area of the XRPD peaks are obtained using the FULLPROF profile fitting of the experimental data using Xpert High Score Plus software and fitting with respect to the standard XRPD patterns. The average size of the crystallites could be estimated from the width of the diffraction peaks. This is equivalent to the diffraction of light from an ordinary optical grating where the line width is proportional to the number of diffracting

grooves in the grating. The crystallite size can be quantified by Scherrer's formula [CULL2001] as,

$$D = \frac{k\lambda}{\delta(2\theta)\cos\theta} \tag{3.02}$$

Where *D* is the average size of the crystals.

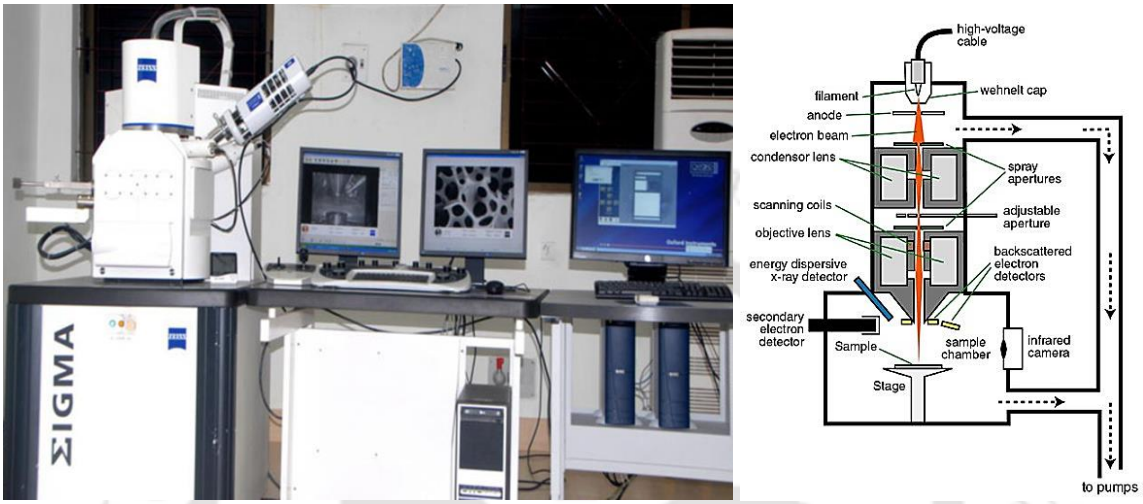

Figure 3.05: (left) Photographic view, and (right) schematic view of a field-emission scanning electron microscope.

3.3.2. Scanning electron microscopy:

Scanning electron microscope (SEM, Leo 1430VP) and field-emission scanning electron microscope (FE-SEM, Sigma Zeiss, Germany) equipped with energy dispersive spectroscopy (EDS) attachment (Oxford) were used to study surface morphology and the elemental compositions of the milled samples. A photographic view of the FE-SEM used in the present study is displayed in Figure 3.05. SEM is a microscopic technique used for the observation of specimen surfaces and provides the topographical, morphological, and compositional information in detail. It utilizes a focused beam of electrons with relatively low energy to obtain a high-resolution, three-dimensional image of objects, and to study surface morphologies, fractured components, foreign particles and residues, polymers, electronic components, biological samples, *etc*. The thermionically emitted electrons or field emission controlled electrons are drawn to an anode, focused by two successive condenser lenses into a beam with a narrow fine spot size (~ 50 Å). The shorter wavelength of electrons allows image magnifications of up to 100,000 times in SEM. Pair of scanning coils located at the objective lens deflects the beam either linearly or in raster fashion over a rectangular area of the specimen surface, and the intensities of various signals, *i.e.*,

secondary electrons, backscattered electrons and characteristic X-rays created by the electrons-specimen interactions are collected by one or more detectors and processed.

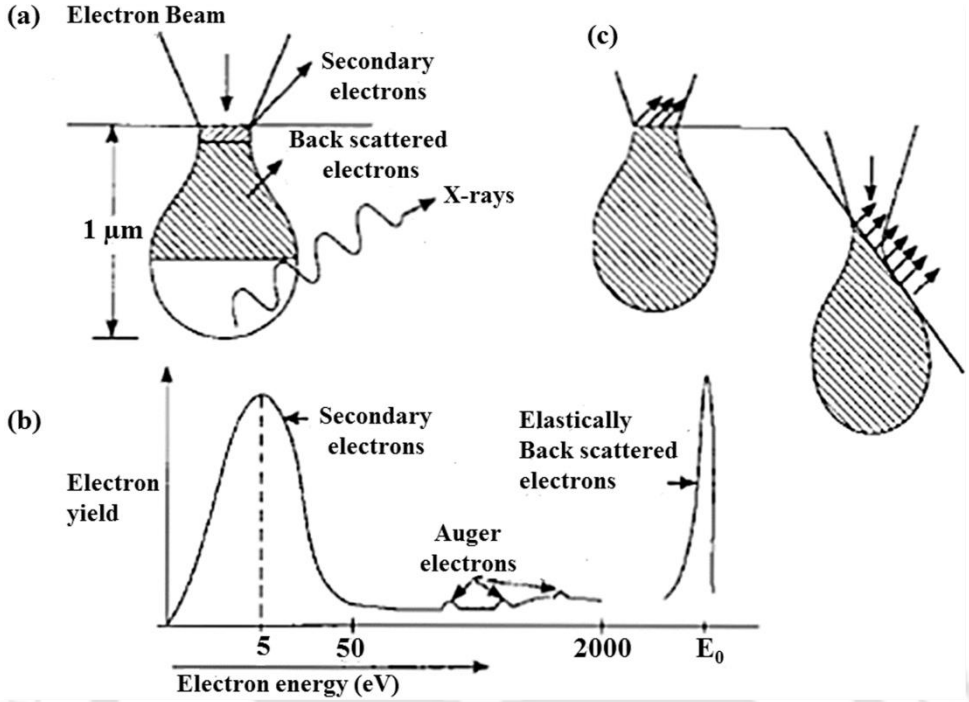

Figure 3.06: (a) Electron and photons signals emanating from tear-shaped interaction volume during electron beam impingement on the specimen surface, (b) Energy spectrum of electrons emitted from the specimen surface, and (c) Effect of surface topography on electron emission.

Figure 3.06 displays the interaction of electrons on the specimen surface. As shown in the figure, upon electron impingement on the surface, the interaction volume approaches the classical teardrop shape. These primary bombarding electrons on the surface dislodge valence electrons from the constituent atoms known as secondary electrons from the specimen. These dislodged secondary electrons are attracted and collected by a grid (positively biased) or detector, and afterward translated into a signal. Subsequently, these signals are amplified, analyzed, and translated into images of the topography of the specified specimen surface. Eventually, the image is shown on a cathode ray tube. The most common imaging mode counts on the detection of the very lowest portion of the emitted energy distribution. Here the 'very lower energy' means these are originated from a subsurface depth of no deeper than a few angstroms.

Apart from the secondary electrons, the primary electron beam results in the emission of backscattered (or reflected) electrons (BSE) from the specimen. While the

secondary electrons are generated from the surface or near-surface atoms of the sample via inelastic interactions between the primary electron beams and the sample, BSEs are originated from the deeper regions through the elastic electron-atom interactions. BSEs possess more energy than the secondary electrons and have a definite direction. All emissions beyond 50 eV are considered to be backscattered electrons. Here, it may be noted that the BSE imaging is useful to distinguish one material from the other, as the yield of the collected BSE monotonically increases with atomic number Z (~ 0.05 $Z^{1/2}$) of constituent atoms in the specimen. BSE imaging can easily distinguish elements with atomic number differences of at least 3, *i.e.*, elements with atomic number differences of at least 3 show images with a discernible contrast.

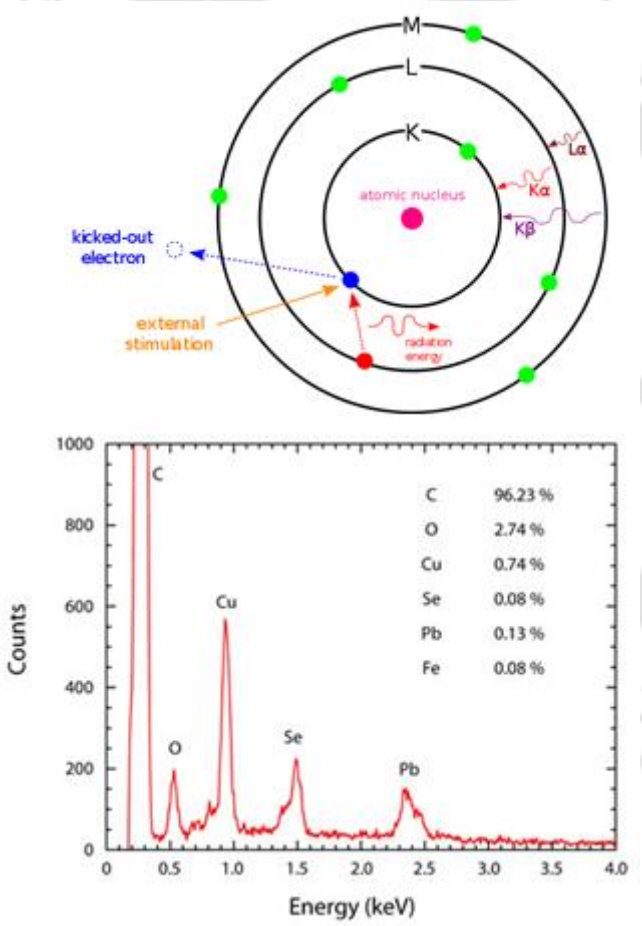

Figure 3.07: Schematic of X-ray generation and the plot of intensity versus X-ray energy to quantify the content. EDS data for the PbSe -MWNT sample. Copper and iron are from the formvar TEM grid and residual nanotube growth catalyst, respectively [HTTP0007].

Energy dispersive spectroscopy (EDS) analysis is quite useful in the identification and evaluation of materials, identification of contaminants as well as estimation of their relative

concentrations on the specimen surface. The electrons colliding with the specimen knock off some of the electrons from the inner shells of the atoms, as shown in Figure 3.07. During EDS analysis, the specimen is bombarded with an electron beam inside the SEM. The bombarding electrons, colliding with the specimen, transfer part of its energy to the atoms of the sample. This energy leads to the electrons of the atoms to jump to an energy shell with higher energy or knocking-off of some of the electrons from the atoms. A position vacated by an ejected inner shell electron due to the aforementioned transition is eventually occupied by a higher-energy outer shell electron. However, to be able to do so, the transferring outer electron is obligated to give up some of its energy in the form of X-ray emission. This amount of energy released by the transferring electron relies on which shell it is transferring from, as well as which shell it is transferring to. Besides, a unique amount of energy as an X-ray is released by the atoms of every element during the transferring process. Hence, by measuring the amount of energy present in the emanated X-ray during electron beam bombardment, the identity of the atom from which the X-ray was emitted can be found out. The output of an EDS analysis is an EDS spectrum, which is just a plot of how frequently an X-ray is received for each energy level. An EDS spectrum typically illustrates peaks corresponding to the energy levels for which the most X-ray had been received. Each of these peaks is unique to an atom and thereby corresponds to a particular element. The higher the peak in a spectrum, the more concentrated the element is in the specimen.

In the present work, a thin layer of the as-milled powders were spread on carbon-coated tape and mounted on the FE-SEM stub. Gold coating, wherever necessary, was then applied over it to yield an electrically conducting surface for SEM observation.

3.3.3. Transmission electron microscopy:

Transmission electron microscope (TEM, JEOL 2100, JEOL2100F, TECNAI TF20) has been used to study the microstructure of the powders depending upon its availability. Figure 3.08 depicts the cut-view of a TEM (Figure 3.08a), schematic ray diagrams of imaging (Figure 3.08b), and diffraction modes (Figure 3.08c). TEM is an optical equivalent to the conventional light microscope, which is based not only on the fact that electrons can have an ascribed wavelength (order of 0.25 nm) but also can interact with magnetic fields as a point charge. A beam of electrons is used instead of the rays of visible light and the glass lenses are replaced by magnetic lenses. As the wavelength of electrons is much smaller than that of light, the magnitude of optical resolution attainable by TEM is many orders

higher than the light microscope. Hence, the lateral resolution of the best microscopes is down to atomic resolution.

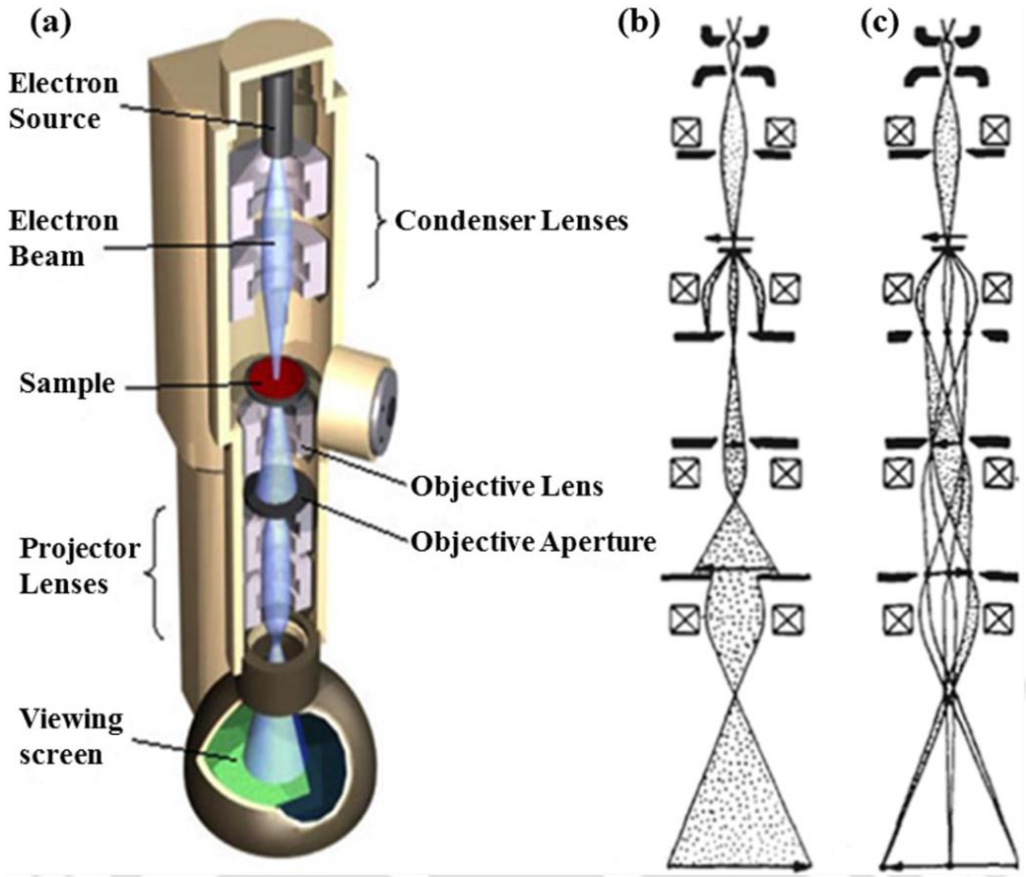

Figure 3.08: (a) Cut view of the transmission electron microscope and (b) schematic ray diagrams of image mode and (c) diffraction mode.

In a TEM, electrons emitted from the electron gun are accelerated to 200 keV or higher and first projected on to the specimen by means of the electromagnetic condenser lens system. During their passage through the specimen, the scattering processes experienced by the electrons determine the kind of information obtained (shown in Figure 3.09), which may possibly happen in three different ways: (i) the electrons pass being unobstructed, (ii) elastically scattered without the loss of energy when electrons interact with the potential field of the ion cores and gives rise to a diffraction pattern. (iii) in-elastically scattered where there is an energy exchange between the electron beam and matrix electron at heterogeneities such as grain boundaries, dislocations, second-phase particles, defects, and scattering effects, *etc*. The characteristic X-ray and Auger electrons are also generated but are normally not collected in a typical TEM measurement. The emergent primary and diffracted electron beams are now made to pass through a series of

post-specimen lenses. The objective lens produces the first image of the object. Depending upon how the electron beams reach the back focal plane of the objective lens, the beams are processed subsequently using various operation modes. Basically, either magnified images or diffraction patterns are obtained, which are projected on a fluorescent screen.

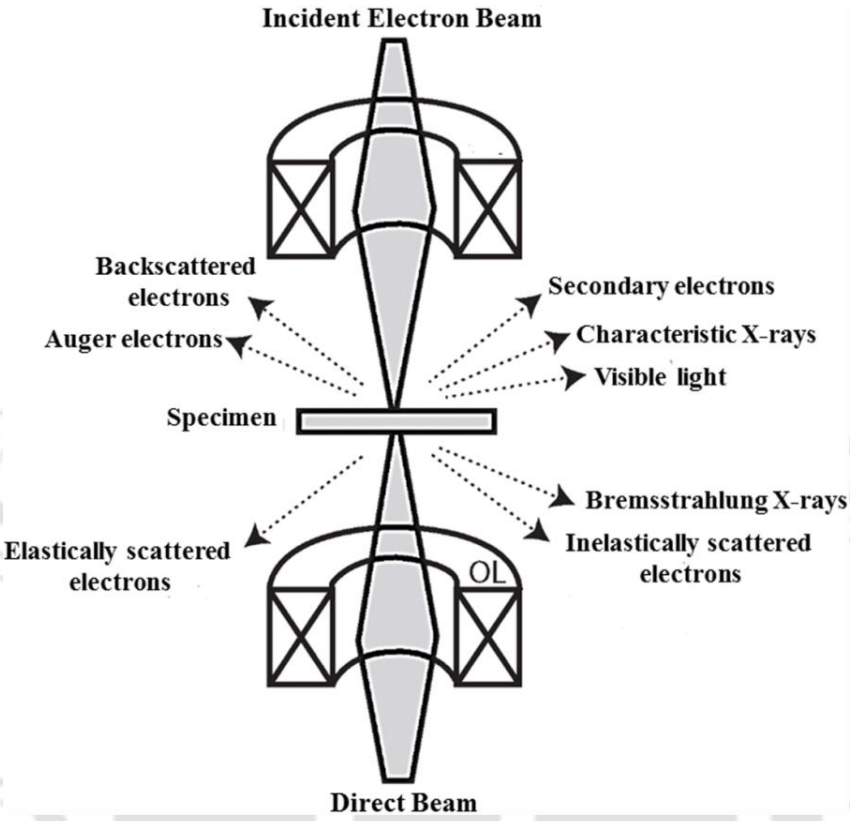

Figure 3.09: Various signals generated as a result of electron beam interaction with a thin solid specimen in TEM.

Images can be formed in a number of ways, either by using the central spot or some/all of the scattered electrons. The bright-field TEM (BF-TEM) image is obtained by intentionally excluding all diffracted beams and only allowing the selected portion of the central beam to pass through the specimen. This is done by inserting a suitably sized objective aperture into the back focal plane of the objective lens. Intermediate and projection lenses then magnify this central beam, and the microstructural image can finally be viewed. Dark-field images are also formed by magnifying a single beam by choosing one of the diffracted beams by means of an aperture that blocks the central beam and the other diffracted beams. In the third mode of imaging, the primary transmitted and one or more of the diffracted beams are made to recombine, thus preserving both their amplitudes and phases. This is the technique employed in high-resolution lattice imaging, which enables

the diffracting planes and arrays of individual atoms to be distinguished. From the high-resolution TEM (HR-TEM) micrograph, average grain size, atomic inter-planar spacing, defects, and dislocations can be evaluated. On the other hand, the selected area electron diffraction (SAED) is performed by excluding the central beam intentionally via the beam blocker and collecting the diffracted beams to form the diffraction patterns. The elemental compositional analysis can also be performed by the X-ray energy dispersive analysis interfaced with the TEM set-up. Emergent electrons from the filament (cathode) are accelerated to high energies, which strikes with the specimen target (anode), and the X-rays of characteristic atoms are emitted from the irradiated area. These atoms can be identified by analyzing their energies, and the concentration of atoms can be evaluated by counting the number of X-rays emitted.

In the current investigation, a tiny amount of sample in the powder form was dispersed by ethanol using an ultrasonicator. A drop of the colloidal solution was placed on a carbon-coated TEM grid and was allowed to dry in a clean environment. The grid with the dried powder particles was then used for the TEM observation.

3.4. Spectroscopic characterization:

3.4.1. Micro-Raman spectroscopy:

Raman spectroscopy is an important analytical tool in the molecular spectroscopy that detects intrinsic rotational, vibrational, and other low-frequency modes in molecules upon the inelastic scattering of monochromatic radiation. This is generally used to study properties such as crystalline phases, defects, crystallographic orientations, strain, *etc*. in a material. Based on the Raman Effect, it is an inelastic light scattering phenomenon corresponding to the photon-phonon interaction. Figure 3.10 depicts the schematic diagram and photographic view of a micro-Raman spectrometer (LabRAM HR-800, Jobin Yvon, USA) equipped with the liquid nitrogen cooled CCD detector used for the present work.

In Raman spectroscopy, the monochromatic laser beam is illuminated to the sample, which interacts with the molecular vibrations and originates a scattered light. A fraction of the scattered light has a wavelength different from the incident wavelength due to the inelastic scattering and thereby constitutes the main features of the Raman spectrum. If the scattered wavelength is shorter than the incident wavelength, the scattered lines are known as the Stokes line, whereas those of the longer wavelengths are called anti-Stokes lines. As the Stokes shifted Raman bands comprise of the molecular transitions from lower to higher

energy vibrational levels, these are more intense than anti-Stokes bands and are thereby measured in the conventional Raman spectrometers. Meanwhile, anti-Stokes shifted Raman bands are measured with fluorescing samples as fluorescence causes interference with Stokes shifted bands [BUMB2016].

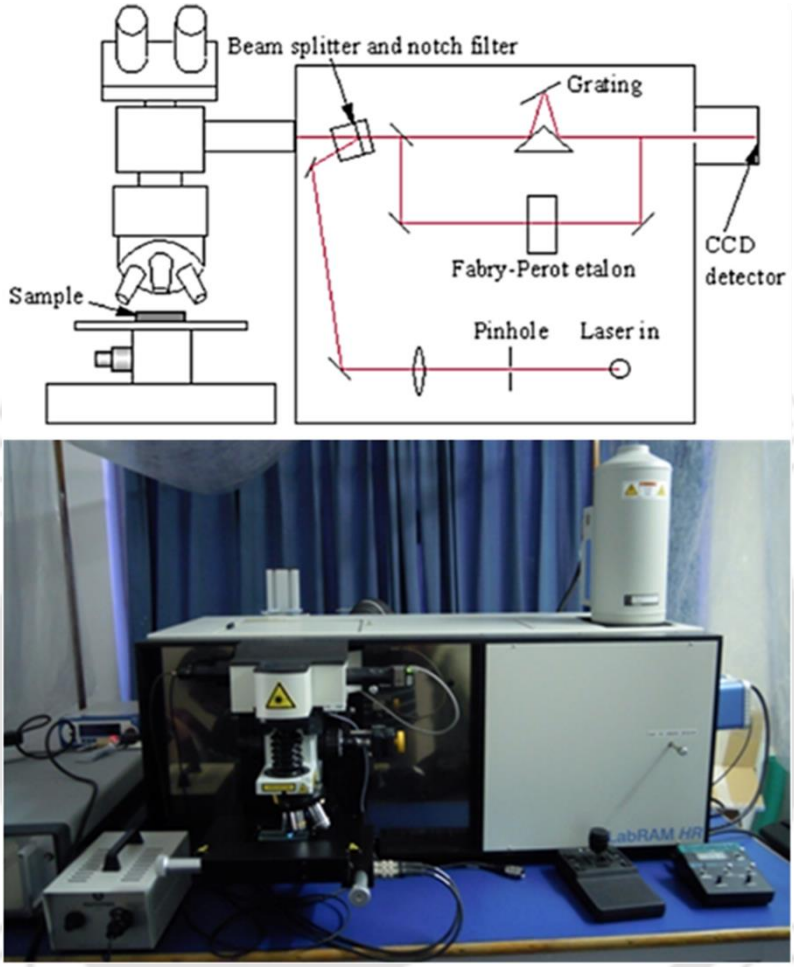

Figure 3.10: Schematic diagram (top) and photographic view (bottom) of a Raman spectrometer.

Raman spectrometers can be dispersive or non-dispersive. Dispersive spectrometers use grating or prism, while non-dispersive spectrometer uses interferometers such as Michelson interferometer. Here, the intense laser beam is incident on the samples through a microscope with the spot size of a few microns. The microscope is confocally coupled to 800 mm focal length spectrograph equipped with two switchable gratings. The excitation photon is obtained by two monochromatic laser sources, *i.e.*, He-Ne laser (λ = 633 nm) or Ar laser (λ = 488 and 514 nm). The laser beam is totally reflected by the beam splitter, which splits the beam into two parts having equal wavelengths. The laser beam is then allowed to

strike the sample where both Rayleigh and Raman scatterings occur, and the notch filter allows only the Raman scattered wavelength to pass through and effectively blocks the incident wavelength. The inelastically scattered light is allowed to pass through the grating and etalon, which in-turn resolves the weak inelastic scattered wavelength coming from the sample more efficiently. Furthermore, the beam is allowed to enter into a charge-couple device that detects the change in polarizability of the sample from the change in wavelength and converts into the intensity, and finally, intensity versus wavenumber graph is observed on the computer screen.

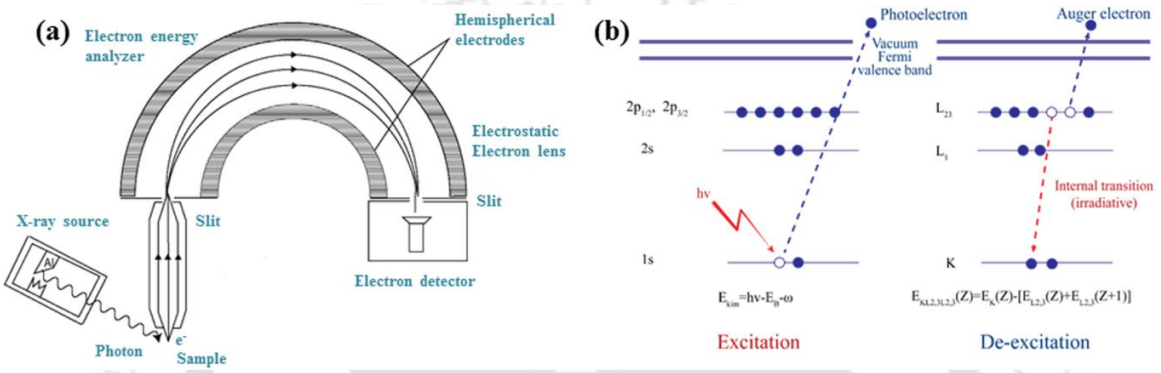

Figure 3.11: (a) Schematic of XPS spectrometer, (b) excitation and de-excitation processes.

3.4.2. X-ray photoelectron spectroscopy:

X-ray photoelectron spectroscopy (XPS) or ESCA (Electron spectroscopy for chemical analysis) is a well-known quantitative surface-sensitive spectroscopic technique. This measures the elemental composition at the parts per thousand range, empirical formula, chemical state, and electronic state of the elements that exist within a material. XPS measurement requires a high vacuum (~ 10^{-5} Pa) or ultra-high vacuum (UHV with pressure better than 10^{-5} Pa) conditions. Based on the Einstein's photoelectric effect and developed by Siegbahn and his research group [SIEG1967], it is accomplished by the irradiation of a sample with monoenergetic soft X-rays and simultaneously measuring the kinetic energy and number of electrons that escape from the top sub-surface (~ 0 to 10 nm) of the material as shown in Figure 3.11.

The basic principle of XPS can be expressed by the following equation,

$$BE = h\nu - KE - \Phi \qquad (3.03)$$

where, *BE* is the binding energy of the electron in the atom, hν is the photon energy of the X-ray source, KE is the kinetic energy of the emitted electron that is measured in the XPS spectrometer and Φ is the spectrometer work function. The XPS principle for ejecting an

electron from the atom as photoelectron during excitation and release of Auger electrons during the de-excitation process is displayed in Figure 3.11.

After the emission of a photoelectron, the atom turns into an excited state. To revert back the ionized atom to the ground state, the electron from an outer shell occupies the inner shell by releasing either an X-ray or Auger electron. For elements having low atomic numbers (Z < 30), Auger emission is the more dominant process. For XPS, Al-K_α (1486.6 eV) or Mg-K_α (1253.6 eV) is generally used as the source of X-ray. The photon is absorbed by an atom of the sample, leading to the emission of a core (inner shell) electron. The energy of the emitted photoelectrons from the sample is determined using an appropriate electron energy analyzer, and this gives a spectrum with a series of discrete photoelectron peaks. For each and every element, there will be characteristic binding energy associated with each core atomic orbital, *i.e.*, each element will give rise to a characteristic set of peaks in the photoelectron spectrum at kinetic energies determined by the photon energy and respective binding energies. The peak intensities measure how much of a material is present at the surface, whereas the peak positions indicate the elemental and chemical composition. Besides this, the FWHM is also a useful indicator of chemical state changes and physical influences.

In the present study, XPS measurements were carried out in standard ultrahigh vacuum surface science chamber consisting of PSP Vacuum Technology electron energy analyzer (angle integrating ±10°) and a dual anode X-ray source with (ULVAC-PHI, Inc.) using Mg-K_α X-ray beam (1253.6 eV) at a base pressure of 2×10^{-7} Pa and energy resolution at full width at half maximum is about 0.8 eV. The spectrometer was calibrated using Au $4f_{7/2}$ at 83.9 eV and used for the calibration of the XPS spectra recorded for various milled samples.

3.5. Thermal property characterization:

3.5.1. Differential scanning calorimetry:

Differential scanning calorimeter (DSC, LABSYS evo, SETARAM Instrumentation (Caluire, France) and NETZSCH STA 449 F3A00) has been used to study the thermal properties of the powders in the present work. Figure 3.12 depicts the photographic view and schematic diagram of a differential scanning calorimeter used for the present work. DSC is a known thermo-analytic technique used to measure the rate of heat flow and characteristic temperatures such as fusion and crystallization points, glass transition

temperatures, *etc.* as well as for the study of redox processes and many other chemical reactions. This not only involves the precise measurement of heat capacities, total heats of reaction, or transitions but also determines the 'partial heats' developed within selected temperature intervals, which are highly valued for the kinetic evaluations, and the advanced determination of crystallinity and purity of samples.

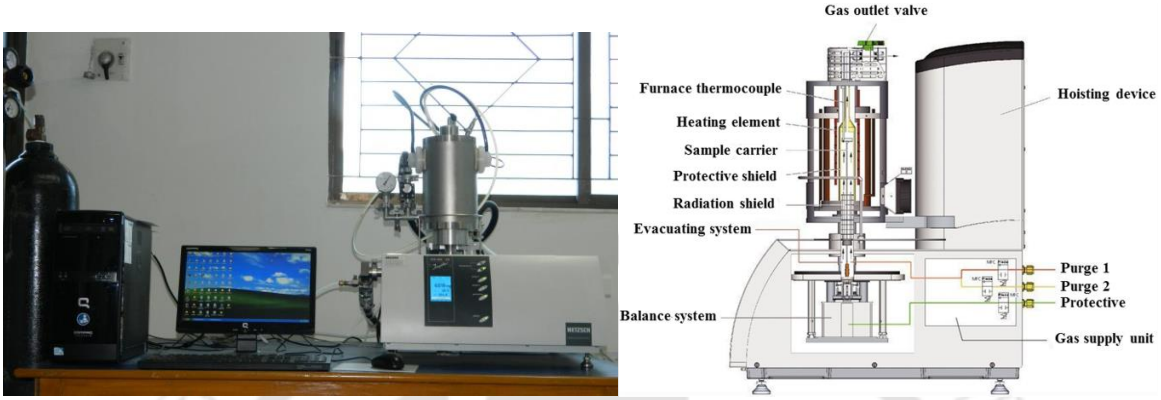

Figure 3.12: (left) Photographic view and (right) schematic view of differential scanning calorimeter [HTTP0008].

The instrument used for the measurement is called a differential scanning calorimeter or DSC. The DSC curves are recorded either under a constant heating (or cooling) rate or under isothermal conditions (time scan at a constant temperature) in a specified atmosphere. A typical DSC consists of two isolated sealed alumina pans, one containing the sample and the other reference material. The pans are covered with a lid, which acts as a radiation shield. The two pans are heated or cooled uniformly in which the heat flow difference between the two is monitored. The basic principle underlying this technique is that, when the sample goes through a physical or chemical transition, either more or less heat flow will be needed than the reference in order to maintain a uniform temperature [HOHN2003]. The more or less heat flow depends on the transition being an exothermic or endothermic type. The DSC is commercially availed as two types, power-compensation DSC or as a heat-flux DSC. In the power-compensation type DSC, which has been used in the present study, the sample and reference holder are heated with separate heaters, and the respective temperatures are measured with separate sensors where both the temperatures can be varied linearly as a function of time being regulated by an average-temperature control loop. When the sample experiences a temperature difference due to any thermal process, a second-differential-control loop tunes the power input, and the differential power signal is recorded as a function of the real sample temperature. Contrariwise, a single heater is used in the heat-flux DSC to

increase the temperature of both the pans and the small temperature difference (ΔT) due to an exothermic or endothermic process between the two isolated pans is recorded from which the heat flow is estimated.

In the current investigation, a measured quantity of 15-20 mg powder was kept in a standard Al_2O_3 pan. The DSC measurements were performed by measuring the heating cycles of the powders at a scan rate of 10 K/minutes, and the scanning was carried out in a controlled Ar atmosphere by raising the temperature up to 1200 °C.

3.6. Magnetic property characterization:

Magnetic properties of the magnetic materials can be characterized by means of various experimental techniques such as physical property measurement system (PPMS), vibrating sample magnetometer (VSM), Faraday balance, ac susceptometer, *etc*. In this section, a brief description of the principles on the basis of various magnetic measurements used in the thesis work has been outlined.

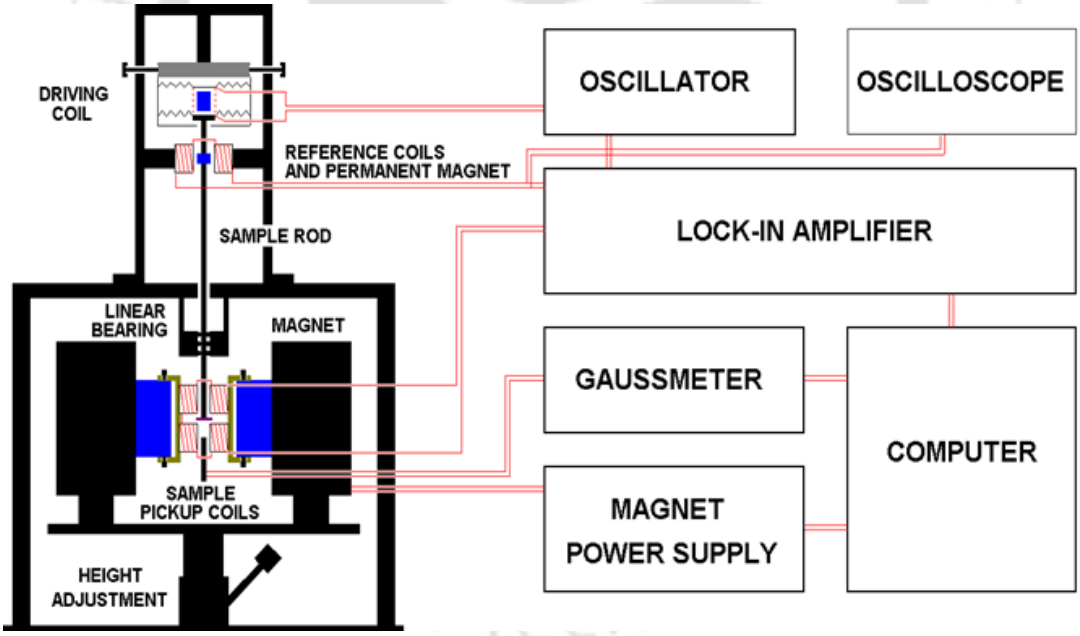

Figure 3.13: Schematic diagram of a vibrating sample magnetometer [HTTP0009].

3.6.1. Vibrating sample magnetometer:

Vibrating sample magnetometer (VSM) is a versatile instrument to measure the net dipole moment of the materials exposed to an external magnetic field [SVOB2004, HORS2006]. By using VSM, the magnetic moment of the material is obtained either as a function of magnetic field, known as the magnetic Hysteresis (*M-H*) curve at a specific temperature to study the evolution of magnetic properties with field or as a function of

temperature, also called as thermomagnetic (*M-T*) curve at a specific magnetic field to study the magnetic transitions of the materials with temperature. Relying on the basic principle of Faraday's laws of electromagnetic induction, VSM was first pioneered by Simon Foner in 1959 at the Lincoln laboratories, MIT, USA [FONE1959]. Subsequently, many modifications have been carried out over the years to improvise the sensitivity of the instrument by keeping the underlying basic principle still the same [SMIT1956].

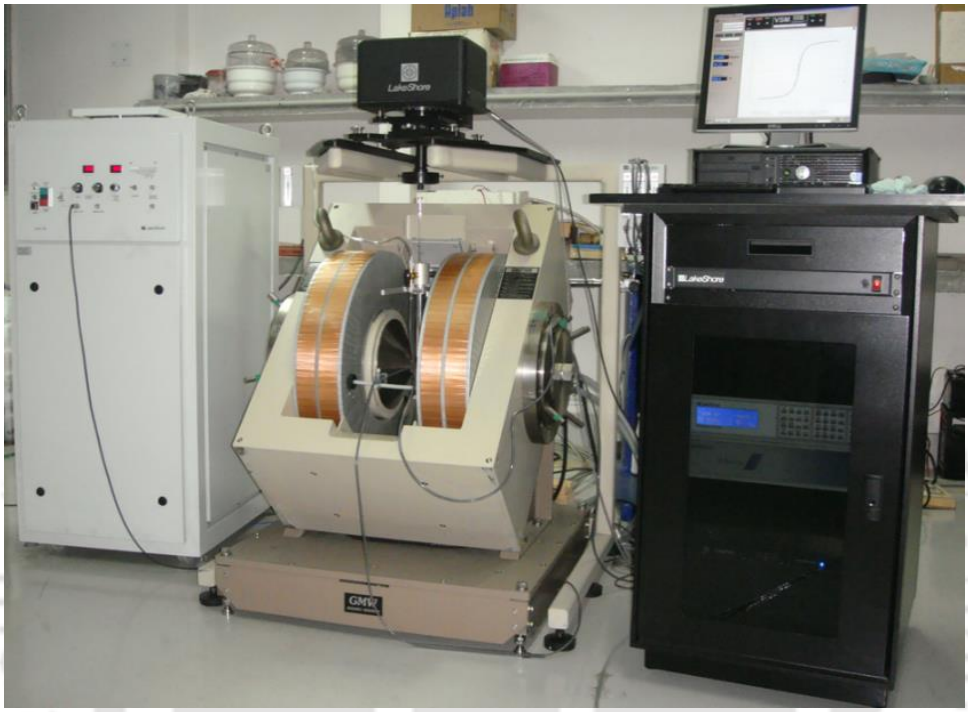

Figure 3.14: Photographic view of a vibrating sample magnetometer (VSM, Lakeshore 7410, USA).

Figure 3.13 displays the schematic diagram of a modern VSM. The instrument comprises of the following major parts: (a) Vibration exciter and sample holder, (b) water-cooled electromagnet and power supply, (c) Hall probe, (d) pick-up coils, (e) amplifier, (f) control panel system, (g) lock-in amplifier and (h) computer interface. When the sample to be analyzed is kept in a uniform magnetic field, a dipole moment proportional to the product of the sample susceptibility and the applied field is induced in the sample. If the sample is made to vibrate through a sinusoidal motion at a constant frequency by using the vibration exciter, an electrical signal can be induced in suitably located stationary pickup coils (see Figure. 3.13). This amplitude of the signal is proportional to the magnetic moment of the sample, the vibrating amplitude, and the vibration frequency. By the use of a lock-in-amplifier and feedback techniques, only that portion of the signal arising from the magnetic

moment is picked up and is converted into direct read-out in the unit of magnetization (*e.g.*, emu) on a digital panel meter.

In the present work, VSM (Lakeshore 7410, USA) was used to investigate the room temperature, and temperature-dependent magnetic behaviors within the temperature range of 300 K – 1100 K. Figures 3.14 displays the photographic view of VSM used in the present study. The sample was fixed at the lower end of the sample holder after carrying out the calibration procedure using a standard spherical Ni sample for the standardization of measured magnetic moment. The measurement sequence is programmed as per the users' choice using the software (IDEASVSM) provided with the instrument in such a way that the program starts either from the maximum field or from the zero applied field. The sequence is created with the intent to collect optimum data, which helps to extract the magnetic parameters (saturation magnetization, remanence magnetization, coercivity, *etc*.) with more accuracy. The exciter is vibrated at a frequency of 72 Hz (Lakeshore model 7410), and the signal received from the hall probe and the pick-up coils is converted into the magnetic moment of the sample. The magnetic field is increased automatically in user-defined steps for measuring *M*-*H* loops. Likewise, in the case of high-temperature *M*–*T* measurements, a high-temperature oven attachment capable of providing a controlled heating/cooling of the sample from room temperature to 1173 K was used. For *M*–*T* measurements, the powder sample in the pellet form was loaded on a high-temperature sustainable holder (ceramic holder or quartz rod) after a calibration run using standard Ni sample. The oven was purged with argon/nitrogen gas to evade the oxidization of the sample at high temperatures. Magnetization was recorded at different temperatures for a constant applied magnetic field. The heating rate and the *M*–*T* sequences were programmed via the IDEASVSM software.

3.6.2. Physical property measurement system:

The physical property measurement system (PPMS) is a sensitive and versatile technique for the characterization of magnetization, electrical resistivity, Hall Effect, heat capacity, thermal conductivity, and thermal transport with a high degree of accuracy as a function of magnetic field or temperature. Figure 3.15 displays the photographic view of PPMS (Dynacool, Quantum Design) equipped with 9 Tesla conduction-cooled superconducting switch-less magnet system. For the room temperature magnetic measurement, the VSM configuration of the PPMS was used to characterize magnetic properties. The VSM option

transforms the PPMS into a highly sensitive DC magnetometer for faster data acquisition. The VSM option primarily comprises of (a) VSM linear motor transport/head for vibrating the sample, (b) detection coil set puck, (c) electronics for driving the linear motor transport, and detection of the response from the pickup coils, (d) computer interface.

Figure 3.15: Photographic view of a physical property measurement system (PPMS, Dynacool).

The sample to be analyzed is attached to the end of a sample rod and is oscillated sinusoidally with the center of oscillation being positioned at the vertical center of the gradiometer pickup coil. The precise position and amplitude of oscillation are controlled by an optical linear encoder signal readback from the VSM linear motor transport. The induced voltage in the pickup coil is amplified and lock-in detected in the VSM detection module, which uses the position encoder signal as the synchronous detection reference. This encoder signal is obtained from the VSM motor module, which interprets the raw encoder signals. The in-phase and quadrature-phase signals from the encoder and from the amplified voltage (from the pickup coil) are detected by the VSM detection module and sent over to the computer interface. In this technique, by using a suitable pickup coil configuration, a relatively large oscillation amplitude (1-3 mm peak), and a frequency of 40 Hz, a change in magnetization as smaller as 10^{-6} emu can be detected.

भारतीय प्रौद्योगिकी संस्थान गुवाहाटी
Indian Institute of Technology Guwahati

Chapter 4

Milling of NiO-Al powders: Effect of Composition and Milling time

4.1. Introduction:

Nanoscale transition metal (TM) - metal oxide matrix composites are very significant materials for a wide range of potential technological applications because of their tunable physical properties [PATE2019]. These nanocomposites are produced by the addition of reinforcement particles to the metal oxide matrix. Depending upon the processability, the TM nanoparticles embedded in a TM oxide matrix have been extensively applied in different research areas such as catalysis [SONG2017], gas sensors [FASA2013], Li-storage anodes [WENW2011], supercapacitors [NELS2003] or spintronic devices [JOHL2014], and in improving the energy product of hard magnetic materials [SORT2002]. For ferromagnetic (FM) TMs, the progression of *in-situ* or *ex-situ* TM-oxide reduction is accounted for by the change in the magnetic properties. This forms an exciting part of the research for the creation of FM nanoparticles embedded in the antiferromagnetic (AFM) oxide matrix. Among these, NiO based nanocomposites obtained through the *in-situ* reduction process is a significant thrust area for industrial applications [NOGU2005]. Though most of the reductions reported in NiO are high temperature based displacement reactions, a preferable solid-solid or solid-liquid mechanochemical (MC) reduction by reactive milling process can lead to the fabrication of NiO based nanocomposites with tunable structural and magnetic properties [NOGU2008].

The solid-state MC reduction of NiO-Al to produce Ni/Al_2O_3 nanocomposites was first reported by Matteazzi *et al.* [MATT1992] using dry milling under argon (Ar) atmosphere. Later, Oleszak [OLES2004] utilized the mechanical activation of aluminothermic reduction of NiO for the development of $NiAl/Al_2O_3$ nanocomposites. Udhayabanu *et al.* reported the formation of Ni/Al_2O_3 nanocomposites by using toluene as the process controlling agent and revealed that the effect of mechanical activation on the reduction of NiO by Al is gradual one [UDHA2010]. A careful review of the literature summarizes that the process of reduction in NiO and, in particular, studied via the mechanochemical reduction processes, has been carried out randomly on limited compositions without any systematic investigations. Furthermore, the detailed analyses on the tuning of the resulting magnetic properties of the *in-situ* nanocomposites formed due to the reduction reaction are still missing. It may be noted that the study of NiO reduction and the control of properties of subsequent Ni are of practical importance in the fields of ore reduction [HIDA2009], catalysis [LESC2004] and solid oxide fuel cells [SING2003], and resistive random access memory [BRUC2003]. Also, the NiO system exhibits novel

properties when the size is reduced down to nanoscale [SARM2010, RINA2014, KISA20151]. Therefore, in the present study, (i) we report a systematic investigation on the NiO-Al (x at.%) reduction reaction by the effective mechanical activation of NiO-Al reduction reaction as a function of Al addition. (ii) The dynamics of the mechanically activated aluminothermic reduction of NiO [NiO-Al (x at.%, x = 0, 20, 40)] during the reactive milling process as a function of Al content and milling time (t_m).

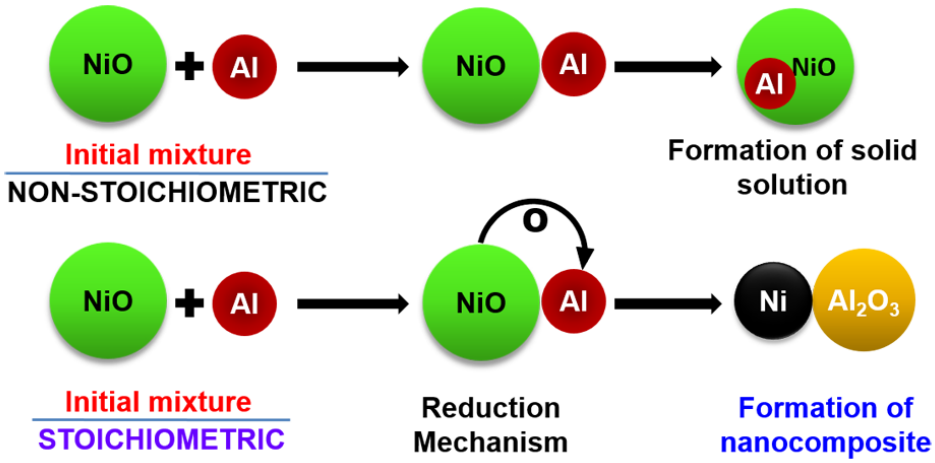

Figure 4.01: Schematic representation of the formation of NiO-Al based solid-solution and nanocomposites.

4.2. Experimental details:

Weighed quantities of high purity (> 99.9%) NiO and Al powders procured from Sigma-Aldrich, India was used as the raw materials. The as-mixed NiO and Al powders were subjected to ball milling under high purity argon (Ar) gas environment in a high-energy planetary ball mill (Insmart make). For the first part of the study, the milling process was carried out for NiO-Al (x at.%) powders with x varying from 0 to 40 for a constant milling time (t_m) of 30 hrs. The NiO-Al powder mixtures were taken as to tune up to the stoichiometric composition of the powders, as NiO-Al (x = 0-40 at.%) to satisfy the reaction,

$$3NiO + 2Al = 3Ni + Al_2O_3 \qquad (4.01)$$

The *in-situ* NiO-Al based nanocomposites (schematically presented in Figure 4.01) were prepared by high-energy ball milling under controlled argon gas environment. For the second part of the study, the milling process of NiO-Al (x at.%) powders with x = 20 and 40, was carried out for different t_m (= 0-30 hrs). The milling process was done in a hardened steel vial together with 8 mm diameter hardened steel balls in the mill operated at 500 rotations per minute with a constant ball-to-powder weight ratio of 10:1 for all the sample

preparation. The optimization of milling time, milling speed, and ball-to-powder weight ratio was done mainly by monitoring the variation in the structural and magnetic properties of the resulting nanocomposites in the milled powders. The mill was programmed to halt for 15 minutes after every 15 minutes of operation to avoid any excess heat generated during dry milling. To study the nanostructural evolution in NiO-Al powders after milling, the milled powders were collected and characterized.

The phase and structural evolutions of the NiO-Al powders were analyzed using X-ray powder diffraction (XRPD) obtained through a high-power X-ray diffractometer (Rigaku TTRAX III 18 kW) using Cu-K_α radiation (λ = 1.54056 Å), and equipped with pyrolytic graphite monochromator and Silicon scintillation counter. The generator was set at 50 kV/180 mA. The divergence and receiving slits were kept at 2/3° and 0.3 mm, respectively. The XRPD data were collected at a slow scan rate of 0.005 °/s with 100 steps per degree for the quantitative analysis of structural parameters. To subtract the instrumental broadening contribution, the diffraction pattern of the standard Silicon reference sample was recorded under similar diffraction conditions. The instrumental broadening corrected line profile full width at half maximum $\delta(2\theta)$, in radians, of each X-ray reflection was calculated from the parabolic approximation correction as [KALI2008],

$$\delta(2\theta) = \sqrt{F^2\left(1 - \frac{f^2}{F^2}\right)} \qquad (4.02)$$

The terms *F* and *f* are the widths (in radians) of the Bragg peaks from the XRPD patterns of the milled powders and standard Silicon reference sample, respectively. Both *F* and *f* were estimated by a non-linear curve fitting routine using Microcal Origin software. The surface morphology of the powders was analyzed by using the field-emission scanning electron microscopy (FESEM, Zeiss Sigma) and scanning electron microscopy (SEM, Leo 1430VP). The presence of any impurity components was analyzed using energy dispersive spectrometer (EDS, Oxford) unit attached to SEM. The microstructural properties of the milled NiO-Al powders were analyzed using a transmission electron microscope (TEM, JEOL 2100, and Technai TF20) technique. X-ray photoelectron spectroscopy (XPS) analyses were carried out in a standard ultrahigh vacuum surface science chamber consisting of a PSP Vacuum Technology electron energy analyzer (angle integrating ±10°) and a dual anode X-ray source with an Mg-K_α source (1253.6 eV) at a base pressure of 2×10^{-10} mbar and energy resolution at full width at half maximum (FWHM) is about 0.8 eV. The spectrometer was calibrated using Au $4f_{7/2}$ at 83.9 eV. Mössbauer spectra were recorded at

room temperature using a standard constant acceleration Mössbauer spectrometer in the transmission geometry. Differential scanning calorimetry (DSC) was carried out for the as-mixed and milled powders in argon (Ar) atmosphere using LABSYS Evo, SETARAM Instrumentation (Caluire, France) and NETZSCH STA 449 F3A00. Magnetic properties were characterized using vibrating sample magnetometer (VSM, LakeShore Model 7410) by performing (i) the room temperature initial magnetization (*IM*) curves and magnetic hysteresis (*M-H*) loops, and (ii) the high-temperature thermo-magnetization (*M-T*) measurements from 300 K to 1200 K temperature range performed at a 4 °C/min heating rate under the applied magnetic field of 2 kOe.

4.3. Results and discussion:

4.3.1. Effect of Al content on the properties of NiO-Al powders:

4.3.1.1. Structural properties:

Figure 4.02(a) displays room temperature XRPD patterns of as-mixed NiO-Al and milled NiO-Al (*x* at.%) powders with *x* = 0-40 for 30 hrs of milling. As-mixed NiO-Al powders exhibit sharp characteristic Bragg reflections corresponding to face-centered cubic (*fcc*) NiO (JCPDS card No. 78-0423, space group $Fm\bar{3}m$) and *fcc* Al (JCPDS card No. 85-1327, space group $Fm\bar{3}m$). However, the Bragg reflections of Al disappear after 30 hrs of milling. This can be attributed to the dissolution of Al in the NiO matrix. No additional Bragg peaks corresponding to any other phases or compounds were observed within the resolution of a high-power X-ray diffractometer. With increasing *x* up to 7.5, XRPD patterns show only the Bragg peaks of NiO with considerable peak broadening and shift in NiO(200) peak to lower angles. While the first one confirms the formation of a NiO-Al solid-solution with highly-refined crystals, the later one could be attributed to the occurrence of atomic disorder due to the dissolution of Al in NiO, leading to a change in the lattice parameter. On further increasing $x \geq 10$, the NiO(200) peak turns out to be asymmetric by nature and then splits into two peaks for further increase in *x* up to 25 (Figure 4.02b).

The careful analysis of XRPD patterns using multiple peak fitting procedures, as displayed in Figure 4.02c – 4.02f, reveals the formation of an extraneous peak at $2\theta = 44.5°$ as a shoulder peak of NiO(200) peak corresponding to the Ni(111) reflection (JCPDS card No. 04-0850, space group $Fm\bar{3}m$). Besides, we have observed the development of a new broad peak around $2\theta = 52°$ corresponding to Ni(200) peak, which grows continuously as a function of Al content.

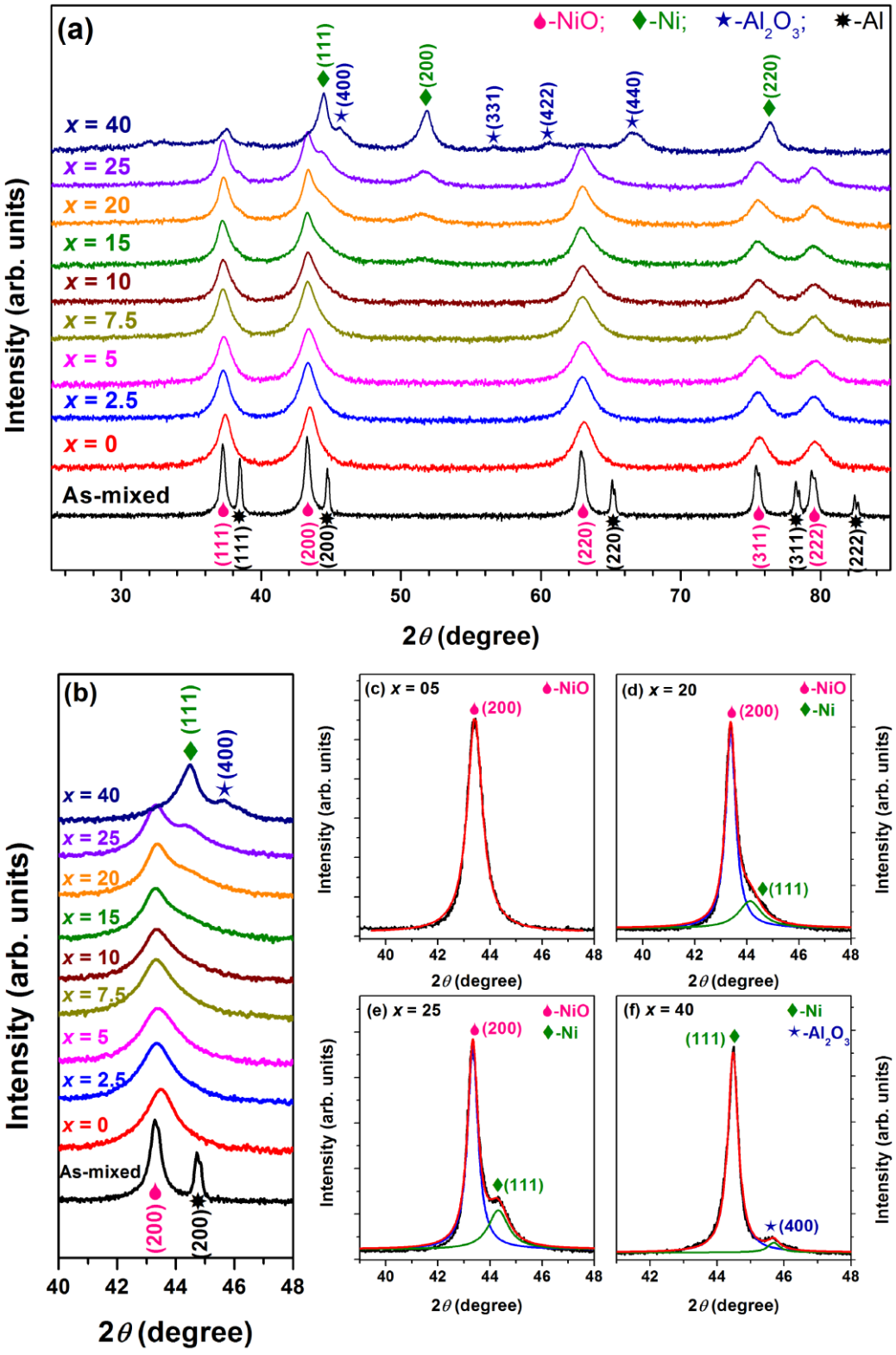

Figure 4.02: Room temperature X-ray diffraction patterns of (a) as-mixed and milled NiO-Al (*x* at.%) powders with *x* = 0 - 40, (b) expanded XRPD patterns in the range of 2θ = 40° - 48° and the multiple profile fittings of NiO(200) peak for *x* = 5 (c), 20 (d), 25 (e) and 40 (f) powders.

This could be attributed to the gradual reduction of NiO by Al into Ni [MATT1992, UDHA2010], also known as the aluminothermic reduction process and the formation of NiO-Ni-Al_2O_3 nanocomposites. On the other hand, for x = 40 powders, it is observed that (i) the intensity of the Ni(111) and Ni(220) peaks increases primarily along with the rapid growth of the Ni(200) peak at around 2θ = 51.8°, (ii) the intensity of NiO(200) peak reduces largely and submerges into Ni(111) peak, and (iii) the development of additional peaks around 2θ = 45.6°, 56.6°, 60.5° and 66.7° corresponding to α-Al_2O_3 phase was observed [UDHA2010]. These results confirm that the addition of Al in NiO forms the solid-solution of NiO-Al for Al up to 7.5 at.% and then reduces NiO gradually into Ni and Al_2O_3, which leads to the formation of *in-situ* NiO-Ni-Al_2O_3 nanocomposite. As a result, the color of the milled powder changes significantly after milling. It may be noted that the as-received pure (un-milled) NiO powder displaying a pale green color turns into the dark green after 30 hrs of milling (see Figure 4.03). This could be well attributed to the development of non-stoichiometry in NiO ensued by the defects, crystallite size reduction, and the oxidization of Ni^{2+} to Ni^{3+} due to the breaking of Ni^{2+}-O^{2-}-Ni^{2+} symmetry [AHMA2006, MIRO2007, GAND2011, KISA2014, RAVI2015]. However, with increasing x, the dark green color of the milled NiO-Al powder transformed into black color due to the significant reduction of nanocrystalline NiO into Ni-Al_2O_3 nanocomposites (see Figure 4.03).

(a) (b) (c)

Figure 4.03: Photo view of the change in the color of the (a) pure un-milled NiO, (b) milled NiO powder for 30 hrs, and (c) milled NiO-Al powders.

To determine the percentage of NiO reduction by MC reaction process, we have utilized the change in the integrated intensity of NiO(200) peak [VENU2005, UDHA2010] using the integrated intensity equation as,

$$C = \left[\frac{(A-B)}{A}\right] \times 100 \qquad (4.03)$$

Where A is the integrated intensity of NiO(200) peak for the pure NiO powder before milling, B is the integrated intensity of NiO(200) peak in milled NiO-Al powders, and C is

the percentage of reduction of NiO. The percentage of reduction of NiO increases gradually with increasing Al content and reaches about 50% and 91% for x = 25 and 40, respectively. Udhayabanu *et al.* [UDHA2010] reported a reduction of 70% at the end of 20 hrs milling for NiO-Al (20 at.%) using toluene as the process-controlling agent.

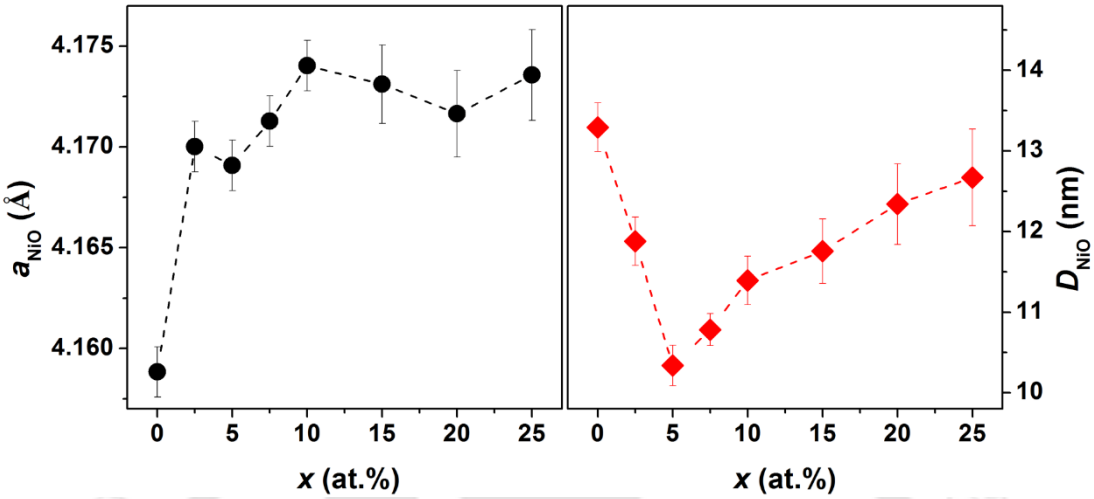

Figure 4.04: The variations of lattice constant (a_{NiO}) and crystallite size (D_{NiO}) as a function of Al content for 30 hrs milled NiO-Al (x at.%) powders.

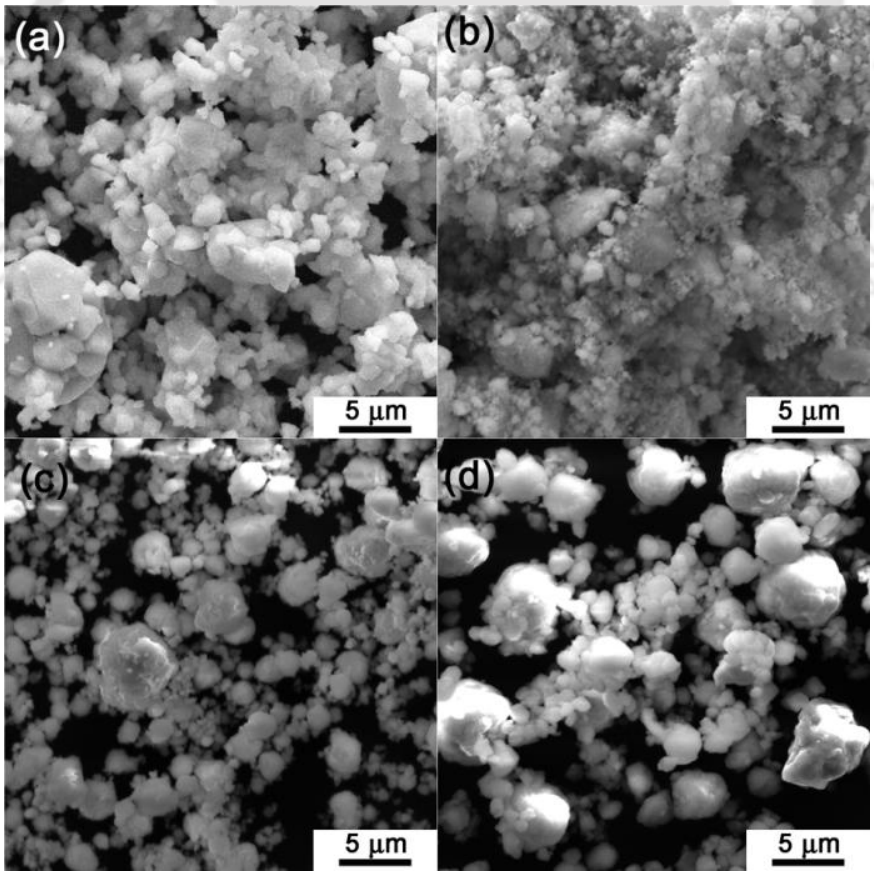

Figure 4.05: SEM micrographs of pure un-milled NiO powder (a) and 30 hrs milled NiO-Al (x at.%) powders with x = 0 (b), 20 (c) and 40 (d).

These observed results in the present study reveal that the MC reduction process in the milled NiO-Al powders strongly depends on the Al content under the present milling conditions. To study the solubility and size refinement, the lattice constant of NiO (a_{NiO}) was calculated from the peak positions, and the crystallite size (D_{NiO}) was calculated from NiO(200) peak using Scherrer's formula after subtracting the instrumental broadening contribution as explained in the experimental section. Figure 4.04 shows the typical variation of a_{NiO} and D_{NiO} for milled NiO-Al (x at.%) powders. The lattice constant increases from 4.159 Å for x = 0 to 4.173 Å for x = 10 powder and then remains nearly constant for higher values of x. This suggests a maximum lattice constant change of 0.0014 Å per at.% of Al due to the addition of large atomic size of the Al atom in NiO. Although the observed increase in the lattice constant is in good agreement with the earlier report [BOUK2012], the actual variation of lattice constant strongly depends on the system due to the change in the dissolution process. The value of D_{NiO} of the as-mixed NiO-Al powders is found to be about 40 nm. Upon milling the pure NiO (x = 0 at.%) powder for 30 hrs, D_{NiO} decreases largely to 13.5 nm. With increasing x, D_{NiO} decreases further to 10.3 nm for x up to 5 and then increases gradually up to 12.5 nm for x = 25. Note that the error in obtaining the peak position and full width at half maximum increases with increasing x above 10 at.% due to overlapping of the NiO and Ni peaks as well as owing to the substantial decrease in NiO(200) peak intensity.

To analyze the changes in surface morphology and the evolution of nanostructured NiO-Al nanocomposites, the structural properties of the milled powders were characterized using FESEM and TEM techniques, respectively. Figure 4.05 depicts the typical SEM micrographs of pure NiO and milled NiO-Al (x at.%) powders with x = 0, 20, and 40. All the micrographs show a clear particle morphology. The average size of the particles for the pure NiO powder is in the range of 1-3 μm. Upon milling for 30 hrs, the particle size reduces down to 300 nm but has a relatively inhomogeneous distribution, which results in an irregular morphology. Besides, these irregular fine particles tend to agglomerate in the form of spherical aggregates, which are typical of ball-milled powders resulting from the repeated cold welding and fracture of the powders during dry ball milling [AHNI2012, HOAN2016]. With increasing x, the size of the particles is marginally refined further due to the dissolution of Al in NiO for x up to 10 and then increases noticeably due to the formation of *in-situ* Ni/Al_2O_3 nanocomposites. Besides, the compositional analysis using EDS confirms the presence of Ni, O, and Al as the only elements present in the milled powders indicating the

purity of the final nanocomposite systems without any robust influence from the milling media.

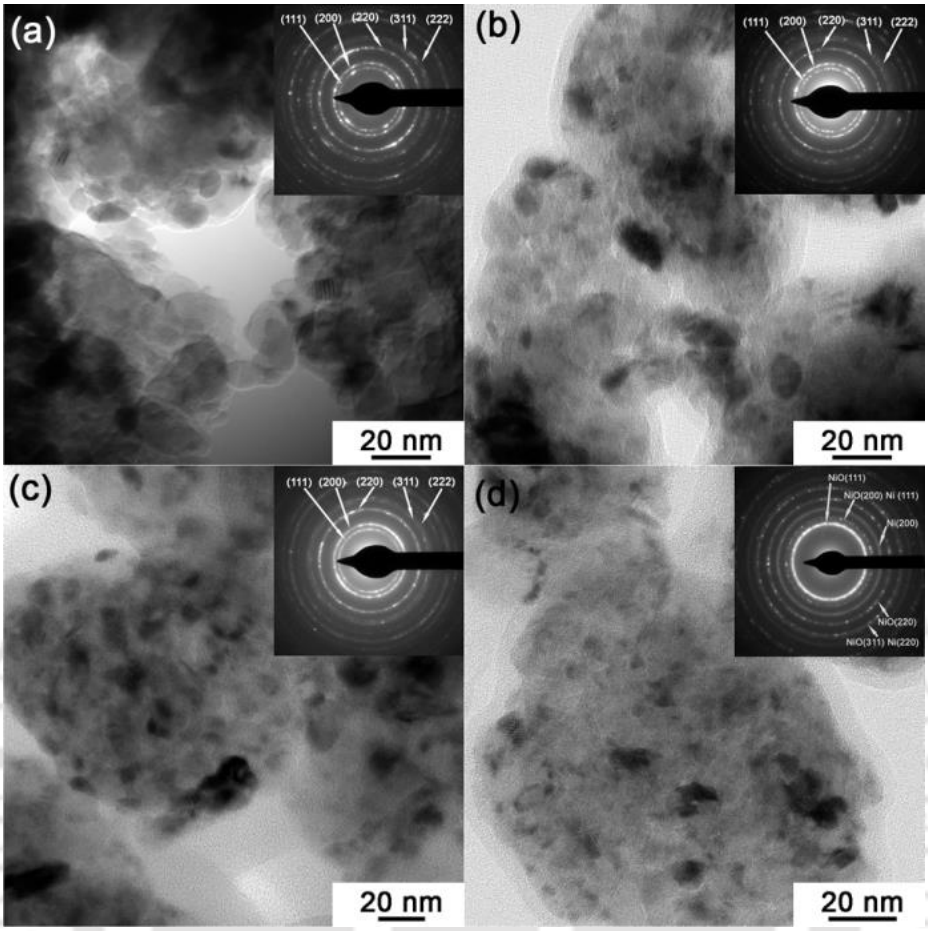

Figure 4.06: Bright-field TEM micrographs and SAED patterns of 30 hrs milled NiO-Al (*x* at.%) powders with *x* = 0 (a), 5 (b), 10 (c) and 20 (d).

The typical bright-field TEM (BF-TEM) micrographs and the selected area electron diffraction (SAED) patterns for milled NiO-Al (*x* at.%) powders with *x* = 0, 5, 10 and 20 are shown in Figure 4.06. The existence of fine nanocrystalline microstructure was observed from the BF-TEM micrographs, and the concentric diffraction rings in the SAED pattern could be indexed to the *fcc* structure of NiO for $x \leq 10$ (see Figure 4.06a-4.06c) and *fcc* structures of NiO and Ni for *x* = 20 (Figure 4.06d) confirming the polycrystalline nature of the milled powders. The estimated mean crystallite size is found to be 13.3, 10.5, 11.6 and 12.5 nm for *x* = 0, 5, 10 and 20 powders, respectively, while the a_{NiO} of milled NiO-Al powders is ranging between 4.1585 Å and 4.1735 Å for varying *x* between 0 and 20, respectively. These results indicate that the aggregated particles with the size ranging from a few hundred nanometers to a few micrometers observed in SEM micrographs consist of

nanosized crystallites, as seen in TEM, oriented randomly with respect to each other. The changes in the structural properties are expected to play a significant role in the resulting magnetic properties of NiO-Al powders. Therefore, we measured the *M-H* loops at room temperature and high-temperature *M-T* curves for pure NiO and milled NiO-Al powders.

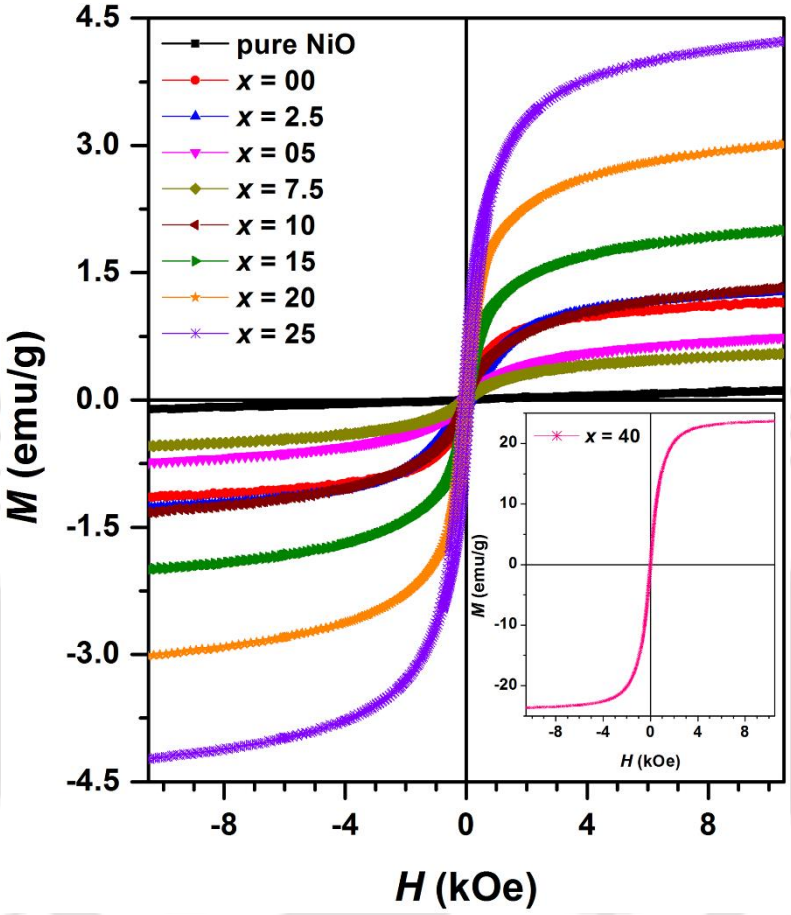

Figure 4.07: Room temperature Magnetic hysteresis (*M-H*) loops of pure NiO and 30 hrs milled NiO-Al (*x* at.%) powders with *x* = 0 - 40.

4.3.1.2. Magnetic properties:

Figure 4.07 displays the room temperature magnetic hysteresis (*M-H*) loops of pure NiO and milled NiO-Al (*x* at.%) powders measured at a maximum applied field of ±12 kOe. It is observed that (i) Pure NiO and as-mixed NiO-Al powders exhibit a weak and almost linear magnetic response to the applied field, and the loop passes through the origin. This could be correlated to the antiferromagnetic (AFM) nature of the powder in the bulk form. (ii) Nature of *M-H* loops for the 30 hrs milled NiO powder changes significantly, *i.e.*, magnetization increases considerably at lower fields, followed by a gradual increase in the higher field region. The loops do not pass through the origin and hence exhibit a clear

hysteresis loop. This confirms the existence of room-temperature ferromagnetism (RTFM). (iii) For x = 2.5 powders, the magnetization curve shows a feature similar to the one observed for the milled NiO powder, but a weak increase in magnetization was observed. (iv) With increasing x > 2.5, the magnetization decreases slightly for x up to 7.5 and then increases gradually for x up to 25.

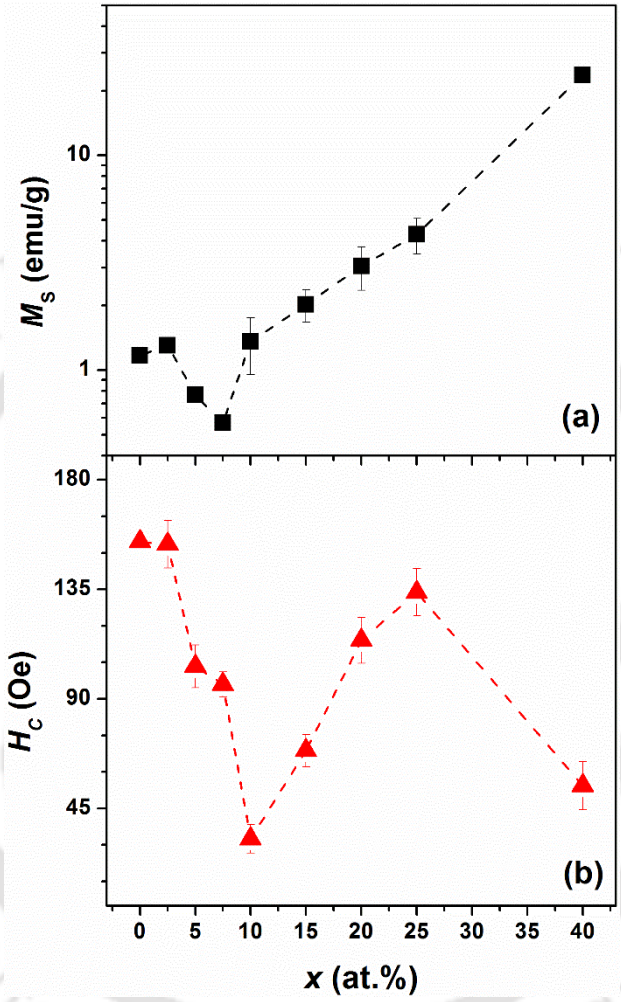

Figure 4.08: The variations of M_S and H_C with Al content for 30 hrs milled NiO-Al (x at.%) powders.

(v) Later, a substantial increase in magnetization is observed for x = 40 powder. To analyze the variations of magnetic parameters with Al addition, the values of magnetization at 12 kOe (M_S) and coercivity (H_C) were extracted from the *M-H* loops and shown in Figure 4.08 as a function of Al content. It is clear from the figure that (i) the pure NiO powder milled for 30 hrs exhibits modest magnetization of 1.17 emu/g. (ii) the addition of a small amount of x (= 2.5 at.%) in NiO increases the magnetization from 1.17 emu/g to 1.3 emu/g. (iii) On further increasing x, the magnetization decreases slightly to 0.57 emu/g for x up to 7.5 and

then increases gradually from 0.57 emu/g to 4.3 emu/g for *x* up to 25. (iv) A sudden jump in the magnetization value to 24 emu/g is observed for *x* = 40 powder. (v) On the other hand, H_C decreases initially from 154 Oe to 32 Oe for increasing *x* up to 10 and then increases significantly to 134 Oe for *x* up to 25. On further increasing *x* to 40, H_C decreases again largely to 54 Oe.

To explain the variations in the magnetic properties of the pure un-milled NiO and milled NiO-Al powders, we correlate both the structural and magnetic properties of NiO-Al powders. In pure NiO, the spins within AFM coupled (111) planes are compensated and hence do not contribute to the net magnetic moment. Accordingly, the *M-H* loop displays a weak response to the applied field [KODA19971, PECK2011] and passes through the origin. On the other hand, the observation of RTFM in milled NiO powder can be attributed to the existence of non-stoichiometry in NiO caused by the defects, size reduction, oxidization of Ni^{2+} to Ni^{3+}, *etc.* [AHMA2006, MIRO2007, THOT2007, PECK2011, RAVI2015]. It is well-known that the milling process promotes significant crystallite size reduction and massive defects, including the formation of vacancies in NiO. The average crystallite size of pure NiO powder decreases from 40 to 13.5 nm after milling for 30 hrs, and the pale green color of the pure NiO powder is changed into dark green. This creates non-stoichiometry in milled NiO powders [AHMA2006, GROS2006].

Furthermore, with the crystal size refinement of NiO, the number of uncompensated spins on the surfaces with respect to the particle core increases due to the breaking of Ni^{2+}-O^{2}-Ni^{2+} superexchange symmetry [CAZZ2003, MIRO2007, PECK2011]. Hence, we observed the alignment of particles' net moment under low applied magnetic fields resulting in RTFM with the modest magnetization of 1.17 emu/g. Kisan *et al.* [KISA2014] reported that the magnetization of the milled NiO powders increases with increasing milling time up to 30 hrs and then decreases slightly for higher milling time. The maximum magnetization of about 1.12 emu/g was observed for NiO powder milled for 30 hrs. Ravi *et al.* [RAVI2015] showed that the magnetization of milled NiO powder increases significantly from 0.54 emu/g to 1.28 emu/g with increasing milling speed. These reported results are in good agreement with the presently investigated samples. On the other hand, Del Bianco *et al.* [DELB2008] reported high values of magnetization of 7 emu/g for the commercial NiO powder milled for 20 hrs and attributed to the presence of Fe impurities in as-milled NiO derived from the milling media. With increasing *x* to 2.5, the magnetization increases from 1.17 emu/g to 1.3 emu/g, which can be attributed to the decrease in the average size of NiO

crystal by introducing Al. This is in close agreement with the earlier reports on similar systems with decreasing the crystallite size [PECK2011, KISA2014, RAVI2015]. With increasing *x* up to 7.5, the magnetization decreases slightly to 0.57 emu/g and can be attributed to the presence of atomic disorder, which weakens the induced FM properties in the non-equilibrium solid-solution of NiO-Al by the substitution of the non-magnetic element, Al, beyond a critical value [DJEG2001, SHYN20151]. On further increasing *x*, the mechanical activation of aluminothermic reduction gets initiated, and hence a gradual reduction of NiO by Al takes place.

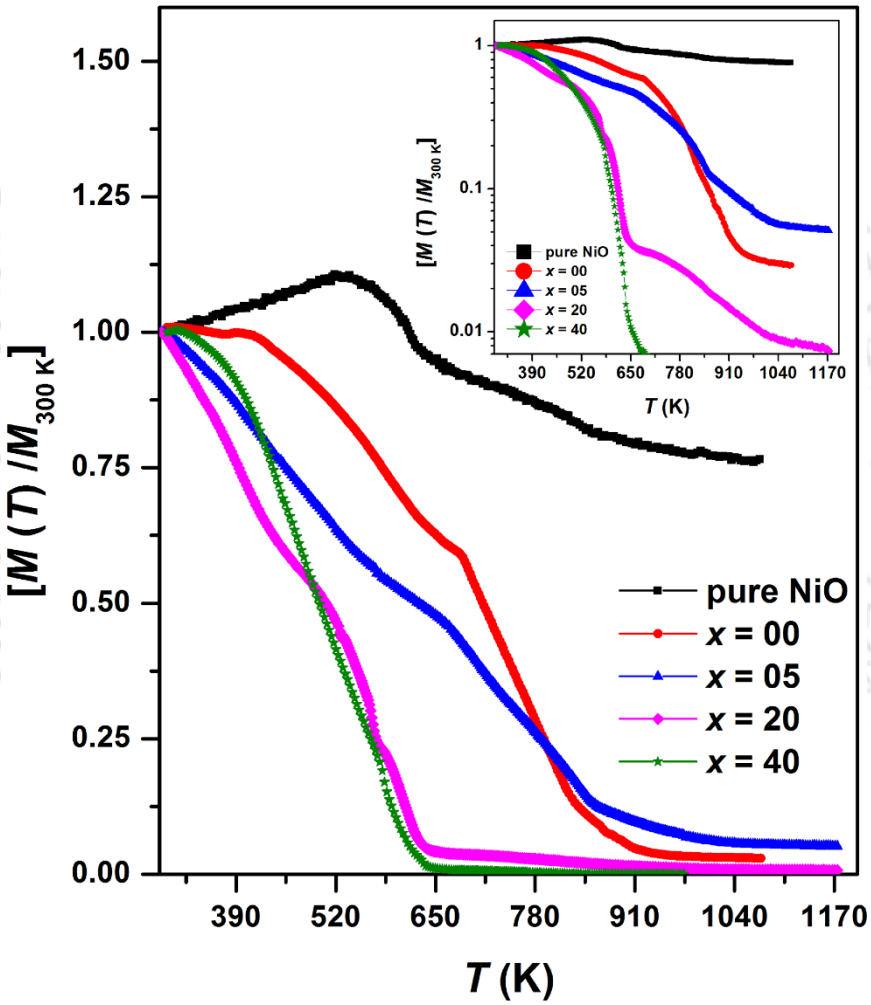

Figure 4.09: High temperature normalized *M-T* data measured under the applied field of 2 kOe for pure NiO, and 30 hrs milled NiO-Al (*x* at.%) powders. The inset shows the same data, but the normalized magnetization is plotted in logarithmic scale.

Therefore, M_S increases gradually with increasing *x* up to 25. Note that H_C is also increased, which could be related to the increased interaction between NiO and Ni since the development of Ni and NiO matrix are nanocrystalline by nature. For *x* = 40 powder, M_S

increases rapidly from 4.3 emu/g to 24 emu/g, and H_C reduces largely from 134 Oe to 54 Oe. This could be related to the formation of Ni/Al_2O_3 nanocomposite with the majority of NiO (~ 91%) reduced into Ni and Al_2O_3, resulting in a soft magnetic nature of the Ni/Al_2O_3 nanocomposite.

High-temperature *M-T* data were obtained by using VSM under the applied field of 2 kOe to study the stability of FM above room temperature in the milled NiO-Al powders. Figure 4.09 shows the typical *M-T* curves obtained for pure NiO and milled NiO-Al (*x* at. %) powders with *x* = 0, 5, 20, and 40. For having direct comparison among all the *M-T* curves, normalized magnetization values of individual *M-T* curves are plotted in the *y*-axis. The Inset of Figure 4.08 displays the same data, but the magnetization is presented with the logarithmic scale to see the variation close to zero. The magnetization of the pure un-milled NiO powder increases gradually with increasing temperature up to 525 K and then decreases above 525 K. Since the pure NiO powder exhibits AFM nature at room temperature, the Néel temperature (T_N) is determined from peak in the *M–T* curve and found to be nearly 525 K. This is in agreement with the earlier reports [THOT2013, RINA2016]. In contrast, the milled NiO powder exhibits an almost constant magnetization close to the room temperature regime. This shows a continuous decrease in magnetization with increasing temperature. The magnetization approaches to zero above 900 K. Thermal derivative of the *M-T* data exhibits two minima: one close to T_N and another broad minimum around 780 K corresponding to possible phase transition (T_C) of induced FM nature caused by the exchange interaction between the Ni magnetic ions with different ionic states (Ni^{2+} and Ni^{3+}) in the non-stoichiometry NiO generated by the defects and size reduction [PECK2011, KISA2014, KISA20152]. However, T_C of the induced FM phase is observed to be significantly large as compared to its bulk Ni counterpart (~ 630 K). This can be attributed to: (i) possible competing exchange interaction between the FM Ni and AFM NiO core, (ii) strain due to lattice mismatch between Ni and NiO arising at the interface [FEYG2010] or high strain induced during the ball milling process [GORR2009], which acts more like a hydrostatic one [LEGE1972]. The presence of strain in the milled powders is also evident from the non-smooth decrease of magnetization with increasing temperature and hence increases T_C [LEGE1972]. It may be noted that such high T_C values have also been reported in a similar Ni/NiO system (~750 K) [FEYG2010] and Ni-doped Titania powders (~ 810 K) [BAHA2012]. With increasing *x* to 5, *M-T* curve exhibits a feature similar to the one observed for *x* = 0 sample, which could be related to the fact that the addition of 5 at.% Al

in NiO forms only solid-solution of NiO-Al without any MC reduction reaction and hence results in similar exchange interaction behavior as described earlier for $x = 0$ sample. On the other hand, the *M-T* curve of the sample with $x = 20$ exhibits two clear magnetic phase transitions (see inset of Figure 4.08) due to the relative changes in the Ni and NiO phases caused by the reduction process. This sample shows a significant magnetization drop around 650 K corresponding to the magnetic phase transition of Ni and then a gradual variation of magnetization up to 1000 K corresponding to the induced FM behavior in NiO by the ball milling process [FEYG2010, KISA2014, RAVI2015]. With increasing $x = 40$, the gradual variation of magnetization above 650 K gets mainly suppressed due to major reduction of NiO by Al into NiO-Ni-Al_2O_3 nanocomposites, which results in a clear magnetic phase transition of majority Ni phase around 650 K. These results illustrate an extensive latitude of tunability of NiO by the MC reduction process to form the NiO-Ni-Al_2O_3 nanocomposites with increasing Al content and show a good correlation between the structural, magnetic and thermomagnetic properties of NiO-Al powders.

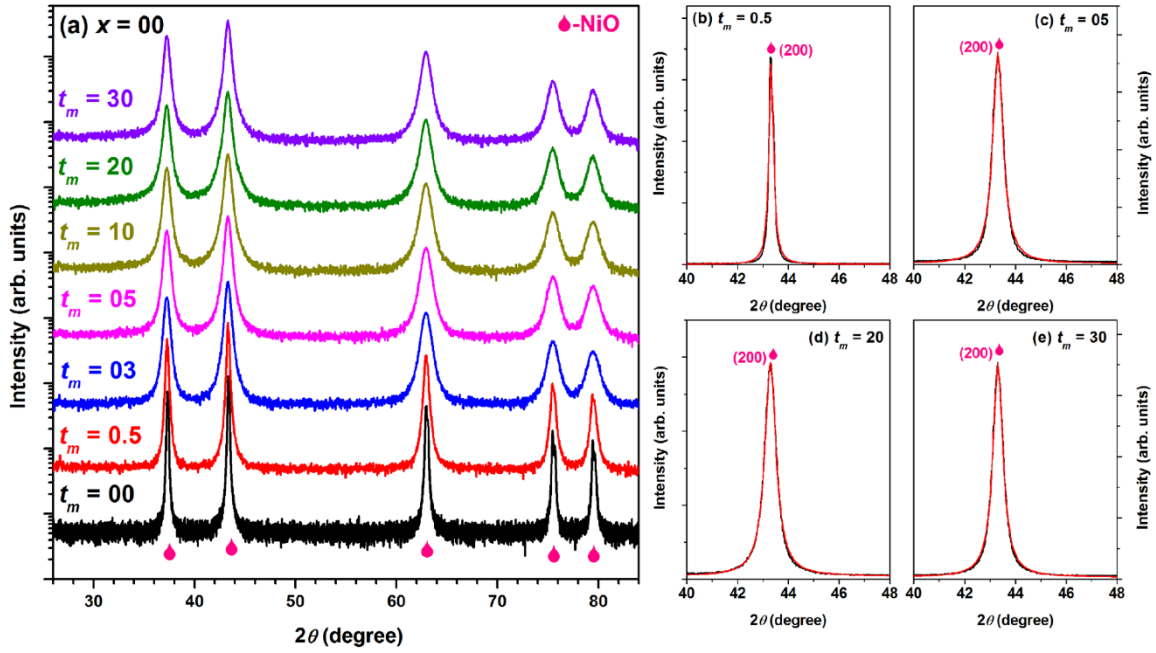

Figure 4.10: Room temperature XRPD patterns of (a) as-mixed and milled NiO-Al ($x = 0$ at.%) powders with t_m = 0-30 hrs and the multiple profile fittings of NiO(200) peak for t_m = 0.5 (b), 5 (c), 20 (d) and 30 (e).

4.3.2. Dynamics of milling on the properties of NiO-Al powders:

In the previous section, we reported tuning of NiO reduction in NiO-Al powder mixtures and the evolution of the structural and magnetic properties of NiO-Al (x at.%) powders as a

function of x in detail. To study the types of NiO reduction and dynamics of the aluminothermic/ mechanochemical reduction process of NiO in detail, in this section, we shall focus on the effect of milling periods for specified Al contents (x = 0, 20, 40).

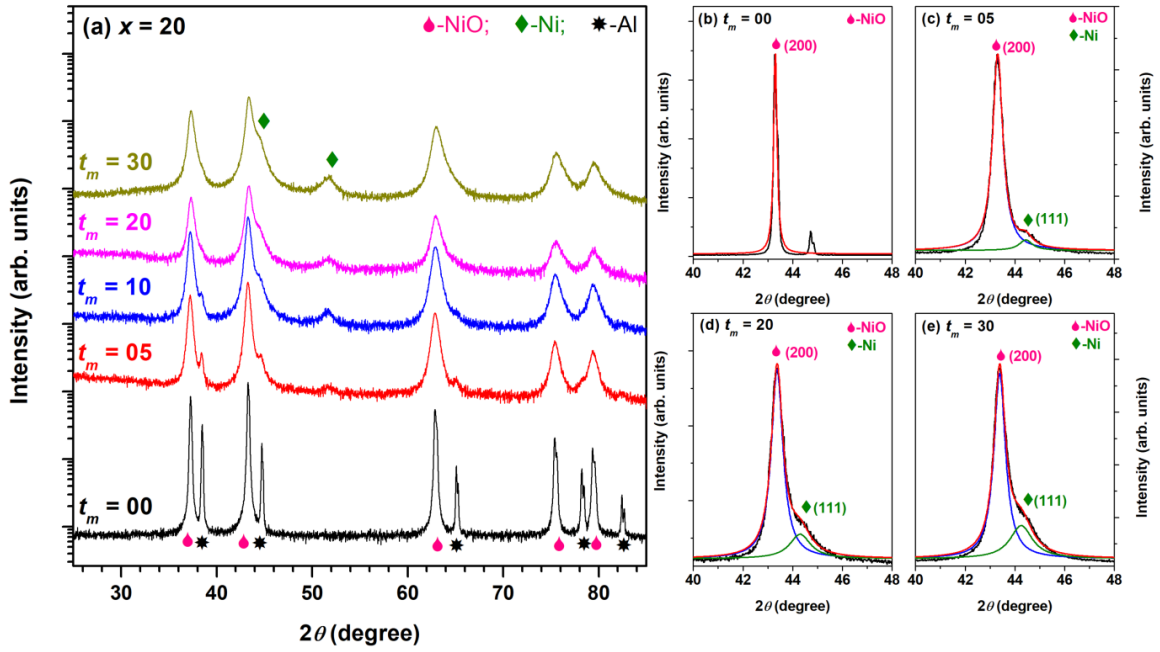

Figure 4.11: Room temperature XRPD patterns of (a) as-mixed and milled NiO-Al (x = 20 at.%) powders with t_m = 0-30 hrs and the multiple profile fittings of NiO(200) peak for t_m = 0 (b), 5 (c), 20 (d) and 30 (e).

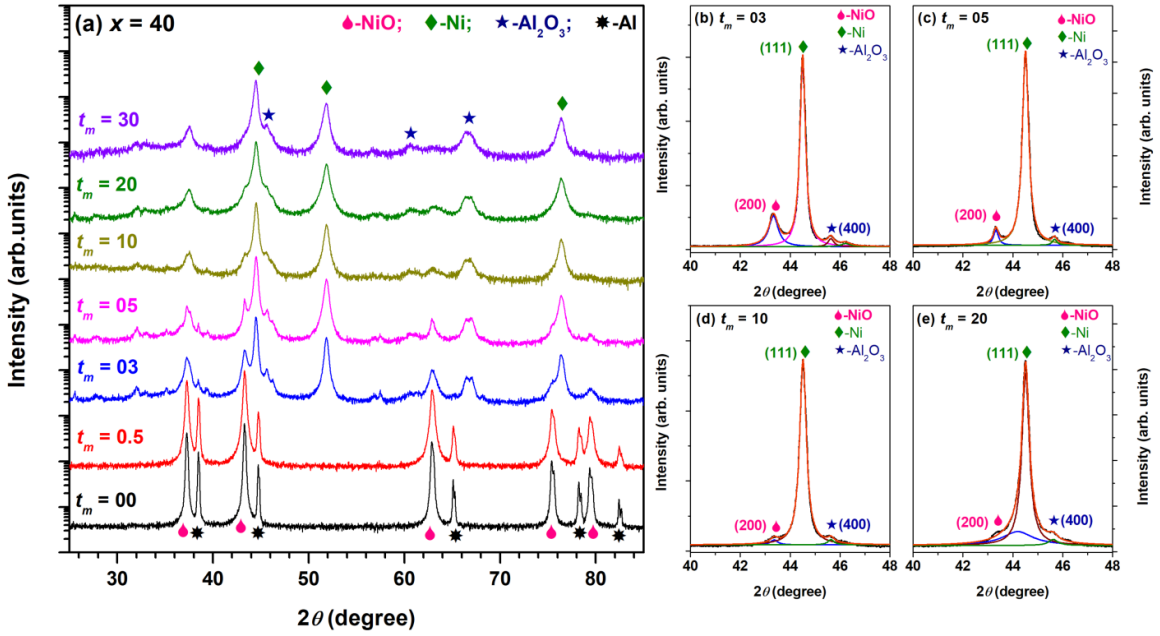

Figure 4.12: Room temperature XRPD patterns of (a) as-mixed and milled NiO-Al (x = 40 at.%) powders with t_m = 0-30 hrs and the multiple profile fittings of NiO(200) peak for t_m = 3 (b), 5 (c), 10 (d) and 20 (e).

4.3.2.1. Structural properties:

Figure 4.10 depicts the room temperature XRPD patterns of pure and milled NiO-Al (x = 0 at.%) powders prepared at different t_m. As the characteristic evolutions of structural properties strongly rely on the Al content, milling has been carried out separately for different milling periods (t_m) with selected Al contents. The pure un-milled and milled NiO powders show Bragg reflections corresponding to the *fcc* structure of NiO only. No additional peaks corresponding to any other phases or compounds were observed within the resolution of the high-power X-ray diffractometer. The broadness of the NiO peaks increases considerably (as shown in the individual peak fittings of NiO(200) peak in Figure 4.10b-4.10e), and the peak position shifts to lower angles with increasing t_m. As described earlier, the peak broadening can well be attributed to effective size reduction, and the shift in peak positions is mainly due to the change in the lattice parameters in the milled powders. As a result, we observed the gradual color change of pure un-milled NiO powder from pale-green into the dark green after milling. This could be attributed to the milling time induced non-stoichiometry in NiO caused by the defects, size reduction with increasing t_m [KISA20152], oxidization of Ni^{2+} to Ni^{3+} [AHMA2006] due to breaking of Ni^{2+}-O^{2-}-Ni^{2+} super-exchange interaction [MIRO2007, RAVI2015].

On the other hand, the as-mixed NiO-Al powder shows individual Bragg reflections corresponding to the *fcc* structure of NiO and Al. However, the XRPD patterns of the milled NiO-Al powders strongly depend on Al content and t_m, and hence the process of milling is described separately. Figure 4.11 shows the characteristic XRPD patterns of as-mixed and milled NiO-Al (20 at.%) powders as a function of t_m with the profile fittings of selected diffraction peaks of NiO-Al powders. All the reflections in the XRPD patterns of the as-mixed powders can be indexed to *fcc* NiO and Al. It is observed for x = 20 powder that (i) after 5 hrs of milling, the intensity of the Al peaks is decreased significantly along with the considerable broadening in NiO peaks. Also, the formation of new peaks at 2θ = 44.5° and 51.8° is observed indicating the commencement of NiO MC reduction reaction, which results in the materialization of Ni. (ii) With increasing t_m > 5, the intensity of Al peaks decreases further and then disappears eventually for t_m > 10. This could be attributed to both dissolution and utilization of Al for the NiO reduction. (iii) A progressive peak broadening of NiO peak, along with a significant shift in the peak position, is observed up to 30 hrs. While the peak broadening confirms the refinement of NiO crystals with increasing t_m, the peak shift is originated due to atomic disorder induced by the dissolution of Al in the NiO

matrix and the reduction. Furthermore, the intensity of the Ni peaks increases gradually with increasing t_m up to 30 hrs. The formation of Ni results in substantial changes in the color of the milled NiO-Al powders as follows: The pale-green color of the as-received NiO powder changes into the dark green after 5 hrs of milling mainly due to the non-stoichiometry in NiO and weak reduction of NiO. On further increasing t_m, the dark green color transforms into a black one due to the formation of Ni. (iv) Nevertheless, no additional Bragg peaks corresponding to any other phases or compounds were observed.

On the other hand, the XRPD patterns of the NiO-Al (40 at.%) powders (Figure 4.12a) reveal that (i) the peak intensities of NiO and Al decrease suggestively for 0.5 hr of milling. (ii) Interestingly, the process of aluminothermic reduction of NiO starts even by 3 hrs of milling, which results in the formation of distinct Ni peaks at 2θ = 44.5°, 51.8° and 76.3°. In addition, the development of additional peaks at 2θ = 45.6°, 60.6° and 66.6° corresponding to Al_2O_3 is observed. (iii) With increasing $t_m > 3$, the NiO(200) and NiO(311) peaks at 2θ = 43.35° and 75.46°, diminish progressively and merge into Ni(111) and Ni(220) peaks at 2θ = 44.5° and 76.3°, respectively at the end of 30 hrs of milling. While the NiO(220) and NiO(222) peaks disappear completely, the existence of a highly strained NiO(111) peak is still observed after 30 hrs of milling. (iv) A close observation of Ni(200) peak at 2θ = 51.8° unveils a considerable peak broadening with increasing t_m from 3 to 30 hrs. This may be correlated to the refinement of Ni crystals after its formation from NiO reduction. These results suggest that the reduction process for x = 40 powders is quite instantaneous and rapid, implying the plausibility of different reaction kinetics for x = 20 and 40 powders.

In a conventional self-propagating high-temperature synthesis process, the temperature of the reaction usually has to be raised at the temperature range of 800 to 1100 °C under the reactive gas atmosphere [BENT1924, BUDA1998, JEAN2013, RASH2013]. However, the reduction of NiO strongly depends on the types of the reducing gas and the processing conditions. The NiO reduction was also carried out by mixing the NiO with C powders, followed by the consecutive heating process under different gases [KIMK2011]. However, the temperature needed for the NiO reduction is still quite high. On the other hand, the reactive milling promotes mechanically activated solid-state chemical reactions between oxides and reducing agents such as Na, Mg, Ca, and Al for the reduction process. This might be because the milling process creates a large number of defects, grain

boundaries, and sub-grain boundaries, which favors mass transfer and diffusion path length with reduced activation energy [LUL1997].

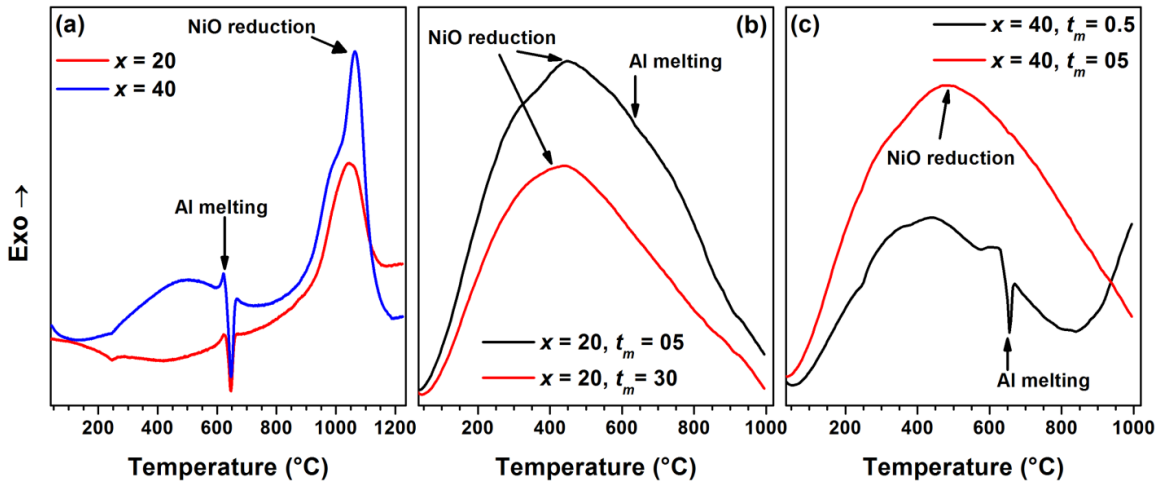

Figure 4.13: DSC curves for un-milled (a) and milled NiO-Al powders with x = 20 (b) and x = 40 (c) at different t_m.

To understand the process of aluminothermic reaction kinetics for the presently investigated samples in correlation with XRPD results, we have carried out the thermal analysis of the un-milled and milled NiO-Al powders using the DSC technique and the curves are depicted in Figure 4.13. The curves show (i) sharp endothermic peaks at around 650 °C corresponding to Al melting and (ii) one exothermic peak at about 1040 °C for x = 20 powder corresponding to NiO reduction and two exothermic peaks at 1000 °C and 1070 °C corresponding to two-stage reduction of NiO [YANG1998].

On the other hand, the milled NiO-Al powders exhibit a broad exothermic peak at 440 °C indicating the partial reduction of unreacted NiO present in the as-milled powders. However, we observed a significant endothermic Al melting peak at 5 hrs milled x = 20 powder, and 0.5 hrs milled x = 40 powder indicating the presence of unreacted Al in the as-milled powders. Similarly, the absence of the Al melting peak in DSC curves of other milled samples confirms the solid-state reduction of NiO in these milled samples. These results are in good agreement with the XRPD patterns (see Figures 4.11 and 4.12) and support the nature of NiO reduction reaction occurring with different Al content at different t_m. Here, it may be noted that based on the milling criteria and the nature of the raw powder mixtures, MC displacement reactions during the reactive milling processes can have two completely different reaction kinetics plausible thermodynamically: (i) Gradual reaction, which progresses in a steady-state through a tiny volume during each collision of the milling balls

or, (ii) The self-sustaining reaction type, where the reaction enthalpy becomes sufficiently high for the reaction to proceed itself. The reaction enthalpies, ΔH, in both cases, are highly negative and hence, correspond to highly exothermic reactions. Therefore, a mechanically induced self-sustaining type of reaction can be triggered by the impact of the milling balls, if the ratio$(-\Delta H^0_{298K})/(\sum C_{P_{298K}}) > 2000\ K$, where $\Delta H^0_{298\,K}$ is the reaction enthalpy and $\sum C_{P_{298K}}$ are the total heat capacity of the products at 298 K [TAKA2002]. For the stoichiometric composition of the as-mixed NiO-Al powder as described in eqn. (4.01), $\Delta H^0_{298\,K}$ is found to be largely negative with the value of -953 kJ/mol and consequently, the value of $(-\Delta H^0_{298K})/(\sum C_{P_{298K}})$ turns out to be around 5349 K [HTTP0010]. Thus, the NiO-Al reduction reaction is highly exothermic by nature, and thermodynamically, a mechanically induced self-sustaining reaction can be expected during ball milling if an abundant amount of reactant, Al, is availed in the as-mixed powder.

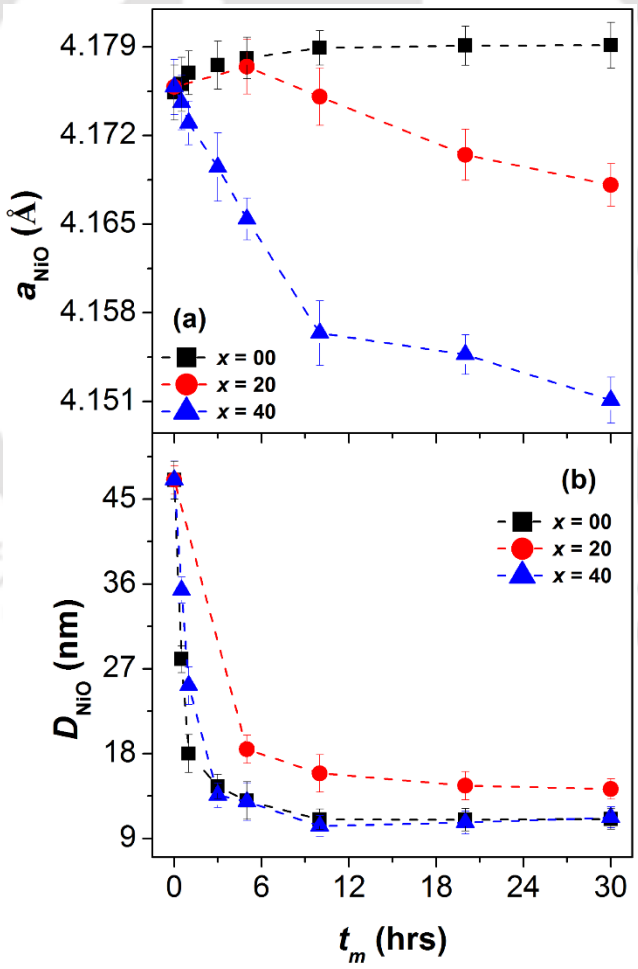

Figure 4.14: The variations of NiO lattice constant, $a_{NiO,}$ and average crystallite size, D_{NiO} as a function of t_m for NiO-Al (x at.%) powders.

Therefore, for x = 40 powder, which has a stoichiometric composition, as stated in eqn. (4.01), the reaction process reveals self-propagating combustion kinetics in agreement with the earlier reports [JONE1994, ZHUH2000] and needs a critical t_m of 3 hrs for the combustion reaction to be ignited. On the other hand, for x = 20 powders, the amount of Al available for the ignition of the above combustion reaction is considerably low and hence promotes only the gradual reduction process. Therefore, the MC reduction process in milled NiO-Al powders relies on t_m and Al content under the present milling conditions. A more detailed thermal analysis and heat treatment at high temperatures of the as-milled samples at different t_m would elucidate the nature of the reactions more in detail.

To study the structural refinement, a_{NiO} and D_{NiO} were calculated after eliminating the contribution from instrumental broadening. Figure 4.14 displays the variations of a_{NiO} and D_{NiO} as a function of t_m for the milled NiO-Al powders with different Al content. The value of a_{NiO} for pure un-milled NiO powder is 4.176 Å, which increases progressively to 4.179 Å for milled NiO powders after 10 hrs of milling and then tends to saturate at higher t_m. D_{NiO} decreases significantly from about 47 nm for the pure un-milled NiO powder to about 13 nm in 5 hrs of milling. With increasing t_m > 5 hrs, D_{NiO} decreases slowly and reaches to about 11 nm. On the other hand, for x = 20 powders, a_{NiO} increases initially to 4.177 Å after 5 hrs of milling and then decreases gradually to 4.168 Å at a rate of 3.8×10^{-4} Å per hr up to 30 hrs of milling. D_{NiO} decreases largely to about 19 nm in 5 hrs of milling followed by a gradual variation at higher t_m, reaching to about 14 nm at t_m = 30 hrs. With increasing x to 40, the variations of a_{NiO} with t_m exhibit two different slopes: *i.e.*, 19.2×10^{-4} Å per hr from 0 to 10 hrs and 2.65×10^{-4} Å per hr from 10 to 30 hrs of milling. D_{NiO} decreases from 47 nm to 13 nm within 5 hrs of milling and then reaches to about 11 nm after 30 hrs of milling. On the other hand, D_{Ni} varies from 7 to 14 nm and from 14 to 23 nm for x = 20 and 40 powders, respectively. These changes could be attributed to the time-dependent aluminothermic reduction of NiO, which changes the formation of eventual nanocomposites with different fractions of NiO, Ni, and Al_2O_3.

To understand the evolution of nanocomposites with different Al content and t_m, the pure NiO and milled NiO-Al powders were characterized using the TEM technique. Figure 4.15 displays the BF-TEM and high-resolution TEM (HR-TEM) images, SAED patterns, and inverse-Fast Fourier transform (i-FFT) images of selected areas of HR-TEM images for pure NiO and milled NiO-Al (x at.%) powders at different t_m. BF-TEM image of the pure NiO powder reveals clear particle morphology with size varying between 40 and 70 nm.

The polycrystalline nature is evident from NiO concentric diffraction rings in the SAED pattern.

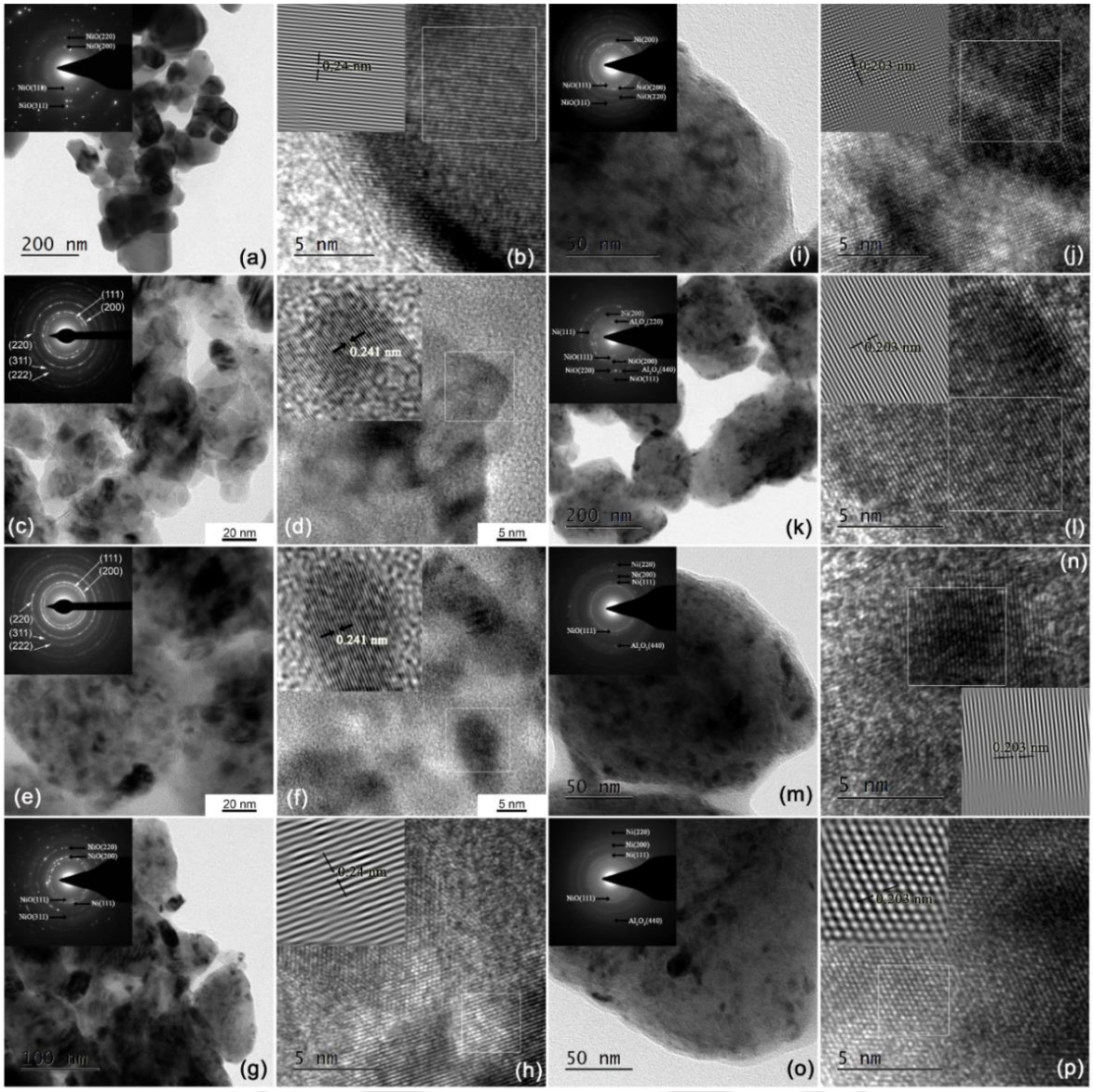

Figure 4.15: BF-TEM and high-resolution TEM (HR-TEM) images, SAED patterns and inverse-Fast Fourier transform (i-FFT) images of selected areas of HR-TEM images for pure NiO [(a) and (b)] and milled NiO-Al (x at.%) powders at different t_m [x=0, t_m=3 (c) and (d); x=0, t_m=30 (e) and (f); x=20, t_m=5 (g) and (h); x=20, t_m=20 (i) and (j); x=40, t_m=5 (k) and (l); x=40, t_m=20 (m) and (n); x=40, t_m=30 (o) and (p)].

On the other hand, BF-TEM images of milled NiO powder confirm the presence of fine nanocrystalline microstructure with irregular morphology. The SAED patterns show diffraction rings corresponding to only *fcc* structure of polycrystalline NiO. D_{NiO} decreases from 40-70 nm for the pure un-milled NiO powder to about 14 nm and 11 nm after milling

for 3 hrs and 30 hrs, respectively. The variations of the TEM crystallite size of NiO exhibit almost a similar trend with that of XRPD results. Nevertheless, the nanoparticles exhibit irregular shapes with broad size distribution. To analyze the lattice parameter prudently, we have carefully resolved the HR-TEM images by the i-FFT method using a GATAN digital micrograph and shown as the insets of all HR-TEM images.

The i-FFT images help to resolve the lattice fringes with the subsequent determination of interplanar spacing of 0.241 nm corresponding to the NiO(111) lattice plane. With increasing x = 20, a similar nanocrystallinity with irregular morphology was observed. The SAED patterns and HR-TEM images support the presence of both NiO and Ni phases with fine nanometer-sized crystallites of NiO and Ni. The i-FFT images reveal the interplanar spacing of 0.24 nm and 0.20 nm corresponding to the NiO(111) and Ni(111) lattice planes, respectively. D_{NiO} decreases to about 14 nm after 30 hrs of milling. Diffraction rings of Ni(111) phase is quite continuous and diffusive by nature, which overlaps with the spotty ring from NiO(200) plane for x = 20 powders (see Figures 4.15g and 4.15i), while clear diffraction rings corresponding to Ni and Al_2O_3 could be observed for x = 40 powders milled above 5 hrs. D_{Ni} calculated from HR-TEM images for x = 40 powders is in the range of 14-22 nm, which is in good agreement with XRPD results. These changes in the structural properties as a function of Al contents and milling times are expected to play a substantial role in the resulting magnetic properties of NiO-Al powders. Hence, we measured room temperature *IM* curves, *M-H* loops, and high-temperature *M-T* curves for milled NiO-Al (x at.%) powders.

4.3.2.2. Magnetic properties:

Figure 4.16 displays room temperature *IM* curves with magnetization in the logarithmic scale and *M-H* loops of pure NiO and milled NiO-Al powders at different t_m. The extracted values of M_S, H_C, and exchange bias [$H_E = (|H_{C+}|-|H_{C-}|)/2$] from the *M-H* loops are depicted as a function of t_m in Figure 4.17. It is observed that (i) the pure un-milled NiO and NiO-Al powders exhibit weak and linear responses to the applied magnetic field due to the AFM nature of NiO. (ii) On the other hand, the milled NiO powder, even at 1 hr, displays different nature of the magnetic response to the applied field, *i.e.*, the magnetic moment increases moderately at lower magnetic fields and then varies gradually at high fields. A clear *M-H* loop confirming the existence of RTFM is observed. Noticeably, the rate of increase in the magnetic moment at lower fields increases with increasing t_m up to 20 hrs (see Figure 4.16a)

and saturates for t_m = 30 hrs. (iii) *M-H* loops are shifted significantly to the negative axis (see inset of Figure 4.16b), but the amount of shift decreases with increasing t_m.

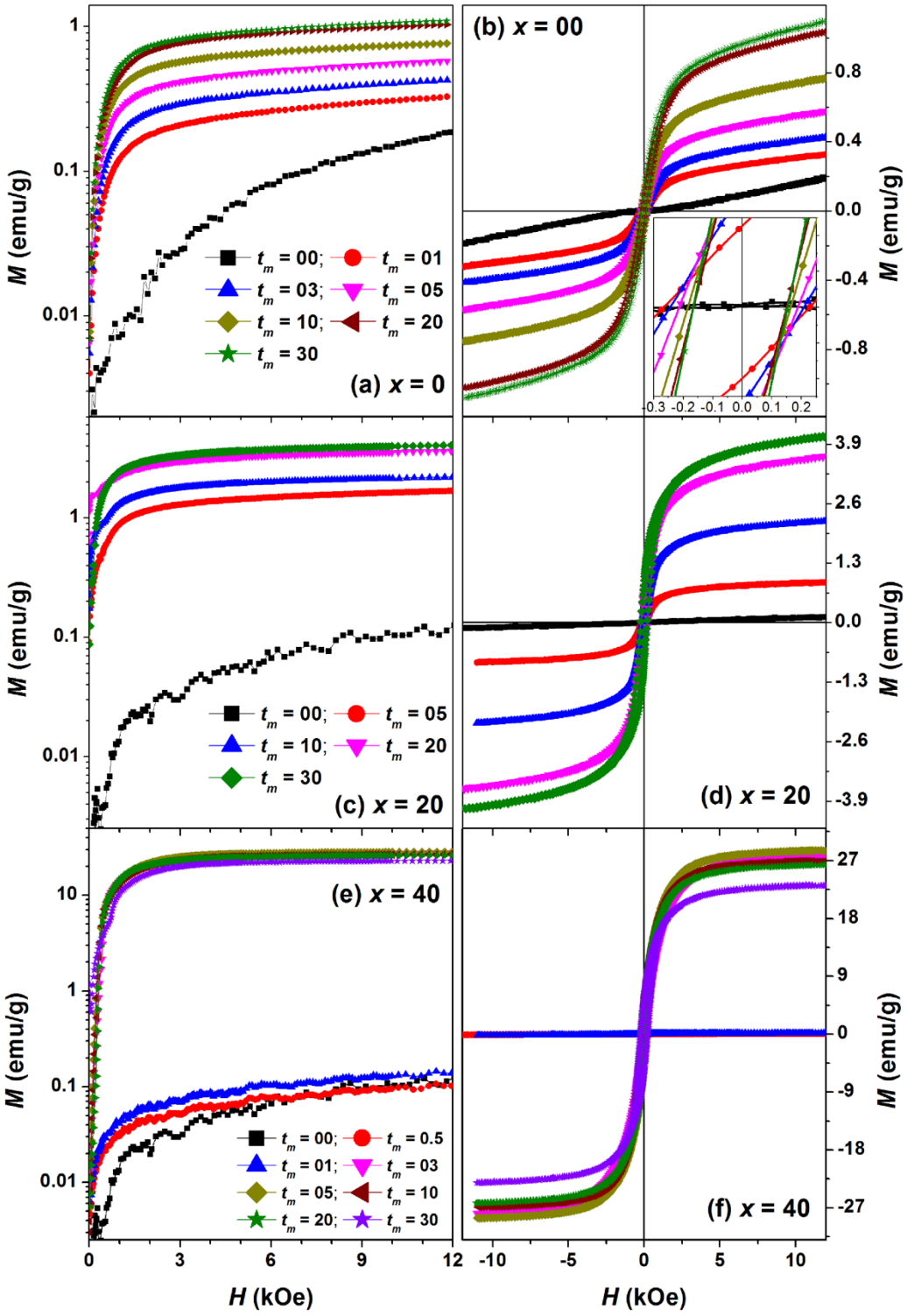

Figure 4.16: Room temperature initial magnetization (*IM*) curves (magnetization in logarithmic scale) and magnetic hysteresis (*M-H*) loops of pure and milled NiO-Al powders at different t_m.

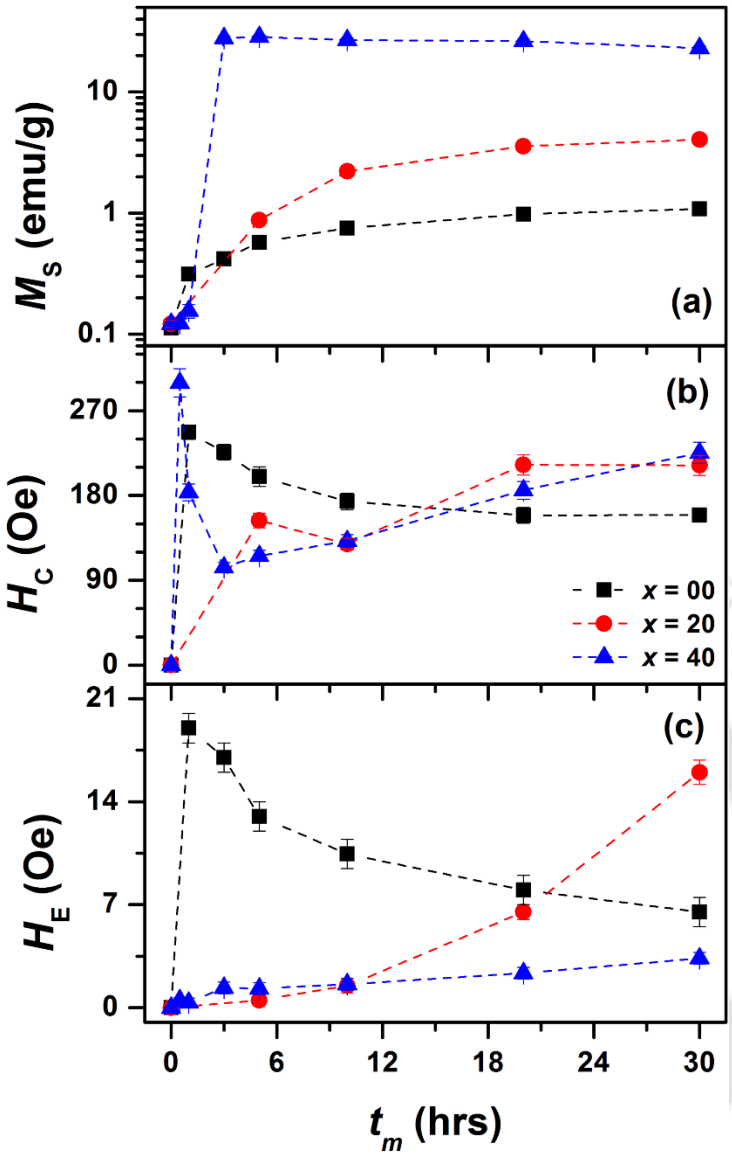

Figure 4.17: The variations of saturation magnetization, M_S (in logarithmic scale), coercivity, H_C, and exchange bias, H_E as a function of t_m for NiO-Al (x at.%) powders.

The extracted values of M_S, H_C, and H_E show that (i) M_S increases progressively for the initial period of milling and nearly saturates at higher t_m. This results in a maximum M_S of 1.02 emu/g after 30 hrs of milling. (ii) H_C, observed as zero for pure un-milled NiO due to its AFM nature, has increased significantly to about 250 Oe after 1 hr of milling. On further increasing t_m, H_C decreases substantially from 250 Oe to about 160 Oe after milling for 20 hrs and then remains almost constant up to t_m = 30. (iii) The variation of H_E with t_m exhibits almost a similar trend of H_C versus t_m, *i.e.*, H_E is observed to be high for the initial period of milling, but decreases with increasing t_m. However, the shape of the *M-H* loops for NiO-Al milled powders changes differently depending on Al content. For x = 20 powder milled for

5 hr, the moment increases noticeably in the lower field region, followed by a progressive increase in higher fields. This results in a clear *M-H* loop with RTFM having M_S of 0.88 emu/g and H_C of 155 Oe. With increasing t_m > 5 hrs, M_S increases substantially and reaches a maximum of about 4.05 emu/g. However, the rate of increase in M_S decreases with increasing t_m > 10. In contrast to pure milled NiO powder, H_C of the milled NiO-Al powder increases steadily with increasing t_m up to 20 hrs and tends to saturate for 30 hrs milled powders. Consequently, the value of H_E also increases up to 30 hr. With increasing *x* to 40, the nature of *IM* curves and *M-H* loops is found to be nearly the same for the powders milled up to 1 hr and then exhibits a rapid change in magnetization with a maximum of 28.5 emu/g. Upon increasing t_m > 5 hrs, M_S decreases almost linearly at a rate of 0.199 emu/g per hr and reaches to 23 emu/g for 30 hrs milled powders. H_C increases largely to 300 Oe for 0.5 hr milled powder and decreases to 104 Oe after 3 hrs of milling. Subsequently, H_C increases almost linearly at a rate of 4.54 Oe per hr and reaches about 225 Oe for 30 hrs milled powders. However, H_E has not increased substantially for x = 40 as compared to x = 20 powders.

To understand the changes in the magnetic properties of NiO and NiO-Al milled powders, we correlate both the structural and magnetic properties. Pure un-milled NiO (pale-green colored) powder displays a weak response to the applied magnetic field [KODA19971] due to its AFM nature. On the other hand, the milled NiO powders undergo a large size reduction with increasing milling time and change in the color due to non-stoichiometry [AHMA2006, GROS2006], which result in a breaking of Ni^{2+}-O^{2-}-Ni^{2+} super-exchange interaction [AHMA2006, MIRO2007, MAKH2008, RAVI2015] and increase in the number of uncompensated spins on the surfaces as compared to the particle core [PECK2011] upon increasing t_m. This leads to an alignment of particles' net moment in a relatively low field and enhances net moments along with high H_C. Also, the exchange coupling between the induced FM and AFM core instigates the exchange bias effect, which decreases progressively with the size reduction of NiO. Furthermore, the lattice expansion observed in finer crystallites plays a crucial role in controlling the magnetic exchange interaction between the uncompensated surface spins and particle core spins. This is in agreement with the earlier report by Li *et al.* [LIL2006] that the room-temperature magnetic crossover of NiO is due to the lattice expansion. Del Bianco *et al.* [DELB2008] reported that saturation magnetization of NiO increases at a rate of 0.62 emu/g per Ni wt.% in

hydrogenated NiO. A quantitative comparison with the presently investigated samples indicates that the as-milled NiO powders have about 1.7 wt.% Ni enriched spatial regions.

To examine the role of unexpected impurity contribution on the magnetic properties, the detailed magnetic structure, chemical bonding, and chemical composition of the milled powders were analyzed using ^{57}Fe Mössbauer spectroscopy, XPS, and EDS, respectively. However, the presence of any impurity phases corresponding to the iron could not be detected at least to the detection limits of these techniques. Additionally, the survey scan of XPS spectra reveals that the milled NiO powders were free from iron impurities. Figure 4.18 displays the Ni 2*p* and O 1*s* XPS spectra for pure un-milled NiO and 30 hrs milled NiO powders.

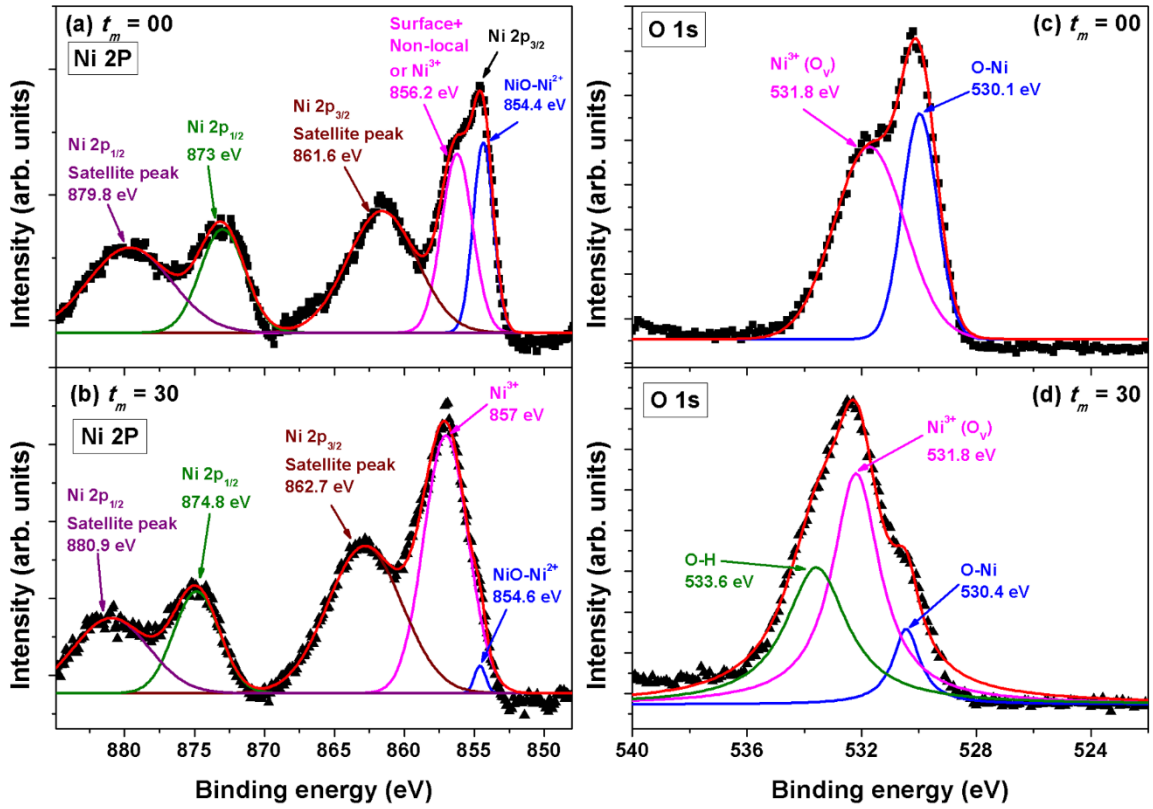

Figure 4.18: Ni 2*p* XPS spectra for pure un-milled NiO (a) and 30 hrs milled NiO (b); O 1*s* XPS spectra for pure un-milled NiO (c) and 30 hrs milled NiO (d).

The Ni 2p XPS spectra reveal the existence of mixed valency state 2+ and 3+ in the milled NiO powders due to the non-stoichiometry caused by the breaking of Ni^{2+}-O^{2-}-Ni^{2+} super-exchange symmetry due to size reduction with the irregular shapes and induced defects. This is in good agreement with the earlier reports [GROS2006] and backed by the color change of the milled NiO powders, as shown in Figure 4.03. Furthermore, the detailed

annealing studies of the as-milled NiO powders carried out in the air [KISA2014, KISA20152] reduced the magnetic moment of the milled powders largely and the rate of decrease of magnetic moment strongly dependent on the milling conditions. This was attributed to the release of strain (defects), reduction of Ni^{3+} to Ni^{2+} [HONG2006], and an increase in the average crystallite size with annealing. The above results, along with the present milling conditions, apparently rule out the possible contribution from the iron impurity phases on the magnetic properties, and therefore, the observed moment in the milled powders is originated mainly from the intrinsic properties.

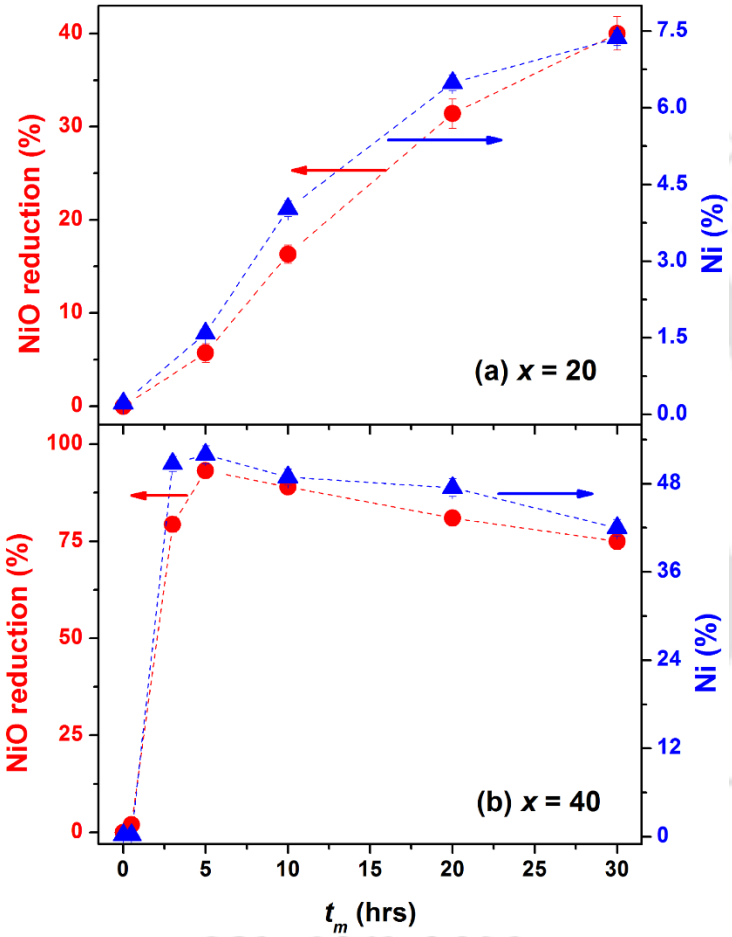

Figure 4.19: The variations of percentage reduction of NiO and percentage of Ni as a function of t_m for NiO-Al (x at.%) powders.

In the case of NiO-Al milled powders, the variation of M_S strongly depends on the amount of NiO reduction. Considering the AFM nature of NiO and ascribing the increase of the magnetization in the nanocomposite is mainly due to the formation of FM Ni from NiO reduction, the percentage of Ni was estimated by relating the values of M_S with respect to saturation magnetization of bulk Ni (~55 emu/g) [WUSH2003, HEX2013]. To evaluate

the percentage of NiO reduction with t_m, we have utilized the change in the integrated intensity of NiO(200) peak using eqn. (4.03). Figure 4.19 depicts the variations of NiO reduction determined from XRPD analysis and the percentage of Ni obtained from magnetic measurements as a function of t_m for x = 20 and 40 powders. It can be observed that the percentage of Ni in the nanocomposite increases progressively up to a maximum of 7.5 at.% with increasing t_m to 30 hrs. This is in good correlation with respect to the gradual reduction of NiO by Al for x = 20 powders. As a result, H_E increases up to 30 hrs supporting the gradual formation of Ni in the NiO matrix, which induces the exchange interaction between FM Ni and AFM NiO. On the other hand, for x = 40 powders, the intensity of NiO and Al XRPD peaks is reduced up to t_m = 1 hr due to the dissolution of Al in NiO without any ignition of NiO reduction. As a result, the formation of Ni is not observed. With increasing $t_m \geq 3$ hrs, the self-propagating combustion reaction is ignited suddenly, which reduces 90% of NiO into Ni/Al_2O_3 nanocomposite and provides about 52% of Ni after 5 hrs of milling. On further increasing $t_m > 5$ hrs, a considerable refinement of Ni nanocrystals occurs. This increases H_C progressively and decreases M_S. Since a larger fraction of NiO is reduced into Ni, H_E turns out to be low value.

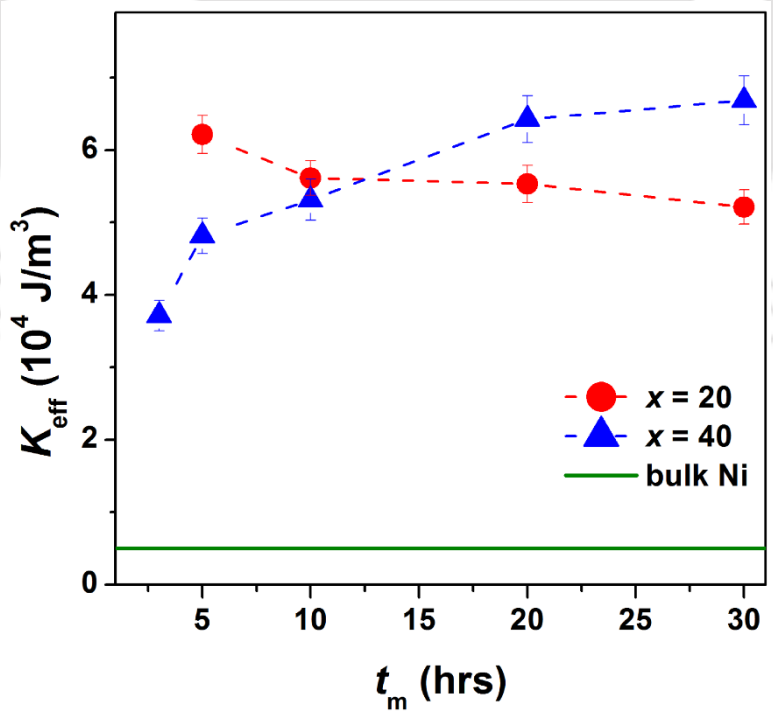

Figure 4.20: The variation of K_{eff} as a function of t_m for NiO-Al (x at.%) powders. K_{eff} of bulk Ni is also shown for comparison.

It may be noted that the milled NiO-Al powders exhibit RTFM despite having the average size of D_{Ni} in the range below 25 nm, which is significantly below the critical size (~ 34 nm) of spherical Ni particles for single domain behavior at room temperature [BALA2004]. Hence, Ni nanoparticles will be of single-domain but prone to thermal fluctuations [SKOM2003, ZHAN2009]. Note that the critical contribution to the K_{eff} in nanoscale magnetic particles can be defined as

$$K_{eff} = K_{mc} + K_{sh} + K_{sur} + K_{st} + K_{ex} \tag{4.04}$$

Where K_{mc} is the magnetocrystalline anisotropy, K_{sh} is the shape anisotropy, K_{sur} is the surface anisotropy, K_{st} is the strain anisotropy, and K_{ex} is the exchange anisotropy. Therefore, the obtained RTFM in the presently investigated samples can be correlated to one or more of the following several origins: (i) The milled powder exhibits quite irregular morphology (see Figure 4.15) and hence the shape anisotropy could play a key role [PARK2000, ROCA2006]. (ii) Since the milled powders are subjected to severe fracture and cold welding during the milling process, the strain anisotropy could contribute to the total anisotropy of the nanoparticles. (iii) Surface anisotropy of the nanoparticles may also play an important role [SKOM2003, YANE2007, YANE2010]. (iv) When the FM nanoparticles are embedded in an AFM matrix, an additional uniaxial type anisotropy is also introduced to the nanoparticles [ROCA2006, ZHAN2009, KRIS2016]. To analyze the effective magnetic anisotropy in the milled NiO-Al powders, we have fitted *IM* curves using the law of approach of the magnetization to saturation (LAS) as defined in eqn. (4.05)

$$M(H) = M_S\left(1 - \frac{a}{H} - \frac{b}{H^2} + \cdots\right) + \chi H \tag{4.05}$$

Where $M(H)$ is the magnetization in an applied magnetic field H, M_S is the saturation magnetization, χ is high-field susceptibility, and, a and b are constant coefficients [KRON2003]. The constant-coefficient b is related to the effective magnetic anisotropy of the cubic crystalline materials as given in eqn. (4.06),

$$K_{eff} = \sqrt{\frac{105}{8} b\mu_0^2 M_S^2} \tag{4.06}$$

The determined values of K_{eff} as a function of t_m for NiO-Al milled powders are shown in Figure 4.20. For the sake of comparison, the K_{eff} of bulk Ni is also shown in the figure. The obtained values of K_{eff} for the milled powders are found to be larger as compared to K_{eff} of the bulk Ni. This could be attributed to the contribution from various anisotropies such as magnetocrystalline anisotropy, shape anisotropy, strain anisotropy, and exchange

anisotropy for these fine nanosized Ni in nanocomposites prepared by the ball milling process.

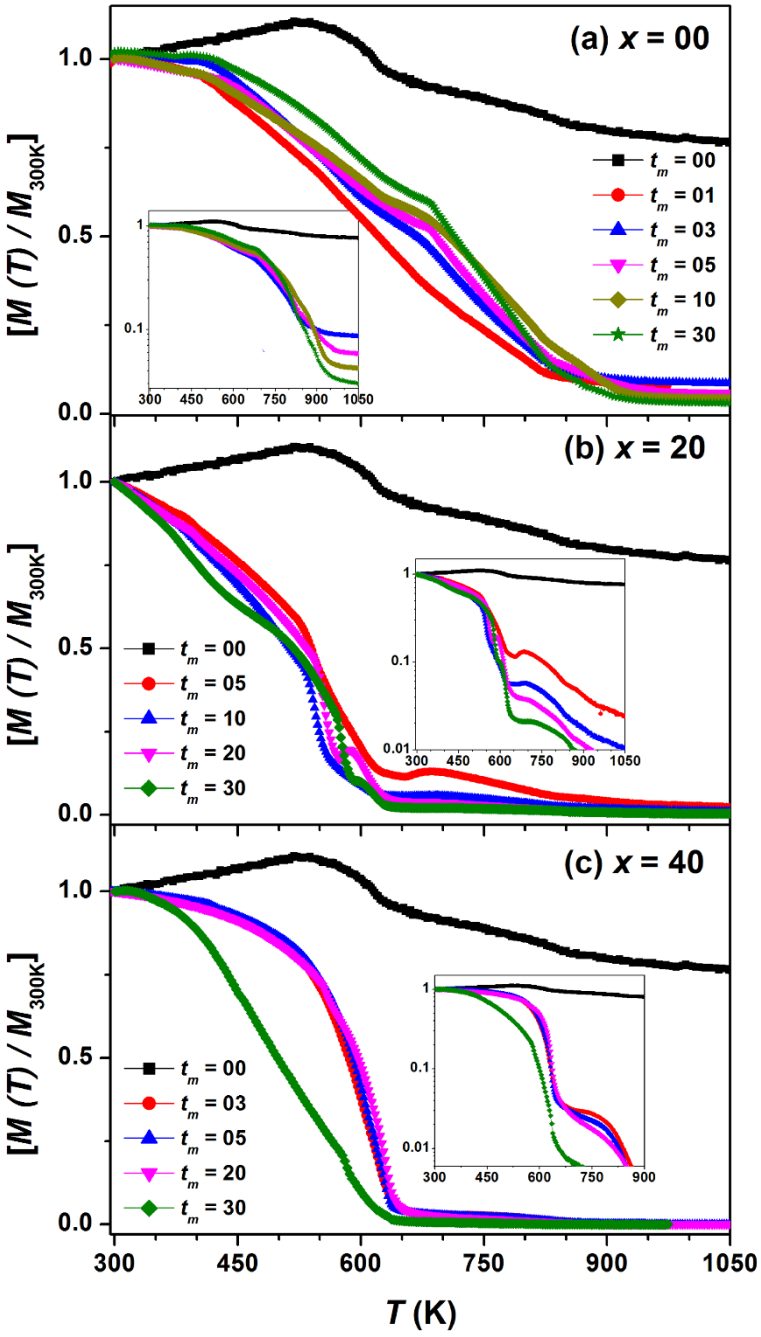

Figure 4.21: High-temperature normalized *M*-*T* curves measured under the applied magnetic field of 2 kOe for pure NiO and milled NiO-Al (*x* at.%) powders at different t_m. The inset shows the same data, but the normalized magnetization is plotted in the logarithmic scale.

Zhang *et al.* [ZHAN2009] also reported size-dependent enhanced K_{eff} of the Ni nanoparticles in the range between 1.2×10^4 J/m^3 and 6×10^4 J/m^3. High values of K_{eff} have

also been reported in other nanocrystalline systems [SHYN20152] prepared by the mechanical alloying process. However, in practice, it is impossible to separate these effects individually. Thus, the larger K_{eff} plausibly shifts the blocking temperature of such fine nanoparticles above room temperature and provides thermal stability at room temperature.

To study the nature of high-temperature FM in the milled NiO-Al powders, high-temperature *M-T* measurements were performed under the applied field of 2 kOe. Figure 4.21 illustrates the normalized *M-T* curves for un-milled and milled powders with x = 0, 20, and 40 at different t_m. The inset in the *M-T* curve is presented for the same data in the logarithmic scale for magnetization to demonstrate the relative variation of magnetization close to zero at higher temperatures. As mentioned previously, the T_N of NiO is found to be 525 K obtained from the peak maximum of the *M-T* curve of the pure un-milled NiO powder [THOT2013, RINA2016]. On the other hand, the NiO powders milled for more than 1 hr show a continuous decrease in magnetization with increasing temperature, and the temperature at which the magnetization becomes zero shifts to higher temperature with increasing t_m up to 30 hrs. Although the high-temperature magnetic phase transition (T_C) should be associated with Ni due to the formation of uncompensated surface spin, T_C is considerably large as compared to its bulk counterpart (~ 630 K). This can be attributed to the stress being induced during the ball milling process or strains due to the Ni and NiO lattice-constant mismatch arising at the interface and the competing exchange interaction between the induced FM and AFM core [LEGE1972, GORR2009]. The existence of stress is evident from the non-smooth decrease of magnetization in *M-T* curves, which acts more like hydrostatic one and hence increases T_C [LEGE1972]. Such high T_C has also been reported in Ni/NiO system [FEYG2010]. In contrast, the magnetization of the milled NiO-Al powders decreases with increasing temperature but exhibits two different magnetic phase transitions: (i) a large magnetization drop at about 640 K and (ii) a gradual decrease of magnetization up to 900 K. While the first one is due to Ni having magnetic phase transition of 630 K, the latter one is due to the magnetic phase transition of induced FM in NiO [FEYG2010, KISA20152]. The increased amount of drop-in magnetization at around 640 K suggests the existence of higher Ni content with increasing t_m, as evidenced from the structural studies. On the other hand, the nature of the magnetic phase transition of Ni in x = 40 powders is quite sharp due to the existence of a large fraction of Ni as compared to x = 20 powders. These results show good correlations between the structural, thermal, magnetic, and thermomagnetic properties of milled NiO-Al powders. Furthermore, the

process of mechanical activation on the aluminothermic reduction allows for a controlled partial reduction of NiO and hence optimized amount of Ni produced.

4.4. Summary:

We have carried out systematic studies on the effects of Al content and milling time on the structural and magnetic properties of NiO-Al nanocomposite prepared by using the high-energy ball milling route under dry milling conditions. The salient features of the current investigations are as follows:

- *In-situ* NiO-Ni-Al_2O_3 nanocomposites by the effective mechanical activation of aluminothermic reduction of NiO could be prepared by, (i) NiO-Al (*x* at.%) powders with varying x = 0-40 for a constant milling period of 30 hrs, (ii) NiO-Al (*x* at.%) powders with x = 0, 20, 40 for varying milling period of 0-30 hrs.
- Structural studies confirmed the aluminothermic reduction process of NiO with increasing *x*, which changed from the gradual type for $x < 25$ to a self-propagating combustion type for x = 40 powder.
- The milling process in bulk NiO reduced the crystallite size down to 13.5 nm without changing the structure of the face-centered cubic. Hence, the antiferromagnetic nature of bulk NiO transformed into ferromagnetic with a maximum magnetization of about 1.17 emu/g and was attributed to the induced ferromagnetism in 30 hrs milled NiO due to non-stoichiometry caused by the defects, size reduction and oxidization of Ni.
- The existence of non-stoichiometry in the milled powders was confirmed from XPS analysis.
- For Al content up to 7.5 at.%, the formation of the non-equilibrium solid-solution of NiO-Al, along with the atomic disorder, was observed. This increased the lattice parameter for Al up to 10 at.% and remained constant for higher values. The crystallite size decreased initially for Al up to 5 at.% and then increased gradually up to 25 at.% of Al.
- The ferromagnetic nature of milled NiO-Al (*x* at.%) powders enhanced slightly for a small addition of Al (2.5 at.%) due to size effect and decreased with increasing Al up to 7.5 at.% due to atomic disorder. Ferromagnetic properties were enhanced for Al addition above 7.5 at.% due to the reduction reaction of NiO by Al into Ni and

Al_2O_3. A maximum of 91% of NiO reduction with the high magnetization of 24 emu/g was observed for NiO-Al (40 at.%) powders.

- The variations of the magnetic parameters exhibited a strong dependence on the relative changes in Ni and NiO phases.
- In the case of NiO-Al (x at.%, x = 0, 20, 40) powders milled at different milling periods, the reduction of NiO occurred progressively up to a maximum of 40% for NiO-Al (20 at.%) powders with increasing milling time. This increased the magnetization gradually from 0.12 emu/g to 4 emu/g due to the increase in Ni content to 7.5%. Contrariwise, the NiO-Al (40 at.%) powder changed the reduction process to self-propagated combustion reaction type, needing a critical time of 3 hrs to ignite the reaction process. Therefore, the magnetization changed drastically to 28 emu/g with a maximum of 90% NiO reduction with a yield of nearly 52% Ni.
- The microstructural studies revealed that the formation of FM Ni in the AFM NiO matrix led to the exchange bias effect. However, the magnitude of exchange bias depends on the relative fractions of Ni and NiO phases.
- High-temperature thermo-magnetization measurements with varying milling time confirmed the presence of mixed magnetic phases in the milled NiO-Al powders, and the nature of the magnetic phase transition strongly depends on the amount of NiO reduction.
- The dynamics of mechanically activated aluminothermic reduction of NiO [NiO-Al (x at.%)] involving two different types of reaction kinetics and the resulting structural and magnetic properties are reported for the first time.
- The observed results showed a good correlation between the structural and magnetic properties of milled NiO-Al powders. The controlled reduction of NiO in NiO-Al powder mixtures under present milling conditions may find suitable applications in the fields of catalysis and ore reduction.

Chapter 5

Milling of NiO-Ti powders: Effect of Composition and Milling time

5.1. Introduction:

In Chapter 4, the detailed mechanical activation of the aluminothermic reduction of NiO was reported. We observed that the reduction kinetics changed from gradual type reaction for NiO-Al (20 at.%) powders to self-propagating combustion reaction for NiO-Al (40 at.%) powders. This succumbed to a maximum NiO reduction of 40% and 90% for x = 20 and 40 at.%, respectively, and the overall change in the magnetic properties could be precisely monitored by the change in the magnetization. A careful review of the literature summarizes that the study on the mechanochemical (MC) reduction of NiO by Al has been relatively more explored as compared to other metallothermic reduction processes in NiO [MATT1992, OLES2004, UDHA2010]. In particular, the reduction of NiO by other transition metals (TM) has been only to a few selected compositions [SETO2015, SETO2016] and the detailed analyses of the resulting magnetic properties due to the reduction reaction are still missing. Therefore, in this chapter, we present a systematic investigation on the dynamics of solid-solid MC reduction of NiO by Ti using the high-energy planetary ball milling technique under dry milling conditions and the correlative study between the structural, vibrational and magnetic properties of the nanocomposites as a function of Ti content and milling time (t_m).

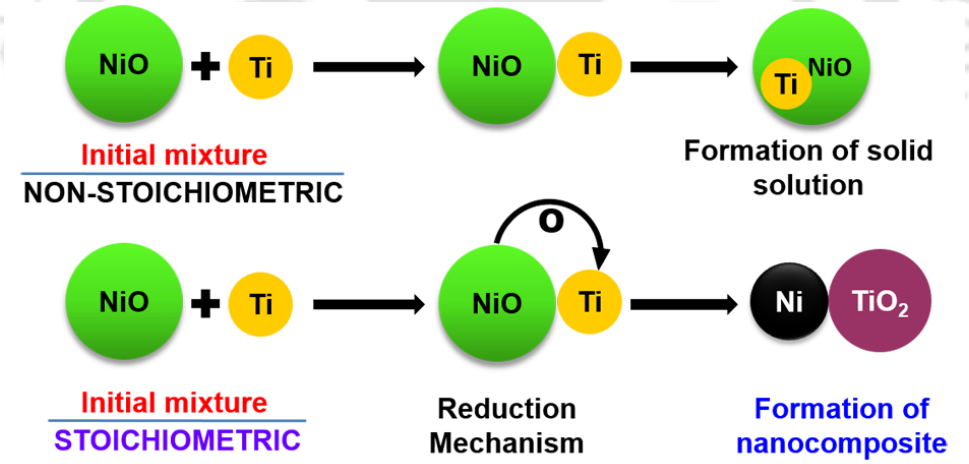

Figure 5.01: Schematic representation of the formation of NiO-Ti based solid-solution and nanocomposites.

5.2. Experimental details:

Commercially available NiO and Ti powders were obtained from Sigma-Aldrich, India, and used as the raw materials. NiO and Ti powder mixtures were taken to tune the composition

of the powders up to the stoichiometric ratio as NiO-Ti (x = 0-35 at.%) and to satisfy the reaction,

$$2NiO + Ti = 2Ni + TiO_2 \quad (5.01)$$

These powder mixers were then subjected to dry milling in a high-energy planetary ball mill (Insmart Make, India) using hardened steel vials and balls (8 mm in diameter). The powders were milled under an ambient temperature and controlled argon (Ar) atmosphere with a constant processing speed of 500 rpm and milling period (t_m) of 30 hrs. Similarly, for the milling time (t_m) dependent study, high purity NiO-Ti (x at.%) powders with x = 20 and 35 were subjected to dry milling under the Ar environment at a milling speed of 500 rpm and t_m of 0-30 hrs. To maintain a constant ball-to-powder weight ratio of 10:1 throughout the milling process, milling was processed by taking fresh samples for each t_m. The milling was programmed to pause for 15 minutes after every 15 minutes of operation to avoid excessive temperature rise in the vials. The milling parameters were optimized carefully by monitoring the structural and magnetic variations of the resulting NiO-Ti based nanocomposites.

Crystal structure and the structural parameters of the milled powders were investigated by employing X-ray powder diffraction (XRPD) obtained by using a high-power X-ray diffractometer (Rigaku TTRAX III 18 kW) with Cu-K_α radiation (λ=1.5406 Å) and having pyrolytic graphite monochromator and Silicon scintillation counter. The generator was set at 50 kV/180 mA condition. Divergence and receiving slits were kept at 2/3° and 0.3 mm, respectively. XRPD data were collected at a slow scan rate of 0.005 °/s and 100 steps per degree. The instrumental broadening was corrected using eqn. (4.02) as described in Chapter 4. The surface morphology of the powders was analyzed using the field-emission scanning electron microscope (FESEM, ZEISS SIGMA). All-inclusive elemental compositions of the powders were analyzed by energy-dispersive X-ray spectroscopy (EDS) unit attached to the FESEM. Transmission electron microscope (TEM) images and the selected area electron diffraction patterns (SAED) were collected with a JEOL 2100F and JEOL2100 TEM instrument operated at 200 kV. The sample was prepared by placing a drop of ethanol solution containing the as-milled powders onto a carbon-coated copper grid. After drying, the sample was examined by TEM. Vibrational properties at room temperature were obtained by using micro-Raman spectroscopy (LabRam HR800, Jobin Yvon), having equipped with an Olympus confocal microscope with 50× magnification for the scattered light. For the measurements, a Laser power of 17 mW and an excitation wavelength of 633 nm were used. The field and temperature-dependent magnetic properties

of the milled powders were characterized by the physical property measurement system (PPMS, Dynacool, USA) and vibrating sample magnetometer (VSM, Lakeshore 7410 USA). Thermomagnetization (*M-T*) measurements at high temperatures were recorded in an inert gas (argon) atmosphere (after pumping down to 10^{-3} Pa) during the warming cycle from 300 K to 1100 K at a constant heating rate of 4 °C/min under the constant applied magnetic field of 2 kOe.

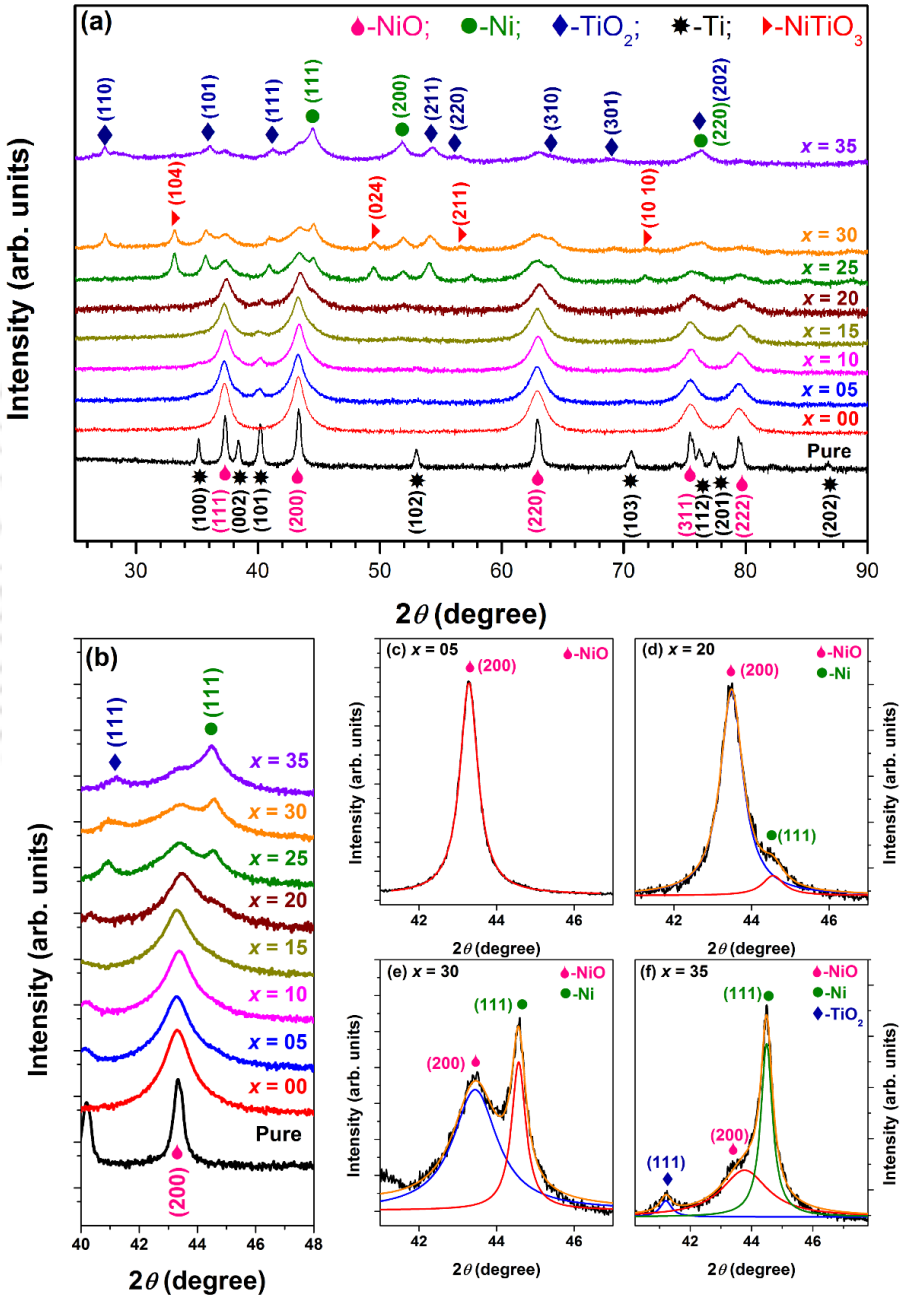

Figure 5.02: Room temperature XRPD patterns of (a) un-milled and milled NiO-Ti (*x* at.%) powders with *x* = 0 - 35, (b) expanded XRPD patterns in the range of 2θ = 40°- 48° and the multiple profile fittings of NiO(200) peak for *x* = 5 (c), 20 (d), 30 (e) and 35 (f) powders.

5.3. Results and discussion:

5.3.1. Effect of Ti content on the properties of NiO-Ti powders:

5.3.1.1. Structural properties:

Figure 5.02 depicts the XRPD patterns of pure as-mixed and milled NiO-Ti (*x* at.%) powders with *x* = 0-35 and multiple profiles fitting of selected XRPD peaks. As-mixed NiO-Ti powders exhibit sharp characteristic Bragg reflections, and all the peaks in as-mixed NiO-Ti powders can be indexed to face-centered cubic (*fcc*) NiO (JCPDS card No. 78-0423, space group $Fm\bar{3}m$) and hexagonal-close-packed (*hcp*) Ti (JCPDS card No. 44-1294, space group *P63/mmc*) without the presence of any impurity phases. On the other hand, the addition of 5 at.% of Ti in NiO powder shows Bragg peaks of *fcc* NiO and a very low intense peak of Ti(101) reflection. This could be described in terms of a possible dissolution of Ti into the NiO matrix, which enhances the NiO peak broadening and peak shift due to the increased atomic disorder and induced defects. With increasing *x* above 10 at.%, NiO(200) peak becomes asymmetric in nature and then splits into multiple peaks for *x* up to 35. The evolution of peaks corresponding to new phases is clearly displayed in Figures 5.02d-5.02f, which reveals the presence of additional peaks at 2θ = 41.23° and 44.5° corresponding to TiO_2(111) and Ni(111), respectively. In addition, the Ni(200) peak at 2θ = 52° becomes more protruding with increasing *x* due to the gradual increase of Ni, resulting from NiO reduction. This forms *in-situ* NiO-Ni-TiO_2 nanocomposites. However, for *x* = 35 powder, highly intense peaks of Ni(111), Ni(200) and Ni(220) at 2θ = 44.5°, 51.8° and 76.4° (JCPDS card No. 04-0850, space group $Fm\bar{3}m$) and the extraneous peaks at 2θ = 27.4°, 35.95°, 54.27°, 64.1°, 68.94° and 76.42° corresponding to the TiO_2 rutile (110), (101), (211), (310), (301) and (202) (JCPDS card No. 87-0710) peak positions are observed due to maximum reduction of NiO. In addition, the signs of weak Nickel Titanate ($NiTiO_3$) phases are observed for *x* = 25 and 30 powders due to *in-situ* chemical reactions during milling.

In-situ MC reactions, as described in detail in Chapter 4, are in general processed through two completely different reaction paths depending on the differences in compositions of the raw powder mixture and milling conditions: (a) If the reaction enthalpy associated with the product phase is low, then the heat generated during the reaction becomes inadequate for the sudden occurrence of the chemical reactions. Hence, the reaction takes place slowly and progresses through a very small volume during each collision of the milling balls, known as the gradual reaction process. (b) On the other hand, a self-sustaining reaction can take place when the reaction enthalpy is amply high for the

reaction to proceed itself. In particular, for the NiO-Ti powders, Gibb's free energy of formation of TiO_2 (ΔG = - 883.3 kJ/mol) is much larger than that of NiO (ΔG = - 211.7 kJ/mol) and hence the solid-state reduction of $2NiO + Ti = 2Ni + TiO_2$ is thermodynamically favored for the stoichiometric composition. Besides, the reaction enthalpy, ΔH, is highly negative and therefore a mechanically induced self-sustaining type reaction can be triggered for NiO-Ti powders during the mechanochemical processing, if $(-\Delta H^0_{298K})/(\sum C_{P_{298K}}) > 2000\ K$, where ΔH^0_{298K} is the enthalpy of the reaction and $\sum C_{P_{298K}}$ is the total heat capacity of the products at 298 K [TAKA2002]. From the thermodynamic calculation for the stoichiometric composition of NiO-Ti powder mixtures (eqn. 5.01), ΔH^0_{298K} is found to be negative at room temperature with the value of -462 kJ/mole. Accordingly, the ratio of $(-\Delta H^0_{298K})/(\sum C_{P_{298K}})$ turns out to be about 4000 K for the as-mixed stoichiometric powder [HTTP0010]. Therefore, the NiO-Ti reduction process is highly exothermic in nature, and self-sustaining kinetics during ball milling is likely to happen thermodynamically if an abundant amount of reactant (Ti) is present in the raw powder mixture. Thus, a mechanically induced self-sustaining reaction can be anticipated thermodynamically during the ball milling if the abundant amount of Ti is availed as a reactant in the as-mixed NiO-Ti powder. Hence, the reduction reaction initially follows a gradual type of reaction for $x \leq 20$ powders due to an insufficient amount of Ti in the as-mixed powders. This is supported by the structural transformations and the occurrence of partial reduction process in milled NiO-Ti powders. Upon attaining the mixtures close to the stoichiometric compositions (x = 35 at.%), the gradual reaction changes into a self-sustaining type and thus reveals self-sustaining reaction kinetics due to the MC activation of NiO-Ti powders during the ball-milling process.

The fraction of NiO reacted with Ti by the MC reduction is calculated using the integrated intensity equation, as described in the eqn. (4.03) [UDHA2010], by comparing the integrated intensity of NiO(200) peak in milled NiO-Ti powders to that of the as-mixed powders. Figure 5.03 shows the variation of NiO reduction plotted as a function of Ti content. The NiO-Ti reduction reaction initiates at x = 20 with a 9% NiO reduction followed by a maximum reduction of 73% for x = 35 powder. This is attributable to the mechanically induced self-sustaining reduction reaction due to the presence of higher Ti content in the initial NiO-Ti mixture. As a result, the dark green color of the non-stoichiometric milled NiO powder transforms into black one as a function of Ti content. Nonetheless, the conversion rate of NiO to Ni increases with increasing Ti content, which aids in achieving

a maximum reduction of 73% at an ambient temperature for x = 35 powder milled up to 30 hrs.

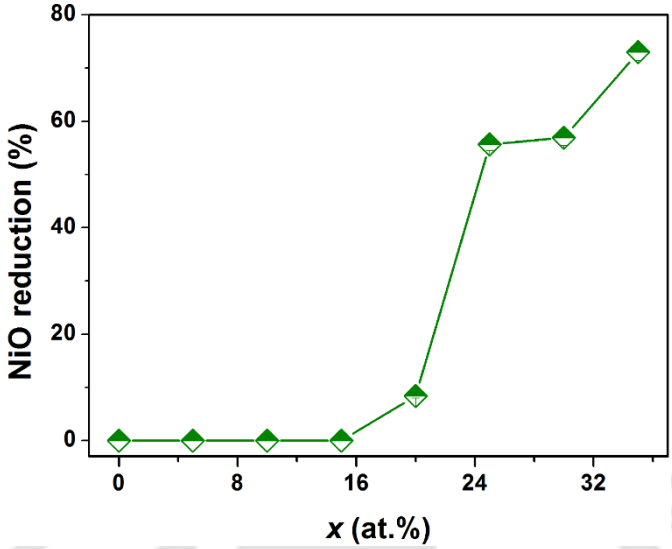

Figure 5.03: Percentage reduction of NiO as a function of Ti content in milled NiO-Ti (x at.%) powders.

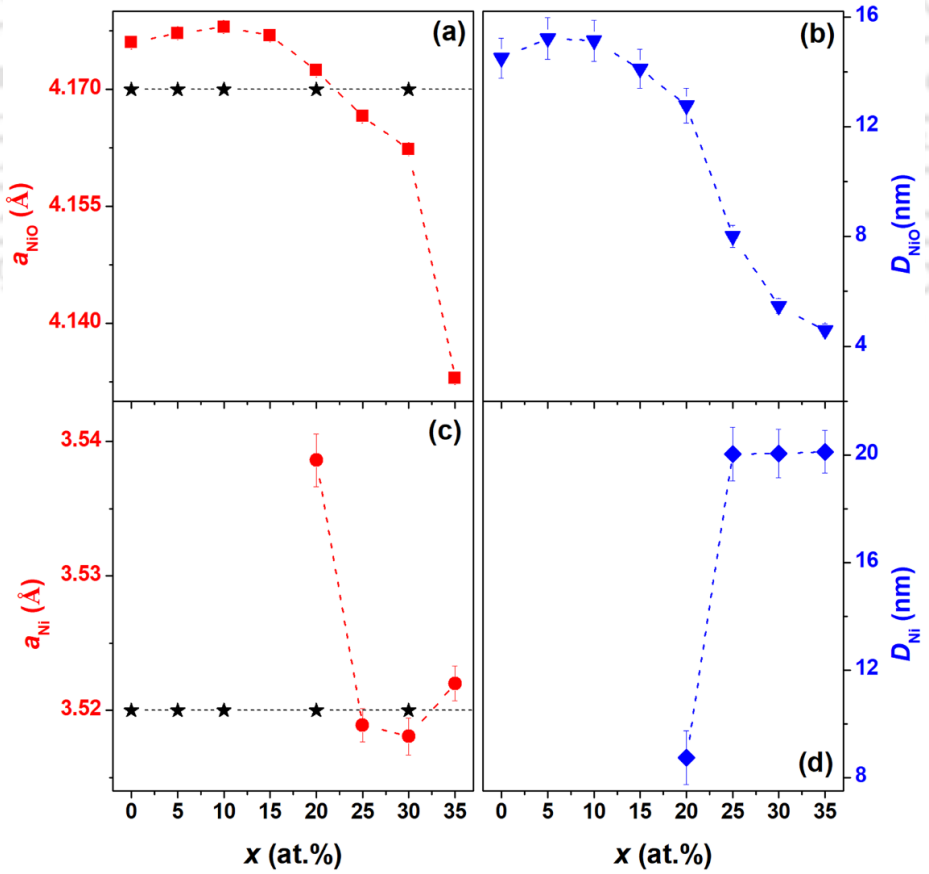

Figure 5.04: The variations of lattice constants (a_{NiO}, a_{Ni}) and crystallite size (D_{NiO}, D_{Ni}) as a function of Ti content for un-milled and milled NiO-Ti (x at.%) powders. The lattice constants of bulk Ni and NiO are also shown for comparison.

To study the effect of *in-situ* reduction of NiO on the structural properties, the respective lattice parameters (a_{NiO} and a_{Ni}), and average crystallite size (D_{NiO} and D_{Ni}) of NiO and Ni were calculated after substrating instrumental broadening, as described in the eqn. (4.02) in Chapter 4. Figure 5.04 shows the variations of a_{NiO}, a_{Ni}, $D_{NiO,}$ and D_{Ni} of as-mixed and milled NiO-Ti powders. The values of a_{NiO} and a_{Ni} for pure un-milled NiO and Ni powders, taken as 4.17 Å and 3.521 Å, respectively, are also shown in the figure for the comparison with the experimental results. The as-milled NiO powder shows a slight increase in a_{NiO} due to the presence of strain during the ball milling process [KISA2014, PADH2017]. The addition of Ti up to 5 at.% in the NiO-Ti powders shows a_{NiO} to be 4.178 Å. This is attributed to the introduction of defects during the dissolution of larger atomic-sized Ti in the NiO matrix to form the NiO-Ti solid-solution. However, with further increasing x beyond the solid solubility limit, a_{NiO} decreases down to 4.132 Å for x = 35 powder due to the reduction of NiO by Ti to form NiO-Ni-TiO_2 nanocomposite at higher x.

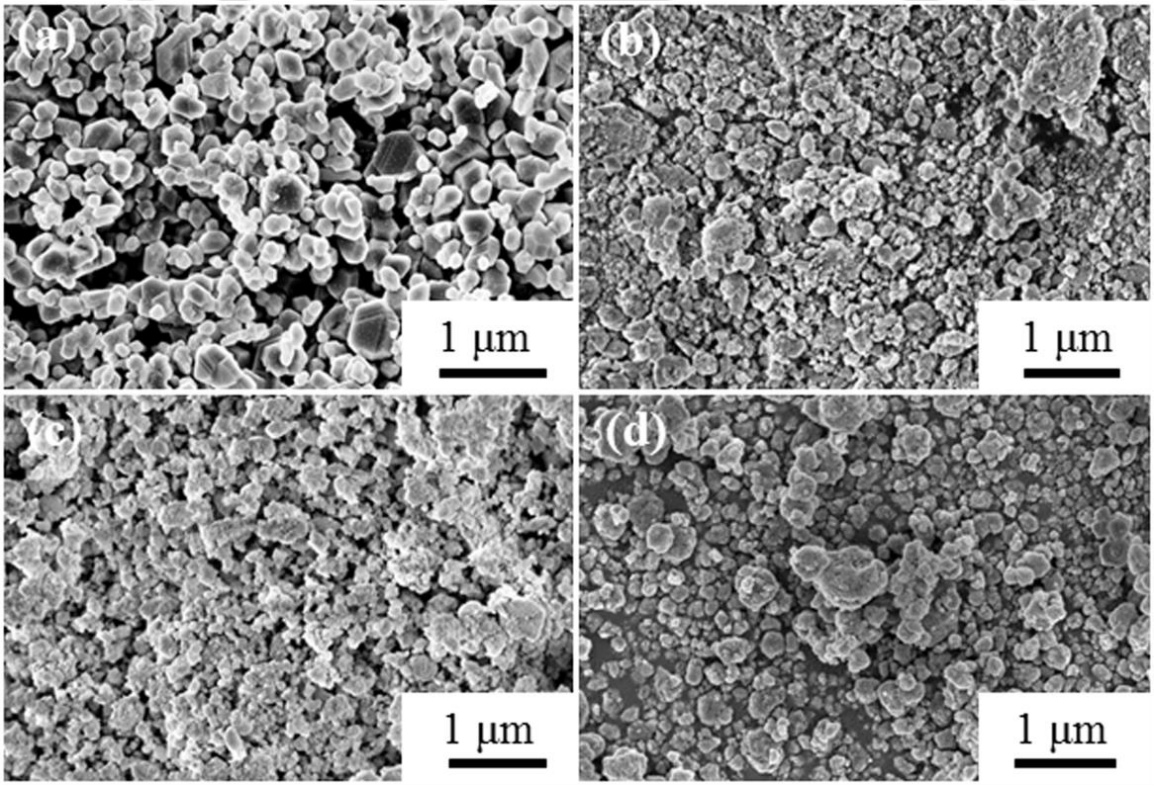

Figure 5.05: FE-SEM micrographs of as-mixed (a) and milled NiO-Ti (x at.%) powders with x = 5 (b), 10 (c), and 35 (d).

Additionally, with increasing x, a_{Ni} approaches towards the lattice parameter of bulk Ni, suggesting to the growth of stable Ni phases in NiO-Ni-TiO_2 nanocomposites. On the other hand, the value of D_{NiO} decreases from about 50 nm for un-milled NiO to 14.5 nm for the

30 hrs milled NiO powder [PADH2017]. In addition, D_{NiO} for the milled NiO-Ti powders decreases largely with increasing x and reaches to about 5 nm for x = 35 powder. Meanwhile, D_{Ni} increases from 8.7 nm to 20.2 nm with increasing x from 20 at.% to 35 at.%, respectively. This can be attributed to the increased crystallinity of Ni in the resulting *in-situ* NiO-Ni-TiO_2 nanocomposite with a maximum NiO reduction. These variations in the structural parameters clearly indicate a decrease in D_{NiO} with the simultaneous increase in D_{Ni} due to the increased NiO reduction as a function of Ti content in the resulting NiO-Ni-TiO_2 nanocomposite.

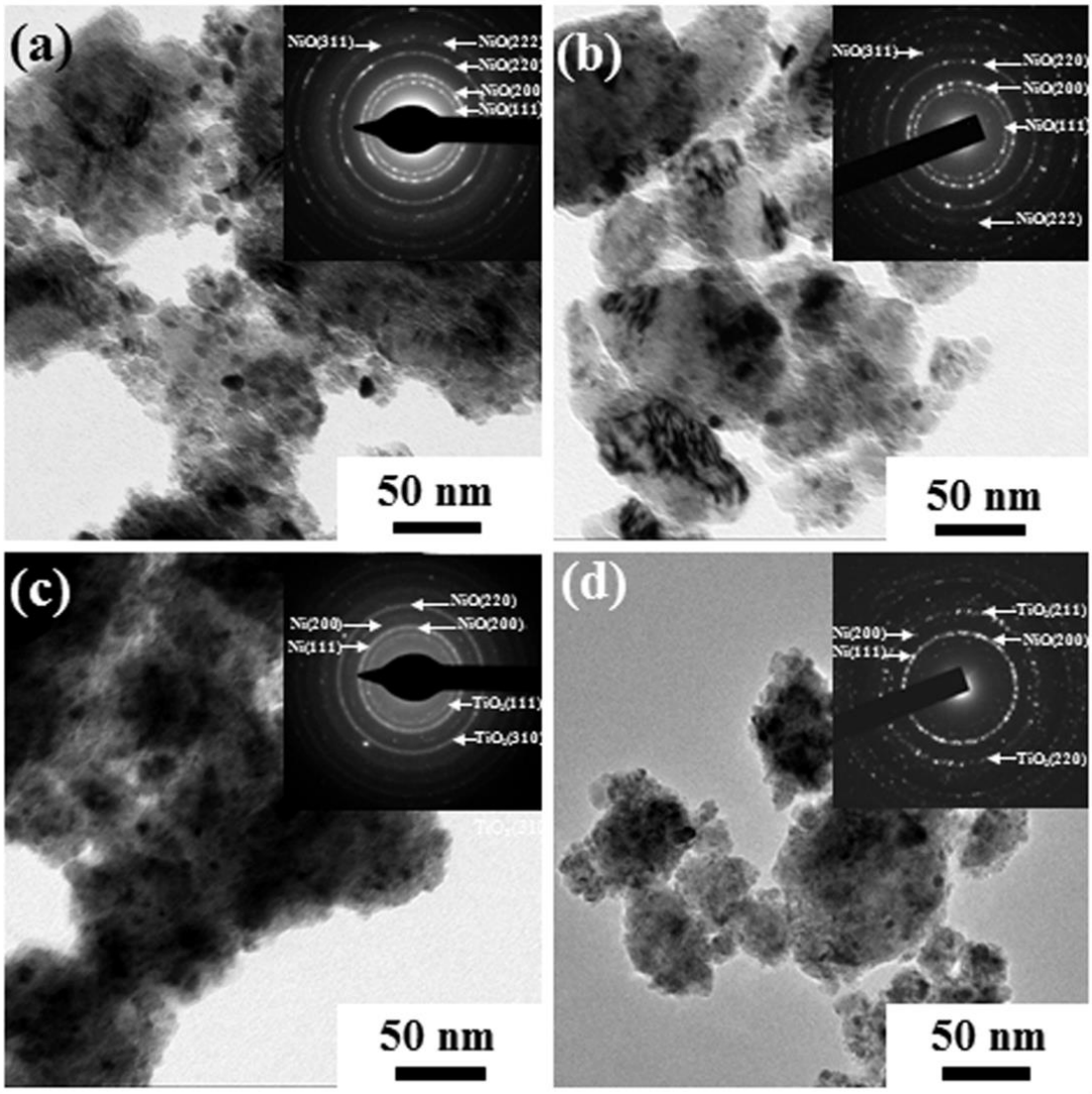

Figure 5.06: BF-TEM images and SAED patterns of milled NiO-Ti powders with x = 10 (a), 20 (b), 30 (c), 35 (d).

To elucidate the changes in the surface morphology of the milled powders with decreasing crystal size and the reduction process, FE-SEM micrographs of as-mixed and

milled NiO-Ti powders as a function of *x* have been obtained and displayed in Figure 5.05. The simultaneous compositional analysis by EDS reveals the presence of Ni, Ti, and O as the only materials in the un-milled and the 30 hrs milled NiO-Ti powders. The FE-SEM micrograph of as-mixed NiO powder shows clear particle morphology with an approximate particle size ranging between 0.5 to 1 μm. In contrast, milled NiO-Ti powders show marginally refined particles with size ranging between 100 and 150 nm due to repeated plastic deformation and cold-welding during the milling process. However, with increasing *x*, the nature of surface morphology changes from fine particles to strongly agglomerated one. This could be correlated to increased NiO reduction and the formation of NiO-Ni-TiO_2 matrix with large Ni content.

To study the evolution of nanocomposite microstructure in further detail and validate the results of XRPD, the milled NiO-Ti powders have been analyzed by the TEM technique. Figure 5.06 shows the recorded bright-field TEM (BF-TEM) image and selected area electron diffraction (SAED) patterns for milled NiO-Ti powders. The BF-TEM images of milled powders show fine nanocrystalline microstructure with irregular particle morphology, and the concentric rings in the associated SAED patterns (shown in the insets of Figure 5.06) confirm the polycrystalline nature of the samples. This is in close agreement with the XRPD results. For the milled NiO-Ti powders with $x \leq 20$ (Figures 5.06a & 5.06b), the SAED patterns show only the presence of NiO phases with fine nanosized crystals ranging between 12-15 nm without the presence of any other phases and without any evidence of NiO reduction. The variations of TEM crystallite size show a similar trend as the XRPD results, but a broader particle size distribution and irregular morphology are observed. With further increasing *x* from 20 to 35, the similar nanocrystalline behavior with irregular morphology is observed. Here, the average crystallite size decreases considerably to 7-9 nm, and the SAED patterns display continuous and diffusive rings corresponding to Ni(111) and NiO(200) phases along with the diffraction rings corresponding to TiO_2 phases. This supports the plausible formation of NiO-Ni-TiO_2 nanocomposites. These microstructural analyses are in close agreement with the XRPD results and show no evidence of any other impurity phases in the as-milled powders.

5.3.1.2. Vibrational properties:

To study the structural defects in the milled powders, Raman spectra were obtained for un-milled pure NiO, milled NiO, and milled NiO-Ti powders and presented in Figure 5.07.

Raman spectra were carefully deconvoluted by Lorentzian curve-fitting with various combinations of bands to find peak position, peak width, and area under the curves. The curve fitting of un-milled NiO reveals the observation of Raman bands in the spectral range above 350 cm^{-1}. While the bands below 1200 cm^{-1} denote the five prominent first-order and second-order Raman scattering by phonons in NiO, the bands above 1200 cm^{-1} come from the strong two-magnon (2M) scattering [MIRO2007, GAND2011, DUAN2012, GAND2013, RAVI2015].

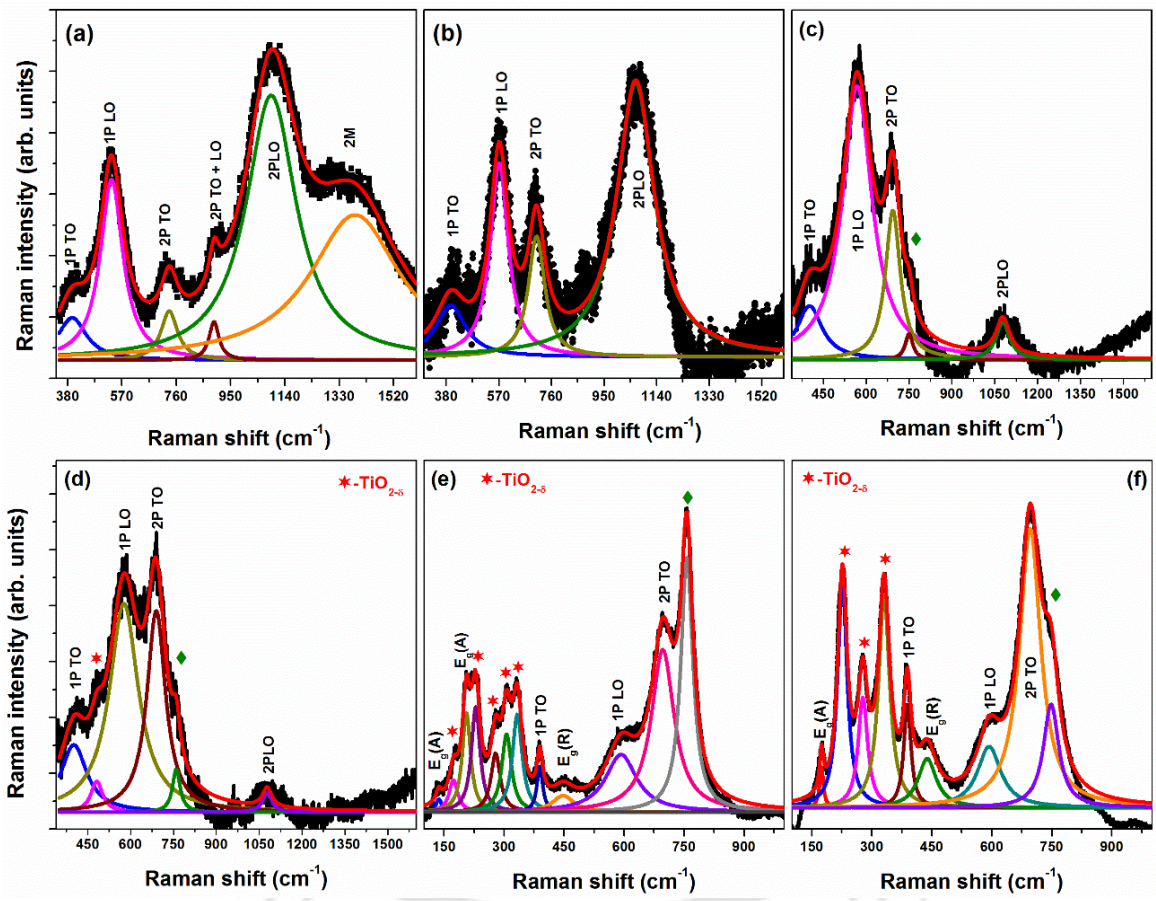

Figure 5.07: Room temperature Raman spectra of pure un-milled NiO (a) and milled NiO-Ti (*x* at.%) powders with *x* = 0 (b), 5 (c), 10 (d), 20 (e) and 35 (f).

Accordingly, the AFM ordered NiO not only has the phonon bands as, one-phonon (1P) transverse optical (TO) at 380-410 cm^{-1}, 1P longitudinal optical (LO) at 520-550 cm^{-1}, two-phonon (2P) TO at 730-780 cm^{-1}, 2P LO+TO at 900-950 cm^{-1}, 2P LO at 1050-1110 cm^{-1}, but also shows a broad and less intense peak at 1450-1500 cm^{-1} due to 2M scattering of bulk NiO. The 2M peak being the foremost feature of the Raman spectrum of NiO originates from the two-Brillouin zone-edge magnons in the AFM NiO structure, which is associated with Ni^{2+}-O^{2-}-Ni^{2+} super-exchange interaction [CAZZ2003, AYTA2017, LIUD2017].

However, for the 30 hrs milled NiO powder, the Raman spectra show the following features: (i) The 2M band disappears due to the breaking of Ni^{2+}-O^{2-}-Ni^{2+} super-exchange interaction between the neighboring Ni^{2+} ions, leading to a weaker AFM [RAVI2015]. This induces non-stoichiometry in milled NiO, which can be supported by the change in the color of the powder from pale-green to dark green [AHMA2006]. (ii) 1P LO mode becomes well pronounced and broadened, suggesting enhanced defects, surface effects, and imperfective nanostructures. (iii) 2P TO+LO mode disappears after milling. (iv) The 2P TO and 2P LO modes get broadened, and the peak positions shift towards lower wavenumber, which signifies a size induced phonon confinement effect. (v) The integrated intensity ratio between 1P LO and 2P LO modes (I_{1PLO}/I_{2PLO}) increases from 0.31 to 0.34, which indicates the existence of induced defects, surface effects, and imperfections in particle shape and size caused by the milling process. On the other hand, the inclusion of Ti up to 10 at.% alters the vibrational bands in NiO significantly. For instance, the addition of 5 at.% Ti increases the spectral intensity ratio, *i.e.*, I_{1PLO}/I_{2PLO} from 0.34 to 7.35 due to the dissolution process of NiO-Ti powders. The 2P TO mode becomes more pronounced, and a relative decrease in intensity of 2P LO spectral band is observed with increasing Ti content. This could be described by means of lowering of local symmetry at Ni^{2+}sites caused by chemical substitution and off-center displacement of Nickel ions [CAZZ2003]. With increasing *x* to 20, concerning the NiO-Ni-TiO_2 nanocomposite formed due to the reduction process, Raman bands observed at around 172 cm^{-1}, 226 cm^{-1}, 277 cm^{-1}, 330 $cm^{-1,}$ and 477 cm^{-1} correspond to the oxygen-deficient TiO_2 ($TiO_{2-\delta}$) phases [WUY2012]. Besides, the Raman spectra of anatase TiO_2 at 143 cm^{-1} and 205 cm^{-1} corresponding to E_g [denoted in figure as E_g(A)] phases and rutile TiO_2 at around 448 cm^{-1} corresponding to E_g [denoted in figure as E_g(R)] phase are observed [FRAN2012]. These findings not only show good agreement with the results of XRPD analysis but also confirm the formation of no other impurity phases in the as-milled powders.

5.3.1.3. Magnetic properties:

The field and temperature-dependent magnetic measurements were carried out to determine the correlation between the nanostructural evolution and the magnetic properties of the resultant nanocomposites. Figure 5.08 presents the room temperature initial magnetization (*IM*) curves and *M-H* loops of un-milled NiO, as-mixed, and milled NiO-Ti powders

measured up to a maximum applied field of ±50 kOe. To analyze the actual variation of magnetization close to origin evidently, the *IM* curves are plotted in the logarithmic scale.

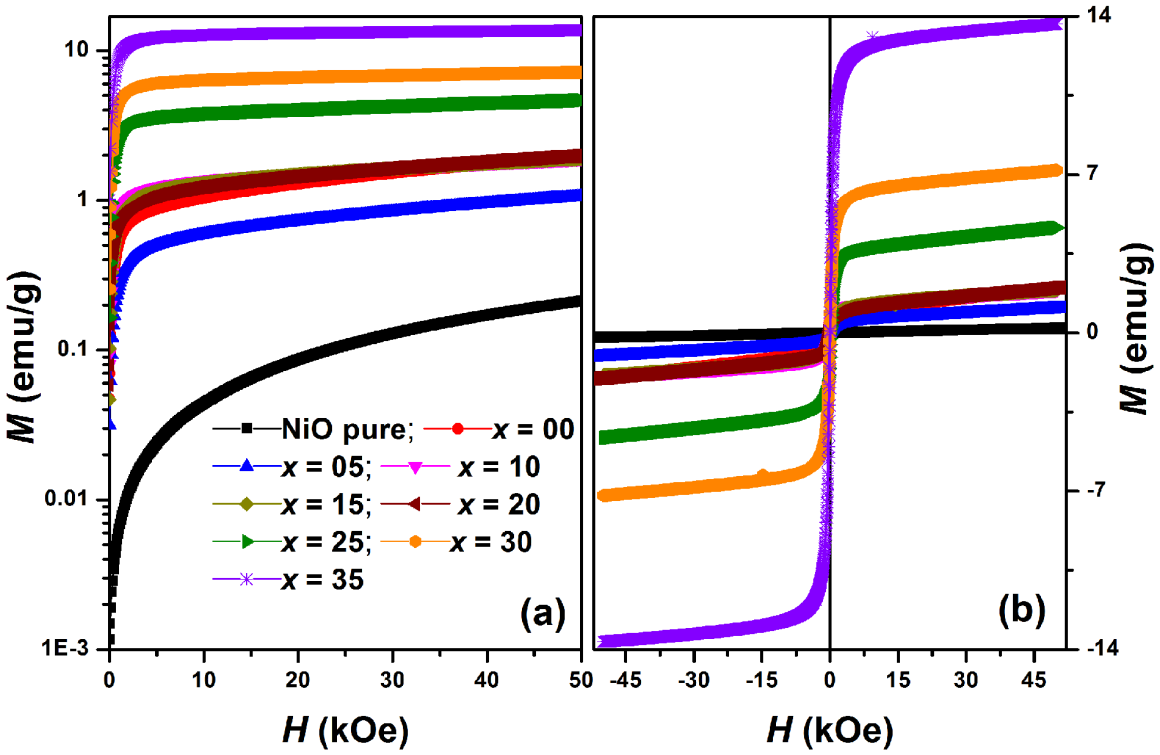

Figure 5.08: Room-temperature initial-magnetization (*IM*) curves (a) and magnetic hysteresis (*M-H*) loops (b) for NiO-Ti (*x* at.%) as a function of Ti content. *M-H* loop of pure NiO without milling is also shown for the comparison.

The extracted parameters, such as magnetization at 50 kOe (M_S) and coercivity (H_C) from the *M-H* loops, are plotted as a function of Ti content in Figure 5.09. It is observed that (i) As-mixed NiO-Ti powders exhibit a weak and almost linear magnetic response to the applied field with zero H_C due to the AFM nature of NiO. Hence, the loop passes through the origin. (ii) 30 hrs milled NiO powder exhibits an unlike response to the applied field, *i.e.*, the magnetic moment increases rapidly at the lower applied field, followed by a progressive variation at the higher field regime. The loop does not pass through the origin and therefore prompts a clear hysteresis loop with a considerable M_S of about 1.96 emu/g and H_C of 155 Oe. This confirms the presence of room temperature ferromagnetism (RTFM) in milled NiO powder. (iii) For $x = 5$ powder, the *M-H* curve shows a cognate feature as that of milled NiO, but a significant decrease in M_S from 1.96 emu/g to 1.07 emu/g is abided. (iv) For $x > 5$ powders, M_S increases progressively and reaches a maximum of 13.7 emu/g for $x = 35$ powder. The rate of increase in magnetization increases for $x > 20$. (v) On the

other hand, H_C decreases initially from 155 Oe to 71 Oe with increasing x from 0 to 15 and then increases suddenly to 147 Oe for x = 35 powder.

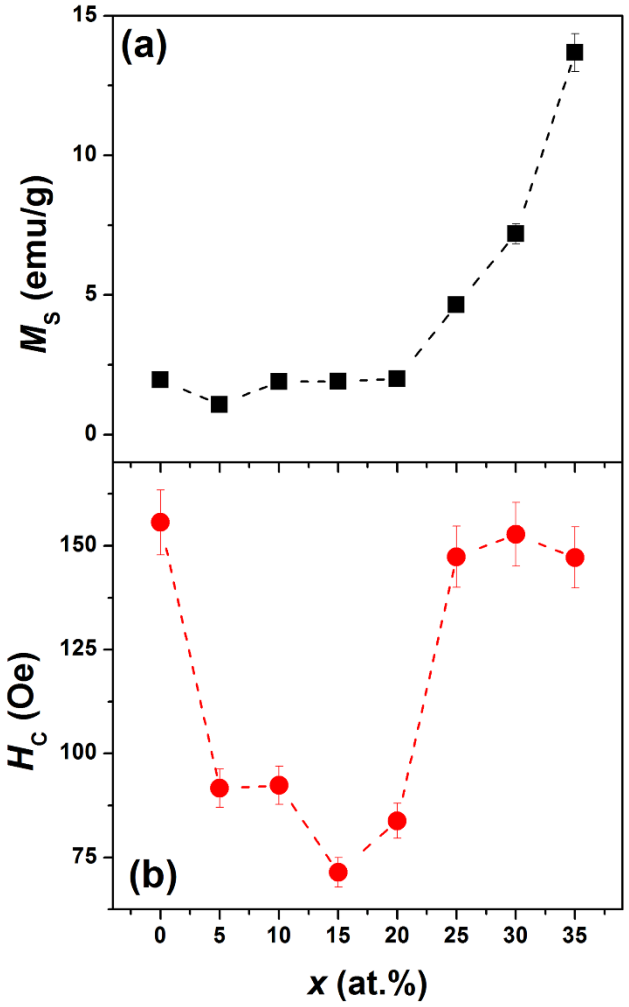

Figure 5.09: Variations of magnetization (M_S) (a) and coercivity (H_C) (b) as a function of Ti (x at.%) content in NiO-Ti powders.

To correlate the effect of Ti substitution and the NiO reduction on the magnetic behavior of milled NiO-Ti powders, the structural and magnetic behavior of the NiO-Ni-TiO_2 nanocomposites are compared in details. Un-milled NiO, due to the dominating 180° super-exchange interaction between the next-nearest-neighbor Ni atoms giving a typical type-II AFM arrangement, showed with no *M-H* loop and zero H_C [KISA2014, SHAH2017]. Contrariwise, the 30 hrs milled NiO exhibit RTFM due to the breaking of Ni^{2+}-O^{2-}-Ni^{2+} super-exchange interaction caused by large crystallite size reduction, the formation of defects, lattice distortion, broken bonds and oxidization of Ni^{2+} to Ni^{3+} ions, *etc*. [AHMA2006, MIRO2007, GAND2011]. As a consequence, the alignment of net magnetic moments occurs at a lower magnetic field region with an unsaturated moment of

1.96 emu/g, and a large H_C of 155 Oe for the applied field of 50 kOe [SHAH2017]. With adding x up to 5 at.%, M_S and H_C decrease to 1.07 emu/g and 92 Oe, respectively, due to the dissolution of non-magnetic Ti, which dilutes the induced FM properties of milled NiO-Ti powder. On further increasing $x > 20$, M_S and H_C increase largely to 13.7 emu/g and 147 Oe, respectively, due to the significant increase in Ni nanocrystals with increasing x in the NiO-Ni-TiO_2 nanocomposite. This ferromagnetic behavior could only be accredited to a stronger magnetic interaction between nanocrystalline FM Ni and AFM NiO matrix in the NiO-Ni-TiO_2 nanocomposites [MAKH2008, KRIS2016].

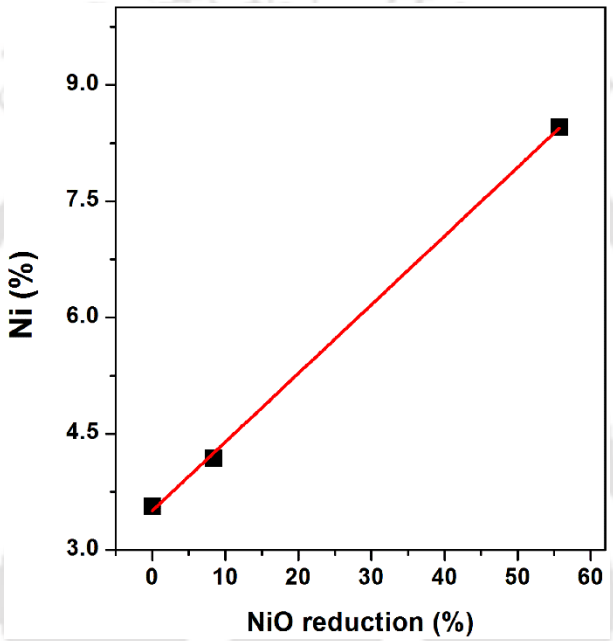

Figure 5.10: Relation between the percentage of Ni and the percentage of NiO reduction for 30 hrs milled NiO-Ti powders.

The correlation between the structural and magnetic properties in the milled powders can also be established by (i) quantifying the percentage of Ni in the milled powders obtained by comparing the magnetization of milled powders with respect to the saturation magnetization of bulk Ni (~55 emu/g) and (ii) calculating the percentage of NiO reduction from the XRPD pattern [WUSH2003]. Figure 5.10 depicts the relation between the percentage of NiO reduction obtained from the XRPD analysis and the attained Ni fraction from the correlative saturation magnetization in the NiO-Ni-TiO_2 nanocomposites. It is observed that milled NiO powder has about 3.56 wt.% Ni enriched spatial regions due to the presence of considerable uncompensated surface spins as compared to the AFM particle core. The comparison between the percentage of Ni and NiO reduction shows that all the

data fall into almost a linear correlation. The straight-line fit to the data reveals that the Ni% in milled NiO-Ti powders increases at a rate of 0.09% per NiO% reduction in the currently investigated samples.

It may be noted that milled NiO-Ti powders show Ni crystallites in the size regime of 8-20 nm, which is within the superparamagnetic critical size limit of single-domain spherical Ni particles [BALA2004]. Hence, the observed FM behavior at room temperature is expected, if the overall anisotropy of milled NiO-Ti powders is higher than bulk Ni anisotropy, which can shift the blocking temperature towards high-temperature regions and provide thermal stability to the nanoparticles.

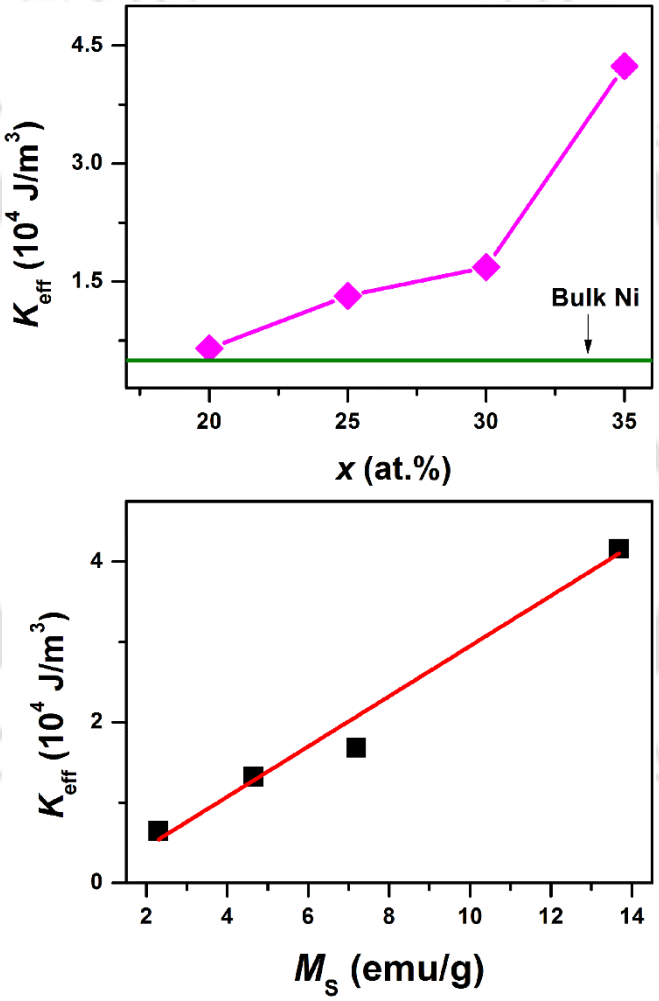

Fig 5.11: Variations of K_{eff} as a function of Ti content (top) and saturation magnetization (bottom), M_S for milled NiO-Ti (x at.%) powders.

Therefore, the obtained FM behavior in milled powders can be explained in terms of various contribution of anisotropies such as (1) surface anisotropy due to increased surface contribution through the large crystallite size refinement [WINK2005, MENE2010], (2)

shape anisotropy due to the uneven morphology of the milled powders [SKOM2003] as confirmed from Figure 5.05 and 5.06, (3) strain anisotropy as the milled powders are subjected to large deformation and cold welding of the powders inside the milling vials and (4) exchange anisotropy due to coexisting coupling between the FM Ni and AFM NiO [SKUM2003, SORT2004, LIS2006, DETO2015]. The values of K_{eff}, deduced from the law of approach to saturation magnetization [KRON2003, MAJ2017] as stated in eqns. (4.05) and (4.06), are depicted in Figure 5.11. The obtained values of K_{eff} are found to be varying in the range of 0.65-4.3×10^4 J/m^3, which is much higher than that of bulk Ni (0.5× 10^4 J/m^3) [ZHAN2009] and is comparative to the K_{eff} of milled NiO-Al powders. The linear variation of K_{eff} with magnetization confirms the single-domain type ferromagnetic Ni with enhanced magnetic anisotropy.

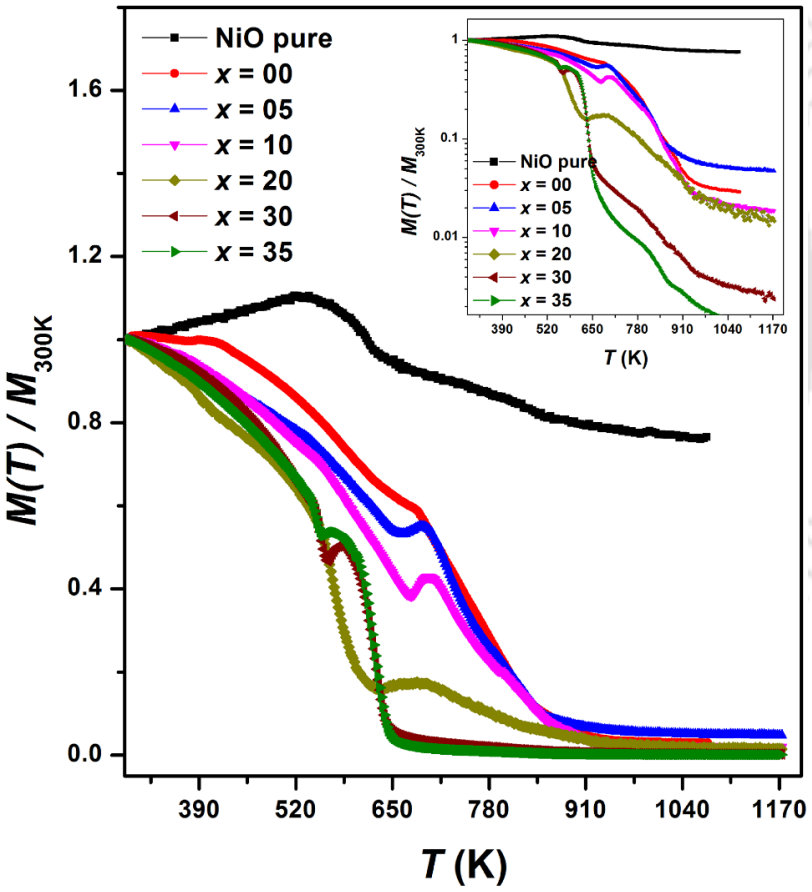

Fig 5.12: High-temperature normalized *M-T* curves measured under the applied field of 2 kOe for NiO and milled NiO–Ti (*x* at.%) powders. The inset shows the same data, but the normalized magnetization is plotted in the logarithmic scale.

To study the effect of particle size variation and the impact of reduction on the FM stability of the milled NiO-Ti powders, temperature-dependent magnetic (*M-T*)

measurements were carried out under an applied field of 2kOe over a temperature range of 300 K - 1050 K. To summarize all the *M-T* curves and to have a direct comparison, normalized magnetization [$M(T)/M_{300K}$] of the *M-T* curves are plotted in *y*-axis in Figure 5.12. To demonstrate the thermal evolution of magnetization at the high-temperature regime close to zero, the same curves have been plotted in the logarithmic scale in the inset. The magnetization of un-milled NiO increases progressively with an increase in temperature up to 525 K and then decreases above 525 K. This forms a peak at 525 K in the *M-T* curve, which is attributed to the Néel temperature (T_N) of NiO. This is in good agreement with the earlier reported results [THOT2013, RINA2016]. On the contrary, the 30 hrs milled NiO powder shows a gradual decrease in magnetization with increasing temperature and approaches to zero at around 900 K. The thermal derivative of magnetization curves ($dM/dT \sim T$) exhibits two magnetic transitions: (i) one close to T_N due to the AFM NiO core and (ii) another one at 780 K, due to the induced FM phase transition (T_C) of the uncompensated surface spins. The value of T_C (~ 780 K) is quite high (>150 K) than that of the bulk Ni (~630 K). This is attributed to the presence of large internal stress accumulated due to mechanical milling or the strain generated due to the interfacial Ni-NiO lattice mismatch and the exchange interaction between FM Ni, and AFM NiO induced FM phase-AFM core interaction. The non-smooth decrease of magnetization in the *M-T* curve evidences the release of stresses with increasing temperature. However, the milled NiO-Ti powders show different behaviors as compared to the bulk NiO and milled pure NiO powder. It is observed that (i) The magnetization decreases gradually with increasing temperature up to 700 K. (ii) With further increasing temperature, the magnetization increases suddenly, forming a peak in the curve, and then decreases gradually to nearly zero magnetization. The strength of the magnetization peak reduces, and the peak width broadens with increasing *x* from 5 to 20. These results suggest that the decrease of magnetization in the *M-T* curves around the T_N of bulk NiO is related to the origin of enhanced T_B of the Ni particles due to the enhanced exchange coupling between AFM NiO and FM Ni inducing large K_{eff}. Besides, as the temperature increases, the NiO matrix becomes paramagnetic, and hence the stabilization of FM Ni by AFM NiO through the exchange coupling is lost, leading to a decrease in magnetization [SORT2004, DETO2015]. To understand the origin of the t_m dependent peak in *M-T* curves, the as-milled powders are heated up to three different temperatures [below the peak position (T_{below}), at the peak maximum (T_{max}) and at 950 K (T_{950K})] by following the same heat treatment procedures of *M-T* measurement described in the experimental

section. The structural variations of as-milled and heat-treated powders were analyzed by obtaining XRPD patterns at room temperature. The observed results reveal that the temperature-induced NiO reduction process with the available unreacted Ti takes place, and the development of Ni initiates at T_{below} followed by the growth at T_{max} and the nearly complete reduction of NiO along with the formation of TiO_2 and Ni at T_{950K}. This temperature-induced irreversible structural change provides a maximum in the *M-T* curve. With increasing $x > 20$, due to the formation of nanocrystalline Ni as confirmed from the structural studies, a sharp magnetic transition is obtained at 645 K. This matches with T_C of bulk Ni. Interestingly, with increasing *x*, the magnitude of magnetization dropping at 645 K increases largely at the expense of magnetization, decreasing gradually at higher temperatures. This is majorly due to the enhanced NiO reduction at higher Ti content to yield large Ni fraction in the NiO-Ni-TiO_2 nanocomposites.

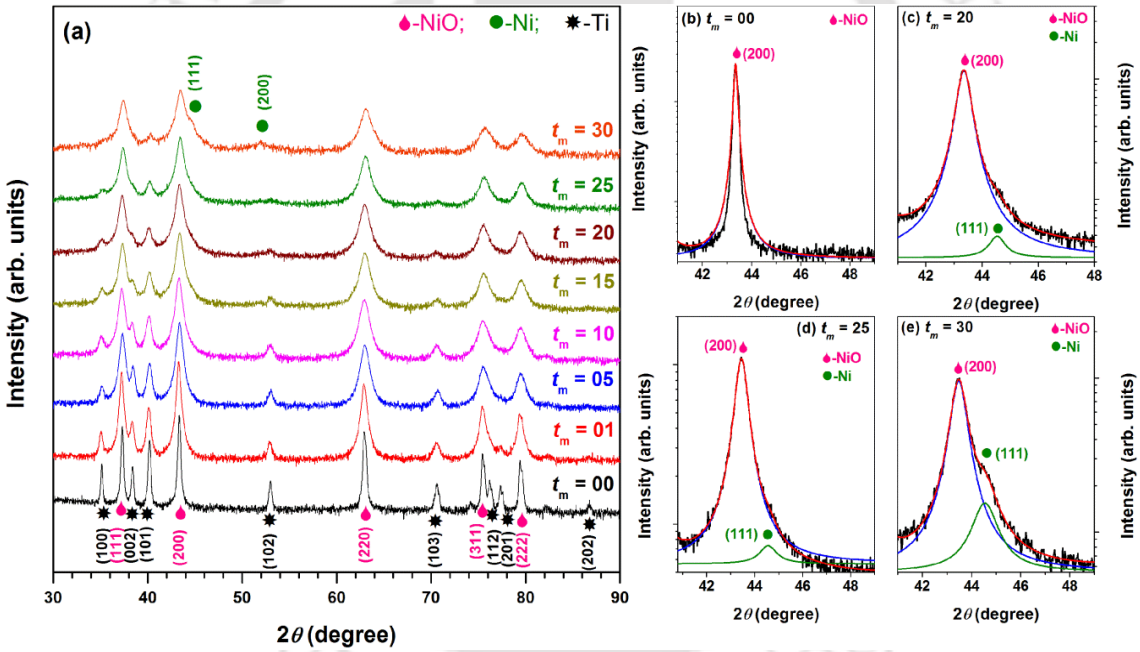

Figure 5.13: Room temperature X-ray powder diffraction patterns of as-mixed and milled NiO-Ti (x = 20 at.%) powders as a function of t_m and profile fitting of selected diffraction peaks.

5.3.2. Dynamics of milling on the properties of NiO-Ti powders:

In the following section, we present the study of structural, vibrational, and magnetic properties of NiO-Ti (x at.%) powders as a function of milling time for the selected Ti contents to discuss the dynamics of NiO reduction by Ti.

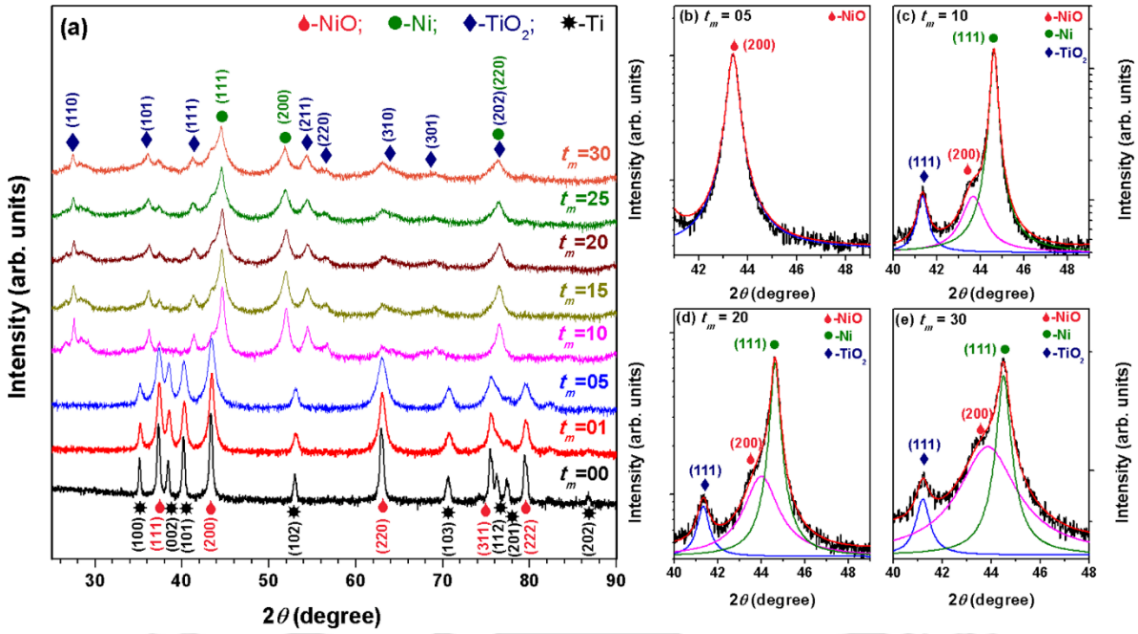

Figure 5.14: Room temperature X-ray powder diffraction patterns of as-mixed and milled NiO-Ti (x = 35 at.%) powders as a function of t_m and profile fitting of selected diffraction peaks.

5.3.2.1. Structural properties:

Figure 5.13 depicts the characteristic XRPD patterns of as-mixed and milled NiO-Ti (x = 20 at.%) powders as a function of t_m along with profile fitting of selected diffraction peaks of NiO-Ti powders. As the structural evolutions rely on x and t_m, milling is carried out separately for x = 20 and 35 powders. All the reflections in the XRPD patterns of the as-mixed powders can be indexed to *fcc* NiO (JCPDS card No. 78-0423, space group $Fm\bar{3}m$) and *hcp* structure Ti (JCPDS card No. 44-1294, space group *P63/mmc*). For x = 20 powders, it is observed that (i) the intensities of NiO and Ti-peaks decrease gradually with increasing t_m. (ii) Up to t_m = 15 hrs, the diffraction peaks of *fcc* NiO dominate the pattern, which reveals the possible dissolution of Ti in the NiO matrix. The peaks are also considerably broadened due to a significant size refinement. (iii) For t_m > 15 hrs, the intensities of NiO peaks decrease further along with the observation of minor peaks at 2θ = 44.5° and 51.8° corresponding to *fcc* Ni(111) and Ni(200), respectively (JCPDS card No. 04-0850, space group $Fm\bar{3}m$) [UDHA2010]. This confirms to the initiation of Ti activated NiO MC reduction beyond 15 hrs, which results in the formation of nanocrystalline Ni. (iv) Moreover, for t_m > 15 hrs, the intensity of Ni peaks increases gradually with increasing t_m revealing a gradual NiO-Ti reduction process. No evidence of additional phases was found

from the powder-diffraction data or by the compositional analysis via EDAX spectra. As shown from the profile fits (Figures 5.13b-5.13e), the clear evolution of Ni(111) as a shoulder peak of NiO(200) peak is observed. The color change of the powders from pale-green to black color after t_m = 15 hrs provides further proof for the non-stoichiometric NiO formed by the presence of defects, size refinement, broken Ni-O-Ni bonds and the gradual reduction of NiO into Ni [PADH2017].

Figure 5.14 displays the XRPD patterns of the NiO-Ti (35 at.%) powders prepared at different t_m along with profile fitting of selected diffraction peaks of NiO-Ti powders. It is seen that (i) up to t_m = 5 hrs, the NiO and Ti peak intensities decrease considerably, suggesting a refinement process. (ii) Interestingly at t_m = 10 hrs, NiO reduction occurs in a remarkable manner, resulting in pronounced Ni and TiO_2 phases and hence forms an *in-situ* nanocomposite (Figure 5.14c) (iii) For t_m > 10 hrs, a gradual diminishment of NiO(200) and NiO(311) peaks is observed along with a successive growth of Ni(111) and Ni(220) peaks, respectively. (iv) However, the Ni peaks show a considerable peak broadening and decreased peak intensity with increasing t_m from 10 to 30 hrs. These results evidence that the NiO MC reduction in x = 35 powders is comparatively instantaneous and rapid with a shorter t_m required for the reduction to proceed as compared to x = 20 powder.

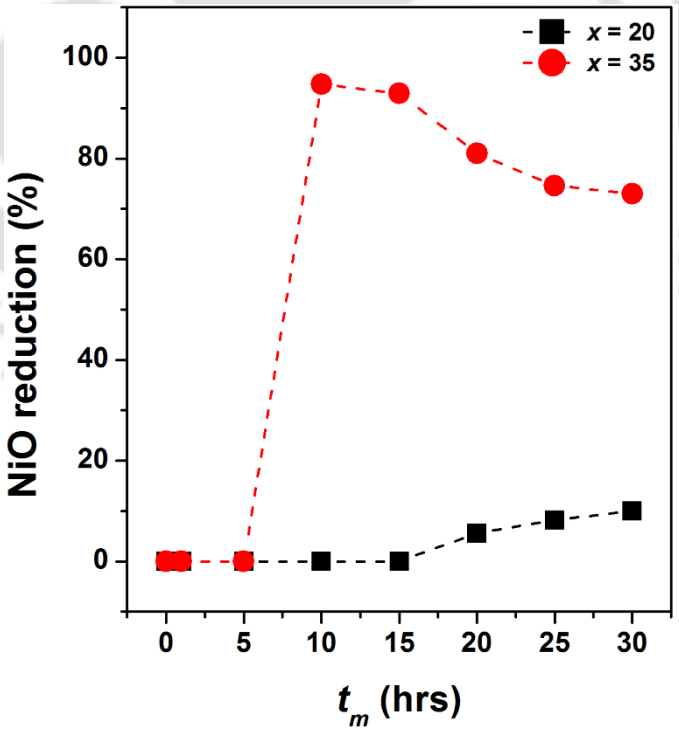

Figure 5.15: Percentage of NiO reduction of as-mixed and milled NiO-Ti (x at.%) powders as a function of milling time (t_m).

The fraction of NiO reacted with Ti by the MC reduction is calculated using the integrated intensity equation [UDHA2010] and shown in Figure 5.15. It is observed that for x = 20 powders, the fraction of NiO reacted increases gradually with increasing t_m, suggesting to a gradual reaction kinetics and reaches to a NiO reduction of about 10% for t_m = 30 hrs. The smaller fraction of NiO reduction in x = 20 powders implies the presence of a lesser amount of Ti in the as-mixed powders, which results in the retention of a comparatively higher quantity of NiO in the resulting nanocomposites. Contrariwise, for x = 35 powders, the maximum NiO reduction of 94% is observed at t_m = 10 hrs due to the ignition of the self-sustaining reduction process in the presence of a sufficient amount of Ti being availed for the almost complete NiO reduction. However, this value decreases with further increasing t_m, and a NiO reduction of 73% is observed for t_m = 30 hrs. Henceforth, it can be concluded that the kinetics of the MC reduction under the current milling conditions strongly depends on the variations of t_m and Ti content in the NiO-Ti powders. These results can also be confirmed from the thermodynamic calculations adopted for the Ti content variation study where the ratio of $(-\Delta H^0_{298K})/(\sum C_{P_{298K}})$ in as-mixed stoichiometric NiO-Ti powder is calculated to be around 4000 K suggesting to the highly exothermic nature of NiO-Ti reduction process. Hence, a gradual type reduction takes place for NiO-Ti (20 at.%) powders due to the insufficient amount of Ti being present in the as-mixed powders, which is mostly incorporated into the NiO matrix and is inadequate enough to start a chemical reaction instantaneously. On the other hand, NiO-Ti (35 at.%) powder having a stoichiometric mixture shows a self-sustaining type of reaction due to the MC activation process and a critical t_m of 10 hrs is needed for the ignition of the self-propagating reaction. This thermodynamic assessment is clearly supported by the structural transformations occurring in milled NiO-Ti (x = 20, 35) powders and also agrees well with the previously reported Ti-Ni-O phase diagram [SEKI2009].

To analyze the structural refinement, the crystallite size of NiO (D_{NiO}) was estimated from the experimental XRPD pattern after subtracting the instrumental broadening contribution. Figure 5.16 shows the variations of D_{NiO} of the milled NiO-Ti powders as a function of t_m and Ti content. For x = 20 powders, the value of D_{NiO} is found to decrease largely from around 50 nm of as-mixed NiO-Ti powder to about 19.7 nm at t_m = 5 hrs followed by a gradual decrease to about 12 nm for t_m = 30 hrs. Meanwhile, for x = 35 powders, D_{NiO} follows an almost similar trend as x = 20 powders, but with a significant reduction in D_{NiO} to about 10 nm after 30 hrs of milling. Moreover, the crystallite size of Ni

(D_{Ni}) for x = 20 powder is calculated to be 12.8 nm after 30 hrs of milling due to the gradual reduction of NiO to form nanocrystalline Ni. D_{Ni} reaches up to 27.5 nm for x = 35 powder after 10 hrs of milling and then gradually decreases to around 20 nm for t_m = 30 hrs.

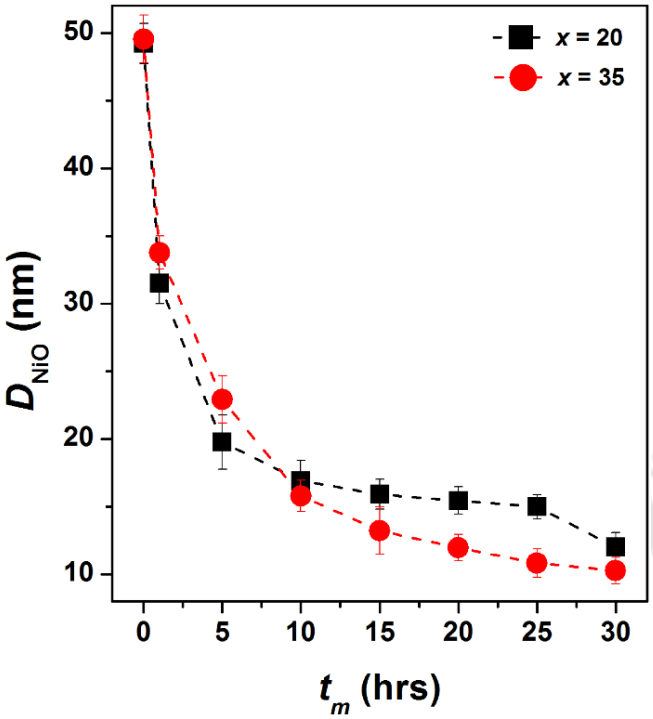

Figure 5.16: Variations of crystallite size of NiO (D_{NiO}) of NiO-Ti (x at.%) powders as a function of milling time (t_m).

The observation of milling time dependence of D_{Ni} is rather interesting. Doppiu *et al.* [DOPP2004] reported that the value of D_{Ni} in ball-milled NiO powders under hydrogen atmosphere at a ball-to-powder weight ratio of 12:1 increases initially from 7 nm to about 13 nm with increasing t_m up to 4 hrs and then remains nearly constant for further increase in t_m to 12 hrs despite observing considerable NiO reduction. Such variation was attributed to two competitive effects, which take place simultaneously: (a) the continuous milling process tends to reduce the crystallite size and (b) the progressive development of Ni nanocrystals during the milling due to the reduction of NiO. The competition between these two effects determines the properties of the final nanocomposites [DOPP2004, KREM2012].

In the present investigation, close observation of Figure 5.14a reveals that with increasing t_m > 15 hrs, the Bragg reflections of Ni not only exhibit a considerable broadening but also show a significant reduction in intensity. This confirms that the formation of Ni with the size of 27.5 nm from the maximum reduction of NiO (~94%) at t_m = 10 hrs is

progressively reduced at longer t_m due to the dominating effect of the milling to reduce the crystallite size over the nearly completed nature of reduction process of NiO.

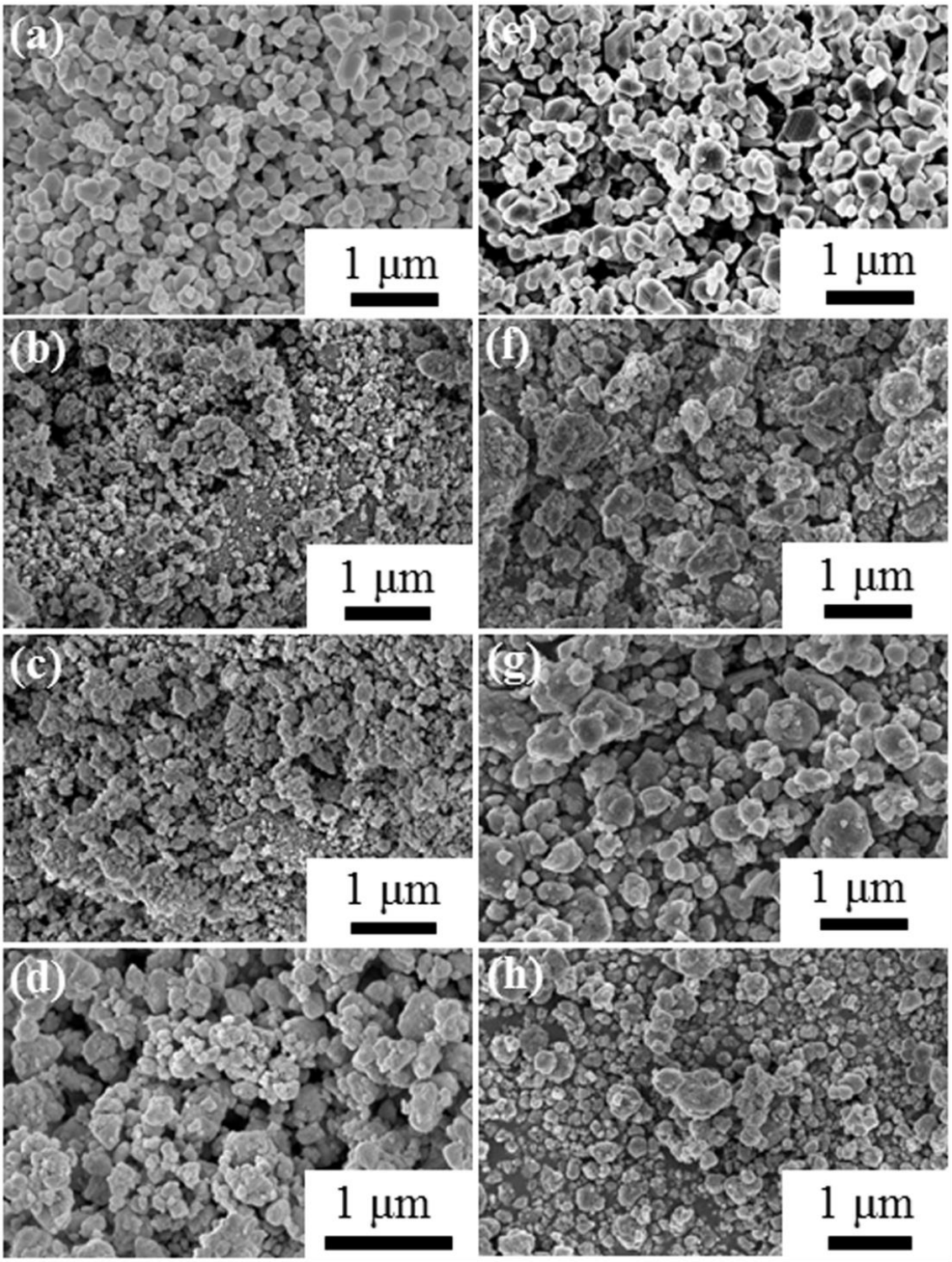

Figure 5.17: FESEM micrographs of NiO-Ti (x at.%) powders milled at different t_m [(a) x=20, t_m= 0; (b) x=20, t_m=10; (c) x=20, t_m=20; (d) x=20, t_m=30 and (e) x=35, t_m= 0; (f) x=35, t_m=10; (g) x=35, t_m=20 and (h) x=35, t_m=30].

This is also justifying the possible decrease of degree of reduction of NiO at longer t_m as displayed in Figure 5.15. The determined lattice parameter of NiO (a_{NiO}) decreases with increasing t_m for both x = 20 and 35 milled powders and reaches down to 4.163 Å and 4.133 Å after 30 hrs of milling for x = 20 and 35, respectively. This can be attributed to the introduction of structural defects, oxygen vacancies, dissolution of Ti in the NiO matrix, and reduction of NiO during the MC reduction process and is in close agreement with earlier reports on similar systems [PECK2012, DOPP2014]. On the other hand, Kremenovic *et al.* [KREM2012] and Gandhi *et al.* [GAND2013, GAND2016] reported grain surface relaxation effect due to lattice expansion with decreasing the size of the NiO. The observed changes in the structural parameters could be well accredited to t_m dependent MC reduction of NiO, which drastically changes the dynamics of formation of the *in-situ* nanocomposites with different fractions of elemental phases and effectively reduces the crystallite size of NiO in comparison with the 30 hrs milled NiO as reported previously [PADH2017].

Figure 5.17 displays the FESEM micrographs of as-mixed and milled NiO-Ti powders as a function of t_m and Ti contents. The micrographs clearly illustrate the morphological changes of the milled powders as compared to its massive counterpart due to the large crystallite size refinement mediated by milling as well as the NiO reduction process. As-mixed NiO-Ti powders (Figures 5.17a & 5.17e). exhibit a clear particle morphology. Meanwhile, FESEM images of the milled NiO-Ti (20 at.%) powders show irregular morphology with the size varying between 100-200 nm. There is also a small degree of agglomeration of the milled powders that occurs due to the repeated fragmentation and cold-welding of the powders inside the vial during the dry milling process. With further increasing x to 35, it is seen that the nature of surface morphology shows strongly agglomerated particles at 10 hrs of milling (Figure 5.17f). A major contributing factor to the agglomeration of x = 35 powders can be due to the heat build-up within the vial during the self-sustaining reactions at the early stages of milling and thereby can be correlated to the increased NiO reduction and the formation of an *in-situ* nanocomposite with high Ni content. The particle size, however, decreases with increasing t_m, and nearly spherical shaped particles can be seen at the end of 30 hrs milling (Figure 5.17h). This clearly indicates the potential role of ball milling on the size refinement with the nanostructure formation, and the MC reduction process is a key factor in the modification of surface morphology of the resulting nanocomposite.

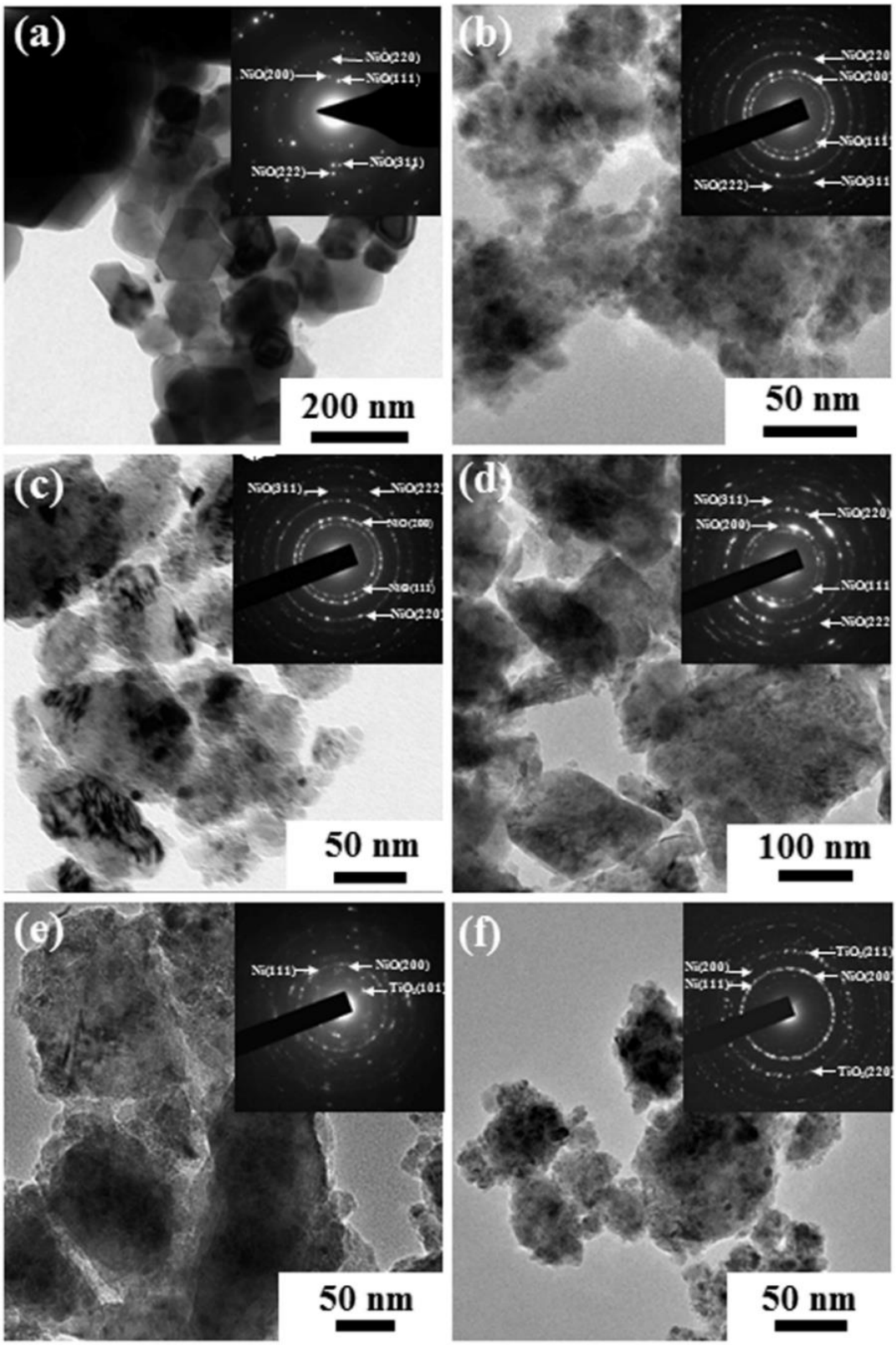

Figure 5.18: BF-TEM micrographs and SAED patterns of un-milled NiO (a), and milled NiO-Ti (x at.%) powders at different t_m [(b) x=20, t_m=20; (c) x=20, t_m=30 and (d) x=35, t_m=05; (e) x=35, t_m=10 and (f) x=35, t_m=30].

Furthermore, to understand the evolution of the nanocomposites with increasing t_m and to confirm the XRPD results, the bulk NiO and milled NiO-Ti powders were characterized by means of TEM technique. The bright-field TEM (BF-TEM) images and the SAED patterns were recorded to analyze the nanoparticle size and crystal structure, respectively, and shown in Figure 5.18. The BF-TEM images show fine nanocrystalline microstructure and the SAED patterns (inset of Figure 5.18), have concentric rings that suggest to the characteristic polycrystalline behavior. The un-milled NiO depicts the existence of clear particle microstructure with estimated large-scaled crystals ranging between 40~70 nm and the SAED pattern could be indexed to the *fcc* type NiO (Figure 5.18a). Conversely, following the addition of Ti and the subsequent NiO reduction, the milled NiO-Ti (20 at.%) powders show aggregated nanocrystalline particles with an irregular morphology (Figures 5.18b & 5.18c). However, the SAED patterns could only be indexed with reference to NiO *fcc* phases and suggest an inadequate NiO reduction. The TEM crystallite size variation follows a similar trend as the XRPD patterns but exhibits a rather broad particle size distribution with irregular shapes. On the other hand, x = 35 powders milled above 5 hrs evidence the presence of both NiO and Ni phases where the diffusive diffraction rings of Ni(111) phase superimposes with the spotty ring of NiO(200) plane (Figures 5.18e & 5.18f). Additionally, at $t_m \geq 10$ hrs, clear diffraction rings corresponding to the Ni and TiO_2 phases are observed, which implies the presence of Ni enriched spatial regions due to the increased NiO reduction and agrees well with the reported XRPD results.

5.3.2.2. Vibrational properties:

To have a further insight into the influence of Ti inclusion with increasing t_m in the lattice dynamics and the subsequent lattice defects, Raman spectra were obtained at room temperature and shown in Figure 5.19. The different vibration modes with their peak positions, width, and integral area have been analyzed by the Lorentzian peak profile method. As described earlier for the Ti content variation study, the AFM ordered NiO is known to have five prominent first order and second-order Raman phonon modes (Figure 5.19a), *i.e.*, 1P TO (~380-410 cm^{-1}), 1P LO (~520-550 cm^{-1}), 2P TO (~ 730-780 cm^{-1}), 2P LO+TO (~ 900-950 cm^{-1}), 2P LO (~1050-1110 cm^{-1}) modes due to vibrational origin and [RAVI2015] and 2M peak at (~1450-1500 cm^{-1}) due to magnetic origin. Peck *et al.* [PECK2012] reported that the prolonged exposure of the bulk NiO to the ambient

environment leads to hydroxylation of NiO, which changes the chemical environment and hence the importance of sample condition.

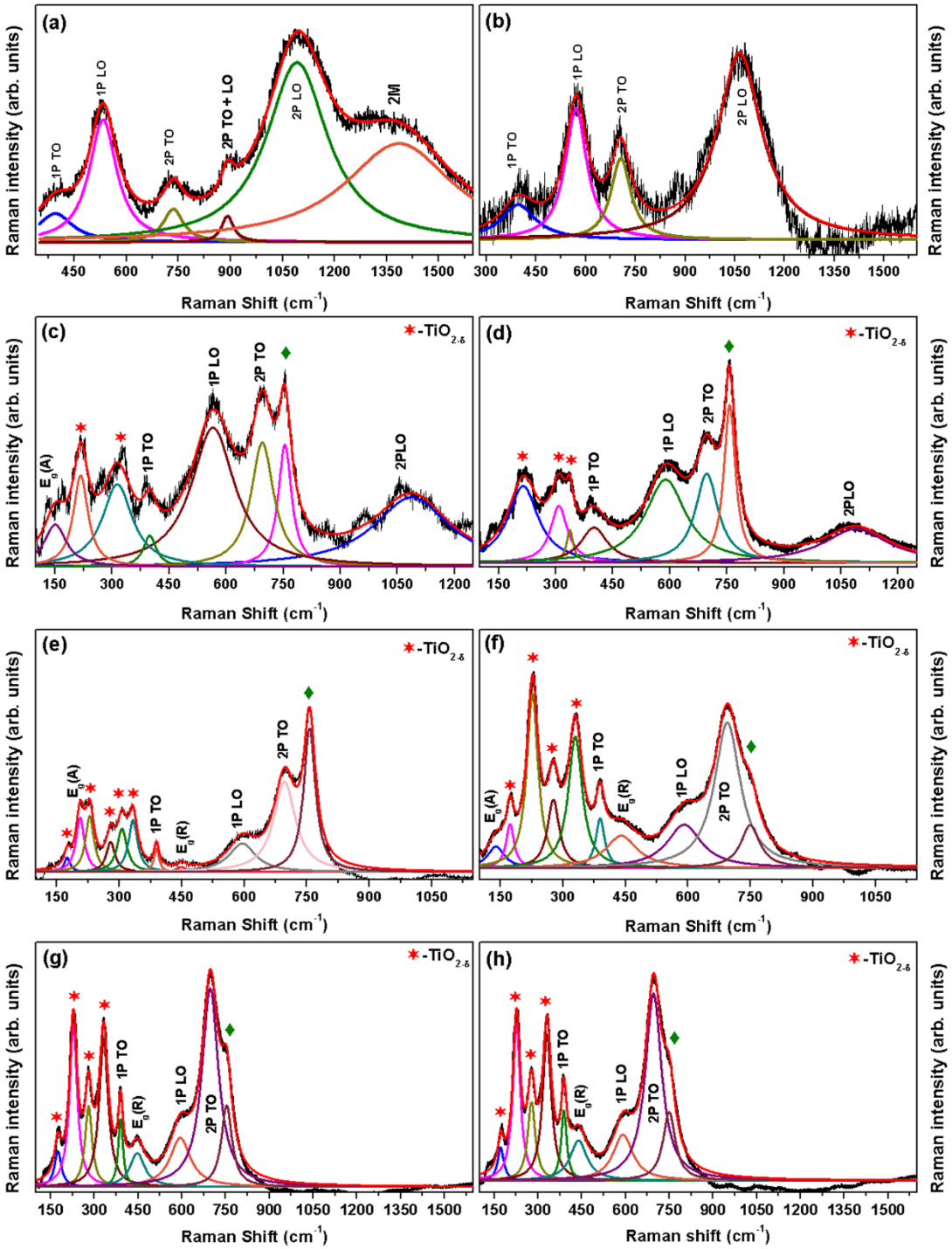

Figure 5.19: Room temperature Raman spectra of un-milled NiO (a); milled NiO (b) and NiO-Ti (*x* at.%) powders at different t_m [(c) *x*=20, t_m=5; (d) *x*=20, t_m=10; (e) *x*=20, t_m=30 and (f); *x*=35, t_m=10; (g); *x*=35, t_m=20 and (h); *x*=35, t_m=30]. The green diamond symbol indicates the presence of an unidentified phase.

On the other hand, 30 hrs milled pure NiO powder (Figure 5.19b) reveals the disappearance of the 2M peak due to the breaking of Ni^{2+}-O^{2-}-Ni^{2+} super-exchange interaction between the neighboring Ni^{2+} ions [RAVI2015]. For milled NiO-Ti powders, it can be seen that (i) The 2M band disappears due to the decrease of AFM spin correlations, (ii) 1P TO mode enhances due to the presence of parity-breaking effects and Nickel vacancies, (iii) 1P LO mode becomes prominent due to enhanced defects, surface effects and imperfective nanostructure, (iv) 2P TO+LO mode disappears, (v) 2P TO and 2P LO modes broaden and (vi) Raman bands are seen at around 172 cm^{-1}, 226 cm^{-1}, 277 cm^{-1}, 330 cm^{-1} and 477 cm^{-1} related to the oxygen-deficient $TiO_{2-\delta}$ phases [WUY2012]. Simultaneously, the Raman spectrum at 143 cm^{-1} and 205 cm^{-1} corresponding to E_g anatase [E_g(A)] TiO_2 phases and Raman spectrum at around 448 cm^{-1} corresponding to E_g rutile [E_g(R)] TiO_2 phase are also observed [FRAN2012] suggesting to the clear formation of TiO_2 as confirmed by the XRPD results. Furthermore, we observed an additional Raman peak at around 745-760 cm^{-1} in milled NiO-Ti powders, which is not attributable to the known phases and therefore necessitates a further careful investigation of vibrational studies to understand the presence of unidentified phase.

5.3.2.3. Magnetic properties:

Figure 5.20 shows the initial magnetization (*IM*) and *M-H* curves of NiO-Ti powders recorded at room temperature as a function of t_m and Ti content. The *IM* curves are presented in the logarithmic scale to find the low field magnetic behaviors and the influence of Ti content on the overall field-dependent magnetic properties of the powders. The parameters obtained from the *M-H* curves, *i.e.*, M_S and H_C, are shown in Figure 5.21. The as-mixed NiO-Ti (x at.%, x = 20, 35) powder has almost zero magnetic moments at no applied field with the loop passing through the origin and has zero H_C. This is due to the almost complete spin compensation in the type-II AFM order inhibiting between the two neighboring (111) planes of bulk NiO in the un-milled state [RINA2016]. For x = 20 powders at different t_m, the characteristic features of the *M-H* loops are: (i) At t_m = 1 hr, the *M-H* loop displays a considerable increase in the moment at lower fields with a gradual variation at higher fields region. This leads to the FM hysteresis with an M_S of 0.4 emu/g and H_C of 144 Oe. This is related to the deviation of surface spins from the AFM alignment, which induces uncompensated moments at the surface and the breaking of a large number of exchange bonds of the as-mixed NiO-Ti powder [RAVI2015]. (ii) With further increasing t_m up to 30

hrs, the magnetization increases notably and attains a maximum M_S of 2 emu/g. However, H_C decreases gradually as a function of t_m and reaches to about 75 Oe after 30 hrs of milling. (iii) All the loops show the non-saturation of the magnetization up to 50 kOe. This could be well ascribed to the combined contribution of NiO MC gradual reduction leading to the simultaneous formation of Ni in the NiO matrix and the increased uncompensated surface moments in the milled powders due to size reduction.

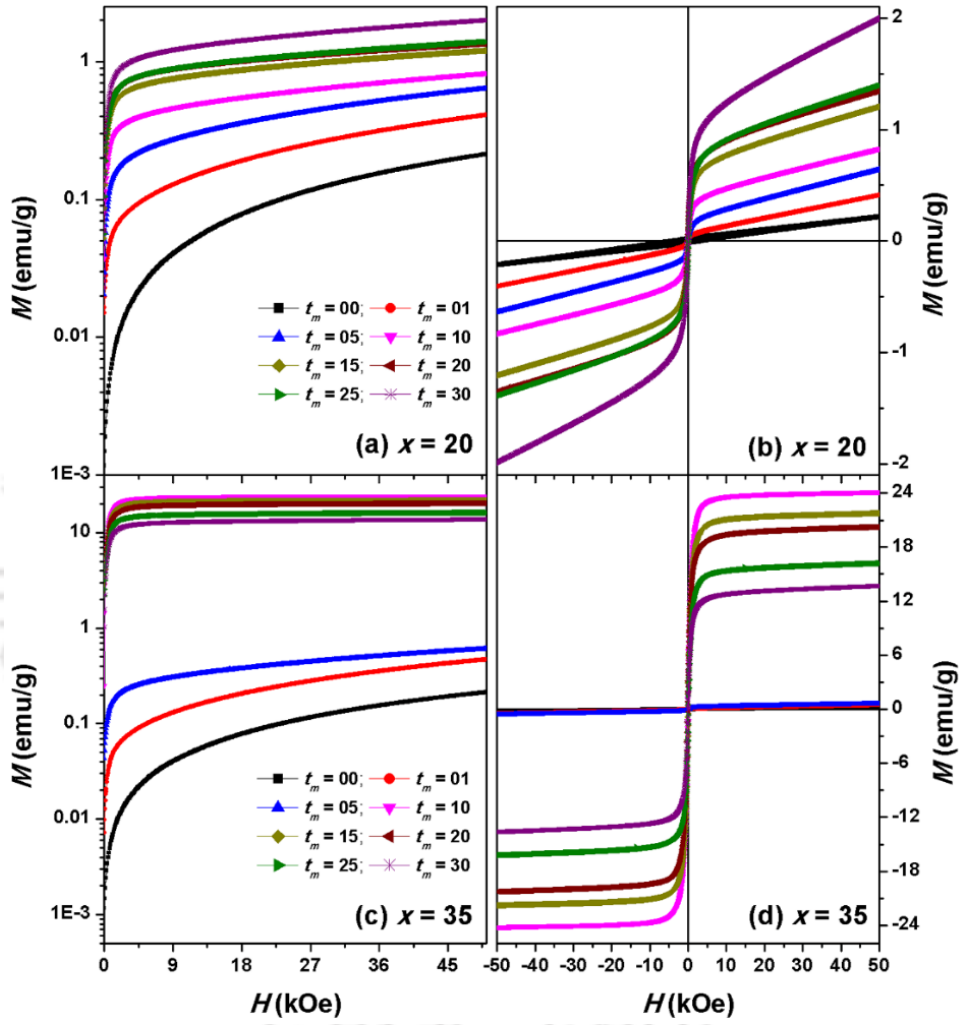

Figure 5.20: Room temperature initial magnetization (*IM*) and magnetic hysteresis (*M-H*) curves of as-mixed and milled NiO-Ti (*x* at.%) powders as a function of milling time (t_m).

Similar behavior of non-saturation of magnetization in nanostructured NiO/Ni with grain-surface relaxation due to increasing in lattice parameter with decreasing crystallite size is reported by Kremenovic *et al.* [KREM2012] in nanostructured NiO/Ni prepared by thermal decomposition of nickel acetate tetrahydrate followed by ball milling in air atmosphere. These results suggest that although the method of preparation of NiO/Ni

nanocomposites is quite different, interestingly, both lattice expansions and contractions exhibit similar *M-H* behaviors in NiO/Ni systems.

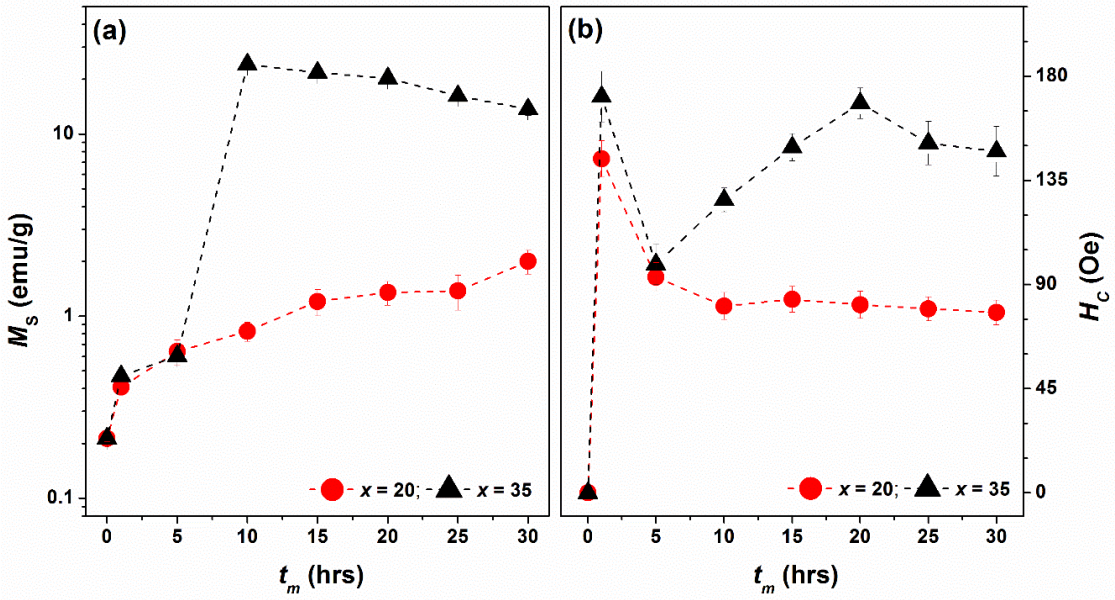

Figure 5.21: Variations of (a) saturation magnetization (M_S); and (b) coercivity (H_C) for the milled NiO-Ti (x at.%) powders as a function of milling time (t_m).

Nevertheless, as nanoparticle properties can be influenced by many variables such as preparation techniques, composition, an annealing process, and surface capping, it may be difficult to compare the results directly at this stage without further systematic analysis. On the other hand, for x = 35 powders, (i) At t_m = 1 hr, the observed feature of the *M-H* loop is in accordance with x = 20 powder and hence shows a weak FM with a M_S of 0.6 emu/g and a large H_C of 171 Oe due to the presence of defects, broken bonds, local periodicity breaking and the effective Ti dissolution in NiO matrix without the initiation of NiO reduction. (ii) Contrariwise, for t_m = 10 hrs, rapid enhancement in magnetization is observed with a maximum M_S of 24 emu/g. This high moment at 10 hrs milling is due to the ignition of NiO MC self-sustaining reduction, as shown in the XRPD results (Figure 5.15), which provided around 94% of NiO reduction. (iii) With further increasing t_m to 30 hrs, M_S decreases to 13.7 emu/g.

This could be attributed to the two competitive effects between the milling to reduce the crystallite size and the reduction of NiO taking place simultaneously at larger t_m. This structural and magnetic correlation can also be confirmed by quantifying the percentage of Ni by comparing the M_S of milled powders with respect to the M_S of bulk Ni (~55 emu/g)

and having a relative comparison with the percentage of NiO reduction obtained from the XRPD pattern.

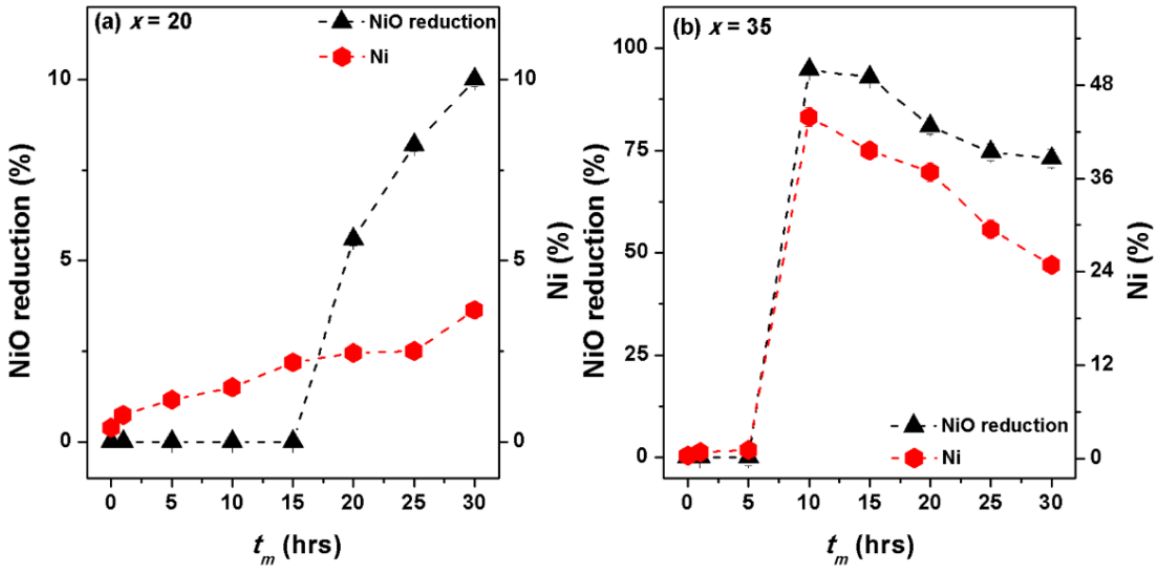

Figure 5.22: Variations of percentage of NiO reduction and Ni percentage for NiO-Ti (*x* at.%) with (a) *x* = 20 and (b) *x* = 35 powders as a function of milling time (t_m).

Figure 5.22 illustrates the correlation between the percentage of Ni obtained and the concurrent NiO reduction in the NiO-Ti powders. It is observed that the percentage of Ni increases almost similar to the percentage of NiO reduction. It is well-known that bulk NiO is AFM in nature, and therefore the magnetization increase in the *in-situ* FM nanocomposite can solely be accredited to the NiO MC reduction and hence gives confirmation for the inevitable dependence of structural and magnetic behavior of the milled powders with varying t_m and Ti content. Here, it can be noted that the milled NiO-Ti powders show Ni crystallites varying in the size regime of 12-28 nm, which is within the superparamagnetic critical size limit of single domain spherical Ni particles (~34 nm) [BALA2004]. Hence, the observed RTFM in milled powders is expected, if the effective magnetic anisotropy (K_{eff}) is higher than bulk Ni anisotropy, which in-turn can shift T_B towards high-temperature regions and provides thermal stability to the fine nanocomposites. The overall contribution of various anisotropies in milled NiO-Ti powders has been stated earlier in the Ti content variation study of NiO-Ti (*x* at.%) powders milled at a constant milling period of 30 hrs. The values of K_{eff}, deduced from the law of approach to saturation magnetization using eqns. (4.05) and (4.06) [KRON2003, MAJ2017], are found to be 0.5 - 0.65 × 10^4 J/m^3 and 1.15 - 4.65 × 10^4 J/m^3 for *x* = 20 and 35, respectively. This is much higher than that of bulk Ni

(0.5×10^4 J/m^3) [ZHAN2009], and such larger K_{eff} in the resulting nanocomposites helps to retain the FM behavior in milled NiO-Ti powders [ZHAN2009, SHYN20152].

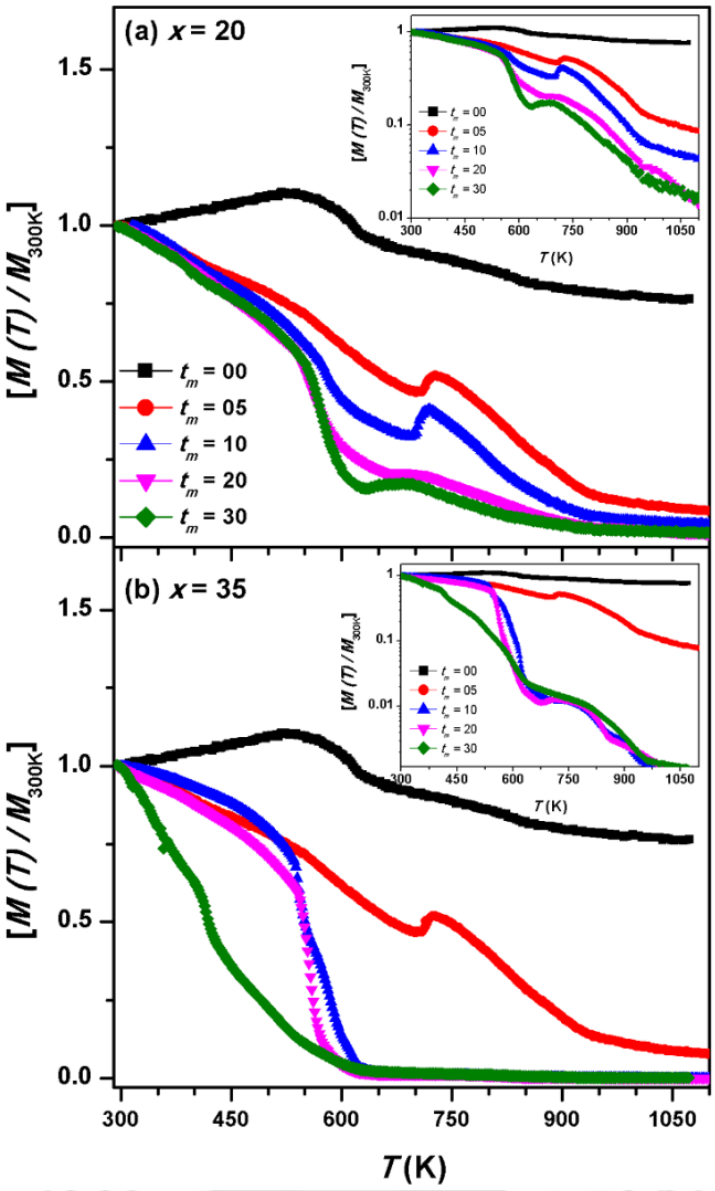

Figure 5.23: High-temperature *M-T* curves for pure NiO and milled NiO-Ti (*x* at.%) powders at different t_m.

To study the FM stability of the nanocomposites with increasing t_m and Ti contents, high-temperature *M-T* measurements were carried out, and the normalized *M-T* curves are plotted in Figure 5.23. The insets of Figure 5.23, plotted for the same data in the logarithmic scale, show the relative magnetic variation close to zero range. As-mixed NiO-Ti powders show a magnetization increase up to 525 K followed by a gradual decrease for $T > 525$ K and thus forms a peak in the *M-T* curve. This is the typical characteristic of AFM material,

and hence the Néel temperature (T_N) of NiO is defined to be 525 K [RINA2016]. However, the milled NiO-Ti (20 at.%) powders show different behaviors as compared to the bulk NiO powder. It is observed that (i) the magnetization decreases gradually with increasing temperature up to 700 K. Also, the temperature up to which the magnetization decreases shifts towards lower temperatures with increasing t_m. (ii) With further increasing temperature, the magnetization increases suddenly, forming a peak in the curve and then decreases gradually to nearly zero magnetization. The strength of the magnetization peak reduces, and the peak width broadens with increasing t_m. These results suggest that the decrease of magnetization in the *M-T* curves around the T_N of bulk NiO is related to the origin of enhanced T_B of the Ni particles due to the enhanced exchange coupling between AFM NiO and FM Ni inducing large K_{eff}. Besides, as the temperature increases, the NiO matrix becomes paramagnetic, and hence the stabilization of FM Ni by AFM NiO through the exchange coupling is lost, leading to a decrease in magnetization [SORT2004, DETO2015]. In order to understand the origin of the t_m dependent peak in *M-T* curves, the as-milled x = 20 powders (t_m = 10 and 30 hrs) are heated up to three different temperatures [below the peak position (T_{below}), at the peak maximum (T_{max}) and at 950 K (T_{950K})] by following the same heat treatment procedures of *M-T* measurement described in the experimental section. The structural variations of as-milled and heat-treated x = 20 powders were analyzed by obtaining XRPD patterns at room temperature. The observed results for the 10 hrs milled and heat-treated x = 20 powders reveal the temperature-induced NiO reduction process with the available unreacted Ti as evidenced from Figure 5.13, *i.e.*, the development of Ni initiates at T_{below} followed by the growth at T_{max} and the nearly complete reduction of NiO along with the formation of TiO_2 and Ni at T_{950K}. This temperature-induced irreversible structural change provides a maximum in the *M-T* curve. On the other hand, for the 30 hrs milled and heat-treated x = 20 powders, (i) the XRPD patterns at T_{below} and T_{max} exhibit a cognate pattern as that of the as-milled powder due to the maximum incorporation of Ti in the NiO matrix and hence, the *M-T* curve does not show a sharp peak at T_{max}. (ii) Nonetheless, the XRPD pattern of the powder heat-treated at T_{950K} shows an almost complete reduction of NiO to form TiO_2 and Ni as similar to the 10 hrs milled and heat-treated powder. These results suggest that the peak in the *M-T* curve is caused by the temperature-induced structural change in the as-milled x = 20 powders. For x = 35 powders, we observed different nature of *M-T* curves depending on the t_m: (i) For t_m < 10 hrs, *M-T* curves show almost the similar behavior as that of x = 20 powder. This is due to the non-

ignition of the self-sustaining reaction. (ii) On the other hand, the nature of the magnetic phase transition changes drastically beyond $t_m \geq 10$ hrs and shows a dominant ferromagnetic to paramagnetic phase transition at 640 K. This is attributed to the presence of a large fraction of Ni in the resulting nanocomposite due to self-sustaining reaction.

5.4. Summary:

We have investigated the effect of mechanical activation on the structural, vibrational and magnetic properties of NiO-Ti powders prepared by the high energy ball milling process as a function of Ti content and milling time in detail. The salient features of the milled NiO-Ti powders from the current investigations are summarized as follows:

- NiO-Ni-TiO_2 nanocomposites with varying Ti (x at.%) content and milling time (t_m = 0-30 hrs) have been successfully prepared by the high-energy ball milling process in dry milling conditions under a controlled argon environment.
- The structural and microstructural analysis carried out for the 30 hrs milled NiO-Ti powders revealed the formation of NiO-Ti solid-solution for Ti up to 5 at.%, followed by a gradual decrease of NiO into NiO-Ni-TiO_2 nanocomposite due to the mechanical activation of Ti reduction process with the NiO matrix. A maximum NiO reduction of 73% is observed for NiO-Ti (35 at.%) powder.
- The milling process effectively reduced the average crystal size of NiO largely down to 5 nm as Ti content was increased to 35 at.%.
- The NiO-Ti solid-solution showed a decrease in magnetization effectively from 1.96 emu/g to 1.07 emu/g, whereas the mechanochemical reduction of NiO with increased Ti content experienced an increase in magnetization up to 13.7 emu/g for NiO-Ti (35 at.%) powder.
- The detailed milling time-dependent study of NiO-Ti (x at.%, x = 20, 35) powders revealed two different reaction dynamics for varying Ti contents. The mechanochemical reduction of NiO in NiO-Ti (20 at.%) powders occurred gradually with a maximum reduction of 10% at 30 hrs of milling. On the other hand, NiO-Ti (35 at.%) powders showed a self-sustained process with a maximum of 94% NiO reduction at 10 hrs of milling time.
- The gradual reduction process of NiO in NiO-Ti (20 at.%) powders produced a maximum magnetization of 2 emu/g, while the NiO-Ti (35 at.%) powders through the self-sustained process exhibited a maximum magnetization of 24 emu/g.

- The structural, vibrational, and magnetic behavior of the *in-situ* nanocomposites illustrated a strong dependence on the correlative fractions of the Ni, and NiO phases and so played a crucial role in defining the overall magnetic anisotropy based ferromagnetic behavior in the milled powders.
- Thermomagnetization studies at high-temperatures revealed that the presence of mixed magnetic phases, temperature-induced structural phase changes, and gradual diminishment of the induced FM phase greatly relied on the relative Ni fractions attained from the partial NiO-Ti reduction process.
- The obtained results confirmed a systematic correlation between the structural, vibrational, and magnetic properties under optimized milling criteria. The ferromagnetic nanocomposites and the controlled reduction process may find suitable applications in the areas of metallurgy and ore reduction.

Chapter 6

Milling of NiO-Mg powders: Effect of Composition

6.1. Introduction:

In the last two chapters, we have reported the nature of NiO reduction by Al and Ti and investigated the changes in the magnetic properties as a function of Al and Ti compositions and milling time. In this chapter, we demonstrate the mechanical activation of the NiO-Mg reduction process as a function of Mg content by using high-energy ball milling technique under dry milling conditions and the correlative study between the structural, vibrational and magnetic properties of the nanocomposites as a function of Mg content. It is well-known that the crystalline structures of NiO and MgO are almost similar, and their lattice constants are very close. Therefore, the addition of low content of Mg (with the ionic radius of 0.086 nm for Mg^{2+}) in NiO is expected to form a solid-solution with stabilized cubic structure and produce a class of the diluted face-centered-cubic (*fcc*) antiferromagnets (AFM), *i.e.*, the magnetic properties vary with the composition from antiferromagnetic like behavior, for pure NiO, to diamagnetic ionic insulator for pure MgO. Setoudeh *et al.* [SETO2017] reported the mechanical synthesis of nanostructured $Mg_xNi_{1-x}O$ compounds by Mg-NiO stoichiometric mixture and showed the mechanically induced self-sustaining reaction by using powder X-ray diffraction (XRPD) studies. However, systematic investigation of the continuous addition of Mg in NiO, the associated reduction process, and the detailed analyses of the resulting magnetic properties have not been explored and are still missing.

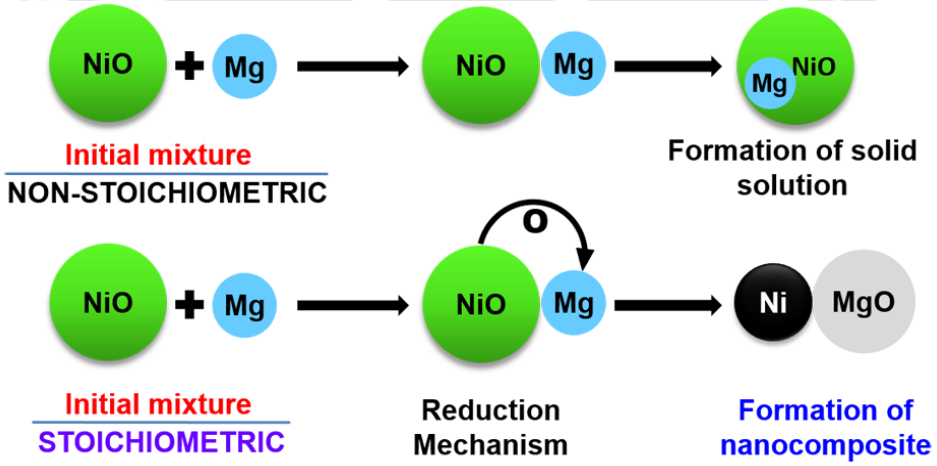

Figure 6.01: Schematic representation of the formation of NiO-Mg based solid-solution and nanocomposites.

6.2. Experimental details:

Commercial NiO and Mg powders were procured from Sigma-Aldrich, India, and used as the starting materials. The mixtures of NiO-Mg powder were taken to tune the composition

of the powders, as NiO-Mg (x = 0-50 at.%) up to the stoichiometric composition to satisfy the reaction equations

$$NiO + Mg = Ni + MgO \quad (6.01)$$

The *in-situ* NiO-Mg (x = 0-50 at.%) based nanocomposites, as schematically represented in Figure 6.01, were prepared by using high-energy ball mill under controlled argon gas environment. The Mg contents were chosen carefully depending on the possible reaction kinetics and tunable magnetic properties of the powders. Dry milling was carried out in a high-energy planetary ball-mill (Insmart, India) using hardened steel vial and 8 mm diameter hardened steel balls at a constant speed of 500 rpm with a milling period of 30 hrs. Throughout the milling process, the ball-to-powder weight ratio was maintained constantly at 10:1. Milling was carried out in cycles of 15 minutes, followed by 15 minutes of idling to avoid excessive heat in the vials. The optimization of the milling parameters was done mainly by analyzing the variations in the structure, type of reduction reaction, and magnetic properties of the milled powders with different Mg contents.

The structural evolution of the milled powders was analyzed from XRPD patterns obtained using a high-power X-ray diffractometer (Rigaku TTRAX III 18 kW) with Cu-K_α radiation (λ = 1.541 Å) and well equipped with pyrolytic graphite monochromator and Silicon scintillation counter. The generator power was set at 50 kV/180 mA. Divergence and receiving slits for the diffraction measurements were kept at 2/3° and 0.3 mm, respectively. The XRPD patterns were collected at a slow scan rate of 0.005 °/s with 100 steps per degree. To subtract the instrumental broadening contribution, the diffraction pattern of standard Silicon reference sample was recorded at the similar diffraction conditions as that of the NiO-Mg (x at.%) powders, and the instrumental broadening corrected line profile breadth $\delta(2\theta)$, in radians, of each reflection was calculated by using the parabolic approximation correction as explained in eqn. (4.02). Surface morphologies were characterized using a field-emission scanning electron microscope (FESEM, Zeiss Sigma) with the compositional study done by energy dispersive X-ray analysis (EDS) unit attached to FESEM. Detailed microstructural analysis was characterized by using transmission electron microscopy (TEM, JEOL2100) technique. The sample for TEM analysis was prepared by placing a drop of ethanol solution containing the as-milled powders onto a carbon-coated copper grid followed by drying. After drying, the sample was examined by TEM. Room temperature Raman spectra were obtained using a micro-Raman spectrometer (LabRam HR800, Jobin Yvon) equipped with an Olympus confocal

microscope with 50× magnification for the backscattering illumination and collection of scattering light. For the measurements, a laser power of 17 mW and an excitation wavelength of 633 nm were used. The isothermal magnetic measurements at room temperature were carried out by using physical property measurement system (PPMS, Dynacool) at a maximum applied field of ±50 kOe, and the thermomagnetic (*M-T*) properties at high temperature (from 300 K to 1200 K) were measured by vibrating sample magnetometer (VSM, Lakeshore 7410, USA) at a heating rate of 4 °C/min under the applied magnetic field of 2 kOe.

6.3. Results and discussion:

6.3.1. Structural properties:

Figure 6.02 shows the typical room temperature XRPD patterns of pure as-mixed and 30 hrs milled NiO-Mg (x = 0 - 50 at.%) powders and multiple profile fitting of selected diffraction peaks. As-mixed NiO-Mg powder exhibits sharp diffraction peaks of face-centered cubic (*fcc*) NiO [JCPDS card No. 78-0423, space group $Fm\bar{3}m$] and hexagonal-close-packed (*hcp*) Mg [JCPDS card No. 04-0770, space group $P63/mmc$]. Contrariwise, the 30 hrs milled pure NiO [NiO-Mg (x = 0 at.%)] displays broad peaks and a peak shift to lower angles. The first one is generally ascribed to crystallite size refinement and increased strain, whereas the latter one happens due to change in lattice parameters [KISA2018]. With increasing x up to 10 at.%, the milled powders display Bragg peaks of *fcc* NiO without any peaks of Mg. This is accredited to the dissolution of Mg into the NiO matrix, which increases the peak broadening and shifts the position of the peaks due to atomic disorder. As depicted in Figure 6.02(b), NiO(200) peak becomes asymmetric initially and then splits into multiple peaks with increasing x from 15 to 40. The careful analysis using multiple peak fitting procedures, as displayed in Figures 6.02(c)-6.02(f), reveals the development of additional peaks at 2θ = 44.5° and 43.02°, representing Ni(111) (JCPDS card No. 04-0850, space group $Fm\bar{3}m$) and MgO(200) (JCPDS No-78-0430, space group $Fm\bar{3}m$) peaks, respectively. Furthermore, the Ni(200) peak at 2θ = 52° becomes more prominent with increasing x from 30 to 45. This indicates a progressive increase of Ni in the milled NiO-Mg powders due to gradual reduction of NiO by Mg and the formation of NiO-Ni-MgO nanocomposites. Remarkably, for x = 50 powder, the Mg activated reduction of NiO at its higher proximity shows highly intense peaks of Ni(111), Ni(200) and Ni(220) at 2θ = 44.5°, 51.8° and 76.4°, respectively and the development of additional peaks at 2θ = 37.05°, 43.07°, 62.46°, 74.76°

and 78.75° due to the formation of *fcc* MgO at the expense of nearly complete NiO reduction.

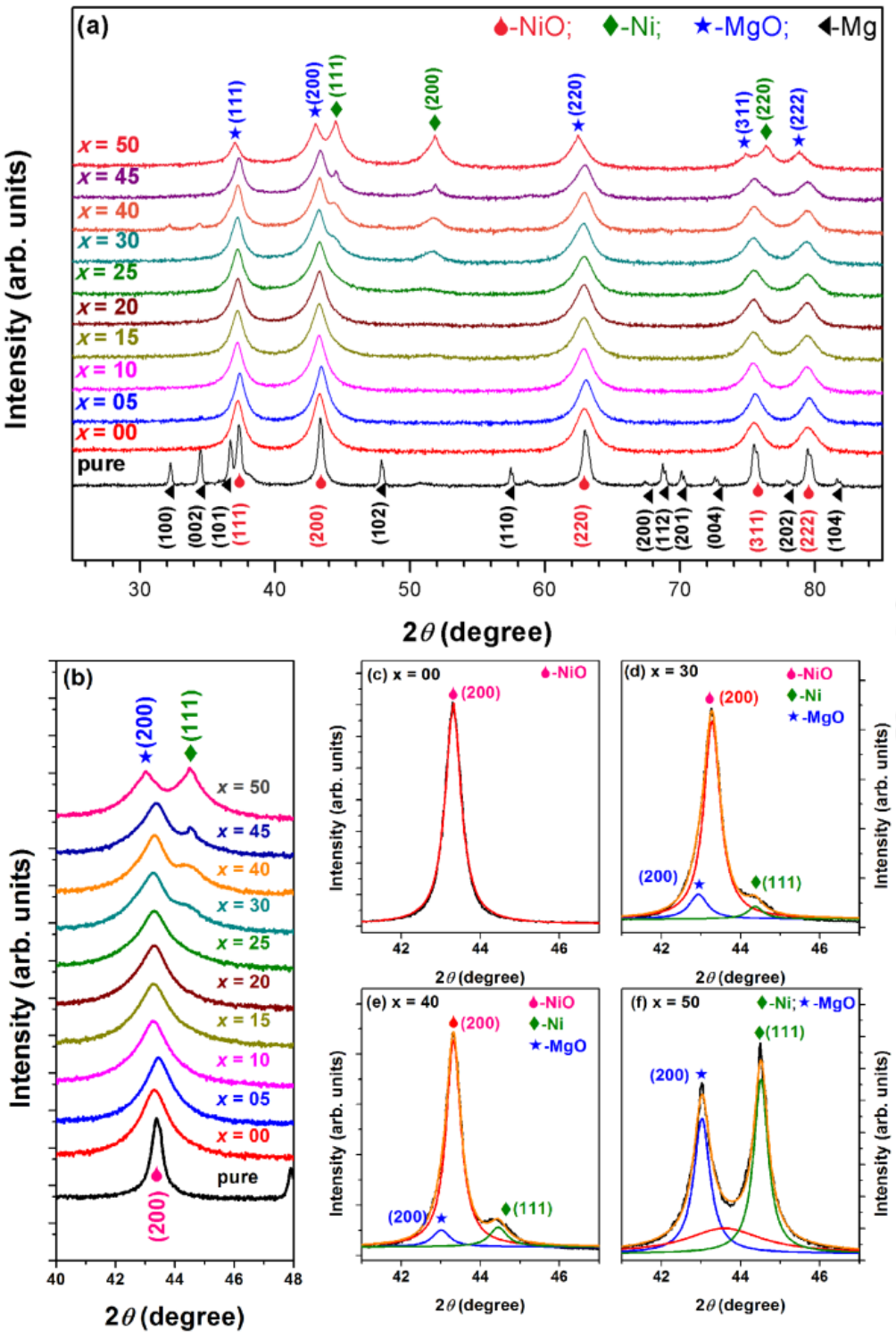

Figure 6.02: Room temperature XRPD patterns of (a) pure as-mixed and 30 hrs milled NiO-Mg (*x* at.%) powders with *x* = 0 - 50, (b) expanded XRPD patterns in the range of 2θ = 40° - 48° and the multiple profile fittings of NiO(200) peak for *x* = 0 (c), 30 (d), 40 (e) and 50 (f) powders.

Here it may be noted that MC displacement reactions in NiO-Mg powders can follow two different reaction paths depending upon the milling conditions and the nature of the as-mixed NiO-Mg powders: (i) gradual reaction, which progresses in a steady-state through a very small volume during each collision of the milling balls, and (ii) a self-sustaining reaction, if the reaction enthalpy, ΔH, is very high for the NiO-Mg reaction to proceed itself. Though ΔH in both the reaction modes are found to be substantially negative, a mechanically induced self-sustaining type reaction can only be initiated, if $(-\Delta H^0_{298K})/(\sum C_{P_{298K}}) > 2000\ K$, where ΔH^0_{298K} being the reaction enthalpy and $\sum C_{P_{298K}}$ being the total heat capacity of the products at 298 K [TAKA2002]. The thermodynamic calculation for the stoichiometric composition of NiO-Mg powder mixtures show that ΔH^0_{298K} is negative at room temperature with the value of -361 kJ/mole for the reaction given in eqn. (6.01). Accordingly, the ratio of $(-\Delta H^0_{298K})/(\sum C_{P_{298K}})$ turns out to be around 5500 K for NiO-Mg (50 at.%) as-mixed powder [HTTP0010].

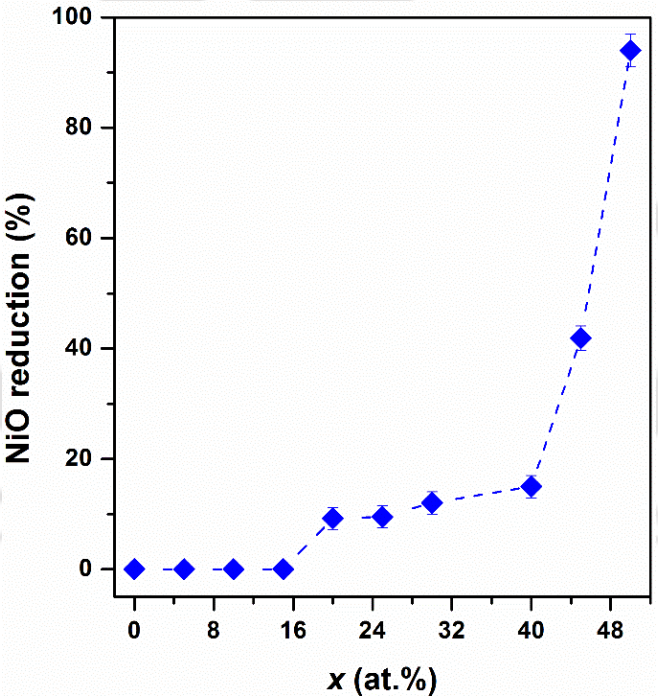

Figure 6.03: Percentage reduction of 30 hrs milled NiO-Mg powders as a function of *x*.

Thus, the NiO-Mg reaction is highly exothermic by nature, and hence a mechanically induced self-sustaining reaction can be anticipated thermodynamically if an abundant amount of Mg is availed in the as-mixed NiO-Mg powder. Therefore, the reduction reaction initially follows a progressive/gradual reaction type due to the presence of an insufficient amount of reactants. Upon attaining the initial powder mixtures close to stoichiometric

compositions, the gradual reaction transforms into a self-sustaining reaction revealing the well-described reaction kinetics due to MC activation of NiO-Mg powders. Similar reduction dynamics were observed in Chapters 4 and 5, where the stoichiometric composition of Al (40 at.%) and Ti (35 at.%) showed the self-propagating reduction reaction during the ball milling process.

To quantify the fraction of NiO reacted with increasing Mg content, we have calculated the change in integrated intensity of NiO(200) peak [UDHA2010] using eqn.(4.03), and by taking into account the relative integrated intensity of NiO(200) in un-milled and milled NiO-Mg powders. Figure 6.03 depicts the variation of NiO reduction as a function of *x*. In NiO-Mg powders, though the MC reduction gets initiated for x = 15 powders, the percentage of reduction could not be calculated precisely due to a lesser fraction of NiO being reduced and the difficulties in the accurate deconvolution of the peaks. Hence, the reduction of NiO can indeed be accounted for x = 20 powders, and a maximum of 95% reduction is observed for x = 50 powder. However, two different reaction rates are observed: (i) NiO reduction happens to be of 9 to 15% with a gradual reaction rate of 0.31% per x for increasing x from 20 to 40. (ii) On further increasing x above 40, the mechanically induced self-sustaining reaction enhances the reduction process at a rate of 8% per x and eventually proximate to 95% due to the maximum reduction of NiO. Interestingly for 30 hrs milled NiO-Mg powders, the color of pure unmilled NiO (pale-green colored) and that of the non-stoichiometric milled NiO (dark green colored) transforms into black color reinforcing the formation of Ni nanoparticles in the milled samples.

To study the effect of NiO reduction on the structural properties, the lattice parameters (a_{NiO}, a_{Ni}, and a_{MgO}) and average crystallite size (D_{NiO}, D_{Ni}, and D_{MgO}) of NiO and Ni, and MgO were calculated for NiO-Mg powders and depicted as a function of Mg content in Figure 6.04. The bulk values of a_{NiO}, a_{Ni}, and a_{MgO} (4.17 Å, 3.521 Å, and 4.2 Å, respectively) are shown in the figure for the comparison. The as-milled pure NiO exhibits a slight increase in a_{NiO} due to negative interface pressure activated by the strain during the milling process [KISA2014]. For NiO-Mg powders, the value of a_{NiO} is obtained to be 4.169 Å for x = 5 at.%, which increases to 4.178 Å at x = 10 at.% and then tends to saturate up to 30 at.% of Mg content. The value of a_{NiO} shows a continuous decrease as x is increased by up to 45 at.%. This could be reasoned to the reduction of NiO into NiO-Ni-MgO nanocomposites at higher Mg content. Moreover, the value of a_{Ni} approaches towards the lattice parameter of bulk Ni with increasing x in the milled powders. This confirms to the

growth of stable Ni phases in the NiO-Ni-MgO nanocomposites. The NiO crystal size (D_{NiO}) decreases largely from about 50 nm for pure un-milled NiO to 14.5 nm for the 30 hrs milled NiO powder.

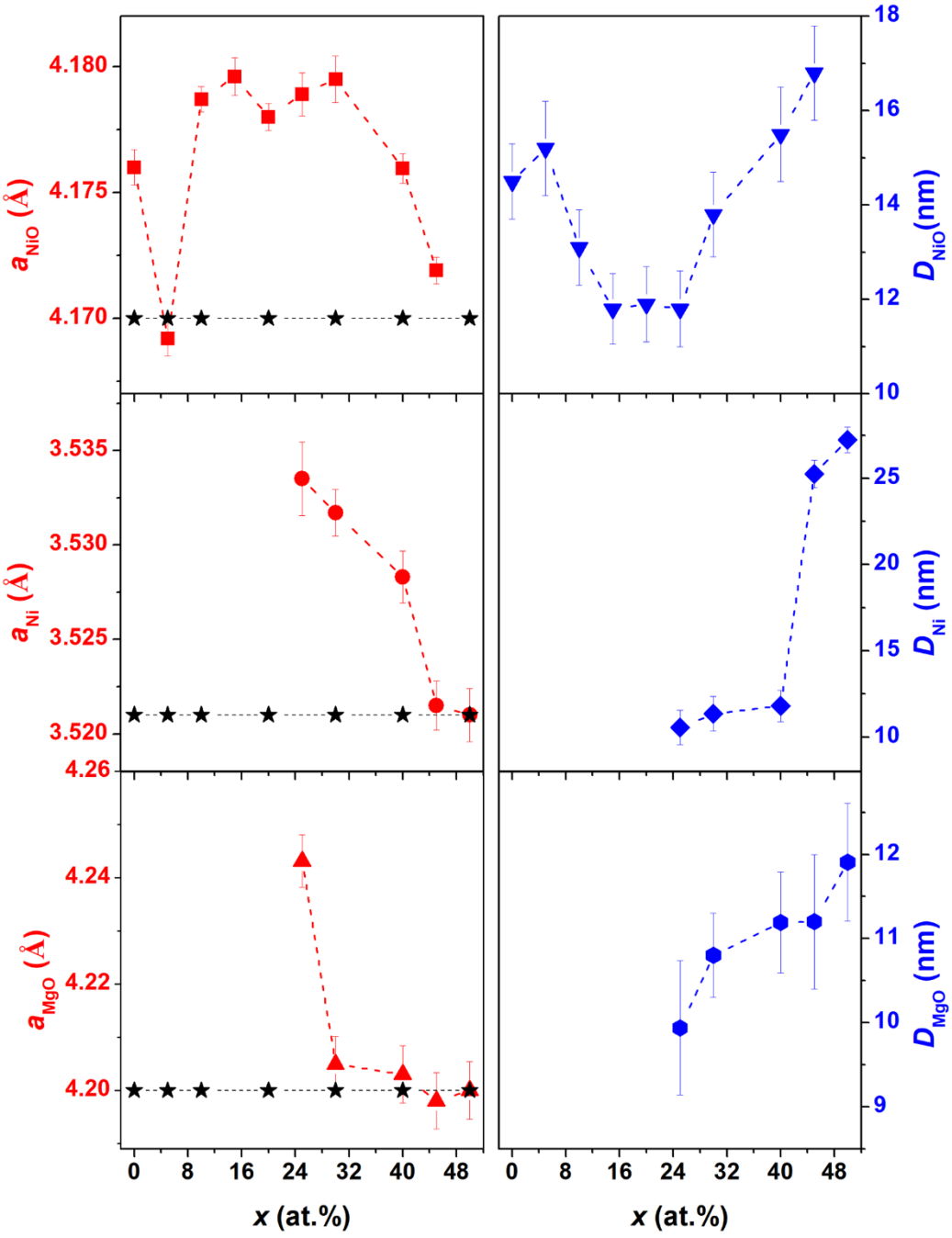

Figure 6.04: Variations in the lattice parameters [a_{NiO}, a_{Ni} and a_{MgO}] and the crystallite size [D_{NiO}, $D_{Ni,}$ and D_{MgO}] as a function of x for 30 hrs milled NiO-Mg (x at.%) powders.

With increasing x, D_{NiO} increases slightly for x = 5 powder and then decreases progressively down to 11.8 nm for x = 25 powder. On further increasing x, D_{NiO} increases considerably up

to 17 nm for $x = 45$. It may be noted that the error in obtaining D_{NiO} increases with increasing Mg due to difficulties in the exact deconvolution of the NiO peak. In contrast, D_{Ni} is found to be increased significantly to around 27 nm for $x = 50$ powders. The large increase in D_{Ni} can be attributed to the increased crystallinity of Ni in the resulting *in-situ* nanocomposites. Moreover, the growth of Ni in the nanocomposites leads to a_{Ni} towards bulk value. Similar behavior is observed for the growth of the MgO in the NiO-Ni-MgO nanocomposite. These variations in the structural parameters indicate a decrease in D_{NiO} with the simultaneous increase in D_{Ni} due to the increased NiO reduction as a function of Mg contents in the nanocomposites.

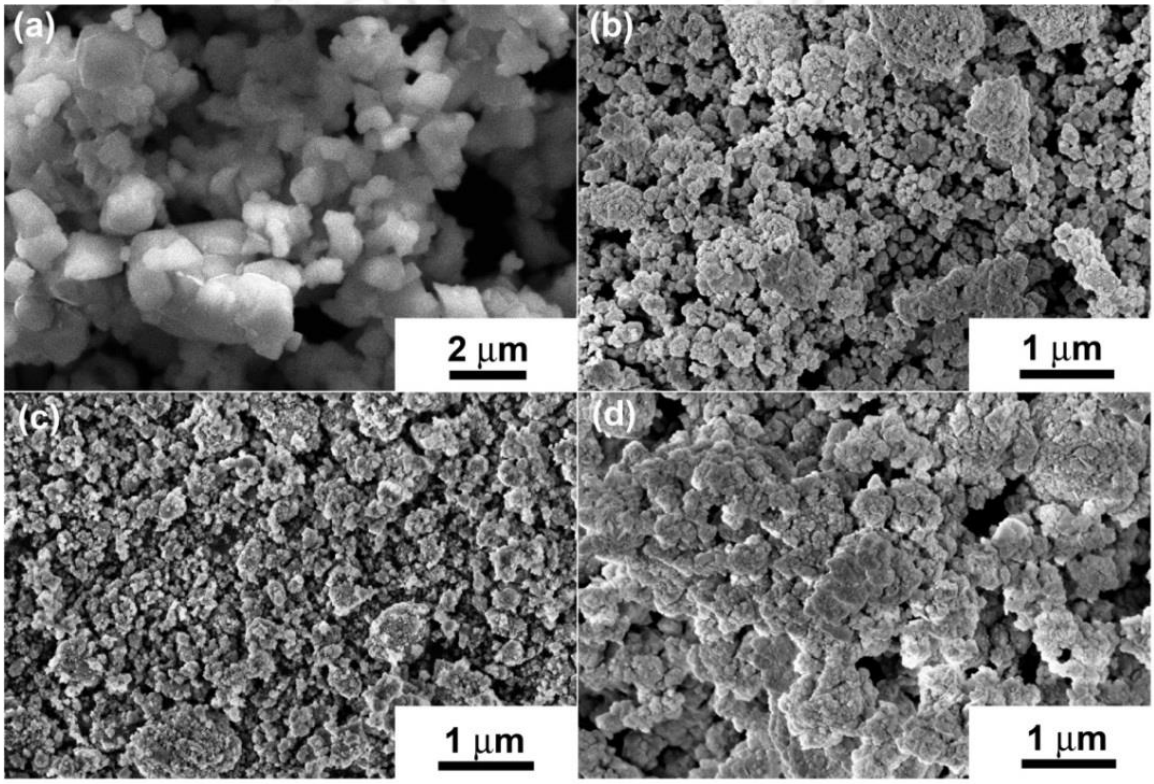

Figure 6.05: FESEM micrographs of pure un-milled NiO (a), and 30 hrs milled NiO-Mg powders with $x = 5$ (b), 10 (c) and 40 (d).

Figure 6.05 illustrates the morphological changes in the milled NiO-Mg powders obtained through FESEM as a function of *x*. Un-milled pure NiO in the present investigation has clear particle morphology with an approximate particle size ranging between 1 to 4 μm. The dissolution of Mg in the NiO matrix refines the particle sizes down to 100-150 nm with large agglomeration. Note that these aggregates are typical characteristics of ball-milled powders resulting from repetitive cold-welding and fracture of powders during the milling process. However, with increasing *x*, the nature of surface morphology depicts strongly

agglomerated particles. This can be correlated to the increased NiO reduction and the formation of *in-situ* nanocomposites with high Ni content. We have observed a particle size refinement down to 50-60 nm for x = 40 powders. This indicates the substantial role of ball milling on the particle size refinement with the nanostructure formation, and the MC reduction process is a crucial factor in the modification of the structural morphology of the milled NiO-Mg powders. The composition analysis using the EDS technique confirms the presence of only Ni, Mg, and O elements in the milled powders.

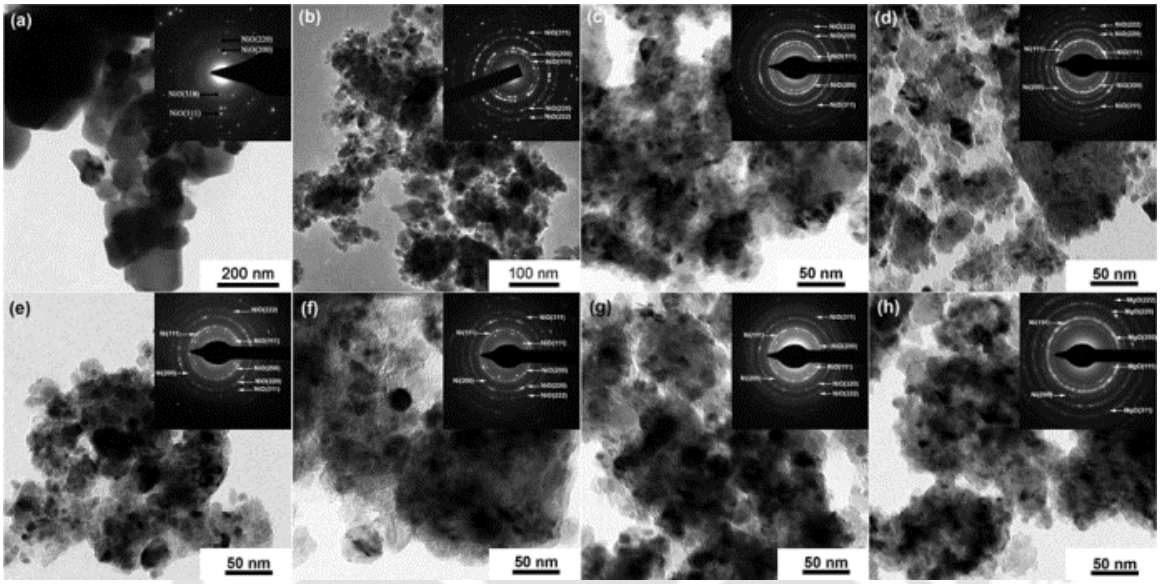

Figure 6.06: Bright-field TEM images and selected area electron diffractions for pure un-milled NiO (a) and milled NiO-Mg (x at.%) powders with x = 10 (b), 20 (c), 25 (d), 30 (e), 40 (f), 45 (g) and 50 (h).

Figure 6.06 displays the bright-field TEM (BF-TEM) image and selected area electron diffraction (SAED) patterns for as-mixed and milled NiO-Mg powders. U-milled NiO powder exhibits large size crystals with size ranging between 50 and 90 nm, and SAED pattern confirms the *fcc* structure with polycrystalline nature. On the other hand, milling powders show fine nanocrystalline microstructures with irregular particle morphology, and the associated SAED patterns shown in the insets of figure having concentric rings confirm the polycrystalline nature of the samples. This is in close agreement with the XRPD results. With increasing x (< 20), the SAED pattern evidences only the presence of *fcc* NiO phase with finer and roughly nanometer-sized crystals of 10-13 nm without any evidence of NiO reduction. The variations of TEM crystallite size show almost similar trend as XRPD results, but with broader size distribution and irregular particle morphology. With increasing x from

20 to 40 at.%, a similar nanocrystalline behavior with irregular morphology is observed. However, the SAED patterns show a quite continuous and diffusive rings corresponding to Ni(111) and NiO(200) phases, respectively. Nevertheless, the presence of MgO(200) phase could not be resolved clearly due to mere overlap of MgO(200) rings with NiO(200) ring. On further increasing *x* to 50, diffraction rings corresponding to Ni and MgO could markedly be observed confirming the formation of NiO-Ni-MgO nanocomposites. The results of microstructural analyses are in close agreement with the XRPD results and show no evidence of any other impurity phases in the as-milled powders.

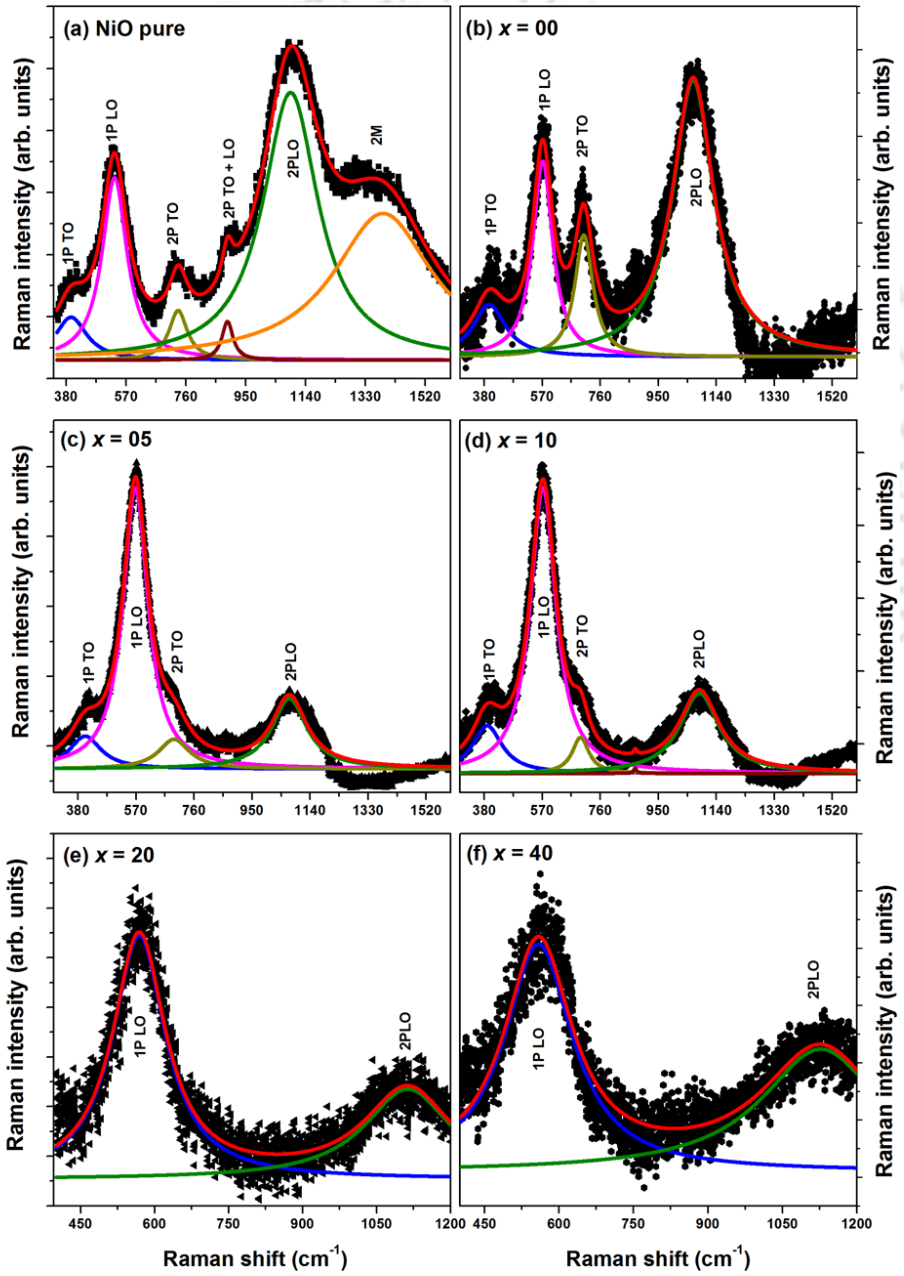

Figure 6.07: Raman spectra of pure un-milled NiO (a) and milled NiO-Mg (*x* at.%) powders with *x* = 0 (b), 5 (c), 10 (d), 20 (e) and 40 (f) obtained at room temperature.

6.3.2. Vibrational properties:

Figure 6.07 presents the Raman spectra of un-milled pure NiO, milled NiO, and milled NiO-Mg powders. Raman spectra were prudently probed by Lorentzian curve-fitting with various combinations of bands to find peak position, peak width, and area under the curves as well as to study the defect structure in milled NiO-Mg powders. The AFM ordered bulk NiO shows five phonon modes, *i.e.*, one-phonon (1P) transverse optical (TO) at 380-410 cm^{-1}, 1P longitudinal optical (LO) at 520-550 cm^{-1}, two-phonon (2P) TO at 730-780 cm^{-1}, 2P LO+TO at 900-950 cm^{-1}, 2P LO at 1050-1110 cm^{-1} associated with vibrational origin and a two-magnon (2M) peak at 1450-1500 cm^{-1} associated with magnetic origin attributed to the existence of Ni^{2+}-O^{2-}-Ni^{2+} super-exchange symmetry [CAZZ2003, LIUD2017]. However for 30 hrs milled NiO, the bands in the Raman spectra show varying features as (i) the 2M band disappears due to the breaking of Ni^{2+}-O^{2-}-Ni^{2+} super-exchange symmetry, (ii) 1P LO mode becomes well pronounced and broadened, (iii) 2P TO+LO mode disappears after milling, (iv) the 2P TO and 2P LO modes broaden with the peak positions shifting towards lower wavenumber, and (v) the integrated intensity ratio between 1P LO and 2P LO modes (I_{1PLO}/I_{2PLO}) increases from 0.31 to 0.34, indicating the induced defects, surface effects and imperfections in particle shape and size caused by the ball milling process. The inclusion of Mg in NiO changes the Raman spectra drastically as compared to the milled NiO powder, *i.e.*, I_{1PLO}/I_{2PLO} increases largely from 0.34 to 2.9, and the weakening of 2P TO mode largely as Mg content is increased to 5 at.%. This could be attributed to the dissolution of Mg into NiO. With increasing $x > 5$, I_{1PLO}/I_{2PLO} decreases progressively to 1.06, 2P TO peak disappears, and only 1P LO and 2P LO modes appear in the Raman spectra with reduced intensity. This could be accredited to the gradual reduction process of NiO into NiO-Ni-MgO nanocomposite with an increased fraction of Ni. These findings not only show good agreement with the results of XRPD analysis but also confirm the formation of no other impurity phases in the as-milled powders.

6.3.3. Magnetic properties:

To understand the effects of NiO reduction and structural refinement due to the inclusion of Mg in NiO matrix on the magnetic properties, room temperature initial magnetization (*IM*) curves, *M-H* loops, and temperature-dependent magnetization data were measured. Figure 6.08 illustrates the *IM* curves and *M-H* loops for as-mixed and milled NiO-Mg powders. In order to see the actual variation close to zero, the *IM* curves are plotted in the logarithmic

scale. The extracted parameters from the *M-H* loops, such as magnetization at 50 kOe (M_S) and coercivity (H_C), are plotted as a function of Mg content in Figure 6.09. It is seen that (i) un-milled NiO and as-mixed NiO-Mg powders show a weak and linear response to the applied field due to its AFM nature, as supported by the Raman study, and therefore the loop passes through the origin. (ii) 30 hrs milled NiO powder, on the other hand, shows a significant change in the magnetization curve, where the moment experiences eloquent increase at lower applied field and then progressively varies at the higher field region.

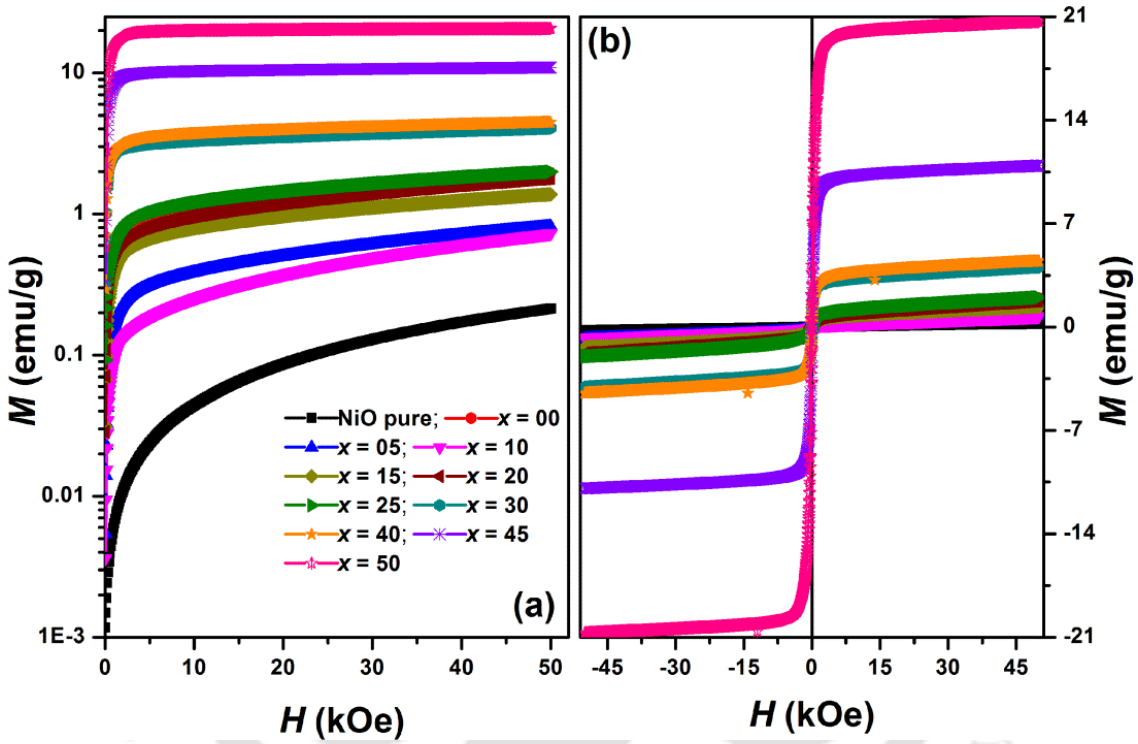

Figure 6.08: Room-temperature initial-magnetization (*IM*) curves (a) and magnetic hysteresis (*M-H*) loops (b) for NiO-Mg (*x* at.%) as a function of Mg content. *M-H* loop of pure NiO without milling is also shown for the comparison.

This leads to a clear *M-H* loop confirming the presence of room temperature ferromagnetism (RTFM) with M_S of 1.96 emu/g and H_C of 155 Oe. (iii) With increasing *x* up to 10 at.%, though the *M-H* curves show a similar feature as that of milled NiO, a significant decrease in M_S from 1.96 emu/g to 0.73 emu/g is observed. (iv) On further increasing $x > 10$, M_S increases gradually to 4.48 emu/g for *x* up to 40 at.%. (v) However, a rapid change in M_S to 10.9 and 20.7 emu/g is observed with increasing *x* to 45 and 50, respectively. H_C decreases from 155 Oe to 13.5 Oe with increasing *x* from 0 to 25, respectively, and then rises again as *x* is increased from 30 to 50 at.%.

To correlate the effect of Mg substitution and the NiO reduction on the magnetic behavior, the structural and magnetic properties of the *in-situ* nanocomposites are compared in detail. Un-milled NiO, having AFM nature due to the existence of Ni^{2+}-O^{2-}-Ni^{2+} super-exchange symmetry, exhibits no *M-H* loop, and the curve passes through origin with zero H_C [SHAH2017]. On the contrary, the 30 hrs milled NiO undergoes drastic size reduction from 50 nm to 14.5 nm along with the formation of defects, lattice distortion, broken Ni-O bonds, and oxidization of Ni^{2+} to Ni^{3+} ions.

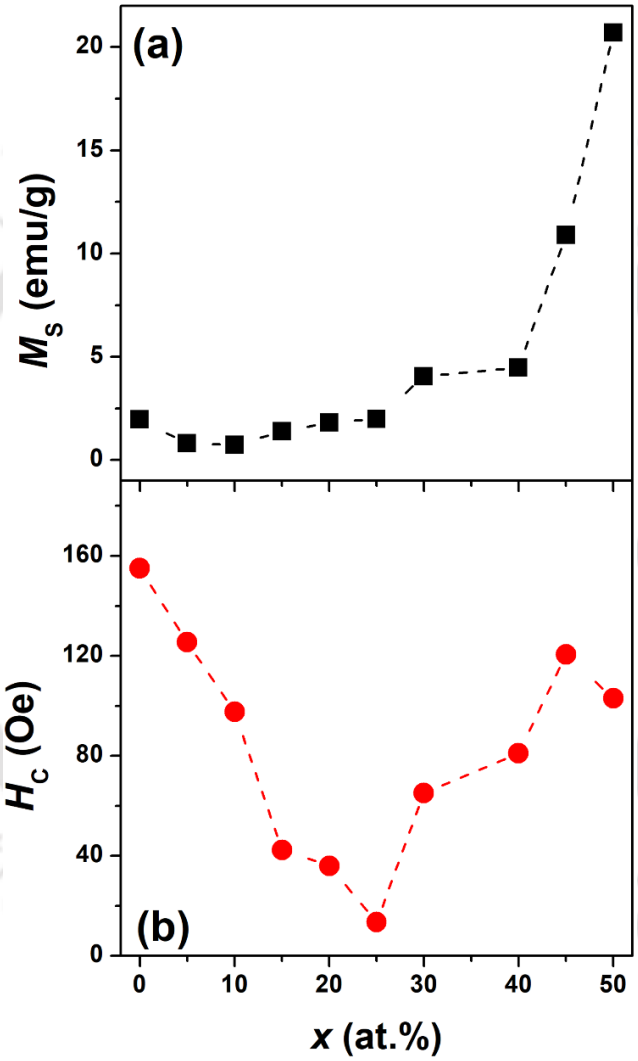

Figure 6.09: Variations of magnetization (M_S) (a) and coercivity (H_C) (b) as a function of Mg (*x* at.%) content in NiO-Mg powders.

This leads to a larger surface-area-to-volume-ratio, and a higher number of misaligned surface spins due to breaking of the Ni^{2+}-O^{2-}-Ni^{2+} super-exchange symmetry [CAZZ2003, AHMA2006, MIRO2007, MAKH2008, GAND2011, RAVI2015]. As a result, the alignment of the particle's net moment at lower field region and non-saturated RTFM with

moderate M_S of 1.96 emu/g and H_C of 155 Oe are observed. With increasing x up to 10, M_S and H_C decrease to 0.73 emu/g and 98 Oe, respectively, due to the dissolution process, which reduces induced FM behavior in NiO-Mg powder.

On further increasing x up to 25 at.%, the Mg stimulated MC reduction process of NiO gets initiated and confirms the formation of Ni with a size smaller than 10 nm. Hence, H_C decreases largely from 98 Oe to 13.5 Oe upon increasing x from 10 to 25 at.%. As displayed in Figure 6.04, the average crystal size of Ni (D_{Ni}) increases due to enhanced reduction of NiO when x is increased above 25, and therefore M_S and H_C increase largely to 20.7 emu/g and 103 Oe, respectively for x = 50 powder. This increased magnetization with the Mg substitution in NiO and the subsequent milling process could only be ascribed to a stronger magnetic interaction between nanocrystalline FM Ni particles and AFM NiO matrix in the NiO-Ni-MgO nanocomposites [MAKH2008, KRIS2016]. Nonetheless, by taking into account the AFM nature of NiO, it is apparent that the all-inclusive hysteresis behavior in the milled powders and the variation of M_S can be accredited to the formation of FM Ni from the NiO reduction. Hence, the percentage of Ni fraction is quantified explicitly by correlating M_S of milled powders with respect to the M_S of bulk Ni (~55 emu/g) [WUSH2003].

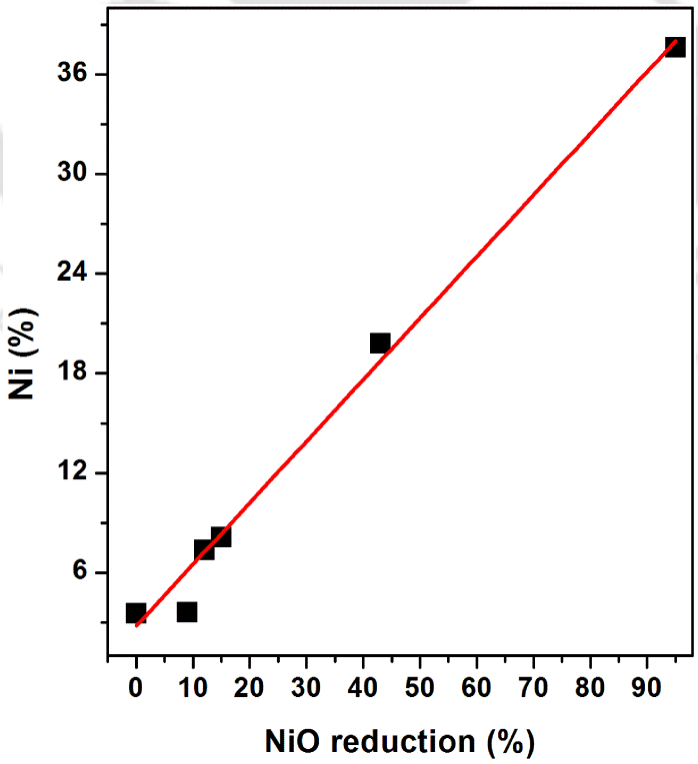

Figure 6.10: Relation between the percentage of Ni and the percentage of NiO reduction for 30 hrs milled NiO-Mg powders.

Figure 6.10 illustrates the correlation between the attained Ni fraction and the percentage of NiO reduction. It can be observed that milled NiO powder has about 3.56 wt.% Ni enriched regions due to the residual magnetic moments of uncompensated surface spins as compared to the AFM particle core and is in accordance with the previous reports [DELB2008]. The percentage of Ni increases with increasing the percentage of NiO reduction, and all the data initially fall into almost linear variation. The straight-line fit to the data reveals that Ni% for NiO-Mg powders increases at a rate of 0.4% per NiO% reduction. Furthermore, the correlation between the structural and magnetic properties reveals that the *in-situ* NiO-Ni-MgO nanocomposites exhibit RTFM even though the crystallite size of fine Ni crystals varies between 11-27 nm for NiO-Mg powders. It may be noted that the size of the Ni crystals is well below the critical size (~34 nm) of spherical Ni particles for exhibiting single-domain behavior at room temperature. Hence, the persistence of RTFM ordering in milled NiO-Mg powders below the critical size is possible only if the total magnetic anisotropy, K_{eff}, is larger than the bulk Ni equivalent [BALA2004]. Note that the major contribution to the K_{eff} in nanoscale magnetic particles can be defined using eqn.(4.04).

The microstructural studies reveal that the milled NiO-Ni-MgO nanocomposites display quite irregular morphology (see Figure 6.06), and therefore, K_{sh} is contemplated to play a dominant role as illustrated by earlier reports on smaller nanoparticles with highly anisotropic shapes [PARK2000, ROCA2006]. It is also known that for smaller particles of nanometer range, the surface anisotropy becomes more prominent with size refinement and thereby plays a crucial role in increasing K_{eff} [YANE2007, YANE2010]. As the milled powders endure severe fracture and cold welding during milling, the strain anisotropty is expected to be an inevitable part of K_{eff}. Also, due to the evolution of FM Ni from the AFM NiO matrix owing to the NiO-Mg reduction reaction, the presence of FM-AFM interfaces enhances K_{ex} in the *in-situ* nanocomposites [ROCA2006, ZHAN2009, KRIS2016]. K_{eff} is determined by fitting the *IM* curves at the high-field region using the law of approach of the magnetization to saturation (LAS) for cubic materials [KRON2003] using eqns.(4.05) and (4.06) as described in Chapter 4 and depicted in Figure 6.11 as a function of Mg content. The K_{eff} of bulk Ni has also been shown in the figure for the comparison with the milled powders. It has been observed that the values of K_{eff} vary between 0.68-5.54×10^4 J/m^3 for NiO-Mg powders. This high K_{eff} in milled NiO-Mg powders as compared to bulk Ni (0.5×10^4 J/m^3) is in accordance with the earlier mentions by Zhang *et al.* [ZHAN2009].

Such a high value of K_{eff} in the ball-milled powders comprises the combined effects of various factors such as shape, surface, strain, exchange, and magnetocrystalline anisotropy of the fine Ni nanoparticles.

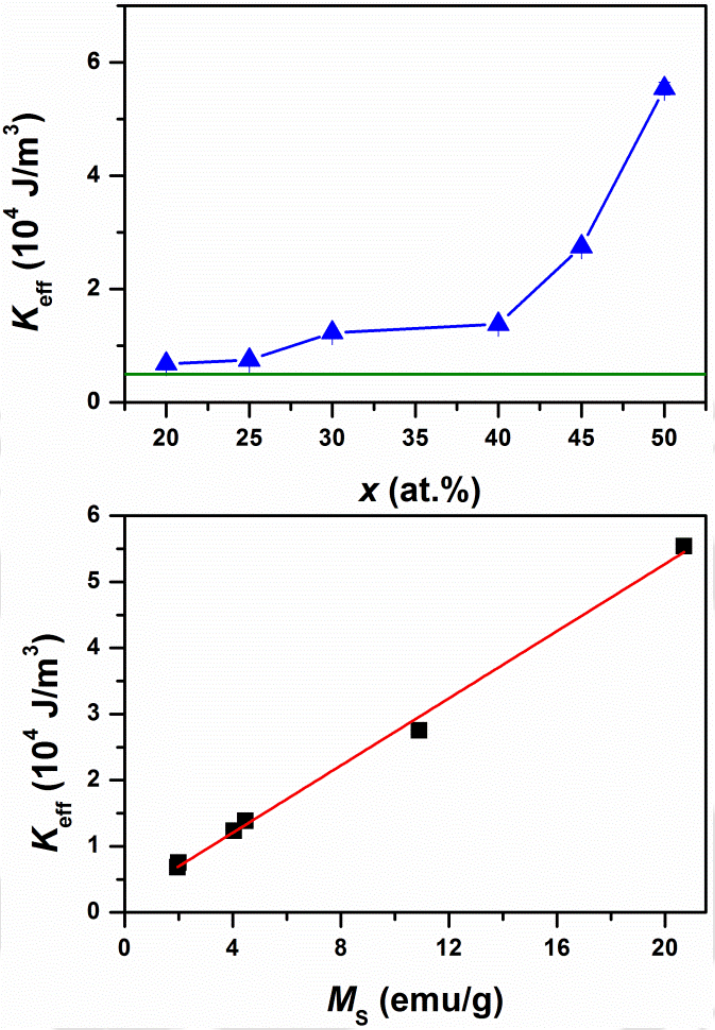

Figure 6.11: Variations of K_{eff} as a function of x and M_S for 30 hrs milled NiO-Mg powders.

To see probable correlation between K_{eff} and M_S due to the formation of Ni nanocrystallites from the NiO reduction process, the variation of K_{eff} is also plotted as a function of M_S. All the data almost fall into linear behavior, and the straight line fitting between K_{eff} and M_S reveals that K_{eff} increases at a rate of 2.54 kJ/m^3 per emu/g for the NiO-Mg powders. This anomalous enhancement of K_{eff} originates to the FM thermal stability of milled powders below the single-domain and thereby shifts the blocking temperature above room temperature regime.

In order to study the FM stability in NiO-Ni-MgO nanocomposites, high temperature thermomagnetic (M-T) measurements were carried out under an external field of 2 kOe over

the temperature range between 300 K and 1050 K. Figure 6.12 illustrates the normalized *M-T* curves of the un-milled pure NiO, milled NiO-Mg powders. In order to show the transition temperature clearly, *M-T* data of each milled powder has been normalized with respect to their individual room-temperature magnetization values.

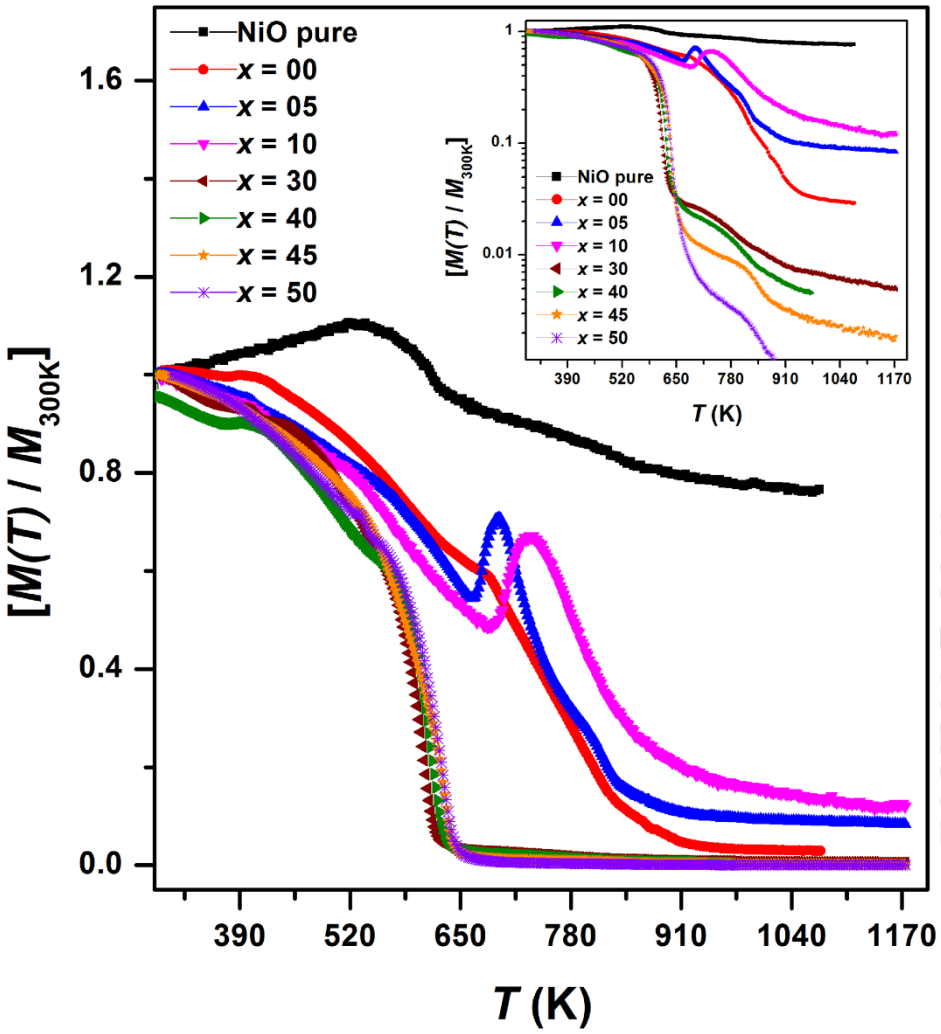

Figure 6.12: High-temperature normalized *M-T* curves measured under the applied field of 2 kOe for NiO and milled NiO–Mg (*x* at.%) powders. The inset shows the same data, but the normalized magnetization is plotted in the logarithmic scale.

In order to demonstrate the correlative high-temperature magnetic variation close to zero, the *M-T* curves are plotted in logarithmic scales in the inset. As discussed earlier, un-milled NiO exhibits AFM nature with a Néel temperature of 525 K, derived from the maximum magnetization in the *M-T* curve [THOT2013, RINA2016]. On the contrary, 30 hrs milled NiO shows two magnetic transitions: one near to T_N due to the presence of AFM NiO core and the other at 780 K as a consequence of plausible magnetic phase transition (T_C) of

induced FM phase due to the uncompensated surface spins of the magnetically disordered shell. The value of T_C in milled NiO is quite high than that of the bulk Ni (~ 630 K) and is correlated to the stress-induced due to the mechanical treatment of the powders, or the strain generated due to the interfacial Ni-NiO lattice mismatch and the induced FM Ni phase-AFM NiO core contending exchange interaction [GORR2009]. The non-smooth decrease of magnetization in the *M-T* curve evidences the presence of stress which acts more like a hydrostatic one and thereby increases T_C [LEGE1972]. On the other hand, the milled NiO-Mg powders exhibit different behaviors: (1) a substantial drop in magnetization at 640 K with a broad magnetic transition having peak temperature (T_P) at 690 K and (2) a gradual decline in magnetization up to 900 K. While the first magnetization drop could be accredited to the magnetic phase transition of Ni due to the increased Ni content, the later one is ascribed to the induced FM phase transition [KISA2014]. With increasing $x > 20$, due to the formation of enriched Ni as seen evidently from the structural studies, *M-T* curves exhibit a sharp magnetic transition at around 645 K, corresponding to T_C of Ni. With increasing x, the magnitude of magnetization dropping at 645 K increases largely at the expense of magnetization decreasing at higher temperatures. This is majorly due to the enhanced NiO reduction with increased Ni fraction at higher Mg contents. The observed results demonstrate a systematic correlation amongst the structural, vibrational, magnetic, and thermomagnetic properties of NiO-Mg based powders.

6.4. Summary:

We have carried out systematic investigations on the structural, vibrational, and magnetic properties of NiO-Mg (x at.%, x = 0-50) powders with nanocrystalline microstructures prepared by the reactive milling process in a high-energy planetary ball mill as a function of Mg content. The salient features of the milled NiO-Mg powders obtained from the current investigations are as follows:

- Structural studies revealed an *in-situ* magnesiothermic reduction of NiO with increasing x, which changes from gradual one for $x < 45$ to self-sustaining type for $x = 50$ to form NiO-Ni-MgO nanocomposites with a maximum NiO reduction of 95%.
- The process of mechanochemical reduction in NiO was confirmed from both the structural and vibrational properties of the NiO-Ni-MgO nanocomposites.

- The magnesiothermic reduction process of NiO transformed the antiferromagnetic behavior of un-milled NiO into ferromagnetic one with increasing *x*. The milled NiO-Mg powders formed a solid-solution for *x* up to 10 at.%. The NiO-Mg solid solution decreased magnetization effectively.
- A gradual reduction of NiO into NiO-Ni-MgO nanocomposites was observed due to the mechanical activation of the Mg reduction process with the NiO matrix. The increase of *x* beyond 10 at.% increased the NiO reduction up to 95% for $x = 50$ powder to yield the magnetization to 20.7 emu/g.
- The progress of NiO reduction was confirmed from the change in magnetization at room temperature and temperature-dependent magnetic behavior at high temperatures.
- The structural, vibrational, and magnetic properties exhibited a strong dependence on the relative changes in the NiO and Ni phases in the *in-situ* nanocomposites. Interestingly, the milled NiO-Mg powders showed strong room-temperature ferromagnetism due to large effective magnetic anisotropy despite having fine Ni crystals below the critical size regime.
- The controlled reduction of NiO by Mg into NiO-Ni-MgO nanocomposite is anticipated to be promising for the possible applications in the fields of ore reduction and catalysis.

Chapter 7

Summary and scope for future work

The overall summary of the notable results obtained on the structural, microstructural, vibrational, and magnetic properties of the NiO-(Al/Ti/Mg) based nanocomposites are listed in this chapter. The major highlights of the current investigations and the possibilities for future work are also summarized below:

7.1. Summary of the results:

NiO-(Al/Ti/Mg) powder mixtures were milled by using the high-energy ball milling technique under dry milling conditions and argon gas atmosphere to produce NiO-(Al/Ti/Mg) based nanocomposites. The milling was carried out (i) by varying the composition of the powder mixtures for a particular milling period (t_m), and (ii) by changing the milling periods for the selected compositions. Systematic studies of the evolution of the structure, microstructure, vibrational, and magnetic properties of NiO-(Al/Ti/Mg) based nanocomposites were carried out to understand the effect of NiO reduction dynamics.

At first, we have carried out systematic studies on the effects of Al (x at.%) content and t_m on the structural and magnetic properties of NiO-Al based nanocomposites. *In-situ* NiO-Ni-Al_2O_3 nanocomposites were prepared by using the high-energy reactive milling route under dry milling conditions and controlled argon gas environment. The nanocomposites were prepared by the effective mechanical activation of aluminothermic reduction (i) using the compositions of the raw powder mixtures as NiO-Al (x at.%) with x = 0 - 40 for a constant t_m of 30 hrs and (ii) varying t_m from 0 to 30 hrs and by fixing the compositions as NiO-Al (x at.%) with x = 0, 20, 40. The milling process in bulk NiO without Al reduced the average crystallite size down to 13.5 nm without changing the bulk structure of face-centered-cubic (*fcc*). As a result, the antiferromagnetic nature of bulk NiO transformed into ferromagnetic one with a maximum magnetization of 1.17 emu/g. This was attributed to induced ferromagnetism in 30 hrs milled NiO due to non-stoichiometry caused by the defects, size reduction, and oxidization of Ni. Non-stoichiometry in milled powders was confirmed from the XPS analysis and well supported by the color change of the powder from pale green to dark green. In contrast, the structural studies of NiO-Al milled powders confirmed (i) the formation of the non-equilibrium solid-solution of NiO-Al with a high atomic disorder for x up to 7.5 at.%; and (ii) the aluminothermic reduction process of NiO, which changed from the gradual type for $x < 25$ to a self-propagating combustion type for x = 40 powder. This increased the lattice parameter for Al content up to 10 at.% and remained constant for higher values. The crystallite size decreased initially for Al up to 5

at.% and then increased gradually up to 25 at.% Al. The induced ferromagnetic nature of milled NiO-Al (*x* at.%) powders enhanced slightly for a small addition of Al (2.5 at.%) due to size effect and decreased with increasing Al up to 7.5 at.% owing to atomic disorder. On further increasing Al content above 7.5 at.%, the ferromagnetic nature was enhanced due to the initiation of reduction reaction of NiO by Al. This formed an *in-situ* NiO-Ni-Al_2O_3 nanocomposite. A maximum of 91% of NiO reduction with a high magnetization of 24 emu/g was observed for the stoichiometric NiO-Al (40 at.%) powder. The variations of the magnetic parameters exhibited a strong dependence on the relative changes in Ni and NiO phases.

For NiO-Al (*x* at.%, *x* = 0, 20, 40) powders milled at different t_m, the aluminothermic reduction of NiO occurred gradually up to a maximum of 40% for NiO-Al (20 at.%) powders with increasing t_m. This increased the magnetization progressively from 0.12 emu/g to 4 emu/g due to the increase in Ni content to 7.5%. On the other hand, the NiO-Al (40 at.%) powder changed the reduction dynamics to a self-propagated combustion reaction type, with a critical milling time of 3 hrs to ignite the reduction reaction. Therefore, the magnetization drastically increased to 28 emu/g with a maximum of 90% NiO reduction and yielded nearly 52% of Ni. The microstructural studies revealed the formation of ferromagnetic Ni in the antiferromagnetic NiO matrix, leading to the exchange bias effect. However, the magnitude of exchange bias relied mainly on the relative fractions of Ni and NiO phases. High-temperature thermo-magnetization measurements confirmed the presence of mixed magnetic phases in the milled NiO-Al powders, and the nature of the magnetic phase transition was reflective of the amount of NiO reduction. The mechanically activated aluminothermic reduction dynamics of NiO [NiO-Al (*x* at.%)] involving two different types of reaction kinetics and the resulting structural and magnetic properties were reported for the first time. The observed results exhibited a good correlation between the structural and magnetic properties of the milled NiO-Al powders.

Secondly, the systematic investigations of the effect of the mechanochemical reduction on the structural, vibrational, and magnetic properties of NiO-Ti powders were reported. The initial powder mixtures were milled by using a high-energy ball milling technique under the dry milling condition. The nanocomposites were prepared not only by varying the compositions of the raw powder mixtures as NiO-Ti (*x* at.%) with *x* = 0 - 35 for a constant t_m of 30 hrs, but also by changing t_m from 0 to 30 hrs and by fixing the compositions as NiO-Ti (*x* at.%) with *x* = 20, 35. The structural and microstructural analyses

carried out for the 30 hrs milled NiO-Ti powders revealed the formation of NiO-Ti solid-solution for Ti up to 5 at.%, followed by a reduction of NiO into NiO-Ni-TiO_2 nanocomposite for higher Ti contents. A maximum NiO reduction of 73% was observed for the stoichiometric NiO-Ti (35 at.%) powder. The milling process effectively reduced the average crystal size of NiO largely down to 5 nm as Ti content was increased to 35 at.%. The NiO-Ti solid-solution showed a decrease in magnetization effectively from 1.96 emu/g to 1.07 emu/g, whereas the mechanochemical reduction of NiO with increased Ti content experienced an increase in magnetization up to 13.7 emu/g for the stoichiometric NiO-Ti (35 at.%) powder. The presence of Ni content in the milled NiO-Ti powders increased at a rate of 0.09% per NiO% reduction.

The detailed milling time-dependent study of NiO-Ti (x at.%, x = 20, 35) powders revealed two different reaction dynamics for varying Ti contents. The mechanochemical reduction of NiO in NiO-Ti (20 at.%) powders occurred gradually with a maximum reduction of 10% at 30 hrs of milling. On the other hand, NiO-Ti (35 at.%) powders exhibited a self-sustained process with a maximum of 94% NiO reduction at 10 hrs of milling time. The gradual reduction process of NiO in NiO-Ti (20 at.%) powder produced a maximum magnetization of 2 emu/g, while the NiO-Ti (35 at.%) powder through the self-sustained process exhibits a maximum magnetization of 24 emu/g. The structural, vibrational, and magnetic behaviors of the *in-situ* nanocomposites were found to have a strong dependence on the correlative fractions of the Ni and NiO phases. This played a crucial role in defining the overall effective magnetic anisotropy based ferromagnetic behavior in the milled powders. Thermomagnetization studies at high-temperatures revealed that the presence of mixed magnetic phases, temperature-induced structural phase changes, and gradual diminishment of the induced FM phase greatly relied on the relative Ni fractions attained from the partial NiO-Ti reduction process. The obtained results confirmed a systematic correlation between the structural, vibrational, and magnetic properties under optimized milling criteria.

Finally, the systematic investigations were carried out on the structural, vibrational, and magnetic properties of NiO-Mg based nanocomposites prepared by using the reactive milling process in a high-energy planetary ball mill and by varying the composition of the powders as NiO-Mg (x at.%) with x = 0 - 50. Structural studies revealed an *in-situ* magnesiothermic reduction of NiO with increasing x, which changed from gradual one for $x < 45$ to self-sustaining type for x = 50 to form NiO-Ni-MgO nanocomposites with a

maximum NiO reduction of 95%. The process of magnesiothermic reduction from both the structural and vibrational properties of the NiO-Ni-MgO nanocomposites was confirmed. The milled NiO-Mg powders formed a solid-solution for *x* up to 10 at.%, which decreases the induced magnetization effectively. On the other hand, a gradual reduction of NiO into NiO-Ni-MgO nanocomposites was observed due to the NiO reduction by Mg. This transformed the antiferromagnetic behavior of un-milled NiO into ferromagnetic one with increasing *x*. The increase of *x* beyond 10 at.% enhanced the NiO reduction up to 95% for the stoichiometric (*i.e.*, $x = 50$) powder to yield maximum magnetization of 20.7 emu/g. This revealed that Ni% in milled NiO-Mg powders increased at a rate of 0.4% per NiO% reduction. The progress of NiO reduction was also confirmed from the change in the magnetization at room temperature and temperature-dependent magnetic behavior at high temperatures. Interestingly, the milled NiO-Mg powders showed strong ferromagnetism with enhanced blocking temperature above room temperature due to large effective magnetic anisotropy despite having fine Ni crystals below the critical size regime. The structural, vibrational, and magnetic properties exhibited a strong dependence on the relative fractions of NiO and Ni phases in the *in-situ* nanocomposites.

The systematic investigations in the present thesis have brought out several interesting outcomes, which contributed to the understanding of (i) the reduction dynamics and the resulting physical properties of NiO-(Al/Ti/Mg) powders under different compositions and milling periods, (ii) the magnetic phase transitions, temperature-induced structural phase transistions, and the associated magnetic behaviors, and (iii) the exchange bias effect and its magnitude depending on the relative fractions of NiO and Ni phases. Furthermore, the present studies have also revealed the strong correlation between structure, vibrational, and magnetic properties of NiO-(Al/Ti/Mg) based nanocomposites prepared under optimum milling conditions. We reported the mechanochemical reduction dynamics and the correlative magnetic behavior over a wide range of compositions for the first time. The controlled reduction of NiO by Al/Mg/Ti into the *in-situ* nanocomposites is anticipated to be promising for the possible applications in the fields of ore reduction, and catalysis.

7.2. Scope for future work:

The present studies on the NiO-(Al/Ti/Mg) based nanocomposite systems prepared by using high-energy reactive ball milling revealed that how the structural, vibrational, and magnetic properties could be tailored by the atomic substitution and the mechanochemical reduction

process by varying reactant composition and milling periods. The obtained results not only exposed the potential of mechanochemical reduction processes in NiO but also established the quantification of dynamics of reduction by correlating the structural and magnetic behavior of the milled powders. This work is suitably extending for future studies, and some of those possibilities are briefly discussed below to serve as an appropriate conclusion to the present thesis work.

As the current study is focused on the varying reactant compositions and milling periods, this leads to an ample opportunity to conduct further research on other essential processing parameters, for example, ball-to-powder weight ratio and milling speed, *etc*. In such a case, it is anticipated that entirely different reduction mechanism and tunable physical properties of the *in-situ* nanocomposites. The current dissertation consists of the study of the magnetic behavior of the nanocomposites at room temperatures and high-temperature regimes. As the nanocomposites have ferromagnetic Ni nanoparticles embedded in the antiferromagnetic NiO matrix, they may possess a significant degree of exchange bias, loop shift, and coercivity enhancements. This can be studied in details via the low-temperature magnetic measurements. The field-cooled and zero-field-cooled low-temperature investigations of these powders would help in the understanding of the nature of the magnetically ordered and disordered phases at low temperatures. In the present work, the room-temperature vibrational properties of the milled powders were studied, and a systematic correlation was provided between the structural and magnetic behaviors. However, we observed a peak at around 750 cm^{-1} in the Raman spectrum of NiO-Ti based nanocomposites, which is possibly related to the splitting of phonon modes. Hence, further study is required to find the cause and nature of the Raman mode. The systematic investigation of annealed nanocomposites will be of exciting work. This study will provide the change in the nanocomposite microstructure, high-temperature magnetic behaviors, and the difference in the ratio of NiO/Ni fractions on the overall physical properties of the as-prepared nanocomposites.

References

[ABIY2007] Abiyasa A, Yu S, Lau S, Leong E.S.P, Yang H, Appl. Phys. Lett. 90 (2007) 231106.

[AHMA2006] Ahmad T, Ramanujachary K.V, Lofland S.E, Ganguli A.K, Sol. Stat. Sci. 8 (2006) 425.

[AHNI2012] Ahn I.-S, Liu X, Ahn H.-J, J. Korean Powder Metall. Inst. 19 (2012) 182.

[ANDE1950] Anderson P.W, Phys. Rev. 79 (1950) 350.

[ANDE1955] Anderson P.W, Hasegawa H, Phys. Rev. 100 (1955) 675.

[ANDE1958] Anderson P.W, Phys. Rev. 109 (1958) 1492.

[ANVA2009] Anvari S.Z, Karimzadeh F, Enayati M.H, J. Alloys compd. 477 (2009) 178.

[ARAG2012] Aragón F.H, de Souza P.E.N, Coaquira J.A.H, Hidalgo P, Gouvêa D, Phys. B 407 (2012) 2601.

[ARCI2018] Arciga-Duran E, Meas Y, Pérez-Bueno J.J, Ballesteros J.C, Trejo G, Electrochim. Acta 268 (2018) 49.

[ASTO1977] Aston M.E, Railw. Eng. 2(3) (1977) 40.

[ATZM1990] Atzmon M, Phys. Rev. Lett. 64(4) (1990) 487.

[AYTA2017] Aytan E, Debnath B, Kargar F, Barlas Y, Lacerda M.M, Li J.X, Lake R.K, Shi J, Balandin A.A, Appl. Phys. Lett. 111 (2017) 252402.

[BAHA2012] Bahadur N, Govind R. P, Chand S, Kotnala R. K, Mat. Chem. Phys. 133 (2012) 471.

[BALA1971] Balakir E.A, Bareskov N.A, Bushuev YU. G, Kosyakin A.E, Kudryavtsev YU.V, "Metalloterm. Protsessy Khim. Met. Nater. Konf." edited by A. T. Dogrinenko et al., Izdatel'stvo Nauka, Sibirskoe Otdetenie Novosibirsk, USSR (1971) 311.

[BALA2004] Bala T, Bhame S.D, Joy P.A, Prasad B.L.V, Sastry M, J. Mater. Chem. 14 (2004) 2941.

[BALA2008] Baláž P, Mechanochemistry in Nanoscience and Minerals Engineering, Springer-Verlag, Berlin, Heidelberg (2008).

[BATL2002] Batlle X, Labarta A, J. Phys. D: Appl. Phys. 35 (2002) R15.

[BEHR2011] Behrens S, Nanoscale 3 (2011) 877.

[BELI1972] Belitskus D, JOM 24 (1972) 30.

[BENA2014] Ben Amor M, Boukhachem A, Boubaker K, Amlouk M, Mater. Sci. Semi. Proc. 27 (2014) 994.

[BENT1924] Benton A.F, Emmett P.H, J. Am. Chem. Soc. 46 (1924) 2728.

[BERT1971] Bertel L.C, Morosin B, Phys. Rev. B 3 (1971) 1039.

[BHAN2019] Bhanuchandar S, Vinothkumar G, Arunkumar P, Sribalaji M, Keshri A.K, Babu K.S, J. Alloys Compd. 780 (2019) 256.

[BHUS2007] Bhushan B, Introduction to Nanotechnology. In: Bhushan B. (eds) Springer Handbook of Nanotechnology. Springer Handbooks. Springer, Berlin, Heidelberg (2007).

[BIEN2009] Biener J, Wittstock A, Baumann T.F, Weissmüller J, Bäumer M, Hamza A.V, Materials 2 (2009) 2404.

[BIH2004] Bi H, Li S, Zhang Y, Du Y, J.Magn. Magn. Mater. 277(3) (2004) 363.

[BLUN2003] Blundell S, Magnetism in Condensed Matter, Oxford University Press, Chapter 3 (2003).

[BOLD1971] Boldyrev V.V, Avvakumov E.G, Uspechi chim-iji 40 (1971) 1835.

[BOLD1986] Boldyrev V.V, J. Chim. Phys. 83 (1986) 821.

[BOTT2003] Botta P.M, Marcader R.C, Aglietti E.F, PortóLopez J.M, Script. Mater. 48 (2003) 1093.

[BOUK2012] Boukherroub N, Guittoum A, Souami N, Akkouche K, Boutarfaia S, EJP Web Conf. 29 (2012) 00010.

[BROW1940] Brown W.F, Phys. Rev. 58 (1940) 736.

[BROW1941] Brown W.F, Phys. Rev. 60 (1941) 132.

[BROW2016] Browne M.P, Nolan H, Berner N.C, Duesberg G.S, Colavita P.E, Lyons M. E.G, Int. J. Electrochem. Sci. 11 (2016) 6636.

[BRUC2003] Brückner W, Kaltofen R, Thomas J, Hecker M, Uhlemann M, Oswald S, Elefant D, Schneider C.M, J. Appl. Phys. 94 (2003) 4853.

[BUDA1998] Budarin V.L, Diyuk V.E, Zakharenko N.V, Eichis B.A, Yatsimirskii V.K, Theor. Exp. Chem. 34 (1998) 283.

[BUMB2016] Bumbrah G.S, Sharma R. M, Egy. J. Forensic Sci. 6 (2016) 209.

[CAMA2009] Camargo P.H.C, Satyanarayana K.G, Wypych F, Mater. Res. 12 (2009) 1.

[CARL1973] Carlson O.N, Progress in Extractive Metallurgy, vol. 1, Gordon and Breach, New York, (1973) pp. 187-206.

[CARN2010] Carneiro N.M, Nunes W.C, Borges R.P, Godinho M, Fernandez-Outon L.E, Macedo W.A.A, Mazali I.O, J. Phys. Chem. C 114 (2010) 18773.

[CART1961] Carter R.E, J. Chem. Phys. 34 (1961) 2010.

[CASA20141] Casati R, Bonollo F, Dellasega D, Fabrizi A,. Timelli G, Tuissi A, Vedani M, J.Alloys Compd. 615 (2014) S386.

[CASA20142] Casati R, Vedani M, Metals 4(1) (2014) 65.

[CAZZ2003] Cazzanelli E, Kuzmin A, Mariotto G, Mironova-Ulmane N, J. Phys.: Condens. Matter 15 (2003) 2045.

[CHAI2017] Chai R, Chen P, Zhang Z, Zhao G, Liu Y, Lu Y, Catal. Commun. 101 (2017) 48.

[CHAW2012] Chawla K.K, Composite materials: Science and Engineering, Springer, New York (2012).

[CHEN2018] Cheng Chung-Fu, Chen Yu-Ming, Zou Feng, Yang Kai-Chieh, Lin Tzu-Ying, Liu Kewei, Lai Chih-Huang, Ho Rong-Ming, Zhu Y, J. Mater. Chem. A 6 (2018) 13676.

[CHOI2019] Choi S, Han S.I, Kim D, Hyeon T, Kim D.-H, Chem. Soc. Rev. 48 (2019) 1566.

[CHON2004] Chong K.P, J. Phys. Chem. Solids 65 (2004) 1501.

[CLAV2014] Clavero C, Nat. Photonics 8 (2014) 95.

[COEY2010] Coey J.M.D, Magnetism and Magnetic Materials, Cambridge university press, Cambridge (2010).

[COST2009] Costi R, Cohen G, Salant A, Rabani E, Banin U, Nano Lett. 9 (2009) 2031.

[CULL2001] Cullity B.D, Stock S.R, Elements of X-ray diffraction, 3rd Ed., Pearson Education, Boston (2001).

[DAVI1999] Davis A.P, Nature 401 (1999) 120.

[DAWS2015] Dawson J.A, Guo Y, Robertson J, Appl. Phys. Lett. 107 (2015) 122110.

[DELB2008] Del Bianco L, Boscherini F, Fiorini A.L, Tamisari M, Spizzo F, Antisari M.V, Piscopiello E, Phys. Rev. B. 77 (2008) 094408.

[DELB2011] Del Bianco L, Spizzo F, Tamisari M, Castiglion A, J. Appl. Phys. 110 (2011) 043922.

[DETO2015] De Toro J.A, Marqués D.P, Muñiz P, Skumryev V, Sort J, Givord D, Nogués J, Phys. Rev. Lett. 115 (2015) 057201.

[DJEG2001] Djega-Mariadassou C, Bessais L, Nandra A, Grenèche J.M, Burzo E, Phys. Rev. B 65 (2001) 014419.

[DOBR2005] Dobrynin A.N, Levlev D.N, Temst K, Lievens P, Margueritat J, Gonzalo J, Afonso C.N, Zhou S.Q, Vantomme A, Piscopiello E, Van Tendeloo G, Appl. Phys. Lett. 87 (2005) 012501.

[DOPP2002] Sort J, Suriñach S, Muñoz J.S, Baró M.D, Nogués J, Chouteau G, Skumryev V, Hadjipanayis G.C, Phys. Rev. B 65 (2002) 174420.

[DOPP2004] Doppiu S, Langlais V, Sort J, Surińach S, Baró M.D, Zhang Y, Hadjipanayis G, Nogués J, Chem. Mater. 16 (2004) 5664.

[DUAN2012] Duan W.J, Lu S.H, Wu Z.L, Wang Y.S, J. Phys. Chem. C 116 (2012) 26043.

[DUOL2010] Duo L, Finazzi M, Ciccacci F, Magnetic Properties of Antiferromagnetic Oxide Materials: surfaces, interfaces and thin films, Wiley-VCH Verlag GmbH & Co, Weinheim (2010).

[DUPA2007] Dupas C, Lahmani M, Nanoscience: Nanotechnologies and Nanophysics, Springer Science and Business Medial, France (2007).

[DUTT2010] Dutta T, Gupta P, Gupta A, Narayan J, J. Appl. Phys. 108 (2010) 083715.

[DZYA1958] Dzyaloshinsky I, J. Phys. Chem. Solids 4 (1958) 241.

[EBRA2015] Ebrahimi-Kahrizsangia R, Abdellahi M, Bahmanpour M, Powder Technol. 272 (2015) 224.

[EBRA2016] Ebrahimi-Kahrizsangia R, Abdellahi M, Bahmanpour M, Int. J Self-Propag. High-Temp. Synth. 25 (2016) 5.

[EKUM2011] Ekuma C.E, Bagayoko D, Japn. J. Appl. Phys. 50 (2011) 101103.

[ENNA2004] Ennas G, Falqui A, Marras S, Sangregorio C, Marongiu G, Chem. Mater. 16 (2004) 5659.

[FANG1996] Fan G.J, Song X.P, Quan M.X, Hu Z.Q, Scripta Mater. 35 (1996) 1065.

[FANY2013] Fan Y, Smith K.J, Lüpke G, Hanbicki A.T, Goswami R, Li C.H, Zhao H.B, Jonker B.T, Nat. Nanotechnol. 8 (2013) 438.

[FARA1820] Faraday M, Q. J. Sci. Lit. Arts 8 (1820) 374.

[FARI1998] Faria I.C, Kleinke M, Gorenstein A, Fantini M.C.A, Tabacniks M.H, J. Electrochem. Soc. 145 (1998) 235.

[FASA2013] Fasaki I, Kandyla M, Tsoutsouva M.G, Kompitsas M, Sensors Actuat. B: Chem. 176 (2013) 103.

[FEYG2010] Feygenson M, Kou A, Kreno L.E, Tiano A.L, Patete J.M, Zhang F, Kim M.S, Solovyou V, Wong S.S, Aronson M.C, Phys. Rev. B 81 (2010) 014420.

[FEYN1960] Feynman Richard P, There's Plenty of Room at the Bottom. Engineering and Science 23(5) (1960) 22.

[FIGU2008] Figuerola A, Fiore A, Di Corato R, Falqui A, Giannini C, Micotti E, Lascialfari A, Corti M, Cingolani R, Pellegrino T, Cozzoli P.D, Manna L, J. Am. Chem. Soc. 130 (2008) 1477.

[FLYN2016] Flynn C.J, McCullough S.M, Oh E, Li L, Mercado C.C, Farnum B.H, Li W, Donley C.L, You W, Nozik A.J, McBride J.R, Meyer T.J, Kanai Y, Cahoon J.F, ACS Appl. Mater. Interfaces 8 (2016) 4754.

[FONE1959] Foner S, Rev. Sci. Instrum. 30 (1959) 548.

[FRAN2012] Frank O, Zukalova M, Laskova B, Kürti J, Koltai J, Kavan L, Phys. Chem. Chem. Phys. 14 (2012) 14567.

[FROE1990] Froes F.H, deBarbadillo J.J, Suryanarayana C, Structural Applications of Mechanical Alloying, eds. F.H. Froes and J.J. deBarbadillo, Materials Park, OH: ASM, (1990).

[FROE1995] Froes F.H, et al., Novel Techniques in Synthetics and Processing of Advanced Materials, Singh J and Copley S.M (eds.), Warrendale, PA: TMS, (1995).

[GAND2011] Gandhi A.C, Huang C.Y, Yang C.C, Chan T.S, Cheng C.L, Ma Y.R, Wu S.Y, Nanoscale Res. Lett. 6 (2011) 485.

[GAND2013] Gandhi A.C, Pant J, Pandit S.D, Dalimbkar S.K, Chan T-S, Cheng C-L, Yuan-Ron Ma, Wu S.Y., J. Phys. Chem. C 117(36) (2013) 18666.

[GAND2016] Gandhi A.C, Cheng H-Y, Chang Y-M, Lin J.G, Mater. Res. Express 3 (2016) 035017.

[GAND20171] Gandhi A.C, Chan T.S, Pant J, Wu S.Y, Nanoscale Res. Lett. 12 (2017) 207.

[GAND20172] Gandhi A.C, Wu S.Y, Nanomaterials 7 (2017) 231.

[GHOS2006] Ghosh M, Biswas K, Sundaresan A, Rao C.N.R, J. Mater. Chem. 16 (2006) 106.

[GIBS2013] Gibson E.A, Awais M, Dini D, Dowling D.P, Pryce M.T, Vos J.G, Boschloo G, Hagfeldt A, Phys. Chem. Chem. Phys. 15 (2013) 2411.

[GOKU2015] Gokul B, Saravanan P, Vinod V.T.P, Černík M, Sathyamoorthy R, Powder Technol. 274 (2015) 98.

[GOLD1898] Goldschmidt H, Vautin C, J. Soc. Chem. lnd. 17 (1898) 543.

[GOLD1908] Goldschmidt H, Weil O, US Pat. 895 (1908) 628.

[GOLD1909] Goldschmidt H, US Pat. reissue 13010 (1909).

[GOME1976] Gomes W.P, Dekeyser W, Hannay N.B (ed.), Plenum Press, New York, NY, 4 (1976) 61.

[GOOD1995] Goodenough J.B, Phys. Rev. 100 (1995) 564.

[GORR2009] Gorria P, Martínez-Blanco D, Pérez M.J, Blanco J.A, Hernando A, Laguna-Marco M.A, Haskel D, Souza-Neto N, Smith R.I, Marshall W.G, Garbarino G, Mezouar M, Fernández-Martínez A, Chaboy J, Barquín L.F, Castrillón J.A.R, Moldovan M, Alonso J.I.G, Zhang J, Llobet A, Jiang J.S, Phys. Rev. B 80 (2009) 064421.

[GOTO2013] Gotor F.J, Achimovicova M, Real C, Baláž P, Powder Technol. 233 (2013) 1.

[GOVA2014] Govan J, Gun'ko Y.K, Nanomaterials 4 (2014) 222.

[GROS2006] Grosvenor A.P, Biesinger M.C, Smart R.S, McIntyre N.S, Surf. Sci. 600 (2006) 1771.

[GUIM1998] Guimaraes A.P, Magnetism and Magnetic Resonance in Solids, Oliveira I.S, John Wiley and Sons, New York (1998).

[GUOL2014] Guoliang X, Fanglin C, Front. Energy Res. 2 (2014) 18.

[HABA1969] Habashi F, Extractive Metallurgy, Vol. 1, General Principles. Gordon and Breach, New York (1969).

[HAUS2015] Hauser A.K, Wydra R.J, Stocke N.A, Anderson K.W, Hilt J.Z, J. Control Release 219 (2015) 76.

[HEDV1938] Hedvall J.A, Reaktionsfähigkeit fester Stoffe.Verlag Barth, Leipzig (1938).

[HEID2009] Heidarpour A, Karimzadeh F, Enayati M.H, J. Alloys compd. 477 (2009) 692.

[HEIS1928] Heisenberg V.W, für. Z. Phys. 49 (1928) 619.

[HEX2013] He X, Zhong W, Chak-Tong A, Du Y, Nanoscale Res. Lett. 8 (2013) 446.

[HIDA2009] Hidayat T, Rhamdhani M.A, Jak E, Hayes P.C, Metall. Mater. Trans. B 40 (2009) 474.

[HILL2001] Hillebrecht F.U, Ohldag H, Weber N.B, Bethke C, Mick U, Weiss M, Bahrdt J, Phys. Rev. Lett. 86 (2001) 3419.

[HOAN2016] Hoa N.K, Rahman H. Abd, Somalu M. R, Mater. Sci. Forum 840 (2016) 97.

[HOCH2006] Ho C.H, Lai C.H, IEEE Trans. Magn. 42 (2006) 3069.

[HOHN2003] Höhne G.W.H, Hemminger W.F, Flammersheim H.-J, Differential scanning calorimeter, Springer Verlag, Germany (2003).

[HONC2010] Honciuc A, Laurin M, Albu S, Sobota M, Schmuki P, Libuda J, Langmuir 26 (2010) 14014.

[HONG2006] Hong N.H, Sakai J, Poirot N, Brize V, Phys. Rev. B 73 (2006) 132404.

[HORS2006] Horst C, Saito T, Smith L, Handbook of materials measurements methods, Springer, Berlin (2006).

[HOSS2012] Hosseini S.N, Karimzadeh F, Enayati M. H., Adv. Powder Technol. 23 (2012) 334.

[HOWA2018] Howard J.L, Cao Q, Browne D.L, Chem Sci. 9(12) (2018) 3080.

[HTTP0001] https://www.hikari.uni-bonn.de/research/multiferroics/spin-dynamics-of-antiferromagnetic-compounds

[HTTP0002] https://www.differencebetween.com/difference-between-point-defect-and-line-defect/

[HTTP0003] https://www.slideshare.net/harshaambati9/magnetic-materials-47590107

[HTTP0004] https://codegolf.stackexchange.com/questions/58928/3-d-antiferromagnetism

[HTTP0005] https://en.wikipedia.org/wiki/Bethe%E2%80%93Slater_curve

[HTTP0006] http://clay.uga.edu/courses/8550/XRD.html

[HTTP0007] https://en.wikipedia.org/wiki/Energy-dispersive_X-ray_spectroscopy

[HTTP0008] https://www.netzsch-thermal-academy.com/en/advanced-materials-testing/ methods/simultaneous-tga-dsc/

[HTTP0009] http://family-held.org/Rudy/publications/unpublished/papers/vsm/VMS%20Paper.htm

[HTTP0010] HSC Chemistry for Windows, version 5.1. Outokumpu, Oy, 1994.

[HUAN2011] Huang H, Tian J, Zhang W.K, Gan Y.P, Tao X.Y, Xia X.H, Tu J.P, Electrochim. Acta 56 (2011) 4281.

[HUN2012] Hu N, Composites and their properties, InTech, London, United Kingdom (2012).

[HUTC1972] Hutchings M.T, Samuelsen E.J, Phys. Rev. B 6 (1972) 3447.

[ICHI2003] Ichiyanagi Y, Wakabayashi N, Yamazaki J, Yamada S, Kimishima Y, Komatsu E, Tajima H, Physica B 862 (2003) 329.

[IVAN2000] Ivanov E, Suryanarayana C, J. Mater. Synth. Process. 8 (2000) 235.

[JAGO2009] Jagodic M, Jaglić Z, Jelen A, Lee J.B, Kim Y.-M, Kim H.J, Dolinšek J, J. Phys.: Condens. Matter 21 (2009) 215302.

[JAGT1992] Jagtap S.B, Kale B.B, Gokaran A.N, Metall. Trans. B 23B (1992) 93.

[JALA2013] Jalaly B, Bafghi M, Tamizifar M, Gotor F, Adv. Appl. Ceram. 112(7) (2013) 383.

[JANG2009] Jang W.L, Lu Y.M, Hwang W.S, Hsiung T.L, Wang H.P, Appl. Phys. Lett. 94 (2009) 062103.

[JEAN2013] Jeangros Q, Hansen T.W, Wagner J.B, Damsgaard C.D, Dunin-Borkowski R.E, Hebert C, Van herle J, Hessler-Wyser A, J. Mater. Sci. 48 (2013) 2893.

[JHAB1989] Jha B, Doctoral Dissertation, Illinois Institute of Technology, December (1989).

[JILE1997] Jiles D, Introduction to Magnetism and Magnetic Materials, Chapman and Hall, Boca Raton (1997).

[JOHL2014] Johll H, Lee M.D.K, Ng S.P.N, Kang H.C, Tok E.S, Sci. Rep. 4 (2014) 7594.

[JOHN1996] Johnson M, Bloemen P, den Broeder F, de Vries J, Rep. Prog. Phys. 59 (1996) 1409.

[JONE1994] Jones S.A, Burlitch J.M, Mater. Lett. 19 (1994) 233.

[KALI2008] Kalita M.P.C, Ph.D. Thesis, Indian Institute of Technology Guwahati, India (2008)

[KANA1959] Kanamori J, J. Phys. Chem. Solids 10 (1959) 87.

[KATE2018] Kate R.S, Khalate S.A, Deokate R.J, J. Alloys Compd. 734 (2018) 89.

[KAUP2011] Kaupp G, Cryst. Eng. Comm. 13 (2011) 3108.

[KELS2005] KelsallIan R, Hamley W, Geoghegan M, Nanoscale Science and Technology, John Wiley & Sons (2005).

[KEYA1985] Key A.J, Aust. Weld. J. Autumn (1985) 15.

[KIMK2011] Kim K.D, Oh C.S, Kil S.C, Wang J.P, Kim Y, Rev. Adv. Mater. Sci. 28 (2011) 162.

[KISA2014] Kisan B, Shyni P.C, Layek S, Verma H.C, Hesp D, Dhanak V, Krishnamurthy S, Perumal A, IEEE Trans. Magn. 50 (2014) 2300704.

[KISA20151] Kisan B, Ravikumar P, Das A, Srinivasan A, Perumal A, Sci. Lett. J. 4 (2015) 160.

[KISA20152] Kisan B, Saravanan P, Layek S, Verma H.C, Hesp D, Dhanak V, Krishnamurthy S, Perumal A, J. Magn. Magn. Mater. 384 (2015) 296.

[KISA2018] Kisan B, PhD Thesis, Indian Institute of Technology Guwahati, India (2018).

[KITT2004] Kittel C, Introduction to Solid state Physics, 7th edn Wiley, Singapore (2004).

[KOCH1991] Koch C.C, Mater. Sci. Technol. 15 (1991) 193.

[KOCH2002] Koch C.C, Nanostructured materials: Processing, properties and potential applications, Noyes Publications, New York (2002).

[KODA1996] Kodama R.H, Berkowitz A.E, McNiff Jr. E.J, Foner S, Phys. Rev. Lett. 77 (1996) 394.

[KODA19971] Kodama R.H, Makhlouf S.A, Berkowitz A.E, Phys. Rev. Lett. 79 (1997) 1393.

[KODA19972] Kodama R.H, Berkowitz A.E, McNiff Jr. E.J, Foner S, J. Appl. Phys. 81 (1997) 5552.

[KODA19991] Kodama R.H, J Magn. Magn. Mater. 200 (1999) 359.

[KODA19992] Kodama R.H, Berkowitz A.E, Phys. Rev. B 59 (1999) 6321.

[KOND1964] Kondoh H, Takeda T, J. Phys. Soc. Japan 19 (1964) 2041.

[KRAM1934] Kramers H.A, Physica 1 (1934) 182.

[KREM2012] Kremenović A, Jancar B, Ristic M, Vucinic-Vasic M, Rogan J, Pacevski A, Antic B, J. Phys. Chem. C 116(7) (2012) 4356.

[KRIS2016] Krishnan K M, Fundamentals and Applications of Magnetic Materials, Oxford University Press, United Kingdom (2016).

[KRON1959] Kronmuller H, Z. Physik. 154 (1959) 574.

[KRON2003] Kronmuller H, Fahnle M, Micromagnetism and the Microstructure of Ferromagnetic Solids, Cambridge University Press, United Kingdom (2003).

[KUBI2008] Kubias B, Fait M.J.G, Schlogl R, Handbook of Heterogeneous Catalysis, ed. Ertl G, Knozinger H, Schüth F, Weitkamp J, WileyVCH, Weinheim, 2nd edn, 2008, p. 571.

[KUCH2017] Kucharczyk B, Tylus W, Okal J, Checmanowski J, Szczygieł B, Chem. Engg. J. 309 (2017) 288.

[KWIA2000] Kwiatkowski K.C, Lukehart C.M, Handbook of Nanostructured Materials and Nanotechnology, Academic Press, chapter 8 (2000).

[KWON2000] Kwon S.K, Min B.I, Phys. Rev. B 62 (2000) 73.

[LEAM1866] Lea M.C, Br. J. Photogr. 13 (1866) 84.

[LEAM1893] Lea M.C, Am. J. Sci. 46(3) (1893) 413.

[LEEI2006] Lee I.S, Lee N, Park J, Kim B.H, Yi Y.W, Kim T, Kim T.K, Lee I.H, Paik S.R, Hyeon T, J. Am. Chem. Soc. 128 (2006) 10658.

[LEGE1972] Leger J.M, Loriers-Susse C, Vodar B, Phys. Rev. B 6 (1972) 4250.

[LESC2004] Lescop B, Jay J.P, Fanjoux G, Surf. Sci. 548 (2004) 83.

[LIAN2015] Lian Z, Wang W, Xiao S, Li X, Cui Y, Zhang D, Li G, Li H, Sci. Rep. 5 (2015) 10461.

[LIJ2004] Li J, Li F, Hu K, J. Mater. Process. Technol. 147 (2004) 236.

[LIL2006] Li L, Chen L, Qihe R, Li G, Appl. Phys. Lett. 89 (2006) 1341021.

[LINI2011] Linic S, Christopher P, Ingram D.B, Nat. Mater. 10 (2011) 911.

[LIS2006] Li S, Liu M, Bi H, Lü L, Zou W, Huang Z, Du Y, J. Alloys Compd. 425 (2006) 1.

[LIUD2017] Liu D, Li D, Yang D, AIP. Adv. 7 (2017) 015028.

[LOUD2012] Loudon J.C, Phys. Rev. Lett. 109 (2012) 267204.

[LUL1997] Lu L, Lai M.O, Zhang S, J. Mater. Proc. Technol. 67 (1997) 100.

[LUM2017] Lu M, Fatah N, Khodakov A.Y, J Mater. Sci. 52 (2017) 12031.

[LUQ2011] Lu Q, Lattanzi M.W, Chen Y, Kou X, Li W, Fan X, Unruh K.M, Chen J.G, Xiao J.Q, Angew. Chem. Int. Ed. 50 (2011) 6847.

[LUY1993] Lu Y, Renu R.C, Takacs L, Mat. Res. Soc. Symp. Proc. 286 (1993) 215.

[LUY2015] Lu Y, Guan S, Hao L, Yoshida H, Coatings 5 (2015) 425.

[MACL1994] MacLaren J.M, Victora R.H, J. Appl. Phys. 76 (1994) 6069.

[MADE1984] Madelung O (editor), Schulz M, Weiss H, Landolt-Börnstein Non-Tedrahedrally Bonded Binary Compounds, edited by, New Series, Group III, Vol. 17, Pt. G Springer, Berlin (1984).

[MAJ2017] Ma J, Zhang J, Liu C, Chen K, Phys. Lett. A. 381 (2017) 2973.

[MAKH1997] Makhlouf S.A, Parker F.T, Spada F.E, Berkowitz A. E, J. Appl. Phys. 81 (1997) 5561.

[MAKH2008] Makhlouf S.A, Al-Attar H, Kodama R.H, Solid State Commun. 145 (2008) 1.

[MAND2011] Mandal S, Menon K.S.R, Mahatha S.K, Banerjee S, Appl. Phys. Lett. 99 (2011) 232507.

[MARG2015] Marghussian V, Magnetic Properties of Nano-Glass Ceramics, Nano-Glass Ceramics, Elsevier Science Publishers, North-Holland, chapter 4 (2015).

[MARM1979] Marmeggi J.C, Baruchel J, J. Magn. Magn. Mater. 10 (1979) 14.

[MASS1991] Massarotti V, Capsoni D, Berbenni V, Riccardi R, Marini A, Antolini E, Z. Naturforsch. 46 (1991) 503.

[MAST2014] Master R, Karandikar M, Jambhale R, Tarachand, Shukla D.K, Choudhary R. J, Phase D. M, J. Physics: Conf. Series 534 (2014) 012025.

[MATT1992] Matteazzi P, Le Caër G, J. Am. Ceram. Soc. 75 (1992) 2749.

[MCCO1995] McCormick P.G, Mater. Trans., JIM 36 (1995) 161.

[MCCO1998] McCormick P.G, Froes F.H, JOM 50 (1998) 61.

[MEHR1973] Mehra O.K, Bose D.K, Gupta C.K, Metall.Trans. 4 (1973) 691.

[MEIK1956] Meiklejohn W.H, Bean C.P, Phys. Rev. 105 (1956) 904.

[MENE2010] Meneses C.T, Duque J.G.S, de Biasi E, Nunes W.C, Sharma S.K, Knobel M, J. Appl. Phys. 108 (2010) 013909.

[MILL1997] Miller E.L, Rocheleau R.E, J. Electrochem. Soc. 144 (1997) 3072.

[MIRO2007] Mironova-Ulmane N, Kuzmin A, Steins I, Grabis J, Sildos I, Pärs M, J. Phys. Conf. series 93 (2007) 012039.

[MORI1960] Moriya T, Phys. Rev. 120 (1960) 91.

[MORI2018] Moriyama T, Oda K, Ohkochi T, Kimata M, Ono T, Sci. Rep. 8 (2018) 14167.

[MORI2019] Moriyama T, Hayashi K, Yamada K, Shima M, Ohya Y, Ono T, Phys. Rev. Mater. 3 (2019) 051402(R).

[MOUL2014] Moulki H, Faure C, Michelcic M, Vuk A.S, Svegl F, Orel B, Campet G, Alfredsson M, Chadwick A.V, Gianolio D, Rougier A, Thin Solid Films 553 (2014) 63.

[MOUR2012] Mouritz A.P, Strengthening of metal alloys, Introduction to Aerospace Materials, chapter 4, Woodhead Publishing, (2012) 57.

[MULA2001] Mulas G, Monagheddu M, Doppiu S, Cocco G, Maglia F, Tamburini U.A, Solid State Ionics 141–142 (2001) 649.

[MURA1996] Murai M, Takizawa K, Soejima K, Sotouchi H, J. Electrochem. Soc. 143 (1996) 2481.

[NASU1999] Nasu T, Tokumitsu K, Miazawa K, Greer A.L, Suzuki K, Mater. Sci. Forum 312–314 (1999) 185.

[NEAL1994] Neal H. B, Theory of Magnetic Recording, Cambridge University Press, New York (1994).

[NEEL1953] Néel L, Compt. Rend. 237 (1953) 1468.

[NEEL1954] Néel L, J. Phys. Rad. 15 (1954) 225.

[NELS2003] Nelson P.A, Owen J.R, J. Electrochem. Soc. 150 (2003) A1313.

[NIS2013] Ni S, Li T, Lv X, Yang X, Zhang L, Electrochim. Acta 91 (2013) 267.

[NOGU2005] Nogués J, Sort J, Langlais V, Doppiu S, Dieny B, Munoz J.S, Suriñach S, Baró M.D, Stoyanov S, Zhang Y, Int. J. Nanotechnol. 2 (2005) 23.

[NOGU2008] Nogués J, Langlais V, Sort J, Doppiu S, Suriñach S, Baró M.D, J. Nanosci. Nanotechnol. 8 (2008) 2923.

[OHAN2000] O'Handley R.C, Modern Magnetic Materials Principles and Applications, Wiley, New York (2000).

[OLES2004] Oleszak D, J. Mater. Sci. 39 (2004) 5169.

[PADH2017] Padhan A.M, Sathish M, Saravanan P, Perumal A, J. Phys. D: Appl. Phys. 50 (2017) 21LT01.

[PARK2000] Park S.J, Kim S, Lee S, Khim Z.G, Char K, Hyeon T, J. Am. Chem. Soc. 122 (35) (2000) 8581.

[PARK2008] Park S, Ahn H-S, Lee Choong-Ki, Kim H, Jin H, Lee Hyo-Sug, Seo S, Yu J, Han S, Phys. Rev. B 77 (2008) 134103.

[PATE2004] Patel P, Roy S, Kim I.L.-Seok, Kumta P.N, Mater. Sci. Engg: B 111 (2004) 237.

[PATE2019] Patelli N, Migliori A, Morandi V, Pasquini L, Nanomaterials 9(2) (2019) 219.

[PATI2013] Patil R.A, Devan R.S, Lin J.-H, Ma Y.-R, Patil P.S, Liou Y, Sol. Energy Mater. Sol. Cells 112 (2013) 91.

[PATR2018] Patra J.K, Das G, Fraceto L.F, Campos E.V.R, Rodriguez-Torres Maria del Pilar, Acosta-Torres L.S, Diaz-Torres L.A, Grillo R, Swamy M.K, Sharma S, Habtemariam S, Shin H.-S, J. Nanobiotechnol. 16 (2018) 71.

[PAUL2008] Paul D.R, Robeson L.M, Polymer nanotechnology: Nanocomposites, Polymer, 49(15) (2008) 3187.

[PAVL2018] Pavlov E.A, Udalova T.A, Grigoreva T.F, Vosmerikov S.V, Vorsina I.A, Devyatkina E.T, Lyakhov N.Z, Bull. Russ. Acad. Sci. Phys. 82 (2018) 574–577.

[PEBL2017] Pebley A.C, Decolvenaere E, Pollock T.M, Gordon M.J, Nanoscale 9 (2017) 15070.

[PECK2011] Peck M.A, Huh Y, Skomski R, Zhang R, Allison M.D, Sellmyer D.J, Langell M.A, J. Appl. Phys. 109 (2011) 07B518.

[PECK2012] Peck M.A, Langell M.A, Chem. Mater. 24 (2012) 4483.

[PERF1967] Perfect F.H, Trans. Metall. Soc. AIME 239 (1967) 1282.

[PILB2015] Pilban J.S, Pandikumar A, Goh B.T, Lim Y.S, Basirun W.J, Lim H.N, Huang N.M, RSC Adv. 5 (2015) 14010.

[POLK1995] Polkin I.S, Froes F.H, Int. J. Mater. Prod. Tech. 10 (1-2) (1995) 106.

[POPO1993] Popovich A.A, Reva V.P, Vasilenko V.N, J. Alloys Compd. 190 (1993) 143.

[PRAB2015] Prabhu V.G, Shajira P.S, Lakshmi N, Junaid Bushiri M, J. Phys. Chem. Solids 87 (2015) 238.

[PRAJ2019] Prajapati P.K, Singh H, Yadav R, Sinha A.K, Szunerits S, Boukherroub R, Jain S.L, Appl. Surf. Sci. 467–468 (2019) 370.

[RALP2013] Ralphs K, Hardacre C, James S.L, Chem. Soc. Rev. 42 (2013) 7701.

[RAOC2004] Rao C.N.R, Müller A, Cheetham A.K, The Chemistry of Nanomaterials, Synthesis, Properties and Applications, Wiley VCH, USA (2004).

[RAPP1973] Rapp R.A, Andre E, Yurek G.J, Metall. Trans. 4 (1973) 1283.

[RASH2013] Rashidi H, Ale Ebrahim H, Dabir B, Energy Convers. Manag. 74 (2013) 249.

[RAVI2015] Ravikumar P, Kisan B, Perumal A, AIP Adv. 5 (2015) 087116.

[RICH1956] Richardson J.T, Milligan W.O, Phys. Rev. 102 (1956) 1289.

[RINA2014] Rinaldi-Montes N, Gorria P, Martínez-Blanco D, Fuertes A.B, Fernández Barquín L, Rodríguez Fernández J, de Pedro I, Fdez-Gubieda M.L, Alonso J, Olivi L, Aquilantie G, Blanco J.A, Nanoscale 6 (2014) 457.

[RINA2016] Rinaldi-Montes N, Gorria P, Martínez-Blanco D, Fuertes A.B, Puente-Orench I, Olivi L, Blanco J.A, AIP Adv. 6 (2016) 056104.

[ROBE1984] Roberts M.W, Smart R.S.C, J. Chem. Soc., Faraday Trans. 1, 80 (1984) 2957.

[ROCA2006] Roca A.G, Morales M.P, O'Grady K, Serna C.J, J. Nanotechnology 17 (2006) 2783.

[ROTH19581] Roth W.L, Phys. Rev. 110 (1958) 1333.

[ROTH19582] Roth W.L, Phys. Rev. 111(1958) 772.

[ROTH1960] Roth W. L, J. Appl. Phys. 31(1960) 2000.

[RUBI2001] Rubinstein M, Kodama R.H, Makhlouf S.A, J. Magn. Magn. Mater. 234 (2001) 289.

[RUNN2014] Runnerstrom E.L, Llordes A, Lounis S.D, Milliron D.J, Chem. Commun. 50 (2014) 10555.

[SAHA2014] Sahay R., Reddy V.J, Ramakrishna S, Int. J. Mech. Mater. Eng. 9 (2014) 25.

[SAIT2004] Saito F, Research works for 30-years: report, Institute of Multidisciplinary Research for Advanced Materials. Tohoku University, Japan (2004).

[SALG2008] Salgueiriño-Maceira V, Correa-Duarte M.A, Bañobre-López M, Grzelczak M, Farle M, Liz-Marzan L.M, Rivas J, Adv. Funct. Mater. 18 (2008) 616.

[SANG2006] Sänger I, Pavlov V.V, Bayer M, Fiebig M, Phys. Rev. B 74 (2006) 144401.

[SARM2010] Sarma S.K, Vargas J.M, De Biasi E, Beron F, Knobel M, Pirota K.R, Meneses C.T, Kumar S, Lee C.G, Pagliuso P.G, Rettori C, Nanotechnology 21 (2010) 035602.

[SCHA1989] Schaffer G.B, McCormick P.G, Scripta Metall. 23 (1989) 835.

[SCHA1990] Schaffer G.B, McCormick P.G, Metall. Trans. A21 (1990) 2789.

[SCHO2018] Schommers W, Basic Physics of Nanoscience: Traditional Approaches and New Aspects at the Ultimate Level, Elsevier, The Netherlands (2018).

[SCHU1962] Schuele W.J, Deetscreek V.D, J. Appl. Phys. 33 (1962) 1136.

[SEIF2016] Seifolazadeh A, Mohammadi S, Bull. Mater. Sci. 39 (2016) 479.

[SEKI2009] Sekimoto H, Uda T, Nose Y, Sato S, Kakiuchi H, Awakura Y, J. Mater. Res. 24(7) (2009) 2391.

[SETO2005] Seto T, Akinaga H, Takano F, Koga K, Orii T, Hirasawa M, J. Phys. Chem. B 109 (2005) 13403.

[SETO2015] Setoudeh N, Paydar M.H, Sajjadnejad M, J. Alloys Compd. 623 (2015) 117.

[SETO2016] Setoudeh N, Zamani C, Sajjadnejad M, Mater. Trans. 57 (2016) 1597.

[SETO2017] Setoudeh N, Zamani C, Sajjadnejad M, J. Ultrafine Grained Nanostruct. Mater. 50(1) (2017) 51.

[SHAA2014] Shaaban E.R, Kaid M.A, Ali M.G.S, J. Alloys Compd. 613 (2014) 324.

[SHAH2017] Shahzad F, Nadeem K, Weber J, Krenn H, Knoll P, Mater. Res. Express 4 (2017) 086102.

[SHEN1991] Shen T.D, Wang K.Y, Quan M.X, Wang J.T, Scripta Metall Mater. 25 (1991) 2143.

[SHUL1951] Shull C.G, Strausser W.A, Wollan E.O, Phys. Rev. 83 (1951) 333.

[SHYN20151] Shyni P.C, Perumal A, Sci. Lett. J 4 (2015) 146.

[SHYN20152] Shyni P.C, Perumal A, J. Alloys Compd. 648 (2015) 658.

[SIEG1967] Siegbahn K, Nordling C, Fahlman A, Nordberg R, Hamrin K, Hedman J, Johansson G, Bergmark T, Kerlsson S.E, Lindgren I, Lindberg B, Nova Acta Regiae Soc. Sci., Ser IV 20 (1967).

[SING2003] Singhal S.C, Kendall K, High Temperature Solid Oxide Fuel Cell - Fundamentals, Design and Applications. Elseviser, Oxford (2003).

[SING2011] Singh M, Ohji T, Asthana R, Mathur S, Ceramic Integration and Joining Technologies: From Macro to Nanoscale, John Wiley & Sons, United States (2011).

[SKOM2003] Skomski R, J. Phys.: Condens. Matter 15 (2003) R841.

[SKUM2003] Skumryev V, Stoyanov S, Zhang Y, Hadjipanayis G, Givord D, Nogués J, Nature 423 (2003) 850.

[SLAC1960] Slack G.A, J. Appl. Phys. 31 (1960) 1571.

[SMIT1956] Smith D.O, Rev. Sci. Instrum. 27 (1956) 261.

[SONG2017] Song S, Yao S, Cao J, Di L, Wu G, Guan N, Li L, Appl. Catal. B: Environ. 217 (2017) 115.

[SONI2001] Soni P.R, Mechanical alloying: Fundamental and applications, Cambridge International Science Publishing, UK (2001).

[SORT1999] Sort J, Nogués J, Amils X, Suriñach S, Muñoz J.S, Baró M.D, Appl. Phys. Lett., 75 (1999) 3177.

[SORT2002] Sort J, Suriñach S, Muñoz J.S, Baró M.D, Nogués J, Chouteau G, Skumryev V, Hadjipanayis G.C, Phys. Rev. B 65 (2002) 174420.

[SORT2004] Sort J, Langlais V, Doppiu S, Dieny B, Suriñach S, Muñoz J.S, Baró M.D, Laurent Ch, Nogués J, Nanotechnology 15 (2004) S211.

[SPAI2014] Spain E, Venkatanarayanan A, Comprehensive Materials Processing, Elsevier, 13 (2014) 5.

[SPAL2010] Spaldin N.A, Anisotropy, In Magnetic Materials: Fundamentals and Applications, Cambridge: Cambridge University Press (2010) 135-144.

[SRIN1984] Srinivasan G, Seehra M, Phys Rev B 29 (1984) 6295.

[STEF2018] Stefanos Mourdikoudis, Pallares R.M, Thanh T.K.N, Nanoscale 10 (2018) 12871.

[STOI1985] Stoianvic P, Romanian Pat. RO 86454 B1, 15 March 1985.

[SUGI2013] Sugiyama I, Shibata N, Wang Z, Kobayashi S, Yamamoto T, Ikuhara Y, Nature Nanotech. 8 (2013) 266.

[SUND1987] Sundareson R, Froes F.H, JOM 39 (8) (1987) 22.

[SURY2001] Suryanarayana C, Prog. Mater. Sci. 46 (2001) 1.

[SURY2004] Suryanarayana C, Mechanical alloying and Milling, Marcel Dekker, NewYork (2004).

[SVOB2004] Svoboda J, Magnetic Techniques for the Treatment of Materials, Kluwer Academic Publishers, Dordrecht (2004).

[SWIA2018] Swiatkowska-Warkocka Z, Pyatenko A, Shimizu Y, Perzanowski M, Zarzycki A, Jany B.R, Marszalek M, Nanomaterials 8(10) (2018) 790.
[TADI2010] Tadić M, Panjan M, Marković D, Mater. Lett. 64 (2010) 2129.
[TAKA1992] Takacs L, Mater. Lett. 13 (1992) 119
[TAKA1993] Takacs L, Nanostruct. Mater. 2(3) (1993) 241.
[TAKA2000] Takacs L, JOM 52 (2000) 12.
[TAKA2002] Takacs L, Prog. Mater. Sci. 47 (2002) 355.
[TAKA2007] Takacs L, J. Therm. Anal. Calorim. 90 (2007) 81.
[TAKA2013] Takacs L, Chem. Soc. Rev.42 (2013) 7649.
[TAKA2014] Takacs L, Faraday Discuss. 170 (2014) 251.
[TAMM1932] Tamman, G. Lehrbuch der Metallkunde.Verlag Barth, Leipzig (1932).
[TANN1979] Tanner B.K, Contem. Phys. 20(2) (1979) 187.
[TARL1974] Tarlinski V.D, Kapinos D.B, Neifeld O, Stroit. Truboprovodov 2 (1974) 17.
[TAYL1993] Taylor J, Dinsdale A, Z. Metallkde. 84 (1993) 335.
[THOT2007] Thota S, Kumar J, J. Phys. Chem. Solids 68 (2007) 1951.
[THOT2013] Thota S, Shim J.H, Seehra M.S, J. Appl. Phys. 114 (2013) 214307.
[TIET2015] Tietze R, Zaloga J, Unterweger H, Lyer S, Friedrich R.P, Janko C, Pöttler M, Dürr S, Alexiou C, Biochem. Biophys. Res. Commun. 468 (2015) 463.
[TILL2010] Tilley R.J.D, Defects in Solids, John Wiley & Sons, New York (2010).
[TIWA2005] Tiwari S.D, Rajeev K.P, Phys. Rev. B 72 (2005) 104433.
[TOKU1997] Tokumitsu K, Solid State Ionics 101-103 (1997) 25.
[TSCH1982] Tschakarov, C.G, Gospodinov, G.G, Bontschev Z, J. Solid State Chem. 41 (1982) 244.
[TSUZ2004] Tsuzuki T, McCormick P.G, J. Mater. Sci. 39 (2004) 5143.
[TUW2015] Tu W, Zhou Y, Li H, Li P, Zou Z, Nanoscale 7 (2015) 14232.
[TYAG2013] Tyagi M, Tomar M, Gupta V, Biosens. Bioelectron. 41 (2013) 110.
[UDHA2010] Udhayabanu V, Singh N, Murty B. S, J. Alloys Compd. 497 (2010) 142.
[VAID2009] Vaidya S, Ramanujachary K.V, Lofland S.E, Ganguli A.K, Cryst. Growth Des. 9 (2009) 1666.
[VARD2015] Vardimon R, Klionsky M, Tal O, Nano Lett. 15 (2015) 3894.
[VARN1974] Varnek V.A, Strugova L.I, Avvakumov E.G, Izvestija SO AN SSSR, seria chimiceskich nauk 2 (1974) 26.
[VENU2005] Venugopal T, Rao K.P, Murty B.S, Mater. Sci. Eng. A 393 (2005) 382.
[WANG1993] Wang L.L, Munir Z.A, Maximov Y.M, J. Mater. Sci. 28 (1993) 3693.
[WARD1994] Ward-Close C.M, Froes F.H, JOM 46 (1994) 28.
[WENW2011] Wen W, Wu J.-M, ACS Appl. Mater. Interfaces 3 (2011) 4112.
[WINK2005] Winkler E, Zysler R.D, Mansilla M.V, Fiorani D, Phys. Rev. B 72 (2005) 132409.

[WOLF2012] Wolf E.L, Medikonda M, Understanding the Nanotechnology Revolution, John Wiley & Sons, United States (2012).

[WUH2012] Wu H, Li Q, J. Adv. Ceram. 1 (2012) 130.

[WUSH2003] Wu S.-H, Chen D.-H, J. Colloid Interface Sci. 259 (2003) 282.

[WUY2012] Wu Y, Zhang Q, Wu X, Qin S, Liu J, J. Solid State Chem. 192 (2012) 356.

[XIAK2010] Xia K, Adv. Eng. Mater. 12 (2010) 724.

[XIAO2011] Xiao J, Chen B, Liang X, Zhang R, Li Y, Catal. Sci. Technol. 1 (2011) 999.

[XUC2015] Xu C, De S, Balu A.M, Ojedad M, Luque R, Chem. Commun. 51 (2015) 6698.

[XUD2017] Xu D, Mu C, Wang B, Xiang J, Ruan W, Wen F, Du X, Liu Z, Tian Y, Sci. China Mater. 60 (2017) 947.

[YAMA1966] Yamada T, Saito S, Shimomura Y, J. Phys. Soc. Japan 21 (1966) 672.

[YANE2007] Yanes R, Chubykalo-Fesenko O, Kachkachi H, Garanin D.A, Evans R, Chantrell R.W, Phys. Rev. B. 76 (2007) 064416.

[YANE2010] Yanes R, Chubykalo-Fesenko O, Evans R.F.L, Chantrell R.W, J. Phys. D: Appl. Phys. 43 (2010) 474009 1.

[YANG1994] Yang H, McCormick P.G, J. Solid State Chem. 110 (1994) 136.

[YANG1998] Yang H, McCORMICK P.G, Metall. Mater. Trans. B 29 (1998) 449.

[YAOX2014] Yao X.-J, He X.-M, Song X.-Y, Ding Q, Li Z.-W, Zhong W, Au C.-T, Du Y.-W, Phys. Chem. Chem. Phys. 16 (2014) 6925.

[YIJB2005] Yi J.B, Ding J, Zhao Z.L, Liu B.H, J. Appl. Phys. 97 (2005) 10K306.

[YIJB2007] Yi J.B, Ding J, Feng Y.P, Peng G.W, Chow G.M, Kawazoe Y, Liu B.H, Yin J.H, Thongmee S, Phys. Rev. B 76 (2007) 224402.

[ZHAN2009] Zhang H, Ding J, Chow G, Ran M, Yi J, Chem. Mater. 21 (2009) 5222.

[ZHAN2016] Zhang J, Zeng D, Zhu Q, Wu J, Huang Q, Xie C, J. Phys. Chem. C 120 (2016) 3936.

[ZHAN2017] Zhang N, Magnetic Nanocomposites and Fields for Tissue Engineering Applications, University of California, Riverside, (2017).

[ZHAN2018] Zhang T, Wu Meng-Ying, Yan Dong-Yang, Mao J, Liu H, Hu Wen-Bin, Du Xi-Wen, Ling T, Qiao Shi-Zhang, Nano Energy 43 (2018) 103.

[ZHUH2000] Zhu H.X, Abbaschian R, Mater. Sci. Engg. A 282 (2000) 1.

[ZHUY2019] Zhu Y, Liu X, Jin S, Chen H, Lee W, Liu M, Chen Y, J. Mater. Chem. A 7 (2019) 5875.

[ZYSL2006] Zysler R.D, Winkler E, Mansilla M.V, Fiorani D, Physica B 384 (2006) 277.

Publications

LIST OF PUBLICATIONS:

	Published:
[1].	Enhanced magnetic properties of NiO powders by the mechanical activation of aluminothermic reduction of NiO prepared by a ball milling process. **Aneeta Manjari Padhan**, P. Ravikumar, P. Saravanan, Perumal Alagarsamy *Journal of Magnetism and Magnetic Materials* 418 (2016) 253-259.
[2].	Mechanical activation on aluminothermic reduction and magnetic properties of NiO powders. **Aneeta Manjari Padhan**, M. Sathish, P. Saravanan and Alagarsamy Perumal *Journal of Physics D: Applied Physics* 50 (2017) 21LT01.
[3].	Structural, vibrational and magnetic properties of NiO-(Mg,Ti) powders: The effect of reduction reaction. **Aneeta Manjari Padhan**, Bhagaban Kisan, Perumal Alagarsamy *Journal of Magnetism and Magnetic Materials* 494 (2020) 165784.
[4].	Investigation of NiO reduction dynamics and properties of NiO-Ti powders. **Aneeta Manjari Padhan** and Perumal Alagarsamy *Journal of Alloys and Compounds* 840 (2020) 155769.
	Under communication/ preparation:
[5].	Effect of composition and milling time on the vibrational properties of NiO-Ti nanocomposites. **Aneeta Manjari Padhan** and Perumal Alagarsamy (Under communication)
[6].	Preparation and characterization of NiO based nanocomposites for Gas sensing applications. **Aneeta Manjari Padhan**, Thomas T Daniel and Perumal Alagarsamy (Under preparation)
[7].	Temperature-dependent magnetic properties of NiO-Ti nanocomposite powders. **Aneeta Manjari Padhan**, and Perumal Alagarsamy (Under preparation)

	Publications outside thesis work:
[8].	Size dependent properties of Ni nanopowders prepared by mechanical alloying process. **Aneeta Manjari Padhan**, M Sathish, Perumal Alagarsamy (Under preparation)
[9].	Structural, magnetic and mechanical properties of FeCoNiCuAl high-entropy alloys. **Aneeta Manjari Padhan**, Sutanuka Mohanty, P. Saravanan, Perumal Alagarsamy (Under preparation)

PAPERS ACCEPTED/PRESENTED IN CONFERENCES:

[1].	Enhanced Magnetic Properties Of NiO Nanoparticles By The Mechanical Activation Of Aluminothermic Reduction Of NiO Prepared By High Energy Ball Milling Process **Aneeta Manjari Padhan**, P. Ravikumar, P. Saravanan, Perumal Alagarsamy International conference on magnetic materials and application (IC-MagMA), 02-04 December 2015, VIT Vellore, India.
[2].	Dynamics of mechanical activation on aluminothermic reduction process and magnetic properties of NiO powders **Aneeta Manjari Padhan**, M. Satish, P. Saravanan, Perumal Alagarsamy International conference on magnetic materials and application (IC-MagMA), 01-03 February 2017, Hyderabad, India.
[3].	Dynamics of mechanical activation on aluminothermic reduction and magnetic properties of NiO powders **Aneeta Manjari Padhan**, M. Satish, P. Saravanan, and Perumal Alagarsamy Research Conclave, IIT Guwahati, 16-19 March 2017, Guwahati, India.
[4].	Mechanical activation on aluminothermic reduction process and magnetic properties of NiO powders **Aneeta Manjari Padhan**, M. Satish, P. Saravanan, and Perumal Alagarsamy International Conference on Sophisticated Instruments in Modern Research (ICSIMR-2017), IIT Guwahati, 30th June-1st July 2017, Guwahati, India,

[5].	Mechanically activated magnesiothermic reduction reaction and magnetic properties of NiO nanoparticles **Aneeta Manjari Padhan** and Perumal Alagarsamy Condensed Matter Days (CMDAYS-2017), Tezpur University, 29-31 August 2017, Assam, India.
[6].	Mechanical activation on magnesiothermic reduction reaction and magnetic properties of NiO nanoparticles **Aneeta Manjari Padhan** and Perumal Alagarsamy Research Conclave, IIT Guwahati, 8-11 March 2018, Guwahati, India.
[7].	Size dependent properties of Ni nanopowders prepared by Mechanical Alloying process **Aneeta Manjari Padhan**, M Sathish and Perumal Alagarsamy International conference on magnetic materials and application (IC-MagMA), 09-14 December 2018, NISER, Bhubaneswar, India
[8].	Mechanical activation of NiO-Ti reduction reaction and magnetic properties of NiO nanoparticles **Aneeta Manjari Padhan** and Perumal Alagarsamy Research Conclave, IIT Guwahati, 14-17 March 2019, Guwahati, India.
[9].	Dynamics of NiO reduction and properties of NiO-Ti powders **Aneeta Manjari Padhan**, Dolly Taparia, and Perumal Alagarsamy Accepted for presentation in INTERMAG 2020 Conference, May 04-08, 2020, Montréal, Canada.